



TECHNISCHE
UNIVERSITÄT
WIEN

Vienna University of Technology

DISSERTATION

Thermalization and Prethermalization in an ultracold Bose Gas

ausgeführt zum Zwecke der Erlangung des akademischen Grades eines
Doktors der technischen Wissenschaften

unter der Anleitung von

o.Univ.-Prof. Dipl.-Ing. Dr.techn. Hannes-Jörg Schmiedmayer

E141, Atominstitut

eingereicht an der Technischen Universität Wien

bei der Fakultät für Physik

von

Dipl.-Ing. Maximilian Kuhnert

Matrikelnummer: 0125642

Stadionallee 2, 1020 Wien

Wien, am 21. November 2013

.....
Maximilian Kuhnert

Gutachter:

.....
Jörg Schmiedmayer

.....
Tilman Esslinger

Contents

1. Introduction	14
2. Theoretical Background	18
2.1. Regimes of uniform one-dimensional Bose Gases	19
2.2. The trapped one-dimensional Bose gas	24
2.2.1. The quasi-condensate regime	24
2.3. Correlation properties of a homogeneous quasi-condensate	29
2.4. Describing a 1d Bose Gas as a Luttinger Liquid	35
2.4.1. The Luttinger Liquid Hamiltonian	35
2.5. Interference of two quasi-condensates described as Luttinger Liquids	37
2.5.1. Describing the Non-Equilibrium System	37
2.5.2. Initial State	40
2.5.3. Application	40
3. The Experiment - Some Practical Considerations	41
3.1. Experimental Setup Overview	42
3.1.1. Vacuum System	42
3.1.2. Atom Chip and Mounting	43
3.1.3. Bias Coils	45
3.1.4. Laser System	47
3.1.5. Imaging Systems	47
3.1.6. Experimental Control System and Data Acquisition	51
3.2. Experimental Cycle - A Brief How To Create a BEC	51
3.2.1. Experimental Cycle: An Overview	51
3.2.2. Magneto-Optical Trapping (MOT)	52
3.2.3. Optical Molasses	52
3.2.4. Optical Pumping	53
3.2.5. Loading into the Macroscopic Copper-Z Magnetic Trap	54
3.2.6. Pre-cooling and Compressing in the Macroscopic Copper-Z Magnetic Trap	57
3.2.7. Transfer into the Microscopic Atom Chip Trap	60
3.2.8. Final RF Cooling to degeneracy	60
3.2.9. Imaging	64
3.3. Fragmentation Problems	66

Contents

4. Thermometry	69
4.1. Thermal Bose Gas	70
4.1.1. Density Distributions In Situ	70
4.1.2. Density Distributions in Time-Of-Flight	72
4.2. Partially Condensed Bose Gas: Thermal Wings	72
4.3. Thermometry of pure Quasi-Condensates via Phase Fluctuations	74
4.3.1. Details of this thermometry method	75
4.4. Thermometry via Interference of two Independent Quasi-Condensates in Thermal Equilibrium	79
4.4.1. Creating the Equilibrium System	79
4.4.2. Phase Correlation Properties	79
4.4.3. Matter-wave Interference of two independent Quasi-Condensates	80
4.4.4. Contrast versus Integration Lengths	82
4.4.5. Measuring the Equilibrium Temperature via Contrast Statistics	83
5. Prethermalization	84
5.1. Definition	85
5.2. Creating the non-equilibrium system	87
5.2.1. Creating the initial quasi-condensate in thermal equilibrium	87
5.2.2. Coherent Splitting Process	87
5.2.3. Release process	90
5.2.4. Why does the splitting create a non-equilibrium situation?	90
5.3. Properties of the Prethermalized State	93
5.4. The Contrast as an observable	95
5.4.1. Information encoded in the Contrast: What do we learn?	95
5.4.2. Extracting the Contrast	95
5.4.3. Measuring the Contrast during the Splitting Ramp	96
5.4.4. Time Evolution of the Mean Contrast	99
5.5. Measuring joint FDFs	101
5.5.1. Effects of Number Imbalance	101
5.5.2. Measuring Number Imbalance	103
5.5.3. Fit Uncertainty	103
5.6. Joint FDF Results	103
5.7. Contrast squared FDF Results	105
5.7.1. Measuring the Temperature of the Relative Degrees of Freedom	110
5.7.2. Results	111
5.8. Relative Phase FDF Results	112
5.9. Contrast Decay versus Integration Length	114
5.9.1. Taking Finite Imaging Resolution into Account	114
5.9.2. Comparison of Thermal and Prethermal Correlation Lengths	116
5.10. Summary	117

Contents

6. Going beyond Prethermalization: Is there Thermalization in the long time evolution?	119
6.1. Heating and Loss Processes	120
6.1.1. Heating	120
6.1.2. Atom Loss	123
6.2. Long Time Evolution	129
6.2.1. Long time Evolution of the Mean Contrast	129
6.2.2. Long Time Evolution of the Effective Correlation Length	130
6.3. Probing Thermalization in the 1d/3d Crossover	133
6.3.1. Processes leading to Thermalization	133
6.3.2. Breaking Integrability	137
6.3.3. Results: Squared Contrast FDFs in the 1d/3d Crossover	138
6.3.4. Results: Temperature Evolution of the Relative Degrees of Freedom	140
6.3.5. Results: Evolution of Density Ripples Temperature	140
6.3.6. Results: Time Evolution of the Relative Temperature	142
6.3.7. Conclusions	142
7. Conclusion and Outlook	147
7.1. Conclusion	147
7.2. Outlook	149
A. Relevant Nature Constants	152
B. Useful Conversions	153
C. Bose-Einstein functions $g_n(x)$	154
C.1. Enhanced Computation of the Polylogarithmic / Bose-Einstein Function .	154
C.2. How to calculate $g_n(z)$ reasonably fast	155
D. Error Estimation via Bootstrapping	157
E. List of Publications	159
F. Curriculum Vitae	181

List of Figures

2.1. State diagram of a uniform 1d Bose	20
2.2. Comparison of the polylogarithmic functions $g_{1/2}(z)$ and $g_{3/2}(z)$	22
2.3. Harmonic trapping potentials and state diagram of a trapped 1d Bose gas	25
2.4. Measured Bogoliubov dispersion relation	30
2.5. Density and Phase fluctuations in a quasi-condensate	34
3.1. Vacuum Setup and Mounting of the Atom Chip	42
3.2. KRb Atom Chip Schematics	44
3.3. ^{87}Rb D ₂ -line Level Scheme	46
3.4. Laser System	48
3.5. Orientation of Imaging Systems	49
3.6. Wire Geometries for Creating Macroscopic Magnetic Traps	55
3.7. BECs generated in the Macroscopic Copper-Z Trap	57
3.8. Condensate Expansion	58
3.9. BEC Formation	58
3.10. Magnetic Trapping Potential of Compressed Copper-Z Trap	60
3.11. Overview of the Magnetic Trapping Cycle	61
3.12. Evaporation Sequence	62
3.13. Phase-Space Density during Evaporation	63
3.14. Picture of the Experimental Apparatus	66
3.15. Multiple Condensation in Fragmentation Minima	67
3.16. Fragmentation Effects versus Distance to Chip	68
4.1. Transverse Thermal Density Distributions in Time-Of-Flight	71
4.2. Partially Condensed Longitudinal Density Profile	73
4.3. Emergence of density ripples in time-of-flight	74
4.4. Averaged $g^{(2)}$ correlation functions of density fluctuations	77
4.5. $g^{(2)}$ behaviour	77
4.6. Equilibrium squared contrast distributions	83
5.1. Simulation of the double-well potential in RWA approximation	88
5.2. Schematic drawing of the rf induced horizontal double-well setup	89
5.3. Calculated and measured density profiles before and after splitting	90
5.4. Schematic drawing of the splitting process and subsequent evolution	92
5.5. Probing the Contrast along the longitudinal direction	96
5.6. Fringe spacing and splitting distance in the final part of the splitting ramp	97
5.7. Scaling of Contrast with respect to fringe spacing and splitting distance	98

List of Figures

5.8. Time Evolution of the Mean Contrast	98
5.9. Time Evolution of the Mean Contrast compared to TLL Theory	100
5.10. Mean Contrast Decay at different temperatures	100
5.11. Measuring joint FDFs	102
5.12. Joint FDFs	104
5.13. Squared Contrast FDFs I	106
5.14. Squared Contrast FDFs II	108
5.15. Squared Contrast FDFs III	109
5.16. Reduced- χ^2 Comparison	110
5.17. Scaling of the prethermalized Temperature	111
5.18. Phase FDFs	112
5.19. Phase Spread versus Time	113
5.20. Contrast Decay versus Length Scale	115
5.21. Comparison of prethermal and thermal Phase Correlation Lengths	117
6.1. Estimating heating rates in undressed traps	121
6.2. Estimating heating rates in equilibrium system in the dressed trap	122
6.3. Density loss versus initial density	125
6.4. Estimating 1- and 3-body loss rate in dressed trap	126
6.5. Mean Contrast Evolution for Long Times	129
6.6. Correlation Loss on Long Time Scales I	130
6.7. Correlation Loss on Long Time Scales II	131
6.8. Comparison of Loss of Correlations	132
6.9. Energy redistribution in 1d	134
6.10. Calculated Two- and Three-Body Thermalization Rates	136
6.11. Breaking integrability	137
6.12. FDF Long Time Evolution in the Effectively 1d Regime	139
6.13. FDF Long Time Evolution in the 1d/3d Crossover	139
6.14. Scaling of Final Equilibrium Temperature	140
6.15. Scaling of Density Ripples Temperature after Splitting	141
6.16. Scaling of Final Density Ripples Temperature	141
6.17. Two-Body Thermalization Graphs	143
6.18. Measured Thermalization Rates versus initial Temperature	144
6.19. Measured Thermalization Rates versus initial Phase Correlation Length	145
6.20. Measured Thermalization Rates versus Density	145
6.21. Schematic drawing relaxation processes	146
7.1. Phase Profiles	149
7.2. Virtual Three-Body Rate	150
C.1. Bose-Einstein functions $g_n(x)$	155
D.1. Bootstrapped Histograms	158

List of Tables

3.1. Parameters of Installed Imaging Systems	50
5.1. Typical trap parameters before and after splitting	93
5.2. Energy distribution between common and relative modes	94
A.1. Nature Constants	152
B.1. Useful Conversions	153

List of Acronyms

<i>AOM</i>	<i>acousto-optic modulator</i>
<i>APS</i>	<i>american physical society</i>
<i>BEC</i>	<i>Bose-Einstein Condensate</i>
<i>BK7</i>	<i>Borosilikat-Kronglas, borosilicate glass</i>
<i>BNC</i>	<i>Bayonet Neill-Concelman</i>
<i>CAD</i>	<i>Computer-Aided Design</i>
<i>CCD</i>	<i>charge-coupled device</i>
<i>cMOT</i>	<i>compressed magneto-optical trap</i>
<i>DDS</i>	<i>Direct Digital Synthesizer</i>
<i>DOF</i>	<i>degrees of freedom</i>
<i>ETH</i>	<i>eigenstate thermalization hypothesis</i>
<i>FWHM</i>	<i>Full Width at Half Maximum</i>
<i>GGE</i>	<i>generalized Gibbs ensemble</i>
<i>KAM theorem</i>	<i>Kolmogorow-Arnold-Moser theorem</i>
<i>mMOT</i>	<i>mirror MOT, the MOT created below the atom chip</i>
<i>MOT</i>	<i>magneto-optical trap</i>
<i>OU</i>	<i>Ornstein-Uhlenbeck</i>
<i>PCF</i>	<i>phase correlation function</i>
<i>PSF</i>	<i>point-spread-function</i>
<i>QCD</i>	<i>Quantum Chromodynamics</i>
<i>RWA</i>	<i>rotation wave approximation</i>
<i>SQUID</i>	<i>superconducting quantum interference device</i>
<i>TLL</i>	<i>Tomonaga-Luttinger Liquid</i>

List of Acronyms

<i>TOF</i>	<i>time-of-flight</i>
<i>UHV</i>	<i>ultra-high vacuum</i>
<i>USB</i>	<i>Universal Serial Bus</i>
<i>ZMNS</i>	<i>Vienna Center for Micro- and Nanostructures</i>
<i>FDF</i>	<i>Full Distribution Function</i>
<i>KRb</i>	<i>Kalium Rubidium Experiment (Potassium Rubidium Experiment)</i>

Aknowledgements - Danksagungen

The amount of people that have contributed to this thesis is so numerous that I am having a hard job in writing this aknowledgement section without missing anyone.

Let me start by thanking my main PhD supervisor Jörg Schmiedmaier for his leadership, endless discussions, his deep physical insights and giving me the opportunity to work in a fruitful and international research environment. Furthermore, there was always room and possibilities to exchange and present the latest research results at international conferences, much faciliating and accelerating the research process.

I would also like to thank all current and past members of the atom chip group, for providing a good, almost friendshiplike, working atmosphere, where everyone was keen on being helpful and supportive.

Let me thank Takuya Kitagawa and Eugene Demler for a great collaboration, for establishing and sharing the Luttinger Liquid theory code and the many helpful discussions. I want to thank my external TAC, Tilman Esslinger, for making my research stay at ETH possible, which was indeed a great, unforgettable experience for me.

Let me thank Jun Ye and the cold molecules subgroup for hosting me at JILA and the great time there.

It should be noted that Stephan Schneider always managed to keep buracracy tasks away from our team, which was indeed very helpful and will not be forgotten.

I would like to thank Igor Mazets for sharing his dark humor and theoretical insights and especially for never getting anoed by us experimentalists asking questions.

Let me now come to my closest team members, namely the so-called Fermi (don't miss the Fermions!) team.

At first, I would like to thank David Adu Smith for his great support and advice in working on this project and writing up this thesis.

I am very grateful that Remi Geiger joined our team, where he shared his strong enthusiasm and immediately became integrated into the team, thereby leading to a great collaboration.

Many thanks go to my team mates Michael Gring and Tim Langen. Both for invaluable discussions and team work (only together we have tamed the bitch!). Michael especially for his strong enthusiasm in supplying us with high-resolution imaging systems and Tim for sharing his deep physical insights, his knowledge of Inkscape, his humour and uncounted funny youtube clips. I am always going to miss Schnitzel Wednesday.

Together we were very grateful for sharing our office with Christian Koller (providing a cupboard full of sweets and cookies in case of emotional emergencies and further being responsible for proclaiming Fridays). He always managed to help us see the sweet and funny side of life.

Aknowledgements

Let me also thank our next generation of PhD studets, Thomas Schweigler and Bernhard Rauer, for taking over the experiment and continuing our work.

Great thanks go to Martin Göbel and Christoph Graf vom Hagen for the initial design and setup of the KRb experiment.

I aknowledge support through the FWF grants P22590-N16 and M1040-N16, the FWF Doctoral Programme CoQuS(W1210), the Wittgenstein Prize, and the European Union through the integrating project AQUITE and within the Seventh Framework Program the QIBEC program, Siemens Austria, and the City of Vienna.

Sincere thanks are given to all my friends, especially the swarm lord Lukas, for not loosing faith in me and staying in touch even though I was basically busy all time over.

Ich danke meinen geduldigen Eltern und Verwandten für ihre großartige Unterstützung.

hml

Abstract

Atom chips consist of microscopic current carrying structures that generate magnetic trapping potentials for ultracold neutral atoms. These atom chips provide a high design flexibility of possible trap geometries, making the creation of highly anisotropic trapping potentials feasible. The resulting magnetic traps are characterized by a high isolation from the environment and are used to create degenerate, one-dimensional (1d) Bose gases. On typical experimental time scales, these 1d Bose gases can be described as practically closed quantum many-body systems. By applying a rapid quantum quench, the many-body system is brought out of thermal equilibrium and the resulting dynamics are studied via the statistical properties of matter-wave interference measurements. These measured quantum statistical distributions reveal that thermalization of this effectively integrable 1d Bose gas happens in a two-step process. First, the system rapidly dephases to a prethermalized state, characterized by thermal-like correlation properties, which are still distinctly different from the true thermal equilibrium state. Second, on a much longer time scale, the measured distribution functions indicate a further decay to the true thermal equilibrium state.

Furthermore, by studying a highly non-equilibrium system via matter-wave interferometry, the underlying multimode dynamics, characterizing one-dimensional quantum systems, are revealed. This thesis shows that these dynamics are essential in establishing the prethermalized state and that its properties are defined by the quantum shot noise of the splitting process.

In particular, this thesis discusses the experimental setup used to obtain degenerate 1d Bose gases, summarizes thermometry methods applied throughout this work and reports the first direct experimental observation of prethermalization in a multimode system, generated by a fast, phase-coherent splitting of a 1d Bose gas into a symmetric double-well potential. Finally, the long-time evolution of the non-equilibrium system is studied in detail in the 1d/3d crossover regime, strongly indicating a complete relaxation into the thermal equilibrium state. This work confirms that the observed relaxation time scales can be attributed to two-body thermalizing collisions, lifting the integrability of the system.

In conclusion, this work aims at improving the understanding of quantum thermalization processes in integrable and nearly-integrable systems in the 1d and 1d/3d crossover regimes. Apparently, the general paths to thermal equilibrium in nearly-integrable systems are indirect and complex. This work provides an in depth experimental study of the relaxation dynamics of a highly non-equilibrium system, thereby addressing fundamental questions of ergodicity and thermalization in the context of nearly-integrable quantum systems.

Zusammenfassung

Sogenannte Atom Chips bestehen aus mikroskopisch kleinen, stromführenden Strukturen, die magnetischen Fangpotentiale für ultrakalte, neutrale Atomen erzeugen. Diese Atom Chips bieten eine hohe Flexibilität der möglichen Fallen-Geometrien, die die Erzeugung von stark anisotropen, effektiv eindimensionalen Fangpotentialen ermöglichen. Die resultierenden magnetischen Fallen zeichnen sich durch eine hohe Isolation von der Umwelt aus und werden verwendet um entartete, eindimensionale (1d) Bose Gase experimentell zu realisieren. Auf typischen experimentellen Zeitskalen können diese integrierbaren Systeme als praktisch abgeschlossene Quanten-Vielteilchensystemen beschrieben werden. Durch einen schnellen "Quantum-Quench" wird das Vielteilchensystem aus dem thermischen Gleichgewicht gebracht und die daraus resultierende Dynamik mittels Materiewellen-Interferenz untersucht. Die beobachtbare Dynamik zeigt, dass Thermalisierung dieses 1d Bose Gases in einem zweistufigen Verfahren geschieht. Zuerst dephasiert das System in einen präthermalisierten Zustand, der zwar durch thermische Eigenschaften gekennzeichnet ist, aber immer noch deutlich von dem wahren thermischen Gleichgewichtszustand abweicht. Erst auf einer zweiten, viel längeren Zeitskala bringen Zwei-Körper-Streuprozesse das System in den wahren thermischen Gleichgewichtszustand.

Diese Arbeit beschreibt den zur Erzeugung entarteter 1d Bose Gase verwendeten Versuchsaufbau, fasst die verwendeten Thermometrie Methoden zusammen und diskutiert ausführlich die erste direkte experimentelle Beobachtung von Präthermalisierung in einem multimodalen System. Weiters wird die Entwicklung des Nicht-Gleichgewichts-Systems auf langen Zeitskalen ausführlich untersucht. Die experimentellen Beobachtungen zeigen Anzeichen einer vollständigen Relaxierung in den thermischen Gleichgewichtszustand. Ein Vergleich der gemessenen Thermalisierungsraten mit existierenden Relaxationsmodellen zeigt dass Zweikörper Stöße den treibende Mechanismus im 1d/3d Übergangsregime darstellen.

Das Studium eines Nicht-Gleichgewichts-Systems mittels Materiewellen-Interferometrie ermöglicht eine direkte Beobachtung der durch Multimoden Dynamik charakterisierten eindimensionalen Quantensysteme und führt langfristig zu einem besseren Verständnis der stattfindenden Thermalisierungsprozesse in integrierbaren Quanten-Systemen in 1d und im 1d/3d Übergangsregime.

1 Chapter 1.

Introduction

“A mind needs books as a sword needs a whetstone, if it is to keep its edge.”

- Tyrion to Jon

In 1995, tremendous experimental progress in cooling techniques of neutral atoms led to the observation of Bose Einstein condensation in dilute gases [Anderson 95, Davis 95, Bradley 95]. This was the starting point of a new, exciting research field of atomic physics. Numerous experimental tools to probe and manipulate the ultracold atomic samples were soon developed. These ultracold systems are characterized by precise experimental control and high tuneability of fundamental parameters as well as their good isolation from the environment. Due to this high amount of experimental control, these ultracold gases were soon recognized as ideal test setups for more complicated systems of similar physics in the sense of quantum simulators as originally proposed by Richard Feynman in 1981 [Feynman 82, Cirac 12]¹. One of the most prominent examples coming from condensed-matter physics is to apply ultracold gases to study superconductivity and superfluidity.

At first, the community focused mainly on studying equilibrium physics or small perturbations from equilibrium states, where the calculations can still be based on perturbation theory. Further experimental and theoretical efforts were needed to extend the work towards non-equilibrium quantum physics [Greiner 02, Schollwöck 05, Kinoshita 06, Sadler 06, Hofferberth 07, Donner 07, Widera 08, Haller 09, Strohmaier 10, Trotzky 12], which are much harder to model theoretically due to the involved vastly different energy scales [Strohmaier 10], resulting in the need to formulate truly non-equilibrium theory descriptions [Gasenzer 09]. From an experimental point of view, these ultracold systems are

¹simulating one complex quantum system with another

1. Introduction

ideally suited to examine non-equilibrium physics due to their good isolation from environment, their low energy scales and resulting slow relaxation time scales on the order of milliseconds as well as the ability to reproducibly create well-defined far from equilibrium states in the experiment. Furthermore, it became possible to realize lower dimensional systems. Especially, one dimensional (1d) systems have been the playground of theorists throughout the last century [Cazalilla 11] and now started to become experimentally feasible in ultracold atomic systems [Görlitz 01, Schreck 01, Greiner 01, Moritz 03]. These 1d systems show a high complexity and rich physics [Lieb 63b, Lieb 63a, Giamarchi 04, Kitagawa 10] and open the path to study fundamental questions in well controlled setups. One of the most intriguing questions in the context of quantum statistics is how a non-equilibrium state relaxes towards thermal equilibrium [Rigol 08, Polkovnikov 11].

The aim of this project is to study the relaxation dynamics of an isolated quantum system and, specifically, to understand the pathways and limitations of thermalization in a nearly integrable Bose gas in the 1d/3d crossover regime [Petrov 00, Kheruntsyan 05, Armijo 11b]. In classical statistical mechanics, thermalization and ergodicity are generally accepted fundamental concepts [Neumann 29, Landau 96]. For the special class of integrable and nearly-integrable systems, the inability to relax to a thermal state has been understood in terms of the classical KAM theorem [Arnol'd 63]. However, how the concept of thermalization and how the lack thereof in integrable systems can be properly translated into quantum physics is still elusive [Polkovnikov 11] and has led to the formulation of the eigenstate thermalization hypothesis (ETH) [Deutsch 91, Srednicki 94, Rigol 08] and the quantum ergodic theory [Neumann 10, Goldstein 10], both valid for nonintegrable systems. Relaxation of integrable quantum many-body systems is constrained by the many involved constants of motions and is expected to lead to dephased quasi-stationary states, described by Generalized Gibbs Ensembles [Rigol 07]. How small deviations from integrability affect the relaxation and may ultimately lead to thermalization is an important unresolved question, which has triggered a lot of theoretical attention [Manmana 07, Rigol 09a, Roux 09, Biroli 10, Kollar 11] but is still lacking experimental studies so far.

Interestingly, classical [Bonini 99] and quantum [Gasenzer 05, Bañuls 11] statistical calculations of isolated systems predict that the resulting pathways towards true thermal equilibrium, are indirect and complex. Roughly speaking, these pathways can be differentiated into two time scales, originating from different underlying processes. The first process being in general associated with dephasing, the second process being associated with particle scattering.

Thus far, experimental studies of highly non-equilibrium quantum systems near an integrable point are scarce and do not show the onset of thermalization [Kinoshita 06]. This thesis demonstrates that the relaxation of a nearly-integrable Bose gas indeed consists of two processes. First, a rapid dephasing process establishes a prethermalized state [Bistrizter 07, Kitagawa 10, Kitagawa 11]. Second, on much longer time scales, scattering processes establish the true thermal equilibrium.

The phenomenon of prethermalization was first introduced in 2004 by J. Berges [Berges 04] in the context of high-energy heavy-ion physics and has since been suggested for a large number of other systems, ranging from the dynamics in the early universe

1. Introduction

[Podolsky 06] to ultracold systems [Kollath 07, Moeckel 10, Eckstein 09b, Eckstein 09a, Mathey 10, Barnett 11]. Prethermalization is characterized by the rapid establishment of a quasi-steady state, where some observables already exhibit thermal-like properties. Prethermalization is understood as a long-lived fixed-point [Berges 08] during the evolution, which appears for a large set of initial conditions. This thesis discusses the first direct observation of a prethermalized state and continues with the study of the long time evolution to a thermal equilibrium state.

Structure of this thesis

This thesis is structured as follows:

- Chapter 2 reviews the relevant theoretical background of weakly-interacting Bose gases in one-dimension on which the following chapters will rely on.
- Chapter 3 emphasizes the experimental techniques used to create a Bose condensed atomic cloud in an effectively one-dimensional trapping geometry on an atom chip. The chapter starts with a summary of the experimental setup, continues with the cooling procedure needed to achieve degeneracy and concludes with an insight into atom chip technology.
- In chapter 4, the various thermometry methods relevant for this work are reviewed. Thermal gases obey the Maxwell-Boltzmann momentum distributions in free expansion, partially condensed samples make bimodal fits necessary and, finally, in the case of quasi-condensates the strength of inherent phase-fluctuations are used to determine the temperature.
- Chapter 5 presents the main result of this work, the first direct experimental observation of the prethermalization phenomenon and the underlying multimode dynamics present in one-dimensional quantum systems. The quantum quench creating a well-defined initial state far away from equilibrium conditions is explained in detail. Matter-wave interferometry is used to study the resulting relaxation to the prethermalized state. In particular, the full quantum probability distributions are used to characterize the evolution of the system. The evolution is well captured by a Luttinger-Liquid model, which shows that the system dephases rapidly to a prethermalized state, a state showing thermal-like properties for some observables, yet distinctly different from true thermal equilibrium.
- Chapter 6 studies the long-time evolution of the prethermalized system in the 1d/3d crossover regime, and reports on the results of this work in progress. If thermalization is present in the 1d system, it is supposed to happen on a second much longer time scale than the rapid prethermalization. By going from the truly 1d to the 1d/3d crossover regime, thermalization due to two-body processes is expected to happen on experimentally accessible time scales and indeed a second loss of correlations is observed. A comparison to a two-body thermalization model shows qualitative agreement.

1. Introduction

- In chapter 7, the conclusions of the present work are discussed. Finally, an outlook of possible future research topics is presented.

2

Chapter 2.

Theoretical Background

“First you guess. Don’t laugh, this is the most important step. Then you compute the consequences. Compare the consequences to experiment. If it disagrees with experiment, the guess is wrong. In that simple statement is the key to science. It doesn’t matter how beautiful your guess is or how smart you are or what your name is. If it disagrees with experiment, it’s wrong. That’s all there is to it.”

- Richard P. Feynman, lecture at Cornell University 1964

Abstract

This chapter focuses on the theory description of weakly-interacting Bose gases in one-dimension (1d). It starts with a derivation of temperature and interaction dependant regimes of uniform Bose gases with contact like interactions. The following subsection continues to extend the theoretical description to finite-size, harmonically trapped systems, which is more adequate to capture the conditions found in the experiment. The necessary ingredients for the successful, experimental realization of an effectively 1d system are presented and the properties of a 1d quasi-condensate, formed in a 1d trap, are discussed in detail. Going back to a homogeneous description, a Bogoliubov approach is introduced to derive the strength of phase and density fluctuations. The next subsection introduces a low-energy Luttinger Liquid description of a 1d Bose gas, which is finally used as a tool to model the evolution of interference patterns between two quasi-condensates after a rapid quantum quench.

2.1. Regimes of uniform one-dimensional Bose Gases

Let's assume, we want to describe a system of N interacting Bosons of mass m in one dimension (1d). Furthermore, let's include 2-body interactions through the inter-atomic potential $V_{int}(z_i - z_j)$. The most general form of a Hamiltonian for interacting Bosons placed in an external potential V_{ext} can then be written as

$$\hat{H} = - \sum_i^N \left[\frac{\hbar^2}{2m} \frac{\partial^2}{\partial z_i^2} + V_{ext}(z_i) \right] + \sum_{i < j=1}^N V_{int}(z_i - z_j), \quad (2.1)$$

with the atomic mass m , the reduced Planck's constant \hbar and z_i being the position of the i th particle.

To describe a uniform system we choose $V_{ext}(z) = 0$. In the ultracold regime, we further assume that the exact functional form of $V_{int}(z)$ can be simplified by a repulsive, delta-function (point-like) potential $V_{int}(z) = \frac{g}{2} \delta(z)$, which is intuitively true if the relevant scattering lengths¹ are much smaller than the inter-particle distance $n_{3d}^{-1/3}$ and the thermal deBroglie wavelength $\lambda_{dB} = \sqrt{\frac{2\pi\hbar^2}{mk_B T}}$. A more stringent discussion can be found in [Leggett 01]. Thus by neglecting the short range inter-atomic physics, we arrive at the well-known Lieb-Liniger Hamiltonian [Lieb 63b, Lieb 63a].

$$\hat{H} = - \sum_i^N \frac{\hbar^2}{2m} \frac{\partial^2}{\partial z_i^2} + \frac{g}{2} \sum_{i < j=1}^N \delta(z_i - z_j), \quad (2.2)$$

where $g > 0$ is the 1d coupling constant in Jm. The Lieb-Liniger Hamiltonian has been shown to be analytically solvable and integrable² using a Bethe-Ansatz [Bethe 31]. Its eigenfunctions are linear combinations of plane waves.

The interaction strength is characterized by the Lieb-Liniger parameter

$$\gamma = \frac{mg}{\hbar^2 n}, \quad (2.3)$$

which is the ratio of the interaction energy $\propto gn$ and the characteristic kinetic energy per particle $\propto \frac{\hbar^2 \bar{k}^2}{m} = \frac{\hbar^2 n^2}{m}$ [D.S. Petrov 04], with the linear density n , defined by $N = \int ndz$ and approximating the mean particle separation via $r = n^{-1}$, resulting in the estimate for the mean wavevector $\bar{k} = n$. For $\gamma \ll 1$, interactions are small, leading to the weakly interacting regime, whereas $\gamma \gg 1$ corresponds to the strongly interacting (Tonks-Girardeau) regime, where high correlations are present. Counterintuitively, the interaction strength in a 1d system scales inversely proportional to the linear density n , due to the

¹in the ultracold regime s-wave scattering processes are dominant as higher order scattering processes are essentially frozen out [Weidemüller 03]. For ^{87}Rb in the $F = 2$, $m_F = 2$ state $a_s \approx 5$ nm, which is much smaller than typical experimental values of $\lambda_{dB} = 0.4 - 1.4 \mu\text{m}$ (20 - 200 nK). Typical experimental densities are 10^{14} cm^{-3} , which gives typical inter-particle separations of 200 nm.

²It should be noted that also Hamiltonians for other functional forms of interactions have been shown to be integrable. One example being the interaction potential $V_{int} = g(z - z')^{-2}$, studied by [Calogero 69]. As already mentioned, most relevant for our experiment parameters will be contact-like interactions, so we continue with the Lieb-Liniger Hamiltonian.

2. Theoretical Background

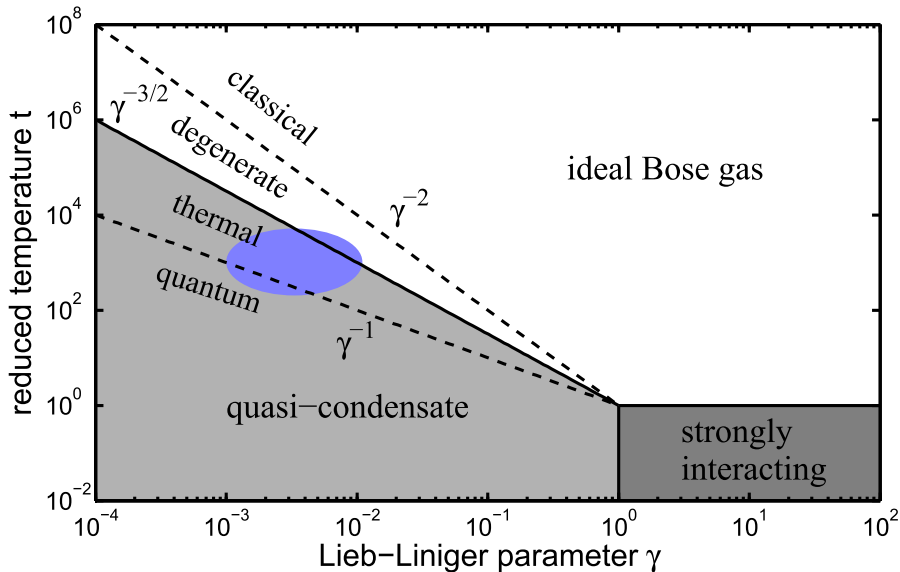


Figure 2.1.: State diagram of a uniform 1d Bose gas based on [Kheruntsyan 05, Jacqmin 11]. The blue circle illustrates typical experimental parameters of $\gamma \approx 0.001 - 0.01$ and $t \approx 200 - 5000$, with linear densities $n \approx 20 - 130 \mu\text{m}^{-1}$ and temperatures $T \approx 20 - 300 \text{ nK}$.

kinetic energy scaling with $\propto n^2$.

To study the Lieb-Liniger model at finite temperature, it makes sense to define the temperature scale according to the degeneracy temperature

$$T_d = \frac{\hbar^2 n^2}{2mk_B}. \quad (2.4)$$

At the degeneracy temperature T_d , the thermal deBroglie wavelength $\lambda_B = \hbar/\sqrt{2\pi mk_B T}$ becomes approximately equal to the mean particle separation $1/n$ and the 1d Bose gas becomes degenerate in the sense that quantum effects like discrete level spacings, quantum statistics and particle indistinguishability become visible.

The interplay between effects driven either by temperature or by interactions, creates three distinct physical regimes with totally different behaviours. Fig. 2.1 shows the state diagram of a uniform 1d Bose gas following [Kheruntsyan 05], with respect to the reduced temperature parameter

$$t = \frac{T}{T_d} \frac{1}{\gamma^2} \quad (2.5)$$

and the Lieb-Liniger parameter γ . The three main regimes are, the strongly interacting (dark grey area), the weakly interacting (light grey area) and the nearly ideal Bose gas regime (white area). The different properties of these regimes are briefly discussed in the following.

2. Theoretical Background

The nearly ideal Bose-gas regime

At sufficiently high temperatures T ($t \gg \max(\gamma^{-3/2}, 1)$), the temperature dominates over the interaction strength. The interactions between atoms can be neglected and the gas can be well described as an ideal Bose gas in 1d (white area in Fig. 2.1). In thermal equilibrium, the mean occupation numbers of the momentum distribution are given by the Bose-Einstein distribution

$$n_k = \frac{1}{e^{\left(\frac{\hbar^2 k^2}{2m} - \mu\right)/k_B T} - 1}, \quad (2.6)$$

with the chemical potential $\mu = \frac{\partial E}{\partial N}$ in the grand canonical ensemble. Each momentum state has energy $E_k = \frac{\hbar^2 k^2}{2m}$, wave vector $k = \frac{2\pi}{L}n$ with $n = 0, 1, 2, \dots$ and the energy scale has been chosen such that the ground state energy E_0 is zero. The population in the ground state n_0 is then given by $n_0 = (\exp(-\mu/k_B T) - 1)^{-1}$, which means that the chemical potential has to be negative to ensure $n_0 > 0$.

For $|\mu| \ll k_B T$, the gas becomes degenerate and Bose-Einstein statistics apply, where the ground state can be macroscopically occupied, but only in the 3d case (see below). This subregime is sometimes referred to as the degenerate Bose gas regime [Jacqmin 11]. Considering $\mu = -|\mu|$, the ground state population is approximately given by $n_0 \approx k_B T / |\mu|$.

On the other hand, for $|\mu| \gg k_B T$, the gas is non-degenerate and classical statistics apply. This is the classical ideal Bose gas subregime [Jacqmin 11]. The ground state population is then approximated by the Boltzmann distribution $n_0 \approx \exp(-|\mu|/k_B T)$.

By summing eq. 2.6 over all momentum states k , the excited state density n_{ex} can be calculated as [Bouchoule 11]

$$n_{ex} = \frac{1}{\lambda_{dB}} g_{1/2} \left(e^{\frac{\mu}{k_B T}} \right), \quad (2.7)$$

with the polylogarithmic function $g_n(z) = \sum_{k=1}^{\infty} \frac{z^k}{k^n}$, the argument of $g_{1/2}$ being the fugacity $z = e^{\frac{\mu}{k_B T}}$ and the thermal deBroglie wavelength $\lambda_{dB} = \sqrt{\frac{2\pi\hbar^2}{mk_B T}}$. Eq. 2.7 leads to a stark difference to the 3d case, where $n_{ex} = \frac{1}{\lambda_{dB}^3} g_{3/2} \left(e^{\frac{\mu}{k_B T}} \right)$ [Pethick 01]. Due to the different behaviour of $g_{1/2}$ and $g_{3/2}$, there is no BEC phase transition in 1d. In 3d, the excited state fraction saturates via $\lim_{z \rightarrow 1} (g_{3/2}(z)) = 2.612$, and the ground state becomes macroscopically populated. In 1d, $\lim_{z \rightarrow 1} (g_{1/2}(z)) = \infty$ and no true Bose-Einstein phase transition is expected to occur in an ideal 1d Bose gas³ (compare Fig. C.1), in agreement with the Mermin-Wagner-Hohenberg theorem, which forbids the existence of long-range order in 1d and 2d systems [Mermin 66, Hohenberg 67]. Fig. 2.2

³A similar argument can be found by considering the scaling behaviour of the density of states (*DOS*) of an ideal, uniform Bose gas. In the 3d case $DOS \propto \sqrt{E}$, meaning that by lowering the temperature, fewer states are accessible and the ground state population has to increase, whereas in the 1d case $DOS \propto 1/\sqrt{E}$, a temperature decrease merely affects the population of the ground state.

2. Theoretical Background

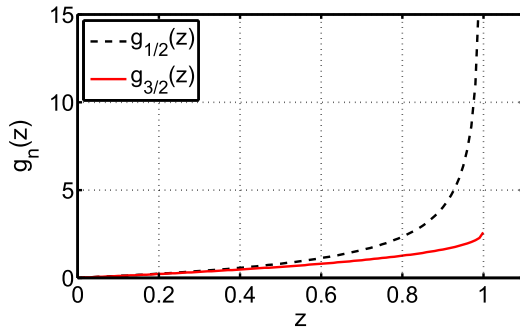


Figure 2.2.: Comparison of the polylogarithmic functions $g_{1/2}(z)$ and $g_{3/2}(z)$. Due to the different asymptotic behaviour of $g_{1/2}$ and $g_{3/2}$, there is no BEC phase transition in 1d.

shows a comparison between the two relevant polylogarithmic functions, calculated using the numerical approximation presented in appendix C.

At high enough temperatures, eq. 2.6 can be approximated by the Boltzmann distribution

$$n_{th} = \frac{1}{\lambda_{dB}} e^{\frac{\mu}{k_B T}}. \quad (2.8)$$

The condition $t = \gamma^{-2}$ marks the border between two sub-regimes, the purely thermal Bose gas ($T > T_d$) and the quantum degenerate regime ($T < T_d$), where the occupation numbers start to follow the Bose-Einstein distribution of eq. 2.6 [Kheruntsyan 03].

In the classical regime $n\lambda_{dB} \ll 1$ and follows eq. 2.8, whereas in the degenerate regime $n\lambda_{dB} \gg 1$ is valid [Bouchoule 11].

The strongly interacting regime

According to Fig. 2.1, for $\gamma > 1$ and $t < 1$, at low density and low temperature, interactions are dominant (dark grey area in Fig. 2.1). Due to strong repulsive interactions, the atoms become impenetrable. This leads to a fermionization of the Bosons as two atoms cannot occupy simultaneously the same position in space, mimicking the Pauli exclusion principle of fermions. On the other hand, the momentum distribution stays bosonic. This impenetrable, bosonic gas is often referred to as Tonks-Girardeau gas [Tonks 36, Girardeau 60], which so far cannot be reached by our atom chip experiments due to the requirement of very low densities and very high trap frequencies. The strongly-interacting regime is accessible in optical lattice experiments [Paredes 04, Kinoshita 04], where a second lattice is used to increase the effective mass m to reach $\gamma > 100$.

The weakly-interacting, quasi-condensate regime

For atom chip experiments, experimentally readily accessible is the weakly-interacting, quasi-condensate regime, for $\gamma \ll 1$ and $t \ll \gamma^{-3/2}$ ($T \ll \sqrt{\gamma} \cdot T_d$), where both the

2. Theoretical Background

interaction strengths as well as the temperatures are moderate (light grey area in Fig. 2.1). In the quasi-condensate regime, density fluctuations are suppressed by the repulsive interactions and phase fluctuations are dominant. As we will discuss in section 2.3 the source of these phase fluctuations can be either thermal or quantum noise, which again leads to two sub-regimes. Above $t = \gamma^{-1}$ ($T > \gamma \cdot T_d$) the phase fluctuations are governed by thermal noise, therefore this is called the thermal quasi-condensate regime [Jacqmin 11]. For very low temperatures ($T < \gamma \cdot T_d$), below $t = \gamma^{-1}$, the phase fluctuations are dominated by quantum noise and we are in the quantum quasi-condensate regime [Jacqmin 11]. Obviously, at $T = 0$, quantum noise is the only remaining noise source.

This thesis mainly focuses on the physics in the quasi-condensate regime. Thus, the next chapter will go beyond the uniform description used so far and present a more realistic discussion on the experimental realisation of the quasi-condensate regime in atom chip traps and give analytic expressions for important parameters like the chemical potential, the density profile etc.

2.2. The trapped one-dimensional Bose gas

The previous section described the case of an infinitely long and uniform 1d Bose gas with a constant linear density, which is not realistically achievable in an experiment. In the experiment, an effectively 1d system is created out of an elongated 3d system. In the following, the tight harmonic confinement is chosen to be in the x, y -direction, which will be referred to as transverse directions. Additionally, there will always be a very shallow harmonic confinement in the z -direction, referred to as longitudinal axis of the elongated, “cigar-shaped” cloud. The trapping potential is given by the expression

$$V(\vec{r}) = \frac{1}{2}m\omega_{tr}^2(x^2 + y^2) + \frac{1}{2}m\omega_{long}^2z^2, \quad (2.9)$$

which is a good approximation for ultracold atoms in atom chip traps, despite fragmentation induced effects (compare section 3.3).

To take the longitudinal finite size of the trapped, non-uniform 1d Bose gas into account, the local density approximation (LDA) is used [Reichel 11]. For a smooth density profile, the system can locally be described as a uniform gas with an effective chemical potential $\mu(z) = \mu_0 - V(z)$ and an interaction parameter $\gamma(z) = mg/\hbar^2n(z)$, characterizing the local properties of the gas. The linear density $n(z)$ is obtained from the 3d density via the integral

$$n(z) = \int \int dx dy n(x, y, z). \quad (2.10)$$

For low temperatures the LDA is easily valid in the central part of the atom cloud and may still work at the edges of the cloud, as long as the density profile stays smooth. At $T = 0$ the LDA breaks down at the sharp edges [Kheruntsyan 05], where the healing length⁴ ξ is on the order of $\frac{n(z)}{|dn/dz|}$, such that a uniform description is not applicable anymore.

2.2.1. The quasi-condensate regime

Creating an effectively one-dimensional system with harmonic traps

For the experimental realisation of an effectively one-dimensional (1d) system, a highly anisotropic harmonic trapping potential is used with the transverse trap frequencies $\omega_{tr} = \omega_x = \omega_y$ much larger than the longitudinal trap frequency $\omega_{long} = \omega_z$, as illustrated in Fig. 2.3b. This leads to a thin elongated atomic cloud, being tightly confined in the transverse direction. In this context, the idea of 1d-ness is purely meant in a quantum mechanical sense. For a longitudinal confinement orders of magnitude lower than the transverse confinement, the transverse degrees of freedom can be essentially “frozen out” and only longitudinal excitations are being populated⁵. On the other hand, the extension of the wave function still remains three-dimensional, and is given in the transverse

⁴The healing length ξ is the correlation length of density fluctuations in the weakly-interacting quasi-condensate regime.[Kheruntsyan 05]

⁵typical aspect ratios of 1:200 were used throughout this thesis.

2. Theoretical Background

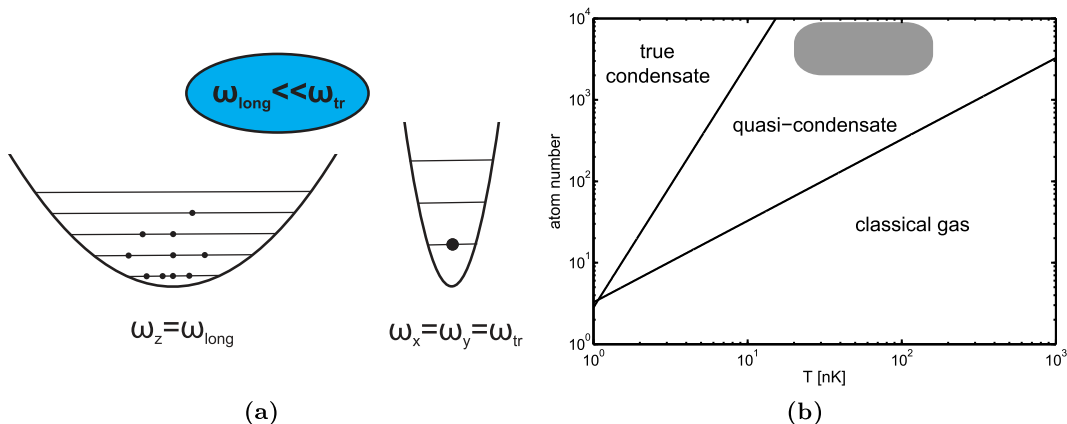


Figure 2.3.: (a) Harmonic trapping potentials and (b) state diagram of a trapped 1d Bose gas. Based on [Petrov 00] using a longitudinal trap frequency of $\omega_{long} = 2\pi \times 7$ Hz. The filled rectangle denotes the typical parameter space investigated in this thesis.

direction by the ground-state oscillator width $a_{tr} = \sqrt{\frac{\hbar}{m\omega_{tr}}}$ [D.S. Petrov 04]. Also the scattering process remains its 3d character, since for scattering length a_s the condition $a_s \ll a_{tr}$ is typically valid.

To effectively “freeze out” the transverse excitations, all relevant energy scales need to be much smaller than the energy of the 1st transverse excited state [Das 03, Kheruntsyan 05, Bouchoule 07]

$$\mu \ll \hbar\omega_{tr} \quad (2.11)$$

$$k_B T \ll \hbar\omega_{tr}, \quad (2.12)$$

with the chemical potential μ and the temperature T . This means, only the ground state with energy $E_0^{trans} = \frac{1}{2}\hbar\omega_x + \frac{1}{2}\hbar\omega_y = \hbar\omega_{tr}$ in the transverse direction is macroscopically populated. Therefore, the dynamics can happen only in the longitudinal direction, where many different energy levels are populated, besides the ground state at energy $E_0^{long} = \frac{1}{2}\hbar\omega_{long}$. This is the so-called quasi-condensate regime, as the ground state is not macroscopically populated in all three spatial directions. This kind of condensation in finite sized traps was first discussed in [Ketterle 96a] and appears only for an interacting Bose gas. True condensation happens on a second step, at much colder temperatures, when also the longitudinal ground state becomes macroscopically populated as depicted in Fig. 2.3a. The idea of a quasi-condensation seems to go back to Popov et al. [Popov 72] in the context of superfluidity Bose gases in lower dimensions. Further experiments, confirming the existence of a quasi-condensate are [Dettmer 01, Hugbart 05].

Fulfilling both criteria (eq. 2.11) needs strong experimental efforts. In practice, experiments fulfil the slightly less strict criteria of $\mu \lesssim \hbar\omega_{tr}$ and $k_B T \lesssim \hbar\omega_{tr}$. Fortunately, going from 1d to 3d is a smooth crossover [Armijo 11b], thus already for temperatures

2. Theoretical Background

T and chemical potentials μ on the order of the transverse trapping frequency ω_{tr} , the system shows 1d like behaviour.

Properties of the trapped quasi-condensate

First of all, one should be aware that a harmonically trapped degenerate gas samples multiple regimes due to the longitudinal variations in density. Throughout this thesis, we will refer to be in the quasi-condensate regime, where strictly speaking only the main, central parts of the cloud are quasi-condensed, while the edges will be in the thermal, ideal Bose gas domain, according to Fig. 2.3b. Experimental densities reported throughout this work, will be the peak densities.

A quasi-condensate shows no true long-range order, as the phase keeps fluctuating along the longitudinal direction, due to the many populated longitudinal modes. As we will motivate later, longitudinal density fluctuations are suppressed by the repulsive interactions [Popov 83], which has been observed in [Esteve 06]. Simplified, the system can be thought of as consisting of many phase domains along the longitudinal direction. Inside each domain the local phase is approximately constant. As we will see in sec. 2.3, the size of these domains is given by the phase correlation length $\lambda_T = \frac{2\hbar^2 n}{mk_B T}$. Once λ_T becomes similar to the system size L , full long-range order is established and we are in the true condensate regime. The finite size helps us here to overcome the limitations of the Mermin-Wagner-Hohenberg theorem [Mermin 66, Hohenberg 67] and establish phase coherence throughout the system. Thus, to reach the true-condensate regime, with almost no phase fluctuations present, the temperature needs to be below

$$T_\phi = \frac{2\hbar^2 n}{mk_B L}. \quad (2.13)$$

The degeneracy temperature T_d of a trapped 1d gas with N atoms is given by [Petrov 00]

$$k_B T_d = N \hbar \omega_{long}, \quad (2.14)$$

under the condition that $k_B T_d < \hbar \omega_{tr}$. Otherwise eq. 2.4 should be applied locally.

However, a real macroscopic occupation of the transverse ground state is expected to occur at a colder crossover temperature T_c , defined by [Ketterle 96a, D.S. Petrov 04]

$$k_B T_c = \frac{N}{\ln(2N)} \hbar \omega_{long}. \quad (2.15)$$

In the thermodynamic limit, $\lim_{N \rightarrow \infty} T_c \rightarrow 0$, therefore it is not a phase transition but a smooth crossover. To get a true phase transition other trap geometries would be needed [Bagnato 91].

Thus, the thermal noise dominated quasi-condensate regime extends in the temperature range of $T_c > T > T_\phi$. Below T_ϕ quantum noise becomes dominant. This regime is hardly reachable in current atom chip experiments due to the very low temperatures that would be required. For typical experimental parameters, T_ϕ is on the order of $T_\phi = 10$ nK in the single trap. The lowest achieved temperatures so far were around $T \approx 16$ nK,

2. Theoretical Background

almost entering the true condensate regime. However, when splitting the trap into two equal parts (for more details please refer to sec. 5.2), T_ϕ drops to about $T_\phi = 5$ nK per part, assuming the atom number is exactly halved. For 6000 atoms, the expected crossover temperature is $T_c \approx 340$ nK in our typical single trap configuration and drops to $T_c \approx 100$ nK in the split trap.

The 1d coupling strength

In the experimentally realized parameter space, the scattering length a_s is much smaller than the ground-state oscillator with $a_{tr} = \sqrt{\hbar/m\omega}$. For ^{87}Rb in the fully stretched ($F = 2$, $m_F = 2$) state, the triplet s-wave scattering length is $a_s = 98.99a_0 \approx 5$ nm [van Kempen 02], with a_0 being the Bohr radius. For transversal trap frequencies in the range of $2\pi \times (10^3 - 10^4)$ Hz, $a_{tr} = 340 - 100$ nm.

In the weak confinement limit [Olshanii 98] $a_s \ll a_{tr}$, the interactions remain a three-dimensional (3d) character and the 1d coupling g can be related to the 3d coupling constant $g_{3d} = 4\pi\hbar^2 a_s/m$ of the Gross–Pitaevskii equation [Gross 61]. Following [Olshanii 98], the 1d coupling constant g is given by $g = 2\hbar^2/ma_{1d}$. For $a_s \ll a_{tr}$, the 1d scattering length a_{1d} , for the 1d potential $U(z) = \frac{g}{2}\delta(z)$, can be approximated as $a_{1d} \approx a_{tr}^2/a_s$ [Olshanii 98] by taking the average of the 3d interaction over the transverse profile

$$\int n_{3d}(r) dr = \frac{1}{\pi a_{tr}^2} \int n(z) dz. \quad (2.16)$$

Finally, this leads to

$$g = \frac{2\hbar^2}{ma_{1d}} \approx \frac{2\hbar^2 a_s}{ma_{tr}^2} = 2\hbar a_s \omega_{tr}. \quad (2.17)$$

In cases where the weak confinement limit $a_s \ll a_{tr}$ is not fulfilled, confinement-induced resonances due to the emergence of bound states can be observed [Moritz 05, Haller 10].

The α - Parameter

Following the description introduced in [Gerbier 04], the chemical potential μ and 1d density profile $n(z)$ of a quasi-condensate can be calculated analytically by using a local density approximation and optimising the local width in the transverse direction in terms of minimizing the local chemical potential $\mu(z)$. The results have been shown to work even in the dimensional crossover region ($\mu \lesssim \hbar\omega_{tr}$) [Gerbier 04]. Key parameters are expressed in terms of a numerical parameter α , which is given by the equation [Gerbier 04]

$$\alpha^3 (\alpha + 5)^2 = \left(15 \frac{N a_s a_{tr}}{a_{long}^2} \right)^2, \quad (2.18)$$

with the total number of condensed atoms N . For typical experimental parameters $0.5 < \alpha < 3$

2. Theoretical Background

Longitudinal Quasi-Condensate Radius

Once, evaluating α for a given atom number N via eq. 2.18, the longitudinal radius $R = L/2$ of the quasi-condensate is then given by the simple expression

$$R = \frac{a_{long}^2}{2a_{tr}} \sqrt{\alpha}. \quad (2.19)$$

Longitudinal Density Profile

The longitudinal density profile $n(z)$ can be calculated via⁶

$$n(z) = \frac{\alpha}{16a_s} \left(1 - \frac{z^2}{R^2}\right) \left(\alpha \left(1 - \frac{z^2}{R^2}\right) + 4\right). \quad (2.20)$$

The main difference between 1d Thomas-Fermi profiles and eq. 2.20 are the calculated peak densities, which are slightly higher following eq. 2.20, in good agreement with the experimentally obtained profiles (compare Fig. 5.3).

Chemical Potential

The local chemical potential $\mu(z)$ with respect to the trap bottom at $E_0 = \hbar\omega_{tr}$ is defined by

$$\mu(n(z)) = \hbar\omega_{tr} \left(\sqrt{1 + 4a_s n(z)} - 1\right). \quad (2.21)$$

For $n(z) a_s \ll 1$, eq. 2.21 can be approximated by $\mu \approx gn(z)$, which is exactly the result obtained in [Pitaevskii 03] for the weakly-interacting Bose-gas.

Eq. 2.17 to 2.21 will be used throughout this thesis to calculate linear peak densities and chemical potentials with respect to two measured input parameters, namely the atom number and trap frequencies. The above equations were reported in [Gerbier 04] and a thorough discussion can be found in [Fuchs 03, Mateo 08].

⁶please note that in [Gerbier 04] a prefactor of 1/4 is missing.

2.3. Correlation properties of a homogeneous quasi-condensate

Now, we come back to the simpler homogeneous case. By adapting a Bogoliubov description of elementary excitations to a quasi-condensate, we want to study the correlation properties and the strength of phase and density fluctuations and to verify the statements made in sec. 2.2.1. The derivation of density and phase fluctuations can be found in [Mora 03, Castin 04, Bouchoule 11] and shall be outlined in the following.

In 3d, a Bogoliubov approach splits the many-body problem into a mean field (condensate) part and the quantized Bogoliubov elementary excitations [Pitaevskii 03]

$$\hat{\Psi} = \hat{a}_0 \Psi_0 + \delta\hat{\Psi}. \quad (2.22)$$

Here $\hat{\Psi}$ is the bosonic field operator, with the mean field component Ψ_0 , being the condensate wave function i.e. in 3d the result of the Gross-Pitaevskii equation

$$i\hbar \frac{\partial}{\partial t} \Psi_0(r, t) = \left[-\frac{\hbar^2}{2m} \nabla^2 + g_{3D} |\Psi_0(r, t)|^2 \right] \Psi_0(r, t), \quad (2.23)$$

with the 3d interaction parameter $g_{3d} = \frac{4\pi\hbar^2 a_s}{m}$. In eq. 2.22, $\delta\hat{\Psi}$ accounts for quantum and thermal fluctuations in other modes than Ψ_0 . \hat{a}_0 annihilates a particle in the ground state. Assuming $|\delta\hat{\Psi}| \ll |\hat{a}_0|$ the field equations of motion can be solved perturbatively. The quasi-condensate case is again special, as a quasi-condensate has a no macroscopically occupied ground-state. However, it has been shown in [Mora 03] that the a priori postulated weak density fluctuations help to circumvent this problem.

Thus, for small density fluctuations and dominant phase fluctuations, the field operator $\hat{\Psi}$ can be defined, in a second quantization approach, as

$$\hat{\Psi}^\dagger = \sqrt{n(z) + \delta\hat{n}(z)} e^{-i\hat{\phi}(z)}, \quad (2.24)$$

with small fluctuations $\langle \delta\hat{n} \rangle \ll n$ around the mean density $n(z) = \langle \Psi^\dagger(z) \Psi(z) \rangle$ and the phase operator $\hat{\phi}$. The operators $\delta\hat{n}$ and $\hat{\phi}$ are conjugate $[\delta\hat{n}, \hat{\phi}] = i\delta(z - z')$ and need to be coarse grained in space to avoid the divergence of \hat{n} in small volume due to quantum shot noise and to be able to properly define the phase operator $\hat{\phi}$ [Mora 03]. Coarse graining here means the discretization of space into small cells of finite size.

Furthermore, only high energy excitations shall contribute to $\delta\hat{\Psi}$, with a momentum cut-off defined by the condensate healing length $\xi = \frac{\hbar}{\sqrt{mgn}}$ as $k_c = \frac{1}{\xi}$. The healing length defines the length scale on which the condensate changes its density. The excitations can be described as collective modes with momentum k

$$\delta\hat{\Psi} = \frac{1}{\sqrt{L}} \sum_k \left(u_k \hat{b}_k e^{ikz} - v_k \hat{b}_k^\dagger e^{-ikz} \right), \quad (2.25)$$

where \hat{b}_k^\dagger creates the Bogoliubov quasi-particles, which are characterized by the coefficients u_k, v_k . These quasi-particle amplitudes fulfil $u_k^2 - v_k^2 = 1$ and are connected to the particle creation a_k^\dagger and annihilation operators a_k via the Bogoliubov transformations

2. Theoretical Background

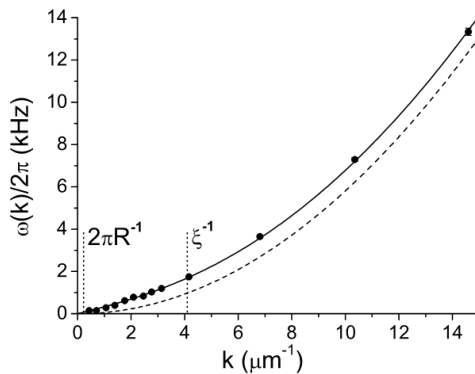


Figure 2.4.: Measured Bogoliubov dispersion relation ω_k of a trapped ^{87}Rb BEC. The transition from phononic (linear dispersion) to particle-like (quadratic dispersion) excitations happens at the momentum cut-off $k_c = \frac{1}{\xi}$. Reproduced from [Steinhauer 02].

[Bogoliubov 47, Brunello 00]

$$b_k = u_k a_k + v_k a_{-k}^\dagger \quad (2.26)$$

and

$$b_k^\dagger = u_k a_k^\dagger + v_k a_{-k}, \quad (2.27)$$

that eventually help to diagonalize the initial many-body Hamiltonian

$$\hat{H} = \frac{\hbar^2}{2m} \int dz \nabla \Psi^\dagger(z) \nabla \Psi(z) + \frac{g_{3D}}{2} \int dr \hat{\Psi}^\dagger(z) \hat{\Psi}^\dagger(z') V(z-z') \hat{\Psi}(z) \hat{\Psi}(z'). \quad (2.28)$$

More details on the necessary approximations can be found in [Pitaevskii 03].

In thermal equilibrium, the population n_k in each Bogoliubov mode is specified by the Bose distribution

$$n_k = \hat{b}_k^\dagger \hat{b}_k = \frac{1}{e^{\frac{\epsilon_k}{k_B T}} - 1}, \quad (2.29)$$

where, for $E_k = \frac{\hbar^2 k^2}{2m}$, the spectrum of Bogoliubov excitations is given by

$$\epsilon_k = \hbar \omega_k = \sqrt{E_k (E_k + 2gn)} \quad (2.30)$$

and gives rise to two regimes. For low k , the Bogoliubov dispersion relation of eq. 2.30 is approximately linear $\omega_k \approx ck$, with a speed of sound $c = \sqrt{gn/m}$, which coincides with the hydrodynamic result [Pethick 01] $c^2 = \frac{dP}{d\rho} = \frac{n}{m} \frac{d\mu}{dn}$, where $\rho = mn$ is the mass density, P is the pressure and $\mu = gn$ is the chemical potential. The repulsive character of the interactions ($g > 0$) guarantees that $\omega_k \in \mathbb{R}$. These low-energy excitations correspond to

2. Theoretical Background

phonons, i.e. collective excitations of a large number of atoms, which was measured in [Andrews 97a, Vogels 02]. For large k , the dispersion relation approaches the free particle energy E_k and becomes quadratic. This corresponds to single-particle excitations with velocities much larger than c . The transition from phononic to particle-like excitations happens at the momentum cut-off $k_c = \frac{1}{\xi}$, as confirmed by [Steinhauer 02] and plotted in Fig. 2.4.

Using this Bogoliubov approach physical quantities of interest like the fluctuation properties can be derived.

Coherence Properties and Correlation Functions

The normalized first order correlation function $g^{(1)}(z, z')$, determining the correlation between separated positions z and z' of the Bose gas, is defined by

$$g^{(1)}(z, z') = \frac{\langle \Psi^\dagger(z) \Psi(z') \rangle}{\sqrt{n(z) n(z')}}. \quad (2.31)$$

Similar, the second order correlation function $g^{(2)}(z, z')$, giving the probability of finding a particle at z and simultaneously at z' , is [Pethick 01]

$$g^{(2)}(z, z') = \frac{\langle \Psi^\dagger(z) \Psi^\dagger(z') \Psi(z') \Psi(z) \rangle}{n(z) n(z')}. \quad (2.32)$$

In terms of quantum optics, the first order correlation $g^{(1)}(z, z')$ gives the phase coherence length of a laser and the second order correlation function $g^{(2)}(z, z')$ is a measure of the intensity fluctuations of the laser field.

Due to the lack of long-range order, a quasi-condensate only exhibits second order coherence ($g^{(2)}(z, z') = 1$), while the $g^{(1)}(z, z')$ is exponentially decaying, as we will establish below. In contrast, a pure 3d BEC, having a constant, global phase, shows both first ($g^{(1)}(z, z') = 1$) and second order coherence [Glauber 63, Pethick 01].

In the ideal Bose gas regime, the $g^{(1)}(z, z')$ starts at 1 ($g^{(1)}(0, 0) = 1$), and decays exponentially to 0 on a length scale of λ_{dB} . For $g^{(2)}(z, z')$, one finds using Wick's theorem [Wick 50] and the commutation relation $[\Psi(z), \Psi^\dagger(z')] = \delta(z - z')$,

$$g^{(2)}(z, z') = 1 + \left| g^{(1)}(z, z') \right|^2, \quad (2.33)$$

which leads to bosonic bunching $g^{(2)}(0, 0) = 2$ at zero distances, as observed in [Hanbury Brown 56] for photons and in [Yasuda 96] for a beam of ultracold atoms. [Schellekens 05] measured the expected bunching behaviour for thermal atoms and, furthermore, proofed that a phase-coherent 3d BEC has indeed a constant correlation function. [Jeltes 07] compared the bunching behaviour of bosons to the anti-bunching of fermions, the latter having no classical analogue and thus can only be understood in terms of quantum destructive interference. In quasi-condensates, bosonic bunching is still present below the critical temperature, due to the lack of long-range phase coherence

2. Theoretical Background

and the associated multimode nature of the source, as discussed in sec. 2.2.1. In this context, correlation measurements have been performed in [Perrin 12] and led to the establishment of a new thermometry method in the quasi-condensate regime, which will be presented in sec. 4.3.

Density fluctuations

Following [Castin 04, Mora 03], the density fluctuations $\delta\hat{n}$ can be expressed as

$$\frac{\langle\delta\hat{n}^2\rangle}{n^2} = \begin{cases} \sqrt{\gamma} & \text{for } \text{quantum} \\ \frac{T^2}{4T_d^2}\gamma^{-\frac{3}{2}} & \text{for } k_B T < \mu \text{ thermal} \\ \frac{T}{2T_d}\gamma^{-\frac{1}{2}} & \text{for } k_B T > \mu \text{ thermal} \end{cases} \quad (2.34)$$

with the degeneracy temperature T_d of a homogeneous system as defined by eq. 2.4. So indeed for small enough temperatures $T \ll T_d\sqrt{\gamma}$ ($t \ll \gamma^{-3/2}$), the a priori assumption of small density fluctuations $\langle\delta\hat{n}^2\rangle \ll n^2$ is satisfied. Basically, this inequality gives the definition of the quasi-condensate regime and dates back to [Popov 83]. Due to their temperature dependence, the local density fluctuations can be used as a tool for thermometry [Armijo 11b] (see sec. 4.3).

Phase fluctuations

As we will see in chapter 5, probing the phase correlations has a high relevance for the conducted experiments reported in this thesis. Therefore, the derivation of the phase correlation length is presented in detail in the following.

To determine the characteristic length scale of the phase-fluctuations, let's have again a look at the first order correlation functions $g^{(1)}(z, z')$ of eq. 2.42. Using eq. 2.24, $g^{(1)}(z, z')$ can be further approximated according to [Mora 03, Castin 04] by

$$g^{(1)}(z, 0) \approx \frac{\langle\sqrt{n(z)}e^{i\phi(z)-i\phi(z')}\sqrt{n(z')}\rangle}{\sqrt{n(z)n(z')}} \approx \langle e^{i\phi(z)-i\phi(0)} \rangle. \quad (2.35)$$

As the Hamiltonian of eq. 2.2 is quadratic, Wicks theorem [Wick 50] $\langle e^{i\Delta\phi} \rangle = e^{-\frac{1}{2}\langle(\Delta\phi)^2\rangle}$, with $\Delta\phi = \phi(z) - \phi(0)$, can be applied and one finds

$$g^{(1)}(z, 0) \approx e^{-\frac{1}{2}\langle(\phi(z)-\phi(0))^2\rangle}. \quad (2.36)$$

To evaluate $\frac{1}{2}\langle(\phi(z) - \phi(0))^2\rangle$, we follow the heuristic derivation of [Reichel 11] and expand the local phase $\phi(z)$ as

$$\phi(z) = \sqrt{2} \sum_{k>0} [\phi_{ck} \cos(kz) + \phi_{sk} \sin(kz)], \quad (2.37)$$

which leads to

2. Theoretical Background

$$\frac{1}{2} \langle (\phi(z) - \phi(0))^2 \rangle = \sum_{k>0} \phi_{ck}^2 (\cos(kz) - 1)^2 + \sum_{k>0} \phi_{sk}^2 \sin^2(kz). \quad (2.38)$$

For low-energy phonons, the local velocity $v(z)$ is given by the velocity of a superfluid $v(z) = \hbar \nabla \phi / m$, and the kinetic energy term reads $Ln\hbar^2 k^2 \phi_{ik}^2 / 2m$. Assuming high enough temperatures such that the thermal mode population is large, classical statistics can be applied and the equipartition theorem gives on average an energy of $\frac{k_B T}{2}$ per quadratic degree of freedom, which gives for the phase fluctuation amplitudes

$$\langle \phi_{ik}^2 \rangle = \frac{mk_B T}{Ln\hbar^2 k^2}. \quad (2.39)$$

Plugging this result into eq. 2.38 and using $(\cos(kz) - 1)^2 + \sin^2(kz) = 2 - 2\cos(kz)$, one finds

$$\frac{1}{2} \langle (\phi(z) - \phi(0))^2 \rangle = 2 \frac{mk_B T}{Ln\hbar^2} \sum_{k>0} \frac{1 - \cos(kz)}{k^2} \quad (2.40)$$

Going from the discrete sum $\sum_{k>0}$ to $\frac{L}{2\pi} \int_0^\infty dk$ in the thermodynamic limit and using $\frac{L}{2\pi} \int_0^\infty \frac{1 - \cos(kz)}{k^2} dk = \frac{Lz}{4}$ results in

$$\frac{1}{2} \langle (\phi(z) - \phi(0))^2 \rangle = \frac{mk_B T}{2\hbar^2 n} \cdot z = \frac{T}{4T_d} n z, \quad (2.41)$$

leading to a pure exponential decay of the correlation function

$$g^{(1)}(z, 0) \approx e^{-\frac{z}{\lambda_T}}, \quad (2.42)$$

which defines the thermal phase correlation length λ_T of a single quasi-condensate as

$$\lambda_T = \frac{2\hbar^2 n}{mk_B T}. \quad (2.43)$$

Similar to density fluctuations, phase fluctuations can be used as a handy tool to measure the temperature of quasi-condensates. This can be achieved by measuring the phase correlation function of interfering quasi-condensates, thereby inferring λ_T . However, to determine the temperature of a single quasi-condensate, another method, relying on density ripples in time of flight, is used heavily throughout this thesis. In fact, these density ripples are produced by phase fluctuations present in the trapped system. The details of this method will be presented in great detail in sec. 4.3.

Fig. 2.5 shows a comparison of phase and density fluctuations present in a quasi-condensate of approximately 5000 atoms, placed in a standard trap as calculated via eq. 2.34 and 2.43. The density fluctuations include both quantum and thermal contributions. The phase fluctuations include only thermal contributions. For the depicted parameter set, the critical temperature T_c (eq. 2.15) is on the order of $T_c \approx 290$ nK and the total longitudinal size L is approximately $L = 100$ μm . As given by eq. 2.34, at $\mu = k_B T$, density fluctuations $\frac{\langle \delta \hat{n}^2 \rangle}{n^2}$ become quadratically suppressed with temperature and tend

2. Theoretical Background

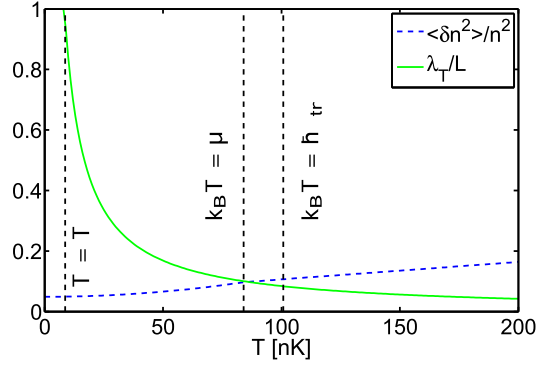


Figure 2.5.: The normalized strength of density and phase fluctuations versus temperature is plotted at typical experimental parameters of $n = 80 \mu\text{m}^{-1}$, $\omega_{tr} = 2\pi \times 2100 \text{ Hz}$ and $\omega_{long} = 2\pi \times 11 \text{ Hz}$. At $\mu = k_B T$, density fluctuations $\frac{\langle \delta \hat{n}^2 \rangle}{n^2}$ become quadratically suppressed with temperature and tend to the pure quantum noise level at $T = T_\phi$, where the true-condensate regime is reached.

to the pure quantum noise level of $\frac{\langle \delta \hat{n}^2 \rangle}{n^2} = \sqrt{\gamma} \approx 0.05$ at $T = 0 \text{ K}$.

2.4. Describing a 1d Bose Gas as a Luttinger Liquid

In this section, we want to simplify the Bogoliubov approach further by restricting us to the linear, phononic part of the Bogoliubov spectrum at low-energy and treat the system in terms of a quantum fluid approach. The respective formalism is called Tomonaga Luttinger Liquid and has become a heavily used theoretical tool, which gives a universal description of low-energy, many-body physics in 1d system with interactions. The current form of the formalism goes back to the works of Haldane [Haldane 81a, Haldane 81b] and shall be outlined in the following.

2.4.1. The Luttinger Liquid Hamiltonian

At low temperatures, the Bose gas can be regarded to be in a liquid phase, where only low-energy, phonon-like excitations are populated with a linear dispersion relation $\omega_k = ck$, as we have seen in Bogoliubov theory in sec. 2.3. This statement can be briefly motivated by the following considerations. Introducing low-energy excitations into a 1d system of interacting Bosons will always lead to a collective response of the system, due to the 1d constraints on particle motion and interaction [Giamarchi 04]. Therefore, describing the system with respect to collective excitations leads to a linearisation of the problem, where the collective excitations follow a linear (phononic) energy spectrum in contrast to free bosons having a quadratic energy spectrum. In fact, this collective nature of the excitations applies for fermionic as well as for bosonic systems and leads to a so-called bosonization of the problem [Giamarchi 04], which is, similar to Bogoliubov theory, best represented with a continuous bosonic field operator

$$\hat{\Psi}^\dagger(x, t) = \sqrt{\hat{\rho}(x, t)} e^{-i\hat{\phi}(x, t)}, \quad (2.44)$$

with the density field $\hat{\rho}(x, t)$ and the phase field $\hat{\phi}(x, t)$ fulfilling the commutation relation $[\rho(x), \phi(x')] = i\delta(x - x')$. In second quantization, the Lieb-Liniger Hamiltonian of eq. 2.2 reads

$$\hat{H} = \frac{\hbar^2}{2m} \int dz \nabla \hat{\Psi}^\dagger \nabla \hat{\Psi} + \frac{g}{2} \int dz \hat{\Psi}^\dagger \hat{\Psi}^\dagger \hat{\Psi} \hat{\Psi} \quad (2.45)$$

Applying eq. 2.44 and keeping only quadratic terms, thus omitting all higher order contributions, leads to the Tomonaga-Luttinger Liquid (TLL) Hamiltonian [Giamarchi 04]

$$\hat{H} = \frac{\hbar c}{2} \int dz \left[\frac{K}{\pi} (\nabla \hat{\phi}(z))^2 + \frac{\pi}{K} \hat{\rho}^2(z) \right], \quad (2.46)$$

with two phenomenological parameters c and K . By adjusting these two parameters to the specific problem, the TLL Hamiltonian is capable of describing the low-energy behaviour of many different 1d systems, being either bosonic or fermionic, in the weakly or strongly interacting regime. As will be shown later, c represents the sound-velocity and the so-called Luttinger parameter K represents the interaction strength of quantum fluctuations. As we will see, the scaling of K with respect to the Lieb-Liniger parameter

2. Theoretical Background

γ will be given by $K \propto \gamma^{-1/2}$. The limit $K \rightarrow \infty$ corresponds to a non-interacting Bose gas. The other limit, $K = 1$, corresponds to a Tonks gas of impenetrable bosons.

Neglecting higher order terms in eq. 2.46 actually leads to a purely harmonic, integrable theory, consisting of uncoupled harmonic oscillator modes with a linear dispersion relation. The problem, given by the Lieb-Liniger Hamiltonian (eq. 2.2), has been linearised up to a cut-off parameter and any unharmonic terms (beyond quadratic) are disregarded. As discussed in the Bogoliubov description, this cut-off parameter for a condensed 1d Bose gas will be given by the healing length ξ as $k_c = \frac{1}{\xi}$. In the context of spin chains, this linearisation leads to the separation of spin and charge waves, which is an ongoing experimental effort [Jompol 09].

In fact, the Luttinger Liquid can be regarded as a quantum hydrodynamics description of a 1D system. One strength of the method is that it is not a mean field description, one weakness being that it is inadequate to describe the high-energy structure [Cazalilla 04].

2.5. Interference of two quasi-condensates described as Luttinger Liquids

In the following, we intend to use the Tomonaga-Luttinger Liquid approach to model the interference of quasi-condensates. Let's consider the following situation that will be relevant for the experiments reported in this thesis. Initially, a single quasi-condensate shall be prepared that is in thermal equilibrium. At time $t = 0$, the gas is rapidly and phase-coherently split along the longitudinal direction. The splitting creates two uncoupled separated quasi-condensates. The splitting acts like a matterwave beam splitter, where each atom is in a superposition state of being in either one of the two gases. As we will see later on, the rapid splitting process imprints strong, long-range correlations into the system, which is in stark contrast to two independent thermal quasi-condensates. This highly correlated system is allowed to freely evolve for a certain evolution time t , after which the confinement is removed, resulting in the interference of the two gases. Following [Bistritzer 07], the dynamical evolution of these interference patterns can be described by TLL theory, which is outlined in the following.

In the experiment, the interference measurement can be regarded as a homodyne measurement that's purpose is to give access to the relative phase profile, which is the main experimental observable, probing the evolution of the created non-equilibrium state.

As we will see in chapter 5, the early evolution of the two quasi-condensates, after this sudden quantum quench, is well captured by the purely harmonic TLL theory. Deviations from the TLL predictions become visibly in the long-term evolution and are examined in chapter 6.

2.5.1. Describing the Non-Equilibrium System

Let's assume we have created a system of two uncoupled ultracold Bose-gases in the quasi-condensate regime. Let's further assume that the two gases can be described by collective excitations, with only low-energy excitations being populated. The dispersion relation is linearised up to the high energy cut-off $k_c = \frac{1}{\xi}$ and the 1d interaction strength g is $g = 2\hbar\omega_{tr}a_s$.

For each 1d Bose-gas, the Bosonic field operator can be expressed, similar to eq. 2.44, as

$$\hat{\Psi}_i^\dagger(z, t) = \sqrt{\rho_i + \hat{n}_i(z, t)} e^{i\hat{\phi}_i(z, t)}, \quad (2.47)$$

now including small density fluctuations \hat{n}_i around the average, linear density ρ_i and small phase fluctuations $\nabla\hat{\phi}$. Similar to the Bogoliubov description, these variables are again coarse-grained over a length scale larger than the spin healing length ξ . The i 's in exponents will always denote complex number and should not be confused with integer indices $i = 1, 2$ for the two gases. Assuming periodic boundary conditions and plugging this Ansatz into the second quantized Hamiltonian of each subsystem

2. Theoretical Background

$$\hat{H}_i = \int dz \left[\frac{\hbar^2}{2m} \nabla \Psi_i^\dagger(z) \nabla \Psi_i(z) + \frac{g}{2} \Psi_i^\dagger(z) \Psi_i^\dagger(z) \Psi_i(z) \Psi_i(z) \right], \quad (2.48)$$

without any external potential $V_{ext}(x) = 0$, leads to the following low-energy effective Hamiltonian

$$\hat{H}_i = \int dz \left[\frac{\hbar^2 \rho_i}{2m} (\nabla \hat{\phi}_i(z))^2 + \frac{g}{2} (\hat{n}_i(z))^2 + \frac{g}{2} \rho_i^2 \right]. \quad (2.49)$$

The total Hamiltonian of the system being the sum of the two split parts of the system

$$\hat{H}_{tot} = \hat{H}_1 + \hat{H}_2. \quad (2.50)$$

In the experiment, the interference pattern can be recorded by switching off the confinement and letting the two quasi-condensates interfere in free expansion. The local phase of these interference fringes is a measure of the relative phase difference between the left (H_1) and right (H_2) gas. To be able to describe the interference measurements, it is thus useful to switch to new variables. The local, relative degrees of freedom (DOF) are

$$\hat{\phi}_r(z) = \hat{\phi}_1(z) - \hat{\phi}_2(z), \quad (2.51)$$

$$\hat{n}_r = (\hat{n}_1 - \hat{n}_2) / 2 \quad (2.52)$$

and the local, common DOF are

$$\hat{\phi}_c(z) = \hat{\phi}_1(z) + \hat{\phi}_2(z), \quad (2.53)$$

$$\hat{n}_c = (\hat{n}_1 + \hat{n}_2) / 2. \quad (2.54)$$

The common and relative DOF are also referred to as symmetric and antisymmetric DOFs or in context of electron systems as spin and charge DOFs. The new Hamiltonian is then given by the sum of relative H_r , common H_c and interaction Hamiltonian H_{int} as

$$\hat{H}_{tot} = \hat{H}_r + \hat{H}_c + \hat{H}_{int} \quad (2.55)$$

$$\hat{H}_r = \int dz \left[\frac{\hbar^2 (\rho_1 + \rho_2)}{8m} (\nabla \hat{\phi}_r)^2 + g \hat{n}_r^2 \right] \quad (2.56)$$

$$\hat{H}_c = \int dz \left[\frac{\hbar^2 (\rho_1 + \rho_2)}{8m} (\nabla \hat{\phi}_c)^2 + g \hat{n}_c^2 \right] \quad (2.57)$$

$$\hat{H}_{int} = \hbar^2 \int dz \left[\frac{\rho_1 - \rho_2}{4m} \nabla \hat{\phi}_r \nabla \hat{\phi}_c \right]. \quad (2.58)$$

As can be seen in eq. 2.58, having the same average density $\rho = \rho_1 = \rho_2$ in both wells gives $H_{int} = 0$, resulting in zero coupling between relative and common degrees of freedom. Therefore, in a number balanced situation, the dynamics of common and

2. Theoretical Background

relative DOFs are independent from one another. Under this condition, \hat{H}_r is sufficient to describe the dynamics in the relative degrees of freedom, occurring after a sudden quantum quench. These dynamics can then be probed by interference measurements.

Eq. 2.56 has again the form of a TLL Hamiltonian (compare eq. 2.46), as can be seen by setting $\frac{\rho}{4m} = \hbar \frac{cK}{2\pi}$, with the relations $c = \sqrt{\frac{\rho g}{m}}$ for the sound velocity and

$$K = \frac{\hbar\pi}{2} \sqrt{\frac{\rho}{mg}} = \frac{\pi}{2\sqrt{\gamma}} \quad (2.59)$$

for the Luttinger parameter of the Bose gas. The TLL Hamiltonian consists of harmonic oscillators [Giamarchi 04] and can be diagonalized by translating the problem into k-space, using the Fourier transforms [Kitagawa 11, Langen 13b]

$$\hat{\phi}_r(z) = \frac{1}{\sqrt{L}} \sum_k \hat{\phi}_{r,k} e^{ikz} \propto \left[\hat{\phi}_{r,k=0} + \sum_{k \neq 0} \frac{-i}{\sqrt{k}} \left(\hat{b}_{r,k}^\dagger - \hat{b}_{r,-k} \right) e^{ikr} \right] \quad (2.60)$$

and

$$\hat{n}_r(z) = \frac{1}{\sqrt{L}} \sum_k \hat{n}_{r,k} e^{ikz} \propto \left[\hat{n}_{r,k=0} + \sum_{k \neq 0} \sqrt{k} \left(\hat{b}_{r,k}^\dagger + \hat{b}_{r,-k} \right) e^{ikr} \right], \quad (2.61)$$

with the total system size L and the bosonic ladder operators for creation $\hat{b}_{r,k}^\dagger$ and annihilation $\hat{b}_{r,k}$ of collective harmonic modes with wave vector $k = \frac{2\pi}{L}l$, $l = 0, 1, 2, \dots$, which fulfil the commutation relation $[\hat{b}_{r,k}, \hat{b}_{r,k}^\dagger] = 1$.

The TLL Hamiltonian in Fourier space is then given by [Gring 12a]

$$H = \frac{\hbar c}{2} \sum_k \left[\frac{K}{\pi} k^2 |\hat{\phi}_{r,k}|^2 + \frac{\pi}{K} |\hat{n}_{r,k}|^2 \right], \quad (2.62)$$

with the equations of motion

$$\frac{d\hat{\phi}_{r,k}}{dt} = -\frac{c\pi}{K} \hat{n}_{r,k} \quad (2.63)$$

$$\frac{d\hat{n}_{r,k}}{dt} = k^2 \frac{cK}{\pi} \hat{\phi}_{r,k}. \quad (2.64)$$

In terms of ladder operators, eq. 2.62 can be diagonalized to

$$H_r = \sum_{k \neq 0} \hbar c |k| \hat{b}_{r,k}^\dagger \hat{b}_{r,k} + \frac{\hbar\pi c}{2K} \hat{n}_{r,k=0}^2. \quad (2.65)$$

The first term describes the phononic eigenenergy of each k -mode and the second term represents the center of mass kinetic energy of the total system ($k = 0$ mode). Each k -mode has a wavelength of $\lambda = 2\pi/k$, a time scale of $\sim 1/c\hbar |k|$ and its energy oscillates between the fluctuations of phase $\hat{\phi}_{r,k}$ and density $\hat{n}_{r,k}$ (compare eq. 2.63 and 2.64). The

2. Theoretical Background

population $\hat{b}_k^\dagger \hat{b}_k$ in each mode is conserved. The modes are uncoupled, which leads to a dephasing of the modes over time. The $k = 0$ mode leads to a global phase diffusion due to interactions, which has been discussed extensively in literature, both theory wise [Lewenstein 96, Castin 97, Sinatra 98, Javanainen 99, Sinatra 08] as experiment wise [Andrews 97b, Hall 98, Orzel 01, Schumm 05b]. Section 5.3 will show that it is exactly the dephasing of harmonic oscillator modes, that describes the early rapid dynamics in a phase-coherently split 1d condensate.

2.5.2. Initial State

In the context of TLL theory, we assume an infinitely-fast and phase-coherent splitting process at $t = 0$. This rapid splitting creates a well-defined, non-thermal initial state $|\psi_0\rangle$ of strong long-range correlations. All k -modes are in phase at $t = 0$. Therefore, the initial state is characterized by large relative density fluctuations $\hat{n}_{r,k}$ and small relative phase fluctuations $\hat{\phi}_{r,k}$, with the following expectation values [Kitagawa 11, Gring 12a]

$$\langle \psi_0 | \hat{n}_r(z) \hat{n}_r(z') | \psi_0 \rangle = \frac{\rho\eta}{2} \delta(z - z') \quad (2.66)$$

$$\langle \psi_0 | \hat{\phi}_r(z) \hat{\phi}_r(z') | \psi_0 \rangle = \frac{1}{2\rho\eta} \delta(z - z'), \quad (2.67)$$

where ρ denotes the density in each gas $\rho = \rho_1 = \rho_2$ for a perfect symmetric splitting. The squeezing parameter η accounts for an imperfect splitting process, resulting in a squeezed initial state with too high ($\eta > 1$) or too low ($\eta < 1$) number fluctuations. By decreasing the initial number fluctuations, the initial phase fluctuations will be increased accordingly, keeping the area on the Bloch sphere constant.

The experimental splitting process and its connection to the TLL description is discussed in detail in sec. 5.2.

2.5.3. Application

The Hamiltonian in eq. 2.65 can be solved analytically as shown in [Bistritzer 07, Kitagawa 11]. The results can be used to calculate the full probability distribution functions (PDFs) of the two main observables of an interference pattern, namely the relative phase ϕ_r and contrast C . An extensive comparison between calculated and measured PDFs in the time evolution after splitting a quasi-condensate will be presented in chapter 5.

3

Chapter 3.

The Experiment - Some Practical Considerations

“There are two possible outcomes: if the result confirms the hypothesis, then you’ve made a measurement. If the result is contrary to the hypothesis, then you’ve made a discovery.”

- Enrico Fermi

Abstract

The experiments reported in this thesis were carried out with Rubidium-87 atoms in the ultracold temperature regime ($< \text{mK}$). In this chapter, the experimental realisation of cooling down to ultra-cold temperatures and achieving quantum degeneracy is discussed. Section 3.1 presents an overview of the most relevant parts of the experimental setup. Section 3.2 explains the experimental procedures, including tricks and tweaks, on how to create a Bose-condensed sample, which is our starting point for studying the physics of many-body quantum systems. Finally, typical technological problems of atom chips are discussed in section 3.3.

3.1. Experimental Setup Overview

This section features a brief presentation of the most important components of the experimental setup. A more detailed description of the experimental setup may be found in previous theses [vom Hagen 08, Göbel 08, Kuhnert 08, Gring 12a].

3.1.1. Vacuum System

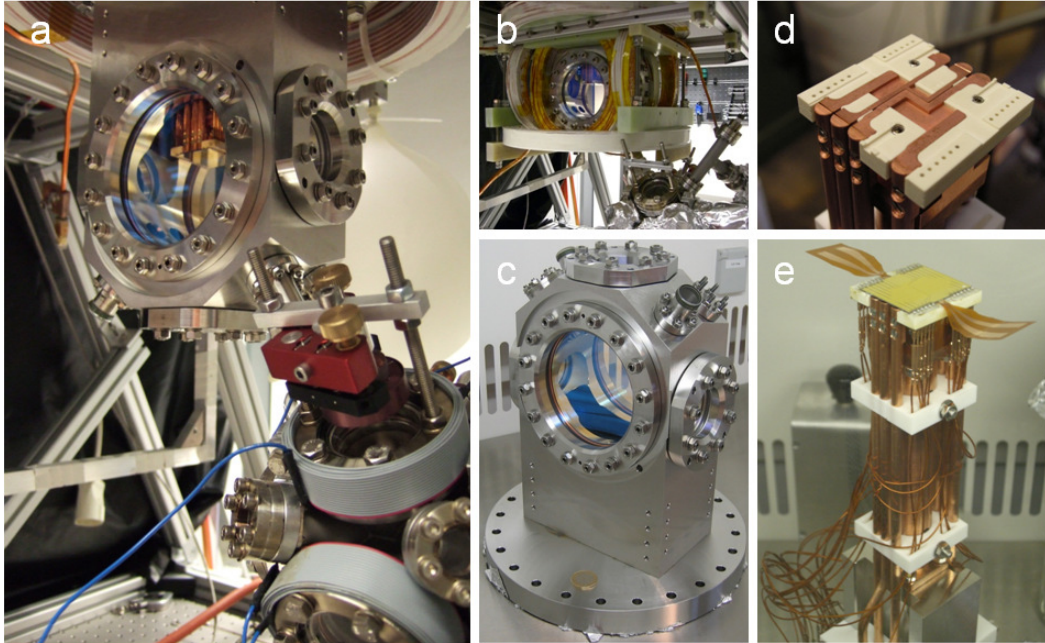


Figure 3.1.: Vacuum setup and mounting of the atom chip. (a) Collection and science chambers in their final setup, connected via a differential pumping tube. The atom chip is mounted upside down in the center of the science chamber. (b) Similar view of the vacuum setup, now with bias coils installed around the science chamber. (c) Close-up of the science chamber, designed by the former PhD student Graf vom Hagen. At the bottom, a 1 € coin gives an impression of the proportions. (d) Top of atom chip mounting (38 x 39 mm), with the white Shapal™ (Shapal™ is a registered trademark of Tokuyama Corporation, Tokyo, Japan) ceramic and the macroscopic copper structures. (e) Side view of the atom chip mounting with a total height above the flange of 31 cm. Gold-coated atom chip on top. The “wings” are Kapton foils carrying copper structures for additional radio-frequency and microwave manipulations of the ultracold atoms.

The vacuum setup consists of two chambers, the science and the collection chambers, connected via a differential pumping stage (compare Fig. 3.1a).

3. The Experiment - Some Practical Considerations

The collection chamber houses the atomic dispenser sources¹, which are permanently under operation. Thus, the typical pressure in the collection chamber is on the order of 10^{-8} mbar, which is maintained by an ion pump².

A close-up of the, science chamber pre-installation is presented in Fig. 3.1c. This is the chamber where the actual experiment takes place under UHV conditions at a pressure of $< 1 \times 10^{-10}$ mbar. The pressure level is maintained by the continuous action of an ion pump³ and the monthly activation of a Titanium sublimation pump. The special design of the science chamber provides good optical access, especially in the transversal direction. To date, four absorption imaging systems have been installed, two in the transversal direction, one in the longitudinal direction and one in the vertical direction (see section 3.1).

3.1.2. Atom Chip and Mounting

The science chamber houses the atom chip, whose surface faces vertically downward. The atom chip is glued to a ceramic⁴ mounting, containing macroscopic copper structures and connections to the current feedthroughs. The whole mounting is UHV-compatible and very rigid, to suppress mechanical vibrations. In contrast to other setups, there is no water cooling installed in this mounting, so the atom chip is operated at room temperature conditions⁵. The ceramic mounting acts as a heat sink for the generated ohmic heat load of the microscopic atom chip structures, carrying currents of up to 1 A, as well as that of the macroscopic copper structures, which can carry a continuous current of up to 60 A.

The atom chip structures are defined in a single layer of gold of 1.2 μm thickness on a silicon substrate, covering an area of $29.7 \times 35.7 \text{ mm}^2$. The central part of the chip is coated with a transparent, 30 nm thick layer of SiO_2 . The coating protects the chip from adsorption of Titanium or rubidium vapour, which has been reported in earlier setups [Göbel 08].

Conventional atom chips are made of gold, copper or silver. Gold is our material of choice for the micro-structures. The micro-wires have to deal with high current densities and high electric fields. Obviously, materials with a high electric and a high heat conductivity are preferred. Even though gold has a slightly worse heat and electric conductivity than copper or silver, it has been shown to feature a lower thermally induced⁶ magnetic noise amplitude (Johnson current noise) at a temperature of 300 K [Dikovskiy 05]. In this context, the term noise means AC fluctuations of the “static” magnetic field of a metallic wire. Such fluctuations can cause trap loss (spin-flips), population of excited states (heating) and coupling to the environment (dephasing,

¹dispensers for two atomic species are installed. First, commercial rubidium dispensers from SEAS Getters, Inc. and second, home-built, enriched (^{40}K : 5,5%) potassium dispensers, which were not under operation when taking data for this thesis.

²Varian 201/s Star-Cell ion pump

³Varian Star Cell 1501/s

⁴made of Shapal, due to its high heat conductivity of $100 \text{ Wm}^{-1}\text{K}^{-1}$

⁵for normal metals Johnson current noise is not reduced at lower temperatures (see below)

⁶besides thermally induced noise, there is technical noise coming from the current supply stability

3. The Experiment - Some Practical Considerations

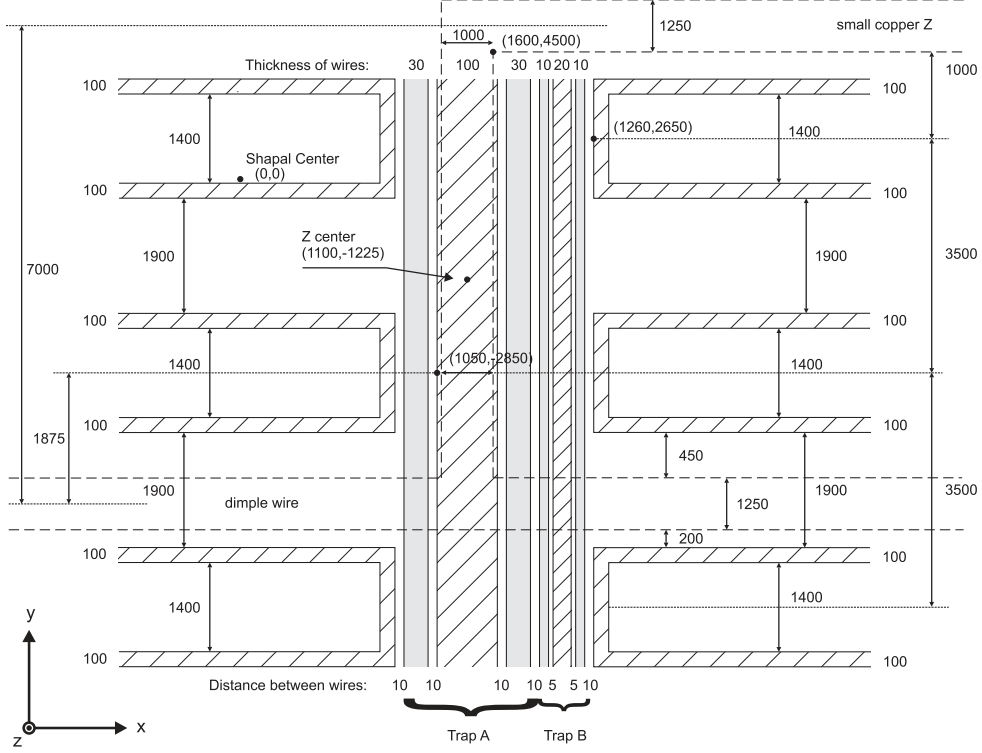


Figure 3.2.: KRb atom chip schematics, not to scale. All values in μm . The coordinate system has been chosen such that the y-axis points in the longitudinal and the x- and z-axes in the radial directions of the microscopic atom chip trap. Details are discussed in sec. 3.1.2.

decoherence). Interestingly, all three processes are proportional to the power spectrum of the magnetic noise. Counter-intuitively, cooling normal metals does not lead to a reduction of the thermally-induced magnetic noise, but rather to an increase at low temperatures, the reason being the following: The power spectrum of the magnetic noise is proportional to the ratio $R = T/\rho$ [Henkel 03], where T is the surface temperature of the metal and ρ the surface resistivity, which scales linearly with T at high temperatures (phonon scattering) and non-linear with T at low temperatures. In view of available technology for the fabrication process (ease of evaporation, etching, electroplating) copper and gold are somewhat equal. Gold becomes preferable to copper due to its high resistance to corrosion and its high reflectivity ($> 95\%$), needed for the operation of mirror MOTs [Reichel 99, Folman 00].

The magnetic trap is formed by a DC-current-carrying straight trapping wire in combination with a homogeneous bias field, which produces a 2d quadrupole confinement along the wire. The trap is closed in the longitudinal direction by two sets of U-shaped wire pairs.

The schematics of the atom chip are illustrated in figure 3.2. The two possible trapping wires are depicted in the central region parallel to the y-axis. The main trapping wire

3. The Experiment - Some Practical Considerations

is 100 μm wide and was used throughout the work on this thesis. The smaller trapping wire has a width of 20 μm , allowing even higher trap anisotropies. Each trapping wire is surrounded by a pair of smaller wires, the wires of each pair being respectively 30 μm and 10 μm wide. These pairs are used to apply the radio-frequency dressing of the chip trap, to generate a double-well potential in the radial x-direction. The longitudinal confinement is provided by a set of 4 U-shaped wires, each 100 μm wide. The dashed line depicts the position of a copper H-shaped structure (beneath the atom chip), that is being 1 mm thick. The straight leg of the H can be used to form a dimple trap. The other leg is used to form the macroscopic copper-Z trap, which is slightly off-center with respect to the four upper Us (as seen in Fig. 3.2). In principle, six different trap positions can be realized using one of the trapping wires and different combinations of U structures. Throughout the work of this thesis, only the trap closest to the copper-Z center was used.

It is actually the ohmic heating of the atom chip wires that limits the duration of the chip traps to 2-3 seconds. Great care needs to be taken not to accidentally vaporize the small gold structures and permanently damage the atom chip. Therefore, the resistance of the wires is continuously monitored and, to be on the safe said, not allowed to increase by more than 1 % during one experimental cycle.

Custom built current drivers, supplied by 12 V car batteries, are used to regulate the chip currents with a maximum current of 2 A. To prevent any damage from malfunctioning current drivers, additional resistors are connected in series, which limit the maximal possible current flow close to the set value of each wire. Fast electronic switches allow switch-off times below 10 μs .

More details on the KRb atom chip and its fabrication process have been reported elsewhere [Göbel 08, Gring 12a].

3.1.3. Bias Coils

Homogeneous magnetic bias fields are generated by three coil pairs in Helmholtz configuration [Kuhnert 08]. These coils are made of hollow copper wires⁷, which are constantly water-cooled, thereby stabilizing their temperature to 12 °C. DC currents of up to 60 A can be applied, generating magnetic field strengths of up to 166 G in the center of the coil pairs. They closely surround the science chamber and are mounted on fiber-glass-reinforced epoxy material⁸, as can be seen in Fig. 3.1b. Typical switch-off times for these coils are below 50 μs at a current of 5 A. The coils were manufactured by the in-house workshop [Göbel 08] and tested during the work presented in [Kuhnert 08].

The power-supplies⁹ of the bias coils are controlled in the constant voltage mode via an analog channel of an ADwin¹⁰ system. Using the constant.voltage mode of the power-supplies to generate the static magnetic fields is preferable as the constant-current

⁷Wire-size: 4.4-4.45 mm; wire size with Kapton insulation layer: 4.6 mm; hole diameter: 2 mm; supplied by S&W Wire Company <http://www.swwireco.com/>

⁸fiber-glass-reinforced epoxy EPG-GC-201, supplied and machined by Hippe, www.hippe.de

⁹Agilent low noise laboratory power-supplies 665xA. Noise characteristics for 6651A between 20 Hz to 20 MHz: voltage rms = 300 μV and current rms = 25 mA.

¹⁰ADwin-Pro, Jäger Messtechnik GmbH

3. The Experiment - Some Practical Considerations

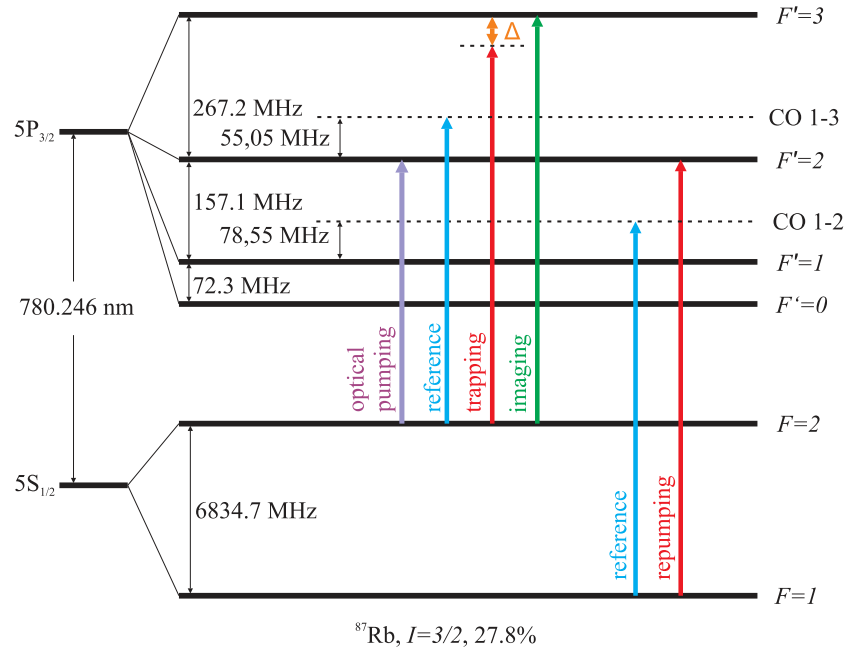


Figure 3.3.: ^{87}Rb D₂-line level scheme of the D₂-line with laser lock-points (reference) and relevant optical transitions.

mode turns out to be noisier according to the specifications and according to heating rate measurements in the magnetic trap. Even long-time temperature drifts were observable in constant current mode. Thus, surprisingly the constant voltage mode turns out to be better. Temperature drifts are suppressed by water cooling the bias coils and having an air-conditioning present that stabilises room temperature to $\pm 1^\circ\text{C}$ and optical bench temperature (flow box) to $\pm 0.5^\circ\text{C}$. The Ioffe field defining the trap bottom of the magnetic trap needs to be stabilized as much as possible. To increase the stability of the Ioffe field, a highly-temperature-stable $1\ \Omega$ resistor was added in series to the circuit, increasing the total resistance almost by an order of magnitude. AC current noise and DC current drifts are further minimized by this trick and the resistor can be used to precisely monitor the Ioffe current as well, being one order of magnitude more sensitive than a usual current clamp of 100 mV/A sensitivity.

Ambient stray fields are compensated by additional, non-water-cooled rectangular copper coils, which are made of thin copper wire.

A set of three circular-shaped coil pairs, made of ribbon cable, are directly attached around flanges of the DNCF40 viewports of the collection chamber. These coil pairs are used to slightly shift the position of the collection MOT with respect to the resonant transfer beam, thereby optimising the loading rate of the mirror MOT in the science chamber.

3. The Experiment - Some Practical Considerations

3.1.4. Laser System

The laser system consists of two home-built rubidium repumping diode lasers¹¹ in a master-slave setup (~ 40 mW optical power) and a commercial Ti:sapphire ring laser system¹² (~ 1.2 W optical power) providing rubidium cooling, imaging and optical pumping light. Both lasers are frequency stabilized to spectroscopy signals, where a Pound-Drever-Hall lock is used for the Ti:sapphire ring laser and a lock-in method is applied for the repumping master laser. Details on the locking schemes are presented in [Kuhnert 08], the relevant lock-points for ^{87}Rb are illustrated in Fig. 3.3. Acousto-optical modulators (AOMs) are used to precisely tune the laser frequencies in the MHz range to the specific frequencies as required for different applications. These applications include cooling and repumping for the collection and science MOTs respectively, optical pumping, imaging, slicing¹³ and, last but not least, atomic transfer from collection to the science MOT. The schematics of the laser system, installed on one optical bench, are drawn in Fig. 3.4, here, for completeness, including the laser system intended for ^{40}K .

3.1.5. Imaging Systems

In total, four different absorption imaging systems have been installed, making it possible to take images of the ultracold atoms from all three spatial directions. Fig. 3.5 shows a 3d CAD drawing of the science vacuum chamber with respect to the imaging directions, which are labelled according to the axes of the cigar-shaped atom cloud, as introduced in sec. 2.2. Therefore, longitudinal imaging, for instance, means that the imaging beam propagates parallel to the longitudinal axis of the atom cloud. Thus, the beam integrates along the longitudinal axis and the final image shows a 2d column density profile, with the two remaining axes being the transverse directions. The atom chip and mounting are shown in the center of the science chamber in Fig. 3.5. Gravity points downwards. The chip surface faces vertically downward, so that the atoms do not hit the chip surface after being released from the trap, but fall away from the chip surface under gravity.

As can be seen, the design of the science chamber has been optimised for the transversal imaging direction, providing good optical access through the large vacuum viewports (one a 10 mm-thick AR-coated quartz glass substrate, the other one being a 15 mm-thick uncoated BK7 window, due to technical reasons [Göbel 08, vom Hagen 08, Kuhnert 08]). The first lens of the high-resolution transversal imaging system is mounted on a motorized translation stage¹⁴ outside the vacuum at a minimal distance to the window surface. The distance between the atom cloud and first lens is approximately 48 mm resulting in a numerical aperture of $NA = 0.26$. The home-built objective of the transverse imaging system consists in total of four commercial lenses and has been designed by a former

¹¹external-cavity laser in Littrow configuration

¹²Verdi V18 in combination with MBR (Monolithic Block Resonator) 110, Coherent, Inc.

¹³The shadow of a line target can be imaged onto the atomic cloud, pumping unwanted parts (longitudinal edges) into dark states for the subsequent absorption imaging. This was the first approach to probe the longitudinal length dependence of interference fringe contrasts. See [Smith 13, Gring 12a]

¹⁴OWIS

3. The Experiment - Some Practical Considerations

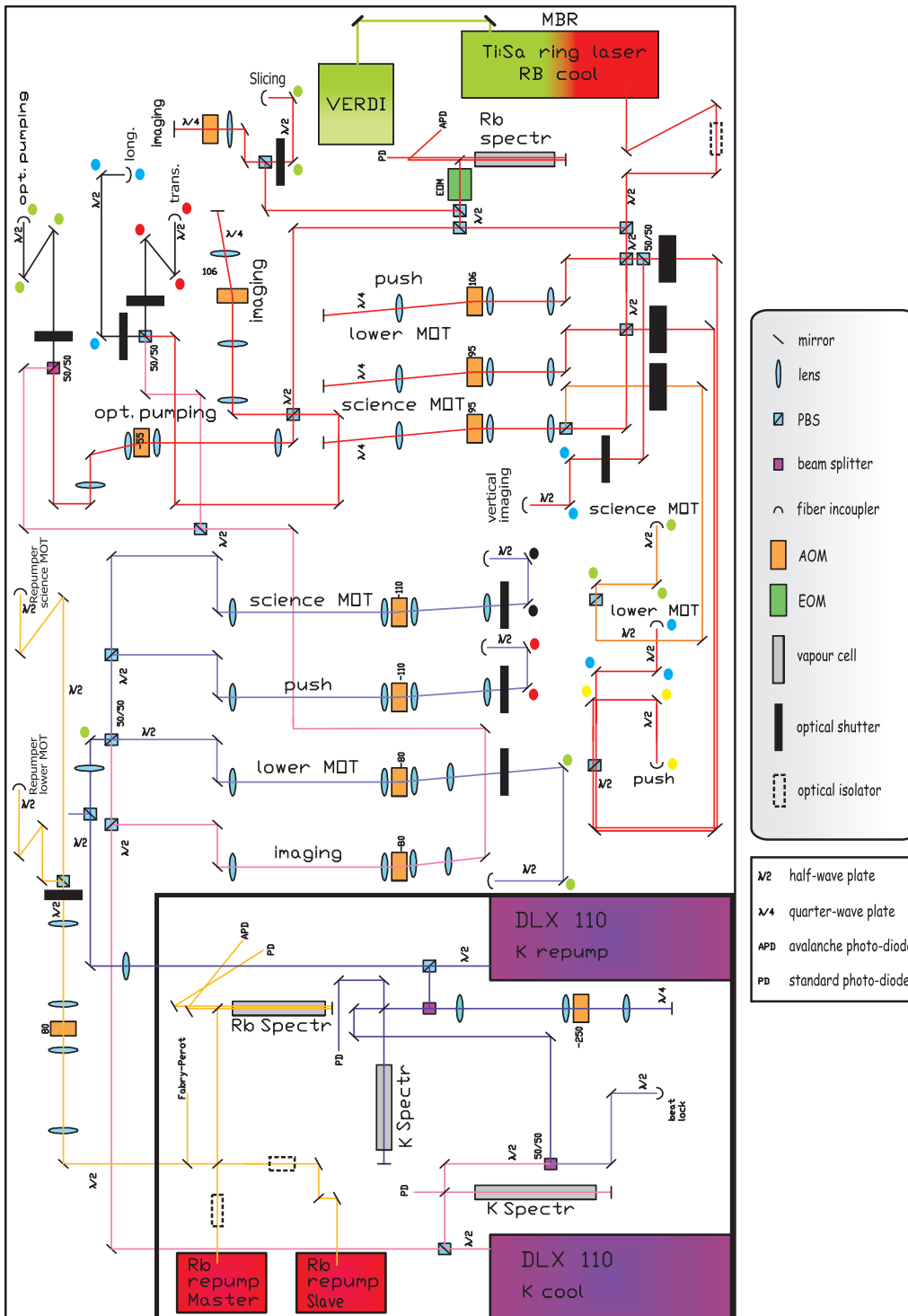


Figure 3.4.: Schematic drawing of the laser system as it is implemented on the optical bench as of 01.2013, including the ^{40}K laser system for completeness.

3. The Experiment - Some Practical Considerations

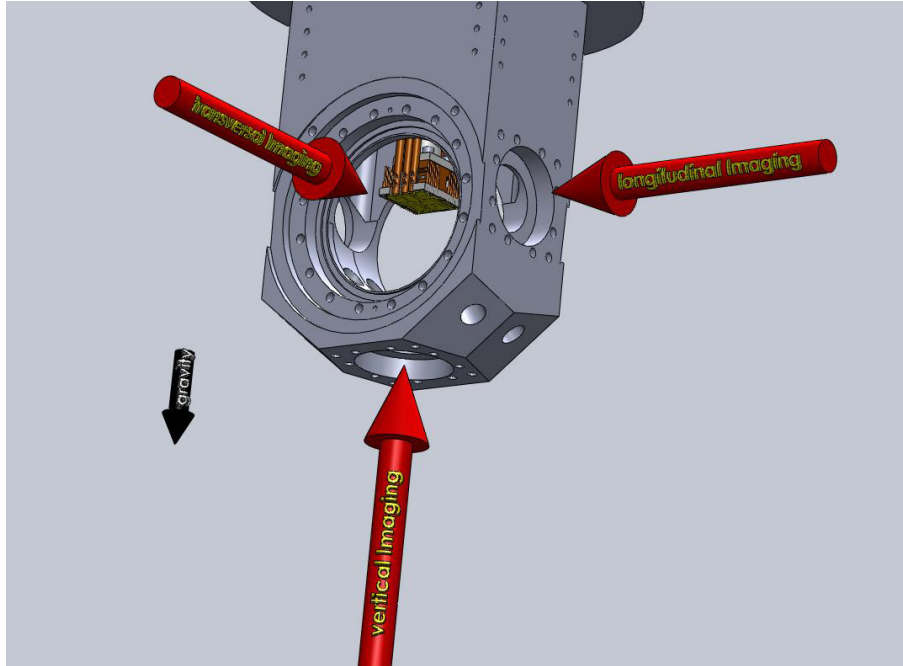


Figure 3.5.: Directions of the imaging systems with respect to the science chamber. The atom chip can be seen at the center.

diploma student [Stix 08] using ray tracing software¹⁵ and rigorously tested [Gring 12a]. The high resolution transverse imaging was mainly intended for in situ measurements of the longitudinal profile of the atom cloud. Currently, it is mainly used to measure the temperature of the quasi-condensate, as discussed in chap. 4. A second overview imaging system with a significantly bigger field of view is also installed in the transverse direction (see table 3.1). It uses the same objective as the high resolution system, just with a different final lens. It suffers from the mechanical vibrations of a flip mirror, which is needed to redirect the light onto a pixelfly camera [Gring 12a]. However, it is only used for optimisation purposes when a large field of view is needed.

Besides imaging the large transverse viewports are used for the optical pumping beam and the two reflecting mirror MOT beams, reflecting at 45° on the gold surface of the atom chip. The other two horizontal mirror MOT beams, closing the MOT confinement, are paraxial to the longitudinal imaging direction, making the installation of the longitudinal imaging difficult but not impossible [Gring 12a].

For the longitudinal imaging, the distance between atom cloud and first lens is approximately 115 mm with a calculated $NA = 0.09$. It can be used to probe the longitudinally integrated interference patterns, thus giving access only to global²¹ but not local properties of interfering quasi-condensates. It is mainly used to measure the total number balance between the two (horizontal) wells of the double-well system, or for Stern-Gerlach

¹⁵ZEMAX, Focus Software Inc., Tucson AZ, USA

²¹This limitation can be overcome by using an optical slicing method. See [Smith 13, Gring 12a]

3. The Experiment - Some Practical Considerations

Imaging system	transversal (high resolution)	transversal (overview)	longitudinal	vertical
Camera	Andor ¹⁶	pixelfly ¹⁷	Andor ¹⁶	Andor EMCCD ¹⁸
magnification (meas.)	12.39 ± 0.04	1.68 ± 0.01	5.30 ± 0.02	7.92
NA (calc.)	0.260	< 0.260	0.096	0.090
field of view [mm ²]	0.7×1	4×5.3	2.5×1.67	1×1
depth of field [μm] (meas.)	5.5 ± 0.9	-	-	-
rms PSF width [μm]	~ 2 resp. ~ 3 ²⁰	-	3.5 ± 0.3	3.7 ± 0.2
pixel to μm	1.05	3.84	2.45	2.02
mainly used for measurements of	temperature, longitudinal trap frequency	overview	number balance of double well, Stern Gerlach, global properties of fringe patterns, transverse trap frequency	local properties of fringe patterns

Table 3.1.: Parameters of installed imaging systems (01.2013)

type of experiments [Gerlach 22].

The chamber design is definitely not advantageous for the vertical imaging system, with a rather small viewport at the bottom of the science chamber and a distance between atom cloud and first lens of approximately 150 mm. Furthermore, the imaging beam needs to be reflected on the atom chip, which generates a second image of the atom cloud and perturbs the image due to the chip structures. To overcome these two problems the imaging beam is focused in the object plane and slightly tilted, so that it passes only once through the atoms and illuminates a small region of the atom chip. We call this method spotlight imaging, which works astonishingly well. For more details the reader is referred to [Rauer 12, Gring 12a]. This imaging system is of particular importance for this thesis as it gives access to relative phase fluctuations along the longitudinal length of the fringe patterns, which are generated by a horizontally split double well (see sec. 5.2). Most of the experimentally obtained interference patterns presented in this thesis have been recorded via this imaging system.

¹⁹Andor DV435-BV-958

²⁰Sony ICX285AL

²¹Andor iXon DV887DCS-BV

²² $2\mu\text{m}$: in situ, $3\mu\text{m}$: in time-of-flight due to limited depth of field (see [Gring 12a])

3. The Experiment - Some Practical Considerations

Table 3.1 gives a summary of the absorption imaging systems.

3.1.6. Experimental Control System and Data Acquisition

The central experimental control unit, where all strings converge, is an ADwin²³ real-time system, with a SHARC-DSP processor running at 80 MHz, 512 kB cache and 128 MB RAM. It feeds 32 analog-output (16 bit), 8 analog-input (16 bit) and 64 digital channels and thereby controlling all relevant equipment during the experimental cycle. Before the start of each experimental cycle, the ADwin is programmed over a TCP/IP connection by a commercial PC, running a user-friendly graphical interface under MATLAB [Brajdic 02]. The time resolution of the cycle is 25 μ s.

Data acquisition is performed simultaneously via a second commercial PC again running a MATLAB code, which acquires, displays and saves the current camera data. All acquired data is stored for post-processing together with a protocol file containing all settings of the control program.

Recently, an additional National Instruments analog-input card²⁴, with 16 channels (16 bit) and 250 kS/s multichannel sampling rate, was installed and is mainly used for monitoring purposes.

3.2. Experimental Cycle - A Brief How To Create a BEC

This section provides a conceptual point of view on how a quasi-condensate is created in an atom chip setup. A brief overview of the experimental cycle in the current setup of the so-called KRb experiment is presented, including some tricks and tweaks that are usually hard to find in the literature. More detailed studies and explanations can be found in the references. A more quantitative description can be found in [Gring 12a]. Details of the laser system and double-MOT setup have been discussed in detail in [Kuhnert 08, Gring 12a, Göbel 08, vom Hagen 08].

3.2.1. Experimental Cycle: An Overview

The experiment runs 24/7 and is operated in cyclic operation, where each cycle can be regarded as one measurement for a specific parameter set. Each experimental cycle lasts for approximately 30-40 s. In short, the experimental cycle can be summarized into seven main steps.

- Laser cooling in a Magneto-Optical Trap (MOT)
- Optical molasses
- Optical pumping and loading of macroscopic magnetic trap
- Evaporative pre-cooling in macroscopic magnetic trap

²³AdWinPro, Jäger GmbH

²⁴NI USB 6218 BNC

3. The Experiment - Some Practical Considerations

- Transfer into microscopic chip trap
- Final evaporative cooling to quantum degeneracy
- Imaging

This is a very simplified recipe to get to quantum degeneracy. The real nuts and bolts will be presented in the next sections.

3.2.2. Magneto-Optical Trapping (MOT)

In the current KRb experimental setup a two-chamber double-MOT setup is used, where a collection MOT feeds a mirror MOT (mMOT) [Reichel 99, Folman 00] (the MOT created below the atom chip, where the gold chip surface acts as a mirror for the MOT beams) via a resonant push beam [Kuhnert 08]. The main advantage of the double-MOT setup is the achievement of UHV conditions in the science chamber, housing the atom chip and where the actual experiments are performed. The better the vacuum, the lower the collision rate with background particles and the longer the lifetimes of the generated cold and ultracold atom clouds. Depending on the alignment [Kuhnert 08], typical loading times up to saturation of the mMOT take between 15 to 30 seconds. The three-beam retro-reflecting collection MOT is loaded within 2-4 seconds from the background pressure (10^{-8} mbar) in the collection chamber, generated by atomic dispenser sources. For details on laser-cooling and trapping the reader is referred to [Kuhnert 08] and references therein.

When the atom number in the mMOT has reached saturation, or when the atom number is high enough to reach quantum degeneracy (a value that needs to be found empirically), the mMOT needs to be mode-matched to the magnetic trap, such that the position and extension of the mMOT is matched closer to the ones of the initial magnetic trap. This is the compressed MOT (cMOT) stage. This means that the mMOT is compressed to a much smaller volume and the distance to the chip is decreased significantly. The magnetic bias fields are increased to move closer to the chip and to increase the gradient of the magnetic quadrupole field for the mMOT. Simultaneously, the power of the MOT beams is increased and the detuning slightly adjusted. Again optimal settings need to be found empirically by optimising the atom number loaded into the magnetic trap. Small misalignments of the magnetic quadrupole reduce the number of trapped atoms significantly. In the current setup, the compression ramp takes 21 ms and the atoms are held in the cMOT not longer than 1 ms. As the density is increased, the MOT loss rate also increases and, furthermore, the atoms start to heat up in this tighter trap. Thus, the duration of the cMOT should be rather short.

3.2.3. Optical Molasses

In order to further cool the atoms, the magnetic fields are completely switched off and the atoms are held in an optical molasses field, providing frictional forces on the atoms and applying the so-called *Sisyphus cooling* scheme. The main optimisation parameters are the detuning and intensity of the laser beams, the molasses duration and the compensation of ambient magnetic fields, which need to be found in an iterative process.

3. The Experiment - Some Practical Considerations

Typical detunings (from the rubidium resonance) of the molasses cooling beams (50 – 70 MHz) are significantly higher than for the MOT beams. As a rule of thumb, at least 2 to 3 times the detuning of the MOT cooling beams (15 – 20 MHz). In order not to pump the atoms into dark states, some repumping light needs to be applied as well.

Typical durations are on the order of some (~ 8) milliseconds.

As the molasses is very sensitive to any remaining ambient magnetic fields it can, in fact, be used to minimize these stray fields using homogeneous bias fields (compensation coils). Stray fields of unknown strength might inhibit the successful magnetic trapping of the atoms. For the initial molasses alignment, the following procedure is recommended. All counter-propagating laser beams need to be balanced in power and optimally aligned. Set the molasses time to five seconds and monitor its expansion and movement on a camera²⁵. The magnetic compensation fields are optimal, when the molasses cloud does not display any translatory movement at all and expands uniformly in all directions. If there is still a magnetic stray field present, the molasses will be pushed in one or another direction. On the other hand, if there is still a slight light force imbalance remaining in the laser beams, due to power imbalance or beam misalignment, it should be almost impossible to get a uniformly expanding molasses. Thus, an iterative alignment process of the light fields and magnetic fields needs to be followed.

After this first rough optimisation process, the molasses can be fine tuned by minimizing the ambient magnetic field further. This can be achieved by scanning the compensation fields and minimizing the molasses temperature [Taglieber 08]. As the field of view of our pixelly camera was not sufficiently huge to measure the molasses temperature and the Firewire camera was not yet available, we never applied this fine tuning step. We typically reached molasses temperature below 50 μK , well below the ^{87}Rb Doppler temperature $T_D = 146 \mu\text{K}$.

3.2.4. Optical Pumping

Neutral atoms with a magnetic moment $\vec{\mu}$ can be trapped in a weak magnetic field via the potential $U = -\vec{\mu} \cdot \vec{B} = m_F g_F \mu_B |\vec{B}|$, as given by the linear Zeeman effect, with the Bohr magneton μ_B , the Landé g-factor g_F and the magnetic quantum number m_F . The magnetically trappable states are low-field seeking states, fulfilling $g_F m_F > 0$, where the atoms are trapped in the minimum of the magnetic field. High-field seeking states cannot be trapped in a static magnetic trap according to the so-called Wing theorem [Wing 84], which is an application of the Earnshaw theorem [Earnshaw 33] on magnetic fields. The Wing theorem shows that Maxwell's equations forbid local maxima in current-free space, while local minima are possible. States with $m_F = 0$ are not affected by the magnetic fields and thus cannot be trapped magnetically.

At the end of the molasses stage, the states of the atoms have some arbitrary distribution among the possible hyperfine states. To maximize the number of trappable atoms, an optical pumping scheme is applied, transferring most of the atoms into the desired

²⁵In the KRb setup, a Firewire camera from ImagingSource (DMK 21BF04) is used for MOT and molasses monitoring

3. The Experiment - Some Practical Considerations

trappable state, which in the case of Rb^{87} is either $|F, m_F\rangle = |1, -1\rangle$, or $|2, 2\rangle$ respectively. In the KRb setup, the latter $F = 2$ hyperfine state is used, meaning that the molasses generates atoms distributed in the manifold of 5 Zeeman sub-levels. Therefore, a factor of 5 is the theoretical limit of an increase in trapped atom number by optimal optical pumping. In reality, a factor of 4 is typically found to be achievable. To define a quantization axis for the atoms, an external bias field, parallel to the optical pumping beam, is linearly ramped up before the optical pumping pulse is applied. The atoms are pumped into the desired m_F state by applying σ^+ -polarized light, resonant on the $|5S_{1/2}, F = 2\rangle \rightarrow |5P_{3/2}, F' = 2\rangle$ Rb^{87} transition [Steck 01]. The circular polarization allows only $\Delta m = +1$ transitions, whereas the spontaneous decay of the excited state allows all three $\Delta m_F = -1, 0, +1$ transitions. Over the course of many excitations, the atoms accumulate in the fully stretched $|5S_{1/2}, F = 2, m_F = 2\rangle$ state, which is a state dark to the σ^+ -polarized light. As there is a small probability of atoms decaying into the $|5S_{1/2}, F = 1\rangle$ state, a repumping beam, resonant at the transition $|5S_{1/2}, F = 1\rangle \rightarrow |5P_{3/2}, F' = 2\rangle$, needs to be applied as well (similar to during the MOT phase), effectively creating a two-level system.

The efficiency of the pumping pulse is determined via measurements of the trapped atoms in the subsequent magnetic trap. The main parameters are the correct timing, the duration and intensity of the pulse as well as the σ^+ -polarization of the light. Only small intensities ($50 \mu\text{W}/\text{cm}^2$) should be used to limit the momentum transfer onto the atoms. After the optical pumping phase, all light sources are switched off via AOMs and mechanical shutters and the atoms are loaded into the macroscopic magnetic trap.

3.2.5. Loading into the Macroscopic Copper-Z Magnetic Trap

The atoms are captured in a shallow Ioffe-Pritchard type magnetic trap [PrPopov 83], typically formed by a macroscopic Z-shaped copper structure in combination with homogeneous bias fields, the bias fields being generated by the water-cooled bias coils in Helmholtz like configuration (compare sec. 3.1.3). The principle is illustrated in Fig. 3.6. The remaining offset field at the minimum of the trapping potential is called the Ioffe field and prevents Majorana spin flips of the trapped atoms. The magnetic moment μ of an atom follows adiabatically the magnetic field as long as the magnetic field change is small compared to the Larmor frequency $\omega_{Larmor} = \mu B/\hbar$. Thus, to fulfil the criterion

$$\omega_{Larmor} \gg \frac{1}{B} \frac{dB}{dt}, \quad (3.1)$$

a Ioffe field needs to be applied. A good estimate for the remaining loss rate Γ in a Ioffe trap is given by $\Gamma \propto \exp(-2\omega_{Larmor}/\omega_{tr})$ [Gov 00, Brink 06]. Here, ω_{tr} is the transversal trapping frequency as defined by the curvature of the harmonic potential, which is only a good approximation at ultracold temperatures. At cold temperatures the Ioffe-Pritchard potential is better approximated by a linear trap as can be seen in Fig. 3.10, which actually gives even higher thermalization rates when modelling the evaporative cooling process [Pethick 01]:

3. The Experiment - Some Practical Considerations

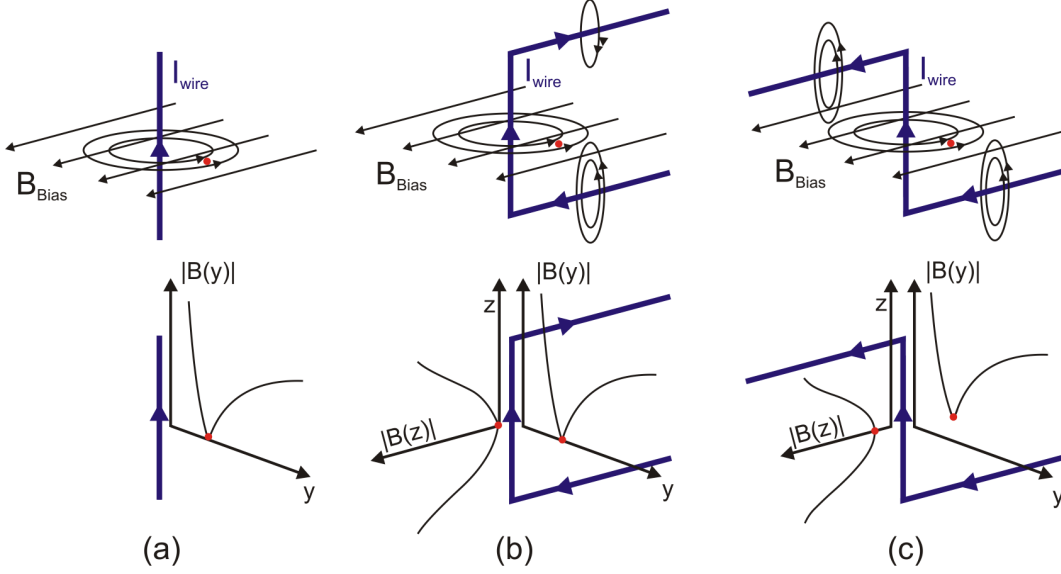


Figure 3.6.: Wire geometries for creating macroscopic magnetic traps. (a) Superimposing the magnetic field of a straight, current carrying wire with a homogeneous external bias field generates a 2D quadrupole trap along the wire. (b) Bending the wires into a U shape generates a 3D quadrupole trap, which is used for the mMOT and cMOT. (c) Z shaped structures generate a Ioffe-Pritchard like trap without a magnetic zero, preventing Majorana spin flips. Red dots illustrate the position of the minimum of the magnetic fields and blue solid lines current carrying structures. Based on [Wildermuth 05a].

$$\omega_i = \sqrt{\frac{1}{m} \frac{d^2 U}{dx_i^2}} = \sqrt{\frac{m_F g_F \mu_B}{m} \frac{d^2 B}{dx_i}}. \quad (3.2)$$

The Larmor frequency of ^{87}Rb in the $F = 2$ state scales with 1.4 MHz/G, making transverse trapping frequencies in the kHz range easily possible. For realistic values of $B_{\text{Ioffe}} > 0.1$ G and $\omega_{tr} > 200$ Hz the Majorana spin flip rate is negligible.

In order to further improve the mode-matching between the capturing magnetic trap and the cMOT, two parallel Z-shaped copper structures are used simultaneously, to generate a very shallow magnetic trap. According to their cross sections, these structures are referred to as the big (1×2 mm) and small (1×1 mm²) copper Z's. The purpose of the big copper Z is mainly to create a bigger trapping volume in the initial magnetic trap. Mode-matching means that the position of the trap center should match as close as possible the center of the optical molasses, which is adjusted with the parameters of the cMOT (see sec. 3.2.2). Furthermore, the steepness of the magnetic trap is defined by the molasses temperature (< 50 μK) and the width of the molasses σ_i in the i -th direction by [Ketterle 99]

3. The Experiment - Some Practical Considerations

$$\omega_i = \sqrt{\frac{k_B T}{m \sigma_i^2}}. \quad (3.3)$$

A trap, that is too steep, results in heating of the atoms, a trap, that is too shallow, leads to a decrease in phase-space density. An asymmetric trap cannot fulfil eq. 3.3 in all directions, so one has to find a compromise with a slightly too steep transverse confinement and a slightly too low longitudinal confinement. In our case, this initial ‘‘capturing’’ trap has calculated trap frequencies of about $\omega_{trans} \approx 2\pi \times 50$ Hz, $\omega_{long} \approx 2\pi \times 17$ Hz and a trap depth of 1.6 mK. The minimum of this trap is located 2.5 mm below the chip surface. We typically capture up to 7×10^7 atoms in this first magnetic trap. The atoms are heated in the loading process up to 300 μ K. Immediately after the loading of the magnetic trap is finished, the current in the big copper Z ($I_{peak} \approx 70$ A) is ramped down in about 350 ms.

The resultant trap, formed solely by the combination of the small copper-Z structure and the main bias field has a much too high Ioffe field (generated by the two legs of the Z), which needs to be compensated. Typical desired Ioffe fields are on the order of one Gauss, which are achieved by superimposing an additional, anti-parallel and homogeneous Ioffe bias field. In this way the so-called uncompressed magnetic Z trap is formed, with typical trap frequencies of $\omega_{trans} = 2\pi \times 126$ Hz, $\omega_{long} = 2\pi \times 21$ Hz, and is located approximately 1 mm below the atom chip and has a typical trap depth of approximately 1.9 mK. This small trap depth explains as well the need to pre-cool the atoms before they can be caught in a magnetic trap, with an energy scaling given by $\mu_B = k_B \cdot 67 \mu\text{K}/\text{G}$.

In practice, loading atoms into the Ioffe-Pritchard type magnetic trap follows relatively simple rule: Catch the untrapped cold atoms before they leave the trapping volume due to gravity and ballistic expansion. In principle, the magnetic fields are ramped up as fast as adiabatically possible. In reality, typical limitations are given by the inductivity of the bias coils that generate the homogeneous bias fields. The voltage-controlled power-supplies (compare sec. 3.1.3) are *pre-charged*, meaning that they are set to output their maximum voltage, before a switch closes the electric circuit, in this way achieving the highest possible dI/dt rates. In the KRb setup, the ramp up of the main bias field takes approximately 2 ms to 16.2 A, where the coils have 100 m Ω resistance and 0.28 mH inductance [Kuhnert 08]. The ramp up of the copper-Z structure, which could be in principle ramped up much faster for its negligible inductance, is done simultaneously. Great care needs to be taken to flatten any over-shootings in the bias coil currents, at the end of the ramp up. Any overshooting deforms the trap and might induce collective oscillations, heating up the cold atoms.

Once the loading into the magnetic trap is finished, evaporative cooling could in-principle be applied. However, the time available for the evaporative cooling process is limited by the lifetime of the atoms in the magnetic trap. Therefore, high collision rates are necessary for the evaporative cooling process to work sufficiently fast compared to trap loss mechanisms. To increase the collision rates and thereby decrease the time needed for re-thermalization, the magnetic trap needs to be compressed further.

3. The Experiment - Some Practical Considerations

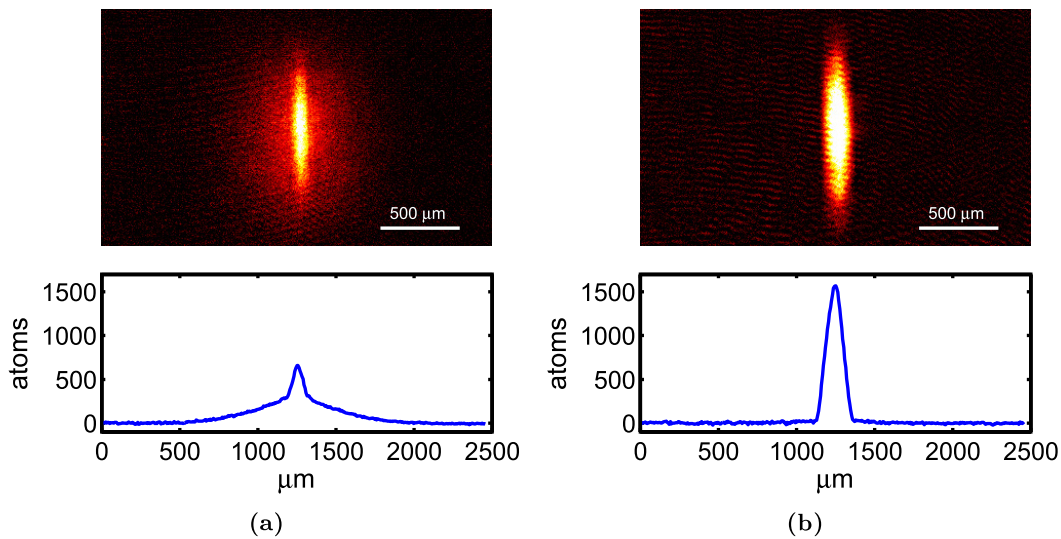


Figure 3.7.: In time-of-flight absorption images (top) of the first BECs created in the copper-Z trap with the vertically integrated density profile (bottom).
 (a) Bimodal density distribution with a significant thermal fraction (b) Almost pure BEC of 3×10^4 atoms.

3.2.6. Pre-cooling and Compressing in the Macroscopic Copper-Z Magnetic Trap

To achieve efficient and fast evaporative cooling of the thermal atoms to quantum degeneracy, a sufficiently high collision rate is necessary. To increase the collision rate, the copper-Z trap is further compressed within 2 seconds to $\omega_{trans} \approx 2\pi \times 800$ Hz, $\omega_{long} \approx 2\pi \times 24$ Hz, a trap bottom of 700 kHz²⁶ and a theoretical trap depth of 3.9 mK. The actual trap depth is limited by atoms hitting the chip surface to approximately 1.5 mK as the minimum of the absolute magnetic field is now 300 μm from the chip surface (compare Fig. 3.10). Starting with the compression ramp, a radio-frequency cooling knife is applied to start the evaporative cooling process [Ketterle 96b].

Actually, it is already possible to achieve condensation in this compressed trap, with typically 10^5 atoms in the condensed fraction. One of the first condensates in the KRb setup is shown in Fig. 3.7. When the trapping potential is switched off suddenly and sufficiently fast, the atoms expand ballistically and fall under gravity (Fig. 3.8). The interaction energy of the condensed atoms is converted into kinetic energy [Mewes 96]. In the case of a strongly asymmetric trap, the condensed atoms expand predominantly in the tightly confined direction as the initial acceleration after switch-off of the trap is dictated by the gradient of the interaction energy and is inversely proportional to the width of the condensate. The anisotropic expansion in time-of-flight (TOF) is an easy to

²⁶A Ioffe field of 1 G gives for ^{87}Rb in the $|F = 2, m_F = 2\rangle$ state a trap bottom of 700 kHz with respect to rf transitions coupling the m_F states.

3. The Experiment - Some Practical Considerations

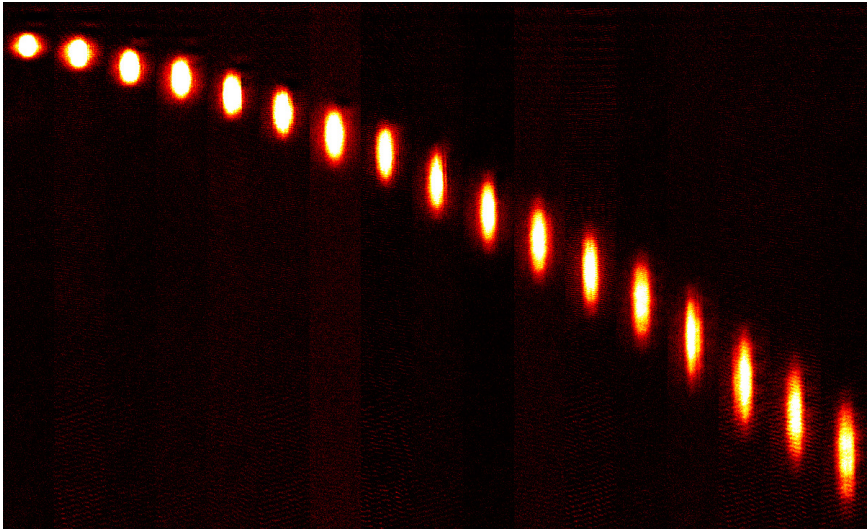


Figure 3.8.: Anisotropic condensate expansion in time-of-flight. The time-of-flight is increased from left to right in steps of 1 ms, starting at 4 ms. Gravity is pointing downwards in the vertical direction.

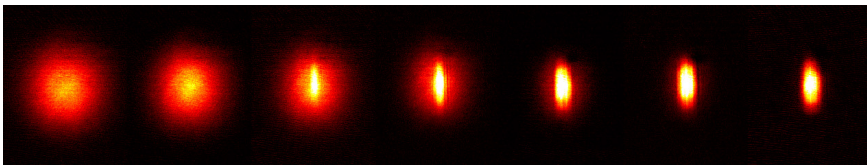


Figure 3.9.: Condensation of a thermal ^{87}Rb cloud in the copper-Z trap. Decreasing the final rf-cooling frequency in steps of 10 kHz illustrates the drastic difference in isotropic expansion of thermal clouds in 8 ms time of flight versus the anisotropic expansion of BECs. Thus, absorption pictures already provide a plain signature of condensation.

use and clear signature of condensation, as illustrated in Fig. 3.9.

Creating a BEC already in the copper-Z trap is a good test for the magnetic trap settings, especially to confirm that the compression is sufficient to allow efficient evaporative pre-cooling before loading the atoms into the atom chip trap. Furthermore, substantial technical noise problems can thereby be ruled out, such as, for example, noise sources emitting broad-band and/or peaked electro-magnetic radiation in the rf-domain (typically ion gauges, all kinds of DC power supplies for network switches, shutters or translation stages, etc.). Resonant rf-frequency couples the Zeeman sublevels and transfers the atoms into untrapped states, severely increasing the atom loss rate and decreasing the lifetime in the magnetic trap. Of course, measuring a long enough lifetime (say >10 s) of thermal atoms in the magnetic trap [Kasper 03] is a necessary precondition before trying condensation and helps to verify that the pressure is sufficiently low. Other possible issues strongly affecting the lifetime in the magnetic trap and thereby preventing

3. The Experiment - Some Practical Considerations

successful condensation, can be stray light leaking into the vacuum chamber or laser light leaking through holes in burned shutter blades or through stalling shutters. To make the point clear, any small amount of stray light is a severe problem (see section 6.1), where the sensitivity level of power meters is typically not high enough. Instead photodiodes can be mounted in the laser beam paths to make sure no laser light is leaking into the MOT/imaging/etc. optics when the magnetic trapping is in effect. Stray light has to be reduced to a minimum by protective covers around the vacuum chamber.

Once a BEC is successfully achieved, it is advisable to measure the lifetime of the BEC, heating rates as well as take rf-spectroscopies of the condensate. All these measurements can be later used as references. Here, the main idea is to find additional noise sources, especially at 50 Hz and higher harmonics thereof resulting from possible ground loops in your setup. For example, the width of the rf-spectroscopy is not only affected by the chemical potential of the BEC, but also by the temperature of the remaining thermal atoms, furthermore by power broadening of the rf transition and, last but not least, by short term variations in the trap bottom (50 Hz from ground loops and power supply ripple noise). Now, by applying short (~ 1 ms) spectroscopy rf-pulses a double-minimum structure may be found, resolving the trap bottom oscillations at 50 Hz. In that way, one finds an estimate of the amplitude of the trap bottom oscillations. On the other hand, rf-pulses longer than the 20 ms period will average over the 50 Hz oscillations and just lead to an increased width of the spectroscopy signal. Hunting and eliminating noise sources and improvements to your setup will decrease the width of the rf-spectroscopy signal. In April 2009, we found a FWHM width of approximately 10 kHz, in June 2009, we found 6 kHz and in December 2011 we found an improvement to 2 – 3 kHz. So clearly our ongoing efforts in improving our setup and identifying and eliminating potential noise sources were indeed successful. A list of the applied changes to the experimental setup is out of the scope of this thesis and the reader is referred to the 16 KRb labbooks.

Another useful and obvious tip is to make use of your working BEC as a very sensitive probe, when the experimental setup is modified and/or additional equipment is installed. This means, whenever possible leave the experimental cycle running in the background, continuously monitoring the atom number of the BEC. If a new ground-loop is created in the process, you might find a change in trap bottom and thereby lose the BEC.

Concerning grounding considerations, one may recommend the books [Morrison 98, Moore 09].

To be able to get into the quasi-condensate regime, very high trap anisotropies are needed (sec. 2.2.1). This is where the atom chip comes into play, providing high transverse and low longitudinal confinements, using microscopic chip structures. The atoms are pre-cooled in the compressed copper Z-trap to $T \approx 1 - 2 \mu\text{K}$ and $N \approx 10^6$ atoms within 6 seconds ready to be transferred afterwards into the microscopic atom chip trap.

3. The Experiment - Some Practical Considerations

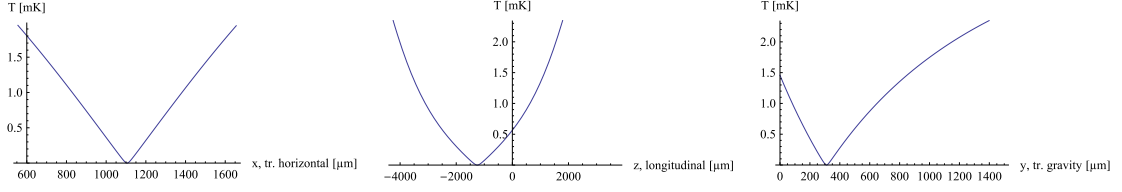


Figure 3.10.: Calculation of the trapping potential in the compressed copper-Z trap. In the cold temperature regime, the trapping potentials can be approximated as linear, which is even better suited for evaporative cooling [Pethick 01]. The harmonic approximation becomes valid for ultracold temperatures. The asymmetry in the z-direction is caused by gravity.

3.2.7. Transfer into the Microscopic Atom Chip Trap

Most of the experiments reported in this thesis were done in a highly anisotropic trap of nearly harmonic confinement with measured²⁷ trap frequencies of $\omega_{trans} = 2\pi \times (2100 \pm 100)$ Hz, $\omega_{long} = 2\pi \times (11 \pm 1)$ Hz, a calculated trap depth of 300 μ K and a distance to the chip surface of 100 μ m. The magnetic trap is formed by a 100 μ m-wide gold trapping wire with a current of 808 mA creating, in combination with a homogeneous bias field of 15 G, a 2d quadrupole confinement along the wire. The trap is closed in the longitudinal direction by two sets of U pairs carrying 410 mA of current. In this way, the trap closest to the copper-Z center was established (sec. 3.1.2).

The transfer from the copper-Z trap into the atom chip trap takes 600 ms. In the case of good mode-matching during the loading process between the two traps, almost all the atoms can be successfully transferred, as shown in Fig. 3.13. We still observe a heating of the atoms by approximately 8 μ K.

In this final chip trap we typically achieve quasi-condensates of 2000 - 10000 atoms, in the temperature range of 20 - 100 nK. As the transverse energy scaling of this trap is $\frac{\hbar\omega_{trans}}{k_B} = 101$ nK, we are in the effective 1d regime (as defined in sec. 2.2.1). Following eq. 2.21, typical chemical potentials are in the range of 750 - 2000 Hz, again fulfilling $\mu < \hbar\omega_{trans}$. Changing the temperature and atom numbers within the specified ranges, allows us to tune the phase correlation length λ_T by one order of magnitude.

Fig. 3.11 shows a schematic summary of the magnetic trapping.

3.2.8. Final RF Cooling to degeneracy

A forced evaporative cooling technique is used to achieve condensation. The hot atoms are removed from the trap by applying a rf-knife in the MHz range, which couples

²⁷Trap frequencies are easily measured by exciting collective excitations of cloud size or position. In our setup, we use a short triangular current-pulse in one of the U structures to excite longitudinal oscillations and, similarly, a short triangular pulse in the main trapping wire to excite transverse excitations.

3. The Experiment - Some Practical Considerations

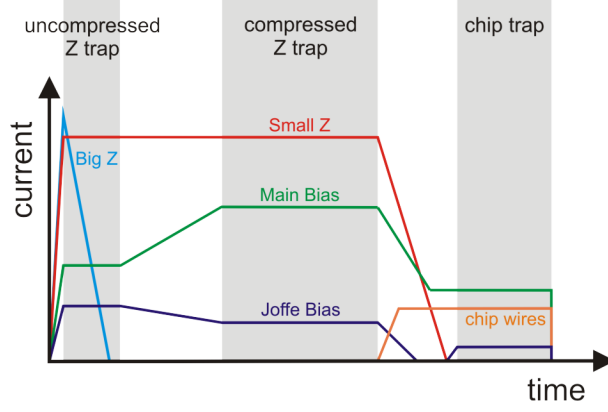


Figure 3.11.: Overview of the magnetic trapping cycle.

the Zeeman levels. By continuously removing the hottest atoms from the trap, the phase-space density PSD can be increased by six orders of magnitude [Ketterle 96b]. The phase-space density is given by

$$PSD = \rho \lambda_{dB}^3 = \rho \left(\frac{2\pi\hbar^2}{mk_B T} \right)^{\frac{3}{2}}. \quad (3.4)$$

The BEC transition occurs at $PSD = g_{3/2}(1) \approx 2.612$, with the Bose-function $g_n(z) = \sum_{k=1}^{\infty} \frac{z^k}{k^n}$ (see appendix C).

For evaporative cooling to work, thermalization times need to be short in comparison to the lifetime of the sample. This means that the ratio of good collisions (elastic collisions) needed for thermalization to bad collisions (inelastic collisions, background gas collisions) leading to atom loss and a decrease in lifetime gives a measure of the efficiency of evaporative cooling. The compressed Z trap (11 s lifetime) and the chip trap provide high enough elastic collision rates to successfully reach degeneracy. A detailed discussion about trap lifetime and loss processes can be found in sec. 6.1.

Fig. 3.12 shows the forced rf-cooling ramp, which consists of several linear frequency ramps. The rf-cooling starts in the compressed Z-trap, pre-cooling the atoms in 5.9 s to about $1 - 4 \mu\text{K}$ leaving up to 10^6 atoms in the trap. After loading into the atom chip trap, the atoms are cooled down further, until degeneracy is reached, which happens within 1340 ms. Finally, the rf-knife is held at a constant value for a duration of 20 ms. This is done for two reasons. First, in order to average over the unavoidable 50 Hz oscillations of the trap bottom (see 3.2.6), decreasing shot-to-shot fluctuations of the atom number, and, second, to give the quasi-condensate some time to equilibrate. Several ms should be more than enough for equilibration of this 1d system according to the theoretical predictions of [Grisins 11] and if thermalization would need much more time, then the evaporative cooling would have ceased to work so efficiently. The output of the rf-generator is switched off and after waiting for an additional equilibration time of 10 ms the experiments on the quasi-condensate can commence.

3. The Experiment - Some Practical Considerations

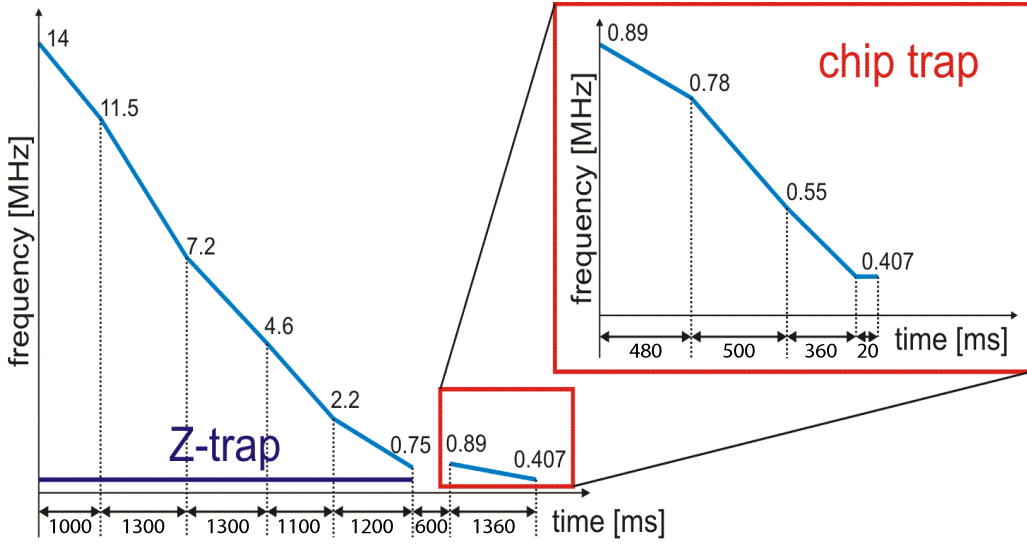


Figure 3.12.: Frequency of the rf-cooling knife versus time. The atoms are pre-cooled in the copper-Z trap before being loaded (within 600 ms) into the atom chip trap, where they are finally cooled to quantum degeneracy. The corresponding trap bottom is typically at 405 kHz. Adapted from [Schreitl 10].

Evaporation ramps in the chip trap faster than 1340 ms are possible, but these fast ramps lead to unwanted collective oscillations of the final quasi-condensate. These may be remnant oscillations coming from the transfer into the chip trap, which get damped in the thermal gas for sufficiently long evaporation ramps.

Fig. 3.13 shows the measured increase in phase-space density in the chip trap. Here $t = 0$ ms is the end of the Z-trap. Almost 100% of the atoms are transferred within 600 ms into the atom chip trap, but, due to the mismatch in trap-frequencies, the mode-matching is not perfect and leads to a temperature increase of almost $8 \mu\text{K}$.

Special care needs to be taken, that the final cooling ramp excites a minimum of dipole and quadrupole modes in the condensate. Dipole modes are center-of-mass oscillations of the condensate and quadrupole modes manifest themselves as breathing like oscillations of the condensate width along the longitudinal direction [Moritz 03]. It is quiet easy to excite these excitations unintentionally in the longitudinal direction by a too fast evaporative cooling scheme. Decreasing the speed of the cooling ramp often helps too decrease the observed oscillation amplitudes. This can be easily understood in an intuitive picture [Rauer 12]. At a specific value of the chemical potential, the rf cooling knife removes trapped atoms. As the density is not constant throughout the harmonic trap, the atoms are mainly removed at the axial-central, high-density region of the cloud. This non-uniform effect leads to a perturbation of the longitudinal profile in comparison to the unperturbed profile in thermal equilibrium. The more atoms are removed in a certain time step, the higher the generated inward flux, which, eventually, increases the amplitude

3. The Experiment - Some Practical Considerations

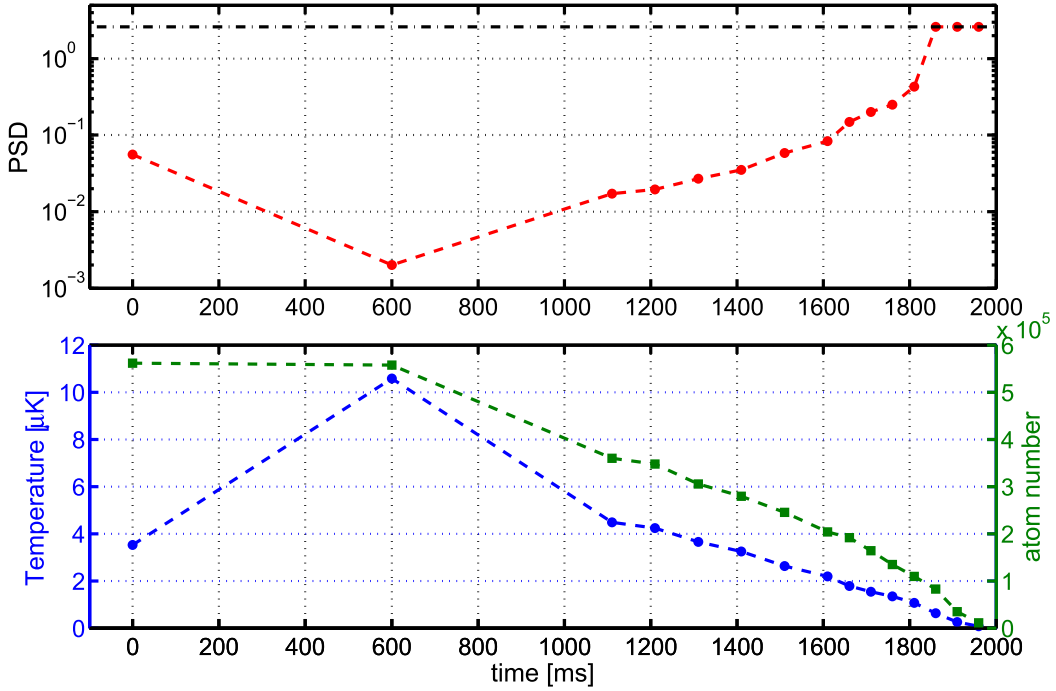


Figure 3.13.: Evolution of the 3d phase-space density (top), temperature (bottom, circles) and atom numbers (bottom, squares) when loading from the copper-Z trap ($t = 0$ ms) into the atom chip trap ($t = 600$ ms) and applying the final rf-cooling stage. Adapted from [Schreitl 10]. The dashed-dotted line (top graph) marks the 3d BEC phase transition. The dashed lines are guides to the eye.

of breathing oscillations after stopping the evaporation process. Therefore, minimal oscillations can be found when applying an exponentially decaying final evaporation stage (compare sec 3.2.8 and [Rauer 12]).

The technical implementation goes as follows. The sinusoidal rf-frequency is generated by a home-built DDS function generator²⁸, programmed by a micro-controller. The DDS output is connected to a rf-switch²⁹ and is fed through a bias-tee³⁰ to the copper U structure, acting as the antenna. As the resolution of the DDS source was not sufficient enough it was recently replaced by a Tabor arbitrary waveform generator³¹ allowing more versatile ramp schemes. Details of both setups can be found in [Rauer 12].

²⁸AD9852

²⁹Mini-Circuits ZX80-DR230-S+

³⁰Mini-Circuits ZFBT-6GW+

³¹Tabor WW1071

3. The Experiment - Some Practical Considerations

3.2.9. Imaging

Finally, we come to the most important step, acquiring the experimental data. In order to measure the atomic density distribution, an absorption picture [Ketterle 99] is taken, measuring the attenuation of a resonant laser beam passing through the atom cloud. This is usually done after several milliseconds of free time-of-flight, after a fast and sudden switch-off of the confining potential. A short (75 μs) resonant laser pulse passes through the atom cloud and is imaged onto a CCD camera, recording the spatial distribution of the intensity of the transmitted light. The interaction between atoms and photons is destructive in the sense that the atoms are “blown” away from the trapping region, leaving no atoms behind (see below). After 11 ms, a second reference picture of the Gaussian imaging beam, with no atoms present, is recorded.

The intensity reduction of the transmitted intensity $I(x, y)$ with respect to the reference intensity $I_0(x, y)$ depends on the column density $\rho(x, y) = \int \rho'(x, y, z) dz$. For small intensities $I \leq 0.1 \times I_{sat}$ compared to the saturation intensity I_{sat} , the intensity reduction can be approximated by the Beer-Lambert law as [Reinaudi 07]

$$I(x, y) = I_0(x, y) \cdot e^{-\sigma_0 \rho(x, y)}, \quad (3.5)$$

with the scattering cross-section $\sigma_0 = 2.906 \times 10^{-9} \text{ cm}^2$ for σ -polarized light [Steck 01]. The column density $\rho(x, y)$ is then given by

$$\rho(x, y) = -\frac{1}{\sigma_0} \ln \left(\frac{I(x, y)}{I_0(x, y)} \right), \quad (3.6)$$

which is a direct measure of the total number of atoms $N = \int \rho(x, y) dx dy$.

So far, so good. Now let's have a look at the CCD detector itself and how to properly apply eq. 3.6 to the actual counts in each pixel $c(i, j)$, with the integer indices i, j . The counts in each pixel are given by the sum of three contributions. First, the actual signal, where the detected photons are (according to the value of the quantum efficiency of the camera) converted into photo-electrons. Second, thermally induced dark currents that continuously build up charge. The number of these dark counts varies slightly in each pixel and depends on the temperature and the exposure time. To decrease the dark count level, the CCD chips are temperature stabilized and cooled to approximately -70°C . Additionally, small exposure times are used. The third contribution is independent of the exposure time and is called bias. It can be measured by setting the exposure time to zero and basically depends on the read-out speed and the used electronics (analog amplifiers, analog to digital conversion, etc.). Let $c_d(i, j)$ be the number of dark counts (including bias counts) of the pixel at position i, j . To properly calibrate the atom number measurement, the dark counts need to be measured by taking the average of several dark images (with closed aperture) for the same exposure times as the usual images. Then eq. 3.6 has to be rewritten as

$$\rho(x, y) = -\frac{1}{\sigma_0} \ln \left(\frac{c(i, j) - \langle c_d(i, j) \rangle}{c_0(i, j) - \langle c_d(i, j) \rangle} \right). \quad (3.7)$$

3. The Experiment - Some Practical Considerations

It is important to keep in mind that this calibration needs to be re-done every time that the exposure time or the temperature of the CCD chip is changed. Another technical noise source depends on the readout process, which has been discussed in detail in [Gring 12a].

Concerning correct atom number calibration, there is another difficulty that needs to be kept in mind. As we can see in eq. 3.7, the measured atom number depends on the scattering cross-section σ_0 , which is dependent on the magnetic field axis (if present) and polarisation of the imaging beam. The ideal imaging would take place at zero magnetic field. Here it gets a bit tricky, as the experimental realisation is never going to be ideal and small deviations from zero magnetic field are to be expected. For such small deviations from zero, a magnetization axis pointing in an arbitrary direction is introduced, which may severely change the value of the effective scattering-cross section σ'_0 , as the population of Zeeman levels gets redistributed [Erhard 04]. To circumvent this problem it is helpful to apply a small (≤ 1 G, $\omega_L \approx \Omega_{optical}$) homogeneous magnetic field, to properly define a polarisation axis with respect to the direction of the imaging beam [Gring 12a]. If the number of absorbed photons per atom is sufficiently high (≥ 200), the scattering-cross section σ_0 is effectively altered by a constant factor α and reads $\sigma'_0 = \alpha\sigma_0$ [Erhard 04]. For circular polarized light and a parallel magnetisation axis $\alpha = 1$, which is what we have for the longitudinal imaging (see 3.1.5). For linear polarized light and a perpendicular magnetization axis $\alpha = 0.54$ [Erhard 04], which applies for the transversal imaging beam.

For ^{87}Rb , the hyperfine transition $|5S_{1/2}, F = 2\rangle \rightarrow |5P_{3/2}, F' = 3\rangle$ is used for absorption imaging (Fig. 3.3). At each photon scattering event, the recoil energy $E_{rec} = \frac{\hbar^2 k^2}{2m} = \frac{k_B T_{rec}}{2}$ is transferred to the participating atom, accordingly adding the recoil temperature $T_{rec} = 362$ nK and the respective recoil velocity $v_{rec} = \frac{2\pi \hbar}{\lambda m} = 5.89$ mm/s. For a number of N scattering events per atom, the atom receives the velocity Nv_{rec} in the direction of the laser beam and additionally performs a random walk due to the spontaneous emissions with a final velocity of $\sqrt{N}v_{rec}$ pointing in a random direction and eventually blurring the image. During the exposure time t_{ex} , the number of scattering events (excluding Doppler effect) can be approximated by $N = \frac{\Gamma}{2} \frac{I_0}{I_{sat}} \cdot t_{ex}$, with the natural linewidth Γ and the saturation intensity I_{sat} . In the experiment, we typically use $I_0 = 0.1I_{sat}$ and an exposure time of $t_{ex} = 75$ μs , which gives a number of $N \approx 141$ photons scattered per atom. This results in a total energy transfer of 50 mK (much bigger than the trap depths of the chip trap of 300 μK) and the atoms travel a distance of ~ 8.3 mm in 11 ms before the reference image is taken, certainly leaving the depth of field of the imaging system.

The time-of-flight is actually limited to > 2 ms, since the fast switch-off of the magnetic fields induces eddy currents in the vacuum steel chamber, lasting for about 2 ms. During this time the measured atom number in time-of-flight is uncertain, due to the unknown Zeeman shift.

It is also possible to take in situ images, while the atoms are still trapped. There are two disadvantages, though. First, the magnetic field gradients lead to a spatially dependant Zeeman shift and thus to a spatially varying detuning of the imaging beam,

3. The Experiment - Some Practical Considerations

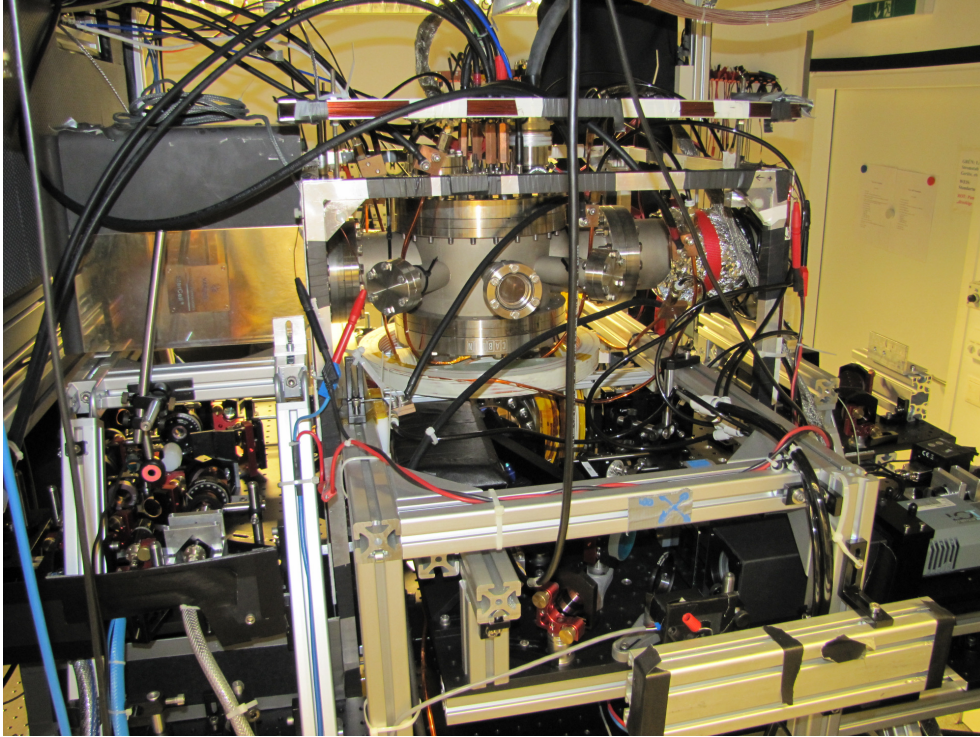


Figure 3.14.: Picture of the experimental apparatus (12.2012)

which needs to be taken into account. Second, the trapped atom cloud might be optically too dense, meaning that the imaging light gets fully absorbed locally, rendering the detection of the trapped density profile impossible. This can be avoided by using higher imaging intensities or by applying off-resonant imaging techniques.

To get the imaging system focused on the position of the atom cloud, a neat trick, as presented in [Marte 03], was used, where the imaging light is detuned from resonance and the dense BEC starts to act as a lens, effectively changing the recorded density profile. This idea works even better when using a fringe pattern [Gring 12a], where the recorded contrast is significantly altered when the system is out of focus.

Fig. 3.14 shows an image of the experimental apparatus, including the vacuum system and current feedthroughs (top), Bias and compensation coils (middle), transverse imaging system (lower right hand side) and MOT optics (lower left hand side) .

3.3. Fragmentation Problems

In reality, the current density in microscopic atom chip wires is not perfectly homogeneous and the current does not follow a straight path along the wire. These small deviations affect the local magnetic field and lead to corrugations of the magnetic potential. Especially for very elongated cold atomic clouds, the longitudinal density profile can be disturbed. Depending on the size of the corrugations and on the distance to the surface, these

3. The Experiment - Some Practical Considerations

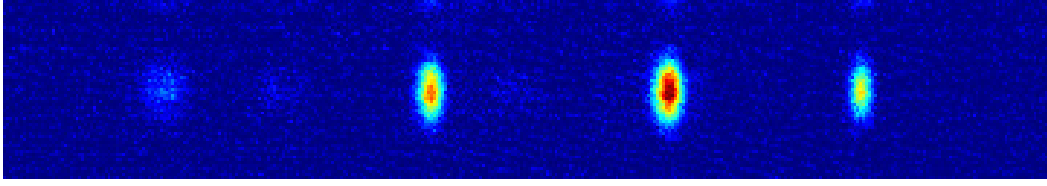


Figure 3.15.: Several condensates are generated simultaneously in fragmentation minima along the trapping wire (parallel to horizontal direction of figure).

corrugations are even able to split up the elongated clouds into several separated fragments, as in Fig. 3.15. Increasing the distance h from the wire helps, as wire roughnesses on length scales $s \ll h$ are averaged out [Fortágh 07].

There are two main reasons causing these fragmentation problems. First, inevitable imperfections in the fabrication process lead to roughness on the surface and on the edges of the microscopic wire structures, locally changing the current flow [Fortágh 02, David 08]. Second, the internal granular structure, bulk inhomogeneities and defects in the metal lead to scattering processes of the conducting electrons [Aigner 08].

Unfortunately, the atom chip installed in the KRb setup turned out to be of intermediate quality. It was the first new chip fabricated in Vienna at the ZMNS, applying the knowledge and techniques developed for the previous chips, which were produced at the Weizmann Institute. Fragmentation effects are reported to be worse, when compared to the old Weizmann chips.. Fig. 3.16 shows the averaged density profile of ultracold thermal atoms in short time-of-flight of 2 ms for the KRb chip. The effective trapping potential (blue) can be inferred by assuming Boltzmann statistics. Huge deviations from the fitted harmonic trapping potential (red line) can be seen below $h = 90 \mu\text{m}$. As seen in Fig. 3.15, it is even possible to create several condensates, each condensed in a different fragmentation minimum. Thus, it was concluded not to trap the atoms at the intended $h = 75 \mu\text{m}$ distance from the chip, but rather to work at $h \geq 100 \mu\text{m}$, paying with a decrease of transverse trap frequency.

To date, it is still unknown, why this new chip shows these strong fragmentation issues. Wire roughness will be open for a serious investigation once the end of the chip lifetime has been reached. As it is an extremely time consuming process³² to exchange an atom chip once fully tested and built into an ultracold experiment, it did not was not appropriate to address this issue immediately. We rather decided to move on and get the most out of the existing, BEC-producing machine. At the moment, other groups are setting up experiments specially designed for fast and efficient atom chip exchange rates [Koller 12], hopefully further improving atom chip fabrication techniques in the near future.

³²exchanging an atom chip may take several month up to half a year. A rough collection of what needs to be done: removal of optic boards, remove chip+mounting out of vacuum, fabricate new chip, build new mounting head, mount new chip, bond new chip, test new chip under UHV conditions, marriage of mounting and vacuum chamber, bake out of vacuum chamber, chip current death tests, get BEC again....

3. The Experiment - Some Practical Considerations

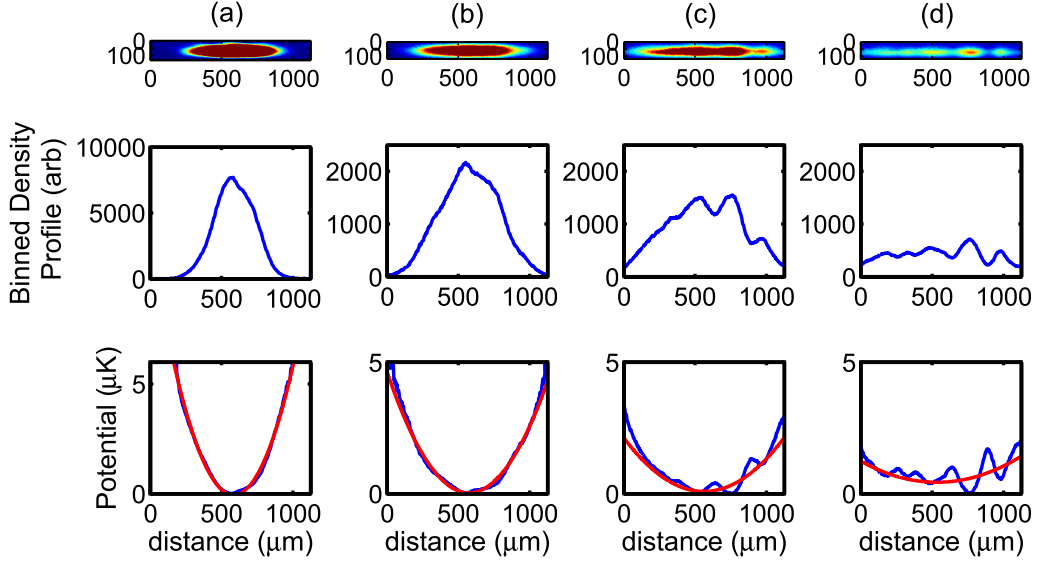


Figure 3.16.: Fragmentation effects versus distance to chip. Measurements of fragmentation effects along the longitudinal direction in the atom chip trap for different distances h to the chip surface. Fragmentation is increased at smaller distances h towards the chip surface. Thermal atoms at $T = 1.5 \mu\text{K}$ are imaged after 2 ms time-of-flight. (top) Averaged absorption picture of 50 realisations, where red denotes high atom density. (center) Binned density profile along the vertical direction. (bottom) Calculated trapping potential according to binned density profile in blue and harmonic fit in red. (a) $h = 120 \mu\text{m}$, $\omega_{long}^{fit} = 2\pi \times (12.82 \pm 0.03) \text{ Hz}$ (b) $h = 95 \mu\text{m}$, $\omega_{long}^{fit} = 2\pi \times (8.20 \pm 0.03) \text{ Hz}$ (c) $h = 51 \mu\text{m}$, $\omega_{long}^{fit} = 2\pi \times (5.58 \pm 0.09) \text{ Hz}$ (d) $h = 25 \mu\text{m}$, $\omega_{long}^{fit} = 2\pi \times (3.70 \pm 0.20) \text{ Hz}$.

Another aspect of fragmentation is the following. Turning this bug into a feature, cold atomic clouds have been used to map out the potential landscape along microscopic structures, sensing magnetic fields and gaining insight into the local current density and current flow [Wildermuth 05b, Wildermuth 06]. Sensing magnetic fields with cold and ultracold atoms provides high spatial resolution and good field sensitivity, bridging the gap between high-field-sensitive but badly resolving SQUIDs on the one hand and magnetic force microscopes with high spatial resolution but low-field-sensitivity on the other hand, leading to new insights in the electronic transport properties [Aigner 08].

4

Chapter 4.

Thermometry

“... began to suffer from the computer disease that anybody who works with computers now knows about. It’s a very serious disease and it interferes completely with the work. The trouble with computers is you ‘play’ with them.”

- Richard P. Feynman, Surely You’re Joking, Mr. Feynman!

Abstract

This chapter focuses on measurement techniques for determining the temperature of cold, ultracold and degenerate Bose gases. Starting with thermal gases obeying the Maxwell-Boltzmann momentum distributions, density profiles in expansion are used as a thermometer. Continuing with partially condensed clouds, where the thermal wings can be used to infer the temperature, we finally end up with almost pure quasi-condensates, where the temperature information is imprinted in the longitudinal phase and density fluctuations. While other research groups make use of density fluctuations, or fits to density profiles, we typically measure the temperature through phase correlations. For a single cloud, these phase correlations are obtained by measuring the two-point correlations in expansion and for two split clouds, the statistics of the interference contrasts provide the necessary information.

4.1. Thermal Bose Gas

4.1.1. Density Distributions In Situ

Starting with a hot Bose gas in thermal equilibrium a semi-classical approximation¹ can be used, where the thermal deBroglie wavelength λ_{dB} is assumed to be much smaller than the average distance on which a particle changes its momentum. In this approximation, one finds [Pethick 01]

$$n_{th}(\vec{r}; 0) = \frac{1}{\lambda_{dB}^3} g_{3/2} \left(e^{\frac{\mu - V(\vec{r})}{k_B T}} \right) \quad (4.1)$$

for the in situ density distribution $n_{th}(\vec{r}; t = 0)$ of an ideal Bose gas at zero time-of-flight ($t = 0$ ms), where a 3d harmonic trapping potential $V(r)$ is included. This is the 3d version of eq. 2.7, with the thermal deBroglie wavelength $\lambda_{dB} = \sqrt{\frac{2\pi\hbar^2}{mk_B T}}$ for temperature T and atomic mass m .

In the following, the temperature scale shall be defined with respect to a characteristic temperature T_c . In highly anisotropic traps, T_c is the crossover temperature of the quasi-condensate, as defined in eq. 2.15. In 3d, isotropic, harmonic trapping confinements, T_c is the critical temperature $T_c = \frac{\hbar\bar{\omega}}{k_B} \left(\frac{N}{\zeta(3)} \right)^{1/3}$ of the BEC phase transition [Pethick 01], with the mean trapping frequency $\bar{\omega} = (\omega_x \omega_y \omega_z)^{1/3}$ and the Riemann zeta function $\zeta(z) = \sum_{m=1}^{\infty} m^{-z} = g_z(1)$ which gives $\zeta(3) \approx 1.204$.

For $T \geq T_c$, $k_B T \gg \hbar\bar{\omega}$ and $\mu \lesssim \frac{1}{2}\hbar \sum_i \omega_i$, $\frac{\mu}{k_B T}$ can be neglected and eq. 4.1 is approximated by

$$n_{th}(\vec{r}; 0) = \frac{1}{\lambda_{dB}^3} g_{3/2} \left(e^{-\frac{m}{2k_B T} \sum_i \omega_i^2 r_i^2} \right) \quad (4.2)$$

However, 3d profiles are hard to measure in the experiment. By taking an absorption image, the distribution is integrated over one spatial direction as discussed in sec. 3.2.9. Thus, by integrating along the x-direction, the 2d column density profile $n_{th}(y, z, 0)$ is recorded on the CCD, which is given by² [Naraschewski 98]

$$n_{th}(y, z; 0) = \frac{2\pi}{\lambda_{dB}^2} g_2 \left(e^{-\frac{m}{2k_B T} (\omega_y^2 r_y^2 + \omega_z^2 r_z^2)} \right), \quad (4.3)$$

A more convenient expression, involving experimentally easily accessible parameters, can be derived by using the peak density $n(0, 0; 0)$ and the in situ rms width $\sigma_{0,i}$, which is defined by the temperature T and the respective trap frequencies ω_i as

$$\sigma_{0,i}^2 = \frac{k_B T}{m\omega_i^2}. \quad (4.4)$$

This results in the following fit function [Ketterle 99]

¹Including quantum statistics.

²Unlike exponential functions, $g_{3/2}$ is not invariant under integration.

4. Thermometry

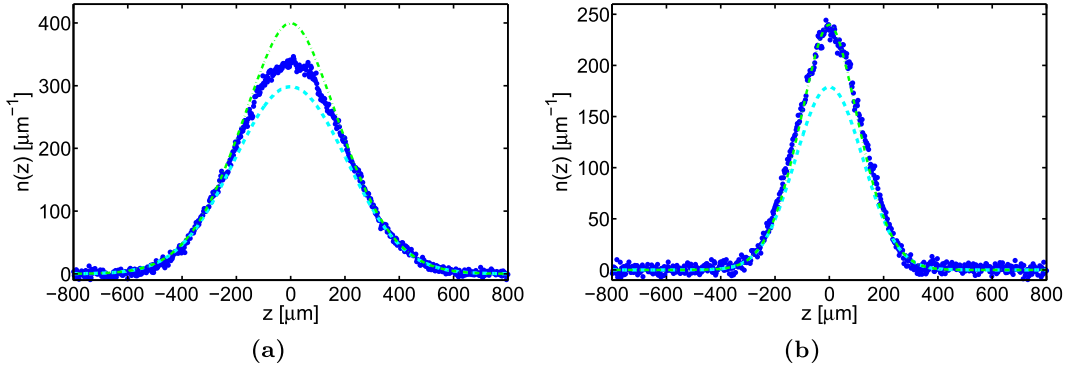


Figure 4.1.: Measured transversal thermal density profiles in time-of-flight (blue dots) in comparison to eq. 4.14 (cyan dashed line) and 4.13 (green dashed dotted line). For $T \approx 2 \mu\text{K} \gg T_c$ (a), the onset of bosonic enhancement is observed. For colder temperatures $T \approx 700 \text{ nK} \gtrsim T_c$ (b), the Gaussian profile clearly underestimates the peak density, which, in contrast, is well captured by bosonic enhancement.

$$n_{th}(y, z; 0) = \frac{n(0, 0; 0)}{g_2(1)} g_2 \left(e^{-\frac{y^2}{2\sigma_{0,y}^2} - \frac{z^2}{2\sigma_{0,z}^2}} \right) \quad (4.5)$$

for the 2d profile, where the $1/g_2(1)$ factor ensures proper normalization.

Furthermore, binning the image along the y -direction results in the 1d density profile $n_{th}(z, 0)$

$$n_{th}(z; 0) = \frac{n(0; 0)}{g_{5/2}(1)} g_{5/2} \left(e^{-\frac{z^2}{2\sigma_{0,z}^2}} \right). \quad (4.6)$$

For $T \gg T_c$, the gas can be assumed to obey classical statistics (as in sec. 2.1) and eq. 4.2 approximates to a Gaussian density distribution of

$$n_{th}(\vec{r}; 0) = \frac{N}{(2\pi)^{3/2} \sigma_{0,x} \sigma_{0,y} \sigma_{0,z}} \cdot e^{-\frac{x^2}{2\sigma_{0,x}^2}} e^{-\frac{y^2}{2\sigma_{0,y}^2}} e^{-\frac{z^2}{2\sigma_{0,z}^2}}, \quad (4.7)$$

where $N = \int n_{th}(r, 0) dr$ is the total number of atoms. In this regime, the width of a Gaussian fit function can be used to probe the temperature of a thermal Bose gas, with the respective 1d profile given by

$$n_{th}(z; 0) = \frac{N}{(2\pi)^{1/2} \sigma_{0,z}} \cdot e^{-\frac{z^2}{2\sigma_{0,z}^2}}. \quad (4.8)$$

4.1.2. Density Distributions in Time-Of-Flight

Let's assume the trap is switched-off at $t = 0$, allowing the ideal Bose gas to freely expand according to its initial momentum distribution $f(\vec{p}, \vec{r})$. Let's further assume that the gas is dilute enough that collisions during the expansion can be neglected. After a certain time-of-flight t , the density distribution $n(\vec{r}; t)$ is recorded via absorption imaging. $n(\vec{r}; t)$ is calculated by integrating over the momentum distribution at time t given in the classical limit as

$$f(\vec{p}, \vec{r}, t) = \exp\left(\frac{\mu}{k_B T}\right) \exp\left(-\frac{p^2 + 2mV(r - pt/m)}{2mk_B T}\right). \quad (4.9)$$

For $T \geq T_c$ one finds [Pethick 01]

$$n(\vec{r}; t) = e^{\frac{\mu}{k_B T}} \frac{1}{\lambda_{dB}^3} \prod_i \left[\left(1 + \omega_i^2 t^2\right)^{-1} g_{3/2} \left\{ \exp\left(-\sum_i \frac{x_i^2}{2\sigma_{0,x}^2 (1 + \omega_i^2 t^2)}\right) \right\} \right] \quad (4.10)$$

and for $T \gg T_c$

$$n(\vec{r}; t) = e^{\frac{\mu}{k_B T}} \frac{1}{\lambda_{dB}^3} \prod_i \left[\left(1 + \omega_i^2 t^2\right)^{-1/2} \exp\left(-\frac{x_i^2}{2\sigma_{0,x}^2 (1 + \omega_i^2 t^2)}\right) \right], \quad (4.11)$$

where the Gaussian widths $\sigma_i^2(t)$ scale as

$$\sigma_i^2(t) = \sigma_{0,i}^2 (1 + \omega_i^2 t^2), \quad (4.12)$$

with the in situ width $\sigma_{0,i}^2$ is given by eq 4.4. The 2d and 1d density profiles can be calculated similarly as for the in situ case and the 1d profiles are given by

$$n_{th}(z; t) = \frac{(2\pi)^2}{\lambda_{dB}} g_{5/2} \left(e^{-\frac{z^2}{2\sigma_z^2(t)}} \right) \quad (4.13)$$

and

$$n_{th}(z; t) = \frac{N}{(2\pi)^{1/2} \sigma_z(t)} \cdot e^{-\frac{z^2}{2\sigma_z^2(t)}}. \quad (4.14)$$

Fig. 4.1 shows thermal density profiles in time-of-flight in the two regimes $T \gg T_c$ and $T \gtrsim T_c$.

4.2. Partially Condensed Bose Gas: Thermal Wings

Studying the isotropic (for $t \gg \omega_i^{-1}$) expansion of a thermal cloud, as given by eq. 4.12, can improve the accuracy of the temperature measurement with respect to in situ, especially in the presence of a condensed fraction. The condensate fraction expands highly anisotropically (see Fig. 3.8) due to the conversion of the interaction energy into kinetic

4. Thermometry

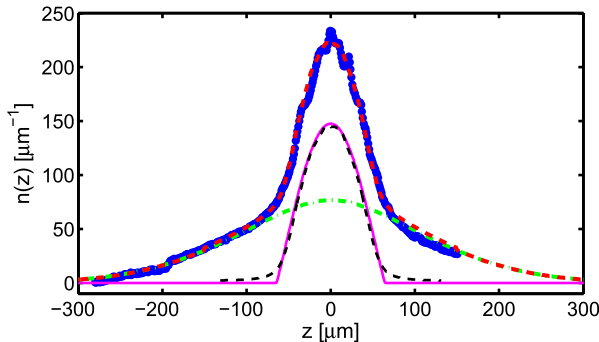


Figure 4.2.: Partially condensed (40 %) longitudinal density profile in time-of-flight (12 ms) at a temperature of $T \approx 450$ nK, and a total atom number of $N \approx 30000$. (blue dots) experimental data, (solid, magenta curve) quasi-condensate profile in situ, (dashed black curve) simulated quasi-condensate profile in time-of-flight, including finite imaging resolution, (green, dashed-dotted curve) thermal Bose gas, (red dashed curve) sum of thermal Bose gas and simulated quasi-condensate profile in time-of-flight.

energy. This strong difference, especially in the longitudinal expansion, can be used to properly distinguish between condensed and thermal part, when comparing profiles taken at different time-of-flights. In a highly anisotropic, harmonic trap, with the initial aspect ratio $\frac{R_{tr}(0)}{R_{long}(0)} = a = \frac{\omega_{long}}{\omega_{tr}} \ll 1$ and the in situ Thomas-Fermi radii $R_i(0) = \sqrt{\frac{2\mu}{m\omega_i^2}}$ the expansion of the condensate fraction follows the scaling laws [Ketterle 99]

$$R_{tr}(t) = R_{tr}(0) \sqrt{1 + \omega_r^2 t^2} \quad (4.15)$$

$$R_{long}(t) = R_{long}(0) \left[1 + a^2 \omega_{tr} t \arctan(\omega_{tr} t) - a^2 \ln \left(\sqrt{1 + \omega_{tr}^2 t^2} \right) \right]. \quad (4.16)$$

In the long time limit, the aspect ratio is given by $\lim_{t \rightarrow \infty} \frac{R_{tr}(t)}{R_{long}(t)} = \frac{2}{\pi a}$.

Fig. 4.2 shows a the longitudinal density profile of a partially condensed Bose gas with a large thermal background, which is used to estimate the temperature. The simulated quasi-condensate profile (black, dashed line) includes the effects of the in situ phase fluctuations (see sec. 4.3) and the finite imaging resolution. Both effects lead to a smooth out of the sharp edges of the quasi-condensate profile.

For $T \approx T_c$ and highly anisotropic, harmonic traps, the equation of state of an ideal Bose gas can be used to derive the linear density profile along the axial direction of the non-condensed fraction. By using a local density approximation and defining the local chemical potential in the longitudinal potential $V(z) = \frac{1}{2} m \omega_{long}^2 z^2$ as

$$\mu(z) = \mu_0 - V(z), \quad (4.17)$$

and averaging over the contributions of the transverse modes, the in situ linear density profile $n_{th}(z; 0)$ can be calculated as [Armijo 11b]

4. Thermometry

$$n_{th}(z; 0) = \frac{1}{\lambda_{dB}} \sum_{m=1}^{\infty} \left[\frac{1}{\sqrt{m}} \cdot \frac{\exp\left(\frac{m\mu(z)}{k_B T}\right)}{\left(1 - \exp\left(-\frac{m\hbar\omega_{tr}}{k_B T}\right)\right)^2} \right] \quad (4.18)$$

This can be used to fit the in situ thermal wings of a partially condensed cloud and estimate the temperature of the thermal fraction.

4.3. Thermometry of pure Quasi-Condensates via Phase Fluctuations

Measuring the temperature of a quasi-condensate via thermal wings becomes increasingly difficult the smaller the thermal fraction gets. Naturally, for a pure quasi-condensate one has to find other ways of thermometry. In this context, one can make use of the thermally populated phase fluctuations [Petrov 01].

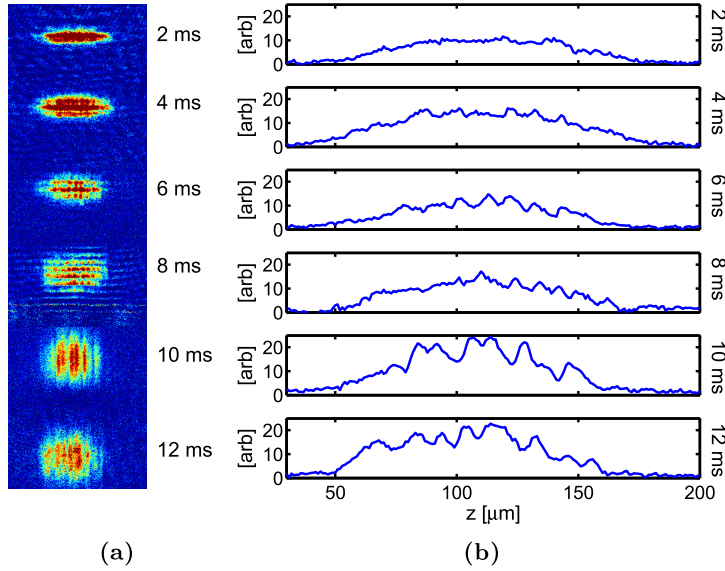


Figure 4.3.: Emergence of density ripples (vertical fringes) in expansion. The horizontal fringes up to 8 ms are from the standing wave patterns of the imaging light below the atom chip. A knife-edge is used to block parts of the imaging beam and thereby to reduce the standing wave pattern for expansion times greater than 8 ms. A fringe-removal image post-processing, as presented in [Ockeloen 10], is to be implemented for early expansion times.

As discussed in chapter 2.2.1, confined quasi-condensates lack a true-long range order and show a fluctuating phase along the weakly confining axis defined by the thermal correlation length $\lambda_T = \frac{2\hbar^2\rho}{mk_B T}$. However, in situ, density fluctuations are largely suppressed by the repulsive interactions, as they are energetically not favourable (see eq. 2.34)

4. Thermometry

[Petrov 00, Dettmer 01, Esteve 06]. As we have seen in chap. 2, these phase fluctuations can be understood as thermally populated axial phonon-like excitations. Upon release from the trap, the interaction energy rapidly decreases, the gas freely expands and the local phase fluctuations are converted into a local velocity field [Kreutzmann 03] as given by the superfluid velocity [Pitaevskii 03]

$$v(z) = \frac{\hbar}{m} \nabla \phi(z). \quad (4.19)$$

The velocity field leads to interference between different phase domains of the quasi-condensate. Due to the randomness of the phase fluctuations the resulting interference pattern differs from shot to shot and leads to fluctuations in the longitudinal density profile in time-of-flight. Therefore, upon expansion, the initial phase fluctuations turn into observable density-fluctuations [Dettmer 01]. These are the so-called density-ripples, which are depicted in Fig. 4.3. As can be seen, the amplitude of the density-ripples depends strongly on the expansion time. Furthermore, as the phase fluctuations are thermally populated, the observed amplitudes strongly depend on temperature [Hellweg 01]. It has been shown, that the shape of density-density correlations is non-monotonic and strongly depends on the thermal correlation length λ_T [Imambekov 09]. Thus the two-point density correlation function can be used as a thermometry tool.

Motivated by the homogeneous theoretical description of [Imambekov 09], we simulate a two-point density correlation function in time-of-flight for a finite-size system. By comparing the simulated correlation functions to the averaged, experimental one, the temperature of the quasi-condensate can be determined [Manz 10]. This method will be employed throughout this work to determine temperatures in the quasi-condensate regime. An in depth description and application of this method can be found in [Manz 11], a brief summary will be presented in the following.

4.3.1. Details of this thermometry method

In contrast to [Manz 10], we do not use the peak value of the correlation function $g^{(2)}(x=0, t)$ at $x=0$, which contains the white noise contributions of the imaging noise, but fit the whole shape of the $g^{(2)}$ function. In this context, t denotes the time-of-flight. Thus, we become independent on white imaging noise and remain only influenced by residual fringe patterns in the absorption image, which are caused by diffraction at dust particles³ and interference effects⁴. It has been shown in [Ockeloen 10], that these additional fringe patterns can be computationally removed as well, a method which might be applied for future temperature analyses in our experiment. For the thermometry results used in this thesis, additional fringe patterns due to vibrations of the setup have not been post processed as their influence at expansion times larger than 8 ms (Fig. 4.3a)

³Small mechanical vibrations lead to a shift of the diffraction patterns at dust particles between the absorption and the reference picture

⁴Reflecting the imaging beam on the atom chip results in standing wave patterns (Fig. 4.3a), the atom chip structures lead to additional patterns in the image, even when out of focus (coherent illumination, Talbot effect). See [Gring 12a].

4. Thermometry

seems marginal to the atomic signal.

Implementation

For a homogeneous system, the resulting density ripples spectrum in time-of-flight can be calculated analytically as reported in [Imambekov 09]. However, there is no analytic model available so far that captures finite-size effects. Therefore, the expected $g^{(2)}$ function is numerically simulated in the following way. The density profile $n(z)$ of the quasi-condensate is calculated via eq. 2.20 and used to define the wave function $\Psi^\dagger(z) = \sqrt{n(z)}e^{i\phi(z)}$. The in situ phase distribution $\phi(z)$ is simulated using a stochastic Ornstein-Uhlenbeck process [Gardiner 85, Gillespie 96] according to [Stimming 10]. This process is, for example, used to simulate random Brownian motion. Under the right constraints [Manz 11], a phase distribution fulfilling first order coherence, as given by eq. 2.42, with a local thermal phase correlation length $\lambda_T(z) = \lambda_T(n(z))$ (eq. 2.43), can be generated. Collisions during the expansion can be neglected, if the transverse confinement is tight enough ($\mu \sim \hbar\omega_{tr}$), such that the transverse expansion happens considerably fast (ω_{tr}^{-1}) [Imambekov 09]. To model the ballistic expansion, the wave function is propagated in time with $\exp\left(-\frac{i}{\hbar}\frac{p^2}{2m}t\right)$. The imaging resolution is accounted for by approximating the airy pattern with a Gaussian point-spread-function [Gring 12a], which is convolved with $|\Psi(z, t)|^2$. The convolution is calculated in k space by multiplying the respective Fourier transforms and then taking the inverse Fourier transform to go back to position space. This process is numerically faster than calculating the convolution in position space. Finally, the expectation values are obtained by averaging over many realisations.

In summary, the simulation needs the following input parameters: the trap frequencies, the time-of-flight t , the density profile $n(z)$ and the point-spread-function (PSF) of the imaging system. These input parameters are inferred via independent measurements. Despite offsets, only the temperature is used as a free fit parameter. The theoretical description is valid as long as we are in the quasi-condensate regime as defined in sec. 2.2.1.

The experimental $g^{(2)}$ is obtained by averaging over at least 50 absorption pictures.

Results

Fig. 4.4 shows a hot (red) and a cold (blue) $g^{(2)}$ profile, where the dots represent the experimental data and the solid lines show the fitted theory model. Both profiles have been taken at the same expansion time, which mainly determines the position of the minimum. As can be seen, the difference between the maximum at zero distance and the minimum is significantly bigger for larger temperatures. That the $g^{(2)}$ function drops below one can be understood in terms of conserved finite atom number. The probability of finding two atoms simultaneously at shorter distances is increased, thereby decreasing the probability to find pairs at larger distances [Manz 10].

Fig. 4.5 shows the scaling of the $g^{(2)}$ function for different time-of-flights and different PSF widths.

4. Thermometry

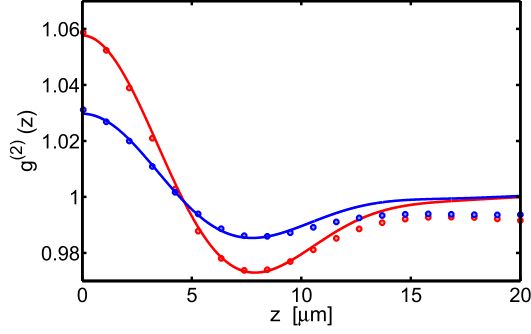


Figure 4.4.: Averaged typical $g^{(2)}$ correlation functions of density fluctuations in 12 ms time of flight pictures, with the temperature as a free fit parameter. (red) $T = 78 \pm 7$ nK, (blue) $T = 29 \pm 2$ nK, (filled dots) experimental data, (solid lines) theory fits (see text).

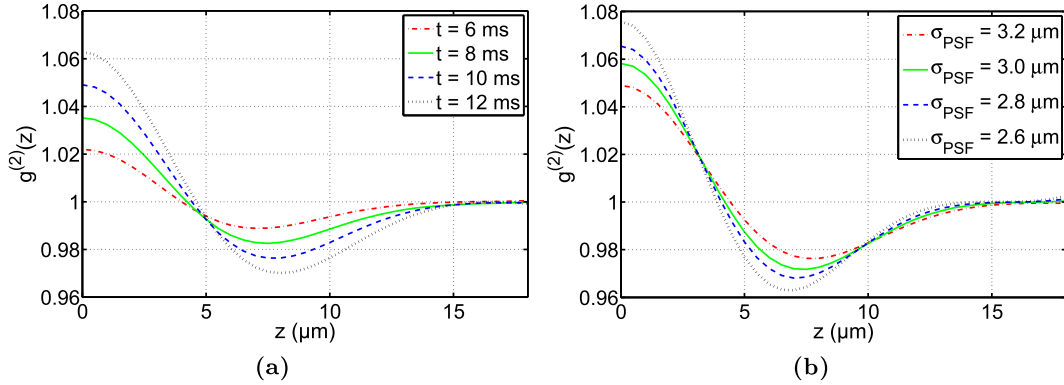


Figure 4.5.: (a) $g^{(2)}(z, t)$ for different time-of-flights. (b) $g^{(2)}(z, t)$ for different PSF widths.

Uncertainty of the Method

The relative fit error of this method is obtained by applying a bootstrapping algorithm [Efron 79, Hughes 10], where typically 150 sets of randomly selected pictures are generated, by random drawing with replacement. Each set is analysed and corresponds to one artificial temperature measurement. The final temperature is then given by the mean and the relative uncertainty by one standard deviation of these bootstrapped temperatures. In this way, we find typical rms errors on the order of 10 – 20 %, which corresponds to the relative error in temperature of this method. The systematic errors are expected to be dominated by the uncertainty in the rms PSF width. A 5 % standard deviation in the PSF rms width already corresponds to 20 – 30 % systematic error. The absolute errors are approximately twice as large as the relative errors. Throughout this thesis, the relative errors are given and not the absolute ones.

The ideal PSF of the transversal high resolution imaging (compare table 3.1) has

4. Thermometry

been determined thoroughly in a test setup of the imaging system [Gring 12a], by three independent methods⁵, giving similar results of approximately $2.0\ \mu\text{m}$ in the longitudinal direction and $2.5\ \mu\text{m}$ in the transverse (gravity-) direction. The imaging system was designed for in situ imaging and short time-of-flights. The density ripples are recorded in 12 ms TOF, where the cloud size is bigger than the depth of field of the imaging system, thus leading to a decrease in resolution. The final resolution is thus expected to be larger and can be measured via the power spectrum of the density ripples as explained in [Gring 12a]. At TOF = 12 ms, the results suggest an effective PSF on the order of $3.00 \pm 0.15\ \mu\text{m}$.

Another way of measuring the effective PSF would be to create a vertical double well in order to get an interference pattern in the transversal imaging direction. For hot quasi-condensates in equilibrium (compare sec. 4.4.1), the shape of the phase correlation function is basically determined by the imaging resolution [Betz 11] if $\lambda_T \ll \sigma_{PSF}$ and thus can be used to accurately determine the PSF. However, it should be noted that creating a balanced vertical double well is experimentally subtle (see sec. 5.2.2) due to the gravity sag and the $1/r$ dependence of the rf-field and thus will be the prospect of future efforts.

Applicable Temperature Range

The density ripples method is applicable in the thermal quasi-condensate regime (sec. 2.1) and thus is limited to low temperatures by the crossover to the true condensate regime at T_ϕ as defined by eq. 2.13. The high temperature limit is given by the crossover to the 3D regime above $k_B T > \hbar\omega_{tr}$, where transversally excited states become significantly populated. In summary, these arguments lead to an applicable temperature range of $T_\phi < T < \frac{\hbar\omega_{tr}}{k_B}$. For our typical parameters this evaluates to $10\ \text{nK} \lesssim T \lesssim 120\ \text{nK}$

Other Thermometry Methods for Quasi-Condensates

Following eq. 2.34, the in situ density fluctuations scale with temperature and thus can also be used for thermometry purposes. Probing in situ density fluctuations imposes stringent requirements on the imaging quality and stability. The imaging resolution needs to be close to the healing length (typically $\leq 1\ \mu\text{m}$), which is the characteristic correlation length of the density fluctuations [Deuar 09]. A detailed discussion is left to literature [Esteve 06, Armijo 11b, Armijo 11a].

Last, but not least, a modified YangYang model [van Amerongen 08, Kheruntsyan 03] can be used to calculate the temperature dependence in situ 1d density profile, a method which even works well in the 1d/3d crossover [Armijo 11a].

⁵1st method: imaging a pinhole in the field of view. 2nd method: moving a knife edge through the focal spot of the objective. 3rd method: resolving structures on a MetroChip calibration target, manufactured by MetroBoost (www.metroboost.com)

Density Ripple Thermometry of Two Split Condensates in Equilibrium

When creating two independent quasi-condensates in equilibrium, as explained in sec. 4.4.1, the density ripples method can be applied as well. In the current setup, we are unable to measure the longitudinal density profile of one quasi-condensate separately and thus can only measure the incoherent sum of the two density profiles. Nevertheless the resulting $g^{(2)}$ can be used for thermometry. The resulting temperatures agree, within the error bounds, with the ones obtained by fitting the squared contrast FDFs (see chapter 6).

4.4. Thermometry via Interference of two Independent Quasi-Condensates in Thermal Equilibrium

The interference of two independent quasi-condensates gives a measure of the strength of relative phase fluctuations. As we will see in this section, the distribution of the squared contrast can be used for thermometry purposes. First of all, the equilibrium properties of matter-wave interference patterns need to be discussed and the close relationship between phase correlations and interference contrast need to be derived.

4.4.1. Creating the Equilibrium System

In order to understand the non-equilibrium dynamics that will be the topic of chapter 5 and to find out if the non-equilibrium state indeed relaxes to a thermal equilibrium state, it is necessary to directly compare the results to such an equilibrium state, both theory wise and experimental wise. In the experiment an equilibrium state can be generated by the following procedure.

1. Generate an ultracold thermal cloud, close to the critical temperature in the nearly ideal Bose gas regime. Then stop the evaporative cooling process.
2. Split the thermal sample by applying the same double-well potential as used for the non-equilibrium state (see sec. 5.2).
3. Proceed with evaporative cooling into the quasi-condensate regime [Gring 12a].

In this way, two completely independent quasi-condensates are formed, where both relative and common degrees of freedom are populated by thermal and quantum phase fluctuations and thus have the same temperature.

4.4.2. Phase Correlation Properties

Following eq. 2.35 and the obtained results thereafter and further assuming that the two wells are independent and uncorrelated, the phase correlation function $PCF(z, z')$ of the resulting interference pattern for the phase $\phi_1(z)$ in one well and $\phi_2(z)$ in the other well, is then given by [Gring 12a]

4. Thermometry

$$\begin{aligned}
PCF(z, z') &\approx \left\langle e^{i[\phi_1(z) - \phi_1(z')]} e^{i[\phi_2(z') - \phi_2(z)]} \right\rangle \\
&\approx \left\langle e^{i[\phi_1(z) - \phi_1(z')]} \right\rangle \left\langle e^{i[\phi_2(z') - \phi_2(z)]} \right\rangle \\
&\approx e^{-\frac{|z-z'|}{\lambda_T}} e^{-\frac{|z-z'|}{\lambda_T}} = e^{-\frac{2|z-z'|}{\lambda_T}} \\
&\approx e^{-\frac{|z-z'|}{\lambda_\phi}}
\end{aligned} \tag{4.20}$$

where the relative phase correlation length of an interference pattern $\lambda_\phi = \frac{\lambda_T}{2}$ is exactly one half of the phase correlation length λ_T of a single condensate as given by eq. 2.43, which finally results in the important expression [Whitlock 03, Betz 11]

$$\lambda_\phi = \frac{\hbar^2 n}{mk_B T}. \tag{4.21}$$

It is important to point out, that quantum phase fluctuations were not included in this derivation as the quasi-condensates studied in this work merely reach close to the quantum quasi-condensate regime as discussed in sec. 2.2.1. A complete numerical treatment, including both thermal and quantum phase fluctuations in matter-wave interference, can be found in [Stimming 10].

4.4.3. Matter-wave Interference of two independent Quasi-Condensates

A short reminder is presented about interference pattern in thermal equilibrium. A brief derivation of important properties, namely the contrast and the phase correlation function and their relationship will be presented.

Similar to sec. 2.2.1, we assume a highly anisotropic harmonic trap with the transversal trap frequencies $\omega_x = \omega_y = \omega_{tr}$ and longitudinal trap frequency $\omega_z = \omega_{long}$. The interference pattern is recorded after a ballistic expansion of time t . The total wavefunction $\hat{\Psi}_i(r, t)$ in each well [Reichel 11]

$$\hat{\Psi}_i(r, t) = \phi(x, y, t) \hat{\psi}_i(z, t) \tag{4.22}$$

factorizes in a longitudinal part given in second quantized form as

$$\hat{\psi}_i(z, t) = \sqrt{\hat{n}_i(z, t)} e^{i\hat{\phi}_i(z, t)} \tag{4.23}$$

and a transverse part given by the harmonic oscillator ground-state [Schumm 05a]

$$\phi(x, y, 0) \propto \exp\left(-\frac{\left(x \pm \frac{d}{2}\right)^2 + y^2}{2\sigma_{tr}^2}\right) \tag{4.24}$$

with the ground state size $\sigma_{tr} = \sqrt{\frac{\hbar}{m\omega_{tr}}}$. In expansion, the width of the transverse density profile scales as given by eq. 4.12. The total wave function is given by the sum of the

4. Thermometry

two condensate wave functions as

$$\hat{\psi}(r, t) = \hat{\psi}_1(r, t) + \hat{\psi}_2(r, t) \quad (4.25)$$

and the density distribution $n(r, t)$ can be calculated as

$$n(r, t) = \left| \hat{\psi}(r, t) \right|^2 = \left| \hat{\psi}_1(r, t) \right|^2 + \left| \hat{\psi}_2(r, t) \right|^2 + 2\text{Re} \left(\hat{\psi}_1(r, t) \hat{\psi}_2^\dagger(r, t) \right). \quad (4.26)$$

The third term represents the interference between the two condensates, separated by a distance $|\vec{d}|$ in the transverse plane, which evaluates to [Pethick 01]

$$2\text{Re} \left(\hat{\psi}_1(r, t) \hat{\psi}_2^\dagger(r, t) \right) = 2e^{-\frac{x^2+y^2}{2\sigma_t^2}} \hat{\psi}_1(z, t) \hat{\psi}_2^\dagger(z, t) \cos \left(\frac{\hbar}{m} \frac{\vec{r} \cdot \vec{d}}{\sigma_{tr}^2 \sigma_t^2} t \right). \quad (4.27)$$

For long expansion times $t \gg \omega_{tr}^{-1}$, $\sigma_t \approx \left(\frac{\hbar t}{m\sigma_{tr}} \right)$ and choosing $\vec{d} = \begin{pmatrix} d \\ 0 \\ 0 \end{pmatrix}$ for the splitting vector, one finds

$$2\text{Re} \left(\hat{\psi}_1(r, t) \hat{\psi}_2^\dagger(r, t) \right) = 2e^{-\frac{x^2+y^2}{\sigma_x^2 \sigma_y^2}} \sqrt{\hat{n}_1(z, t)} \cos \left(\frac{md}{\hbar t} x + \hat{\phi}_1(z, t) - \hat{\phi}_2(z, t) \right) \sqrt{\hat{n}_2(z, t)}, \quad (4.28)$$

which leads to oscillations in the density profile at a wavevector $\frac{md}{\hbar t}$. The distance between adjacent maxima is given by the fringe spacing $\lambda = 2\pi \frac{\hbar t}{md} = \frac{\hbar t}{md}$. The amplitude of these oscillations is given by the contrast \hat{C} , being the prefactor of the cosine term in eq. 4.27 normalized over the density profile. When integrating longitudinally over a length L , the contrast is given by [Gring 12a]

$$\begin{aligned} \hat{C} e^{i\Delta\phi} &= \frac{2}{\int_L dz \left[\left| \hat{\psi}_1(z, t) \right|^2 + \left| \hat{\psi}_2(z, t) \right|^2 \right]} \int dz \hat{\psi}_1^\dagger(z, t) \hat{\psi}_2(z, t) \quad (4.29) \\ &= \frac{2}{\int_L dz [\hat{n}_1(z, t) + \hat{n}_2(z, t)]} \int dz \sqrt{\hat{n}_1(z, t)} e^{-i(\hat{\phi}_1(z, t) - \hat{\phi}_2(z, t))} \sqrt{\hat{n}_2(z, t)} \quad (4.30) \end{aligned}$$

In the following, we assume that density fluctuations are strongly suppressed ($\hat{n}_i = n_i$), which is the case in the quasi-condensate regime (see sec. 2.3), that the densities are equal in each well $n_1 \approx n_2 \approx n$ and that a homogeneous density n can be used. Under these conditions, the denominator can be approximated by $\int_L dz [\hat{n}_1(z, t) + \hat{n}_2(z, t)] = 2Ln$ and eq. 4.30 simplifies to

$$\hat{C} e^{i\Delta\phi} = \frac{1}{L} \int_L dz e^{-i(\hat{\phi}_1(z, t) - \hat{\phi}_2(z, t))}. \quad (4.31)$$

4. Thermometry

The mean squared contrast $\langle |\hat{C}|^2 \rangle$ can be related to the phase correlation function $PCF(z, z')$ of eq. 4.20 via the considerations

$$\langle |\hat{C}|^2 \rangle = \hat{C}^\dagger \hat{C} = \frac{1}{n^2 L^2} \int_L \int_L dz dz' \langle \psi_1^\dagger(z) \psi_2(z) \psi_2^\dagger(z') \psi_1(z') \rangle \quad (4.32)$$

$$= \frac{1}{L^2} \int_L \int_L dz dz' \langle e^{-i[\hat{\phi}_1(z) - \hat{\phi}_2(z)]} e^{-i[\hat{\phi}_1(z') - \hat{\phi}_2(z')]} \rangle \quad (4.33)$$

$$= \frac{1}{L^2} \int_L \int_L dz dz' PCF(z, z'). \quad (4.34)$$

which underlines the close link between relative phase correlations and contrast. The functional form of contrast versus L will be studied in the next section.

4.4.4. Contrast versus Integration Lengths

Using eq. 4.20 for the correlation function and integrating eq. 4.34 leads to the length scale dependence of the mean squared contrast $\langle C^2(L) \rangle$.

$$\begin{aligned} \langle C^2(L) \rangle &\equiv \frac{1}{L^2} \int_L \int_L dz dz' e^{-\frac{|z-z'|}{\lambda_\phi}} \\ &\propto 2 \left[\frac{\lambda_\phi}{L} - \left(\frac{\lambda_\phi}{L} \right)^2 \left(1 - \exp\left(-\frac{L}{\lambda_\phi}\right) \right) \right] \end{aligned} \quad (4.35)$$

For $L \gg \lambda_\phi = \frac{\lambda_T}{2}$, one finds

$$\langle C^2(L) \rangle \approx \frac{\lambda_\phi}{L} = \frac{1}{N_\phi}, \quad (4.36)$$

where N_ϕ defines the number of relative phase domains within length L . This observation coincides with a random walk argument, that by integrating over N_ϕ uncorrelated phase domains, the maximally observable contrast $C(L \rightarrow 0) = 1$ will be diminished by approximately $1/\sqrt{N_\phi}$. In other words, strong decay in the PCF over length L leads to a scrambling of the contrast $C(L)$, whereas high phase coherence, meaning an almost constant phase correlation function on length L , result in high values for the contrast $C(L)$.

Eq. 4.35 shows, that by measuring the contrast on different length scales, the phase correlation length λ_ϕ becomes accessible. Determining the correlation length in this scheme has one important advantage in comparison to other methods⁶. Eq. 4.35 does not depend on density, which makes the determination of λ_ϕ only dependant on the imaging resolution and the contrast fit uncertainties. This fact will be of further use in sec. 5.9, where, based on eq. 4.35, a fit formula is derived, which includes the finite resolution of

⁶Once the temperature and density are known, λ_ϕ can be derived using eq. 4.21.

4. Thermometry

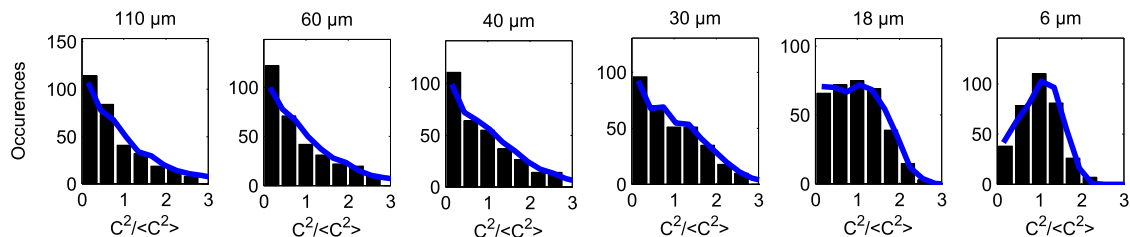


Figure 4.6.: Equilibrium squared contrast distributions for different integration lengths (see sec. 5.4). The equilibrium OU theory (blue solid lines) is fitted to the experimental distributions (black bars) resulting in a temperature of $T_{OU} = 57 \pm \frac{13}{6}$ nK, which is in good agreement with the measured density ripples temperature of $T_{DR} = 48 \pm 5$ nK.

the imaging system.

4.4.5. Measuring the Equilibrium Temperature via Contrast Statistics

As shown in [Hofferberth 08], the shape of the squared contrast distributions $P(C^2)$ are highly dependant on temperature and integration length scale. This fact can be used to determine the temperature of the equilibrium system. The equilibrium distributions can be either calculated in the TLL framework or by using the stochastic Ornstein-Uhlenbeck (OU) process. The OU process has already been introduced in sec. 4.3 to calculate equilibrium density-density g_2 functions of inhomogeneous, trapped quasi-condensates. In a similar fashion, the squared contrast statistics can be calculated starting from the thermal phase profiles generated by the OU process. The main advantage of the OU description in comparison to the equilibrium TLL model is that the inhomogeneous density distribution in the trap is taken into account, which is beyond the homogeneous TLL model. A further advantage is the comparatively faster computation speed.

Fig. 4.6 shows measured equilibrium distributions (black bars) and the resulting OU fits (blue solid lines) in comparison. The resulting temperatures agree within the error bounds. A detailed discussion on squared contrast distributions and the fitting procedure is presented in sec. 5.7.

5 Chapter 5.

Prethermalization

“I suppose there’ll be a war now, hmm? All that running around and shooting at one another. You would have thought sooner or later it’d go out of fashion.”

- Londo Mollari

Abstract

This chapter focuses on the prethermalization phenomenon, its prediction, its properties and discusses the first direct experimental evidence. As a commonly agreed definition of prethermalization has not yet emerged in literature, the discussion starts by reviewing the concept of prethermalization given by Berges et al.

The starting point of the experimental study is the creation of a highly non-equilibrium and well isolated quantum-many body system. The resulting dynamics are studied via matter-wave interferometry, where the contrast is the primary observable of interest. The contrast statistics are probed via full quantum probability distributions also known as full distribution functions (FDFs). These FDFs allow the detailed characterisation of the non-equilibrium dynamics leading to a prethermalized state. Furthermore, the FDFs reveal the intrinsic multi-mode nature of the many-body system. The dynamical evolution of the non-equilibrium system can be well described by the Tomonaga Luttinger Liquid (TLL) formalism, presented in chapter 2. Comparing the FDFs to the TLL predictions shows that the system dephases rapidly to a prethermalized state, a state showing thermal-like properties for some observables (like correlation functions), yet distinctly different from true thermal equilibrium. Finally, the decay of the mean contrast versus integration length is used as an independent measurement to determine the prethermal correlation properties.

5.1. Definition

A clear and common definition of prethermalization has not yet emerged in literature. The term appears to be used slightly different by various fields, originally coming from the high-energy community.

The phenomenon of prethermalization was first introduced in 2004 by J. Berges in the context of high-energy heavy-ion physics. At that time, experiments at RHIC¹ aiming at the production of quark-gluon plasma, yielded collisional data that suggested a rapid thermalization after the collision, much faster than standard QCD predictions [Rapp 04]. To explain these observations, Berges et al suggested that not a complete thermalization of all quantities is necessary, but that reaching the equilibrium equation of state on a faster time scale is already sufficient. Full thermalization of all quantities happens on a second much longer time scale.

The first definition of prethermalization given by Berges et al reads as [Berges 04]

“Prethermalization is a universal far-from-equilibrium phenomenon which describes the very rapid establishment of an almost constant ratio of pressure over energy density (equation of state), as well as a kinetic temperature based on average kinetic energy. The phenomenon occurs on time scales dramatically shorter than the thermal equilibration time. As a consequence, prethermalized quantities approximately take on their final thermal values already at a time when the occupation numbers of individual momentum modes still show strong deviations from the late-time Bose-Einstein or Fermi-Dirac distribution.”

These findings affect theories on the evolution of the early universe. In [Podolsky 06], Podolsky et al find a similar prethermalization effect after preheating of the early universe, where the thermal equation of state is closely, but not exactly reached, due to the effects of additional inflation components and the expansion of the early universe.

In the cold and ultracold atoms community, prethermalization is understood as a transient - on the way to full thermalization - quasi-steady state [Kollar 11, Barnett 11, Eckstein 09b]. Having certain quantities already reaching their final equilibrium values, seems to be commonly regarded of less importance. In [Kollar 11], Kollar et al study the effects of integrability on the prethermalization plateau and show that the prethermalized quasi-steady state can under certain conditions be described by a Generalized Gibbs ensemble which was introduced by [Rigol 07, Rigol 08]. In difference to the usual Gibbs ensemble, where the Gibbs exponent contains conserved energy, the Gibbs exponent of the generalized ensemble, contains a linear combination of the conserved quantities, thereby introducing a large number of Lagrange multipliers that account for the large number of constants of motion of integrable systems. Kollar et al found, that an integrable system decays to non-thermal steady states in the long-time limit, which are actually prethermalized states that never decay. For a nearly integrable system prethermalization plateaus are observed, that subsequently further relax to thermal equilibrium values. In this picture, the lifetime of the prethermalized state should increase when coming closer

¹Relativistic Heavy Ion Collider at Brookhaven National Laboratory, US

5. Prethermalization

and closer to an integrable point. It remains unclear what this means for non-integrable systems. However, [Eckstein 09a] show that even a non-integrable system may show prethermalization and that non-thermal states in integrable systems and prethermalized states in non-integrable systems can be related in the Generalized Gibbs ensemble picture.

A collection of intuitive statements on how to understand prethermalization [Wetterich 12, Eckstein 09a] are listed in the following:

- Thermalization means the complete loss of memory of the initial state, whereas prethermalization means only a partial loss of memory has happened.
- Prethermalization happens on time scales much shorter than thermalization. Thus, prethermalization is characterised by the emergence of different relaxation time scales for different observables.
- Prethermalization is the formation of non-thermal states on intermediate time scales.
- In the prethermalized state, several important features already look similar to thermal equilibrium.
- The prethermalized state is a quasi-stationary state that persists for long (sometimes infinite) time scales.
- The prethermalized state is a partial-fixed point in the space of correlation functions.

The topic of prethermalization has already gathered a lot of interest from the theoretical side, but lacking experimental realisations so far. Experimentally, one of the most prominent problems is to produce repeatedly and well controlled the (almost) same initial, far from equilibrium, quantum-many body state. In [Kinoshita 04] a Newton cradle like experiment of arrays of 1D Bose gases, in an optical lattice trap, was realized. The results showed no signs of thermalization, even for thousands of collisions. The residual slow dynamics of the momentum distribution which is observed is mainly due to the anharmonicity of the dipole trap. As there is no relaxation happening, no distinct relaxation time scales are measurable.

To my knowledge, the first direct experimental observation of the prethermalization phenomenon has been achieved in our setup [Gring 12b] in an atom chip trap. Atom chip traps have the advantage of producing single, highly anisotropic traps in the 1d regime. In contrast to the optical lattice experiments in [Kinoshita 04], where only averaged quantities of many 1d tubes are measurable, we do not have to average over many realisations for slightly different parameters (density, trap frequencies) in one experimental run. In general, atom chips provide well controlled and well isolated single-realizations of 1d Bose gases, that can be brought into a far from equilibrium situation with high reproducibility. Relaxation happens on easily measurable time scales on the order of several ms, compared to condensate lifetimes of up to one second (compare sec. 6.1). The good isolation from the environment, thus enables to probe the intrinsic loss of coherence within a quantum many-body system itself, rather than the decoherence

5. Prethermalization

or loss of information into the environment. Together with lots of theoretical efforts and experimental improvements, we were able to characterize the transient states of the evolution of the non-equilibrium system in great detail, unmasking the emergence of a prethermalized state. The details shall be presented in the next subsections.

5.2. Creating the non-equilibrium system

The following procedure is applied to bring a well-isolated many-body quantum system out of equilibrium and to study its subsequent time evolution and relaxation dynamics.

1. creation of an equilibrium quasi-condensate
2. fast, phase-coherent splitting of the quasi-condensate into two uncoupled Bose gases of similar densities, thereby creating two almost identical “phase-copies”
3. wait for different evolution times, before taking absorption images of the interference patterns in time-of-flight

5.2.1. Creating the initial quasi-condensate in thermal equilibrium

Evaporative Cooling is used to create an almost pure quasi-condensate without any significant thermal fraction. Special care needs to be taken, that the final cooling ramp excites a minimum of dipole and quadrupole modes in the condensate (see sec. 3.2.8). Before the final switch-off procedure of the rf knife, it makes sense, to hold the rf knife at its final value for at least several tens of ms (depends on collision rate), to make sure that a thermal equilibrium can be reached. This makes even more sense, as the thermalization mechanisms in a 1d quasi-condensate are not well understood so far. Currently, a detailed survey of thermalization during and after rf evaporation in 1d quasi-condensates is in progress [Grisins 14]. This constant rf-knife also averages over 50 Hz fluctuations, the technical noise stemming from the main power grid, and thereby increases the shot to shot atom number stability.

5.2.2. Coherent Splitting Process

In order to phase-coherently and adiabatically split the quasi-condensate, radio-frequency dressed state adiabatic potentials are used to form a double-well potential in the transverse direction of the cloud [Lesanovsky 06, Schumm 05b]. The amplitude of the dressing rf is linearly ramped up in typically 17 ms. The frequency is kept constant, red detuned with respect to the $m_{F=2} \rightarrow m_{F=1}$ transition. Typical detunings with respect to the trap bottom are on the order of 20 – 30 kHz. 17 ms is slow compared to the transverse trap frequency of $\omega_{tr} = 2\pi \times 1.4$ kHz in the standard trap and does not lead to additional collective excitations in the system. Splitting too fast can result in oscillations in the transverse direction. Splitting too slow does not result in phase-coherent splitting, meaning that the longitudinal excitations present in the unsplit system would uncouple

5. Prethermalization

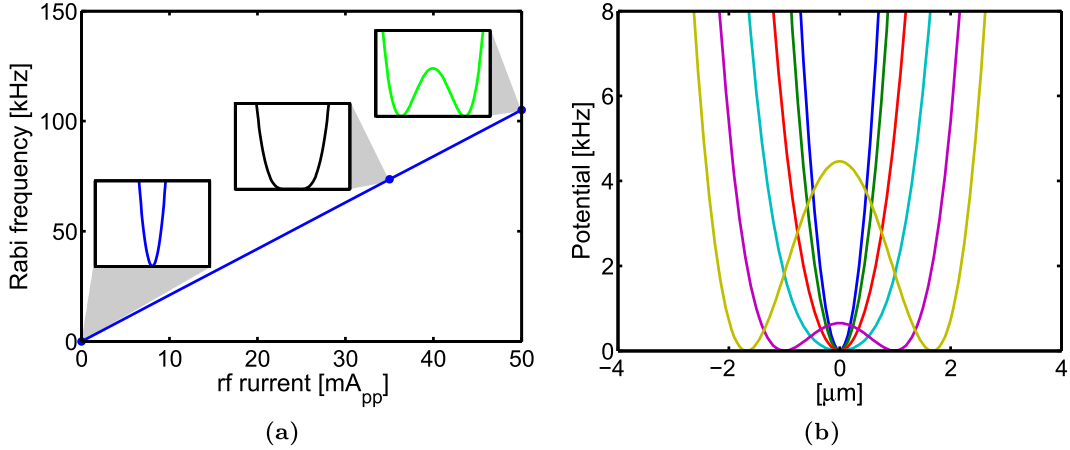


Figure 5.1.: Simulation of the double-well potential in RWA approximation following [Göbel 08]. (a) Rabi frequency versus peak-to-peak rf current. Insets show dressed state potentials for the same scale as in (b). The barrier actually starts to form at rf currents larger than 35 mA_{pp}. (b) Dressed state potentials for a linear increase of rf peak-to-peak current in steps of 10 mA_{pp} from 0 to 50 mA_{pp}.

at different times. The evolution of the k-modes would then start at different times and some modes would be dephasing earlier than others [Langen 13a].

Fig. 5.1 shows a simulation of the dressed state potentials in rotating-wave approximation (RWA), following [Göbel 08], for increasing rabi-frequencies i.e. increasing rf currents in the two parallel, 30 μm wide chip wires as schematically depicted in Fig. 5.2 and Fig. 3.2. The barrier forms rather close to the end of the splitting ramp. The actual decoupling, going from finite to zero tunnel coupling, happens on a much shorter time scale and was measured to happen within less than 0.5 ms [Langen 13a], whereas the theoretical description presented in section 2.5 assumes an infinitely fast splitting. The remaining tunnel coupling J was estimated to be $J \ll 2\pi \times 0.1$ Hz [Ananikian 06] at a splitting distance of $d = 2.8$ μm. To be on the safe side, it was experimentally verified that any residual tunnel coupling has no effects on the reported physics in this thesis. This was confirmed by comparing the obtained results for even larger splitting distances and barrier heights at the same ramp rates. Following [Zhang 01], the tunnel coupling can be estimated within a simple two-mode model, using the single particle ground states of the two harmonic wells. The tunnel coupling then scales exponentially with the square of the splitting distance $J \propto \exp\left(-\frac{d}{a_{tr}}\right)^2$, with the ground state size $a_{tr} = \sqrt{\frac{\hbar}{m\omega_{tr}}}$. No significant dependence on splitting distance was found for $d \geq 2.8$ μm. In conclusion, a significant tunnel coupling between the two wells seems highly unlikely.

To realize an almost perfect symmetric splitting process, the single trap is split in the horizontal direction, perpendicular to gravity and approximately parallel to the atom chip surface. This ensures, that there aren't any asymmetries generated between the two wells by either the gravitational sag nor by the $1/r$ dependence of the rf fields, throughout the

5. Prethermalization

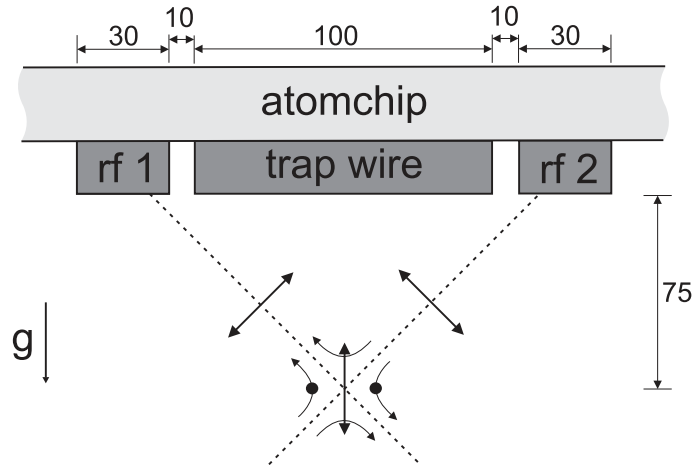


Figure 5.2.: Schematic drawing of the rf induced horizontal double-well setup. The 100 μm wide central wire creating the static trap is enclosed by two 30 μm rf current carrying wires, acting as chip based rf antennas. Together they create a vertical oscillating rf field. As potential minima form where both static and rf fields are parallel a horizontal double-well is created. The chip was designed for an optimal trapping distance of 75 μm . To decrease the strong fragmentation effects discussed in section 3.3, it was decided to trap the atoms at a distance of approximately 100 μm . Values in μm . Not to scale.

whole splitting process. This can hardly be achieved for a vertical splitting process. Thus being able to measure the fringe pattern across the vertical (gravity) direction represents an essential improvement compared to earlier experimental setups [Hofferberth 07].

For a typical rf current of 49 mA_{pp} , a simulation of the dressed state DW potential gives the following parameters: a splitting distance of 3.2 μm , a simulated barrier height of 3.9 kHz, compared of the typical range of the chemical potential μ of 400 – 800 Hz, a distance to the chip of 108 μm , a rf Rabi coupling frequency of 103 kHz and a transverse trap frequency of $2\pi \times 1376$ Hz, which is in good agreement with the experimental data.

In order to avoid collective longitudinal excitations, great care was taken in the positioning of the minimum of the chip trap with respect to the fragmentation problems as explained in section 3.3. By slightly imbalancing the current through the upper and lower U pairs, creating the longitudinal confinement, the trap minimum can be shifted along the trapping wire. This was done in such a way that the trap minimum coincides with a fragmentation minimum, resulting in a nice harmonic confinement. When applying the rf potentials the longitudinal trap confinement is smoothly changed and is minimally disturbed by the fragmentation. Furthermore, the trap frequencies have been chosen such that, before and after splitting the total longitudinal length of the cloud remains almost the same (compare Tab. 5.1 and Fig. 5.3), again inhibiting longitudinal collective excitations.

5. Prethermalization

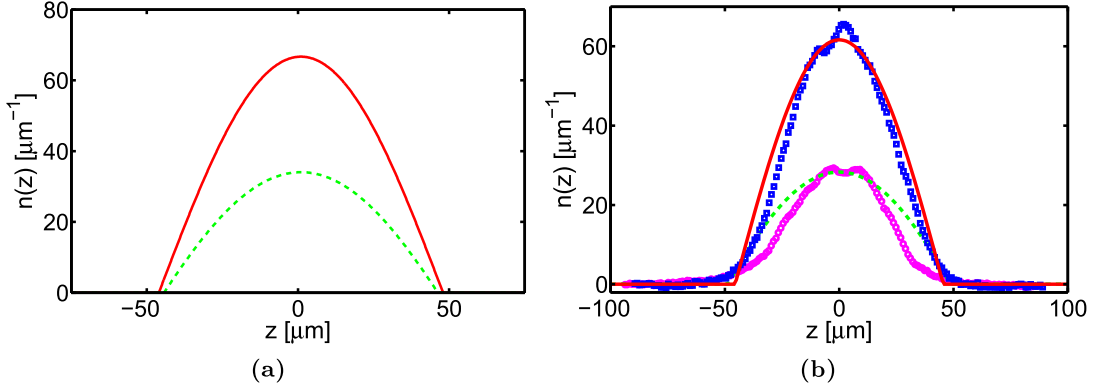


Figure 5.3.: Calculated and measured density profiles before and after splitting. (a) longitudinal density profile of unsplit trap for $N = 4000$ atoms (solid red), longitudinal density profile in one single well (dashed green) of the double-well trap for $N_{tot} = 4000$ atoms. (b) measured longitudinal trap profiles before (blue squares) and after (magenta circles) splitting in comparison to the respective calculated profiles. The calculated peak densities are in good agreement to the measured data. The widths before and after splitting are almost identical leading to minimized breathing oscillations.

5.2.3. Release process

In the experiment, the switch-off process of the double-well trap turns out to be a crucial step, strongly affecting the maximally observable contrasts. The rf currents are not switch-off immediately by an rf-switch, but instead they are linearly ramped down via the rf generator, typically within 5 rf cycles, which corresponds to $t_{ramp} \approx 12.8 \mu\text{s}$ at an rf frequency of $\nu_{rf} = 390 \text{ kHz}$. The corresponding static fields are switched-off within much less than $10 \mu\text{s}$. The observable contrasts of the resulting interference patterns depend crucially on the timing (rf phase at switch-off) and the duration of this ramp down of the rf-currents with respect to the switch-off of the static fields. A too fast switch-off leads to a projection of the m_F states into the $F = 2$ manifold [Langen 13a], which can be detected by applying Stern-Gerlach type measurements [Gerlach 22]. During the switch-off, residual magnetic field gradients induce a phase shift in the interference patterns of the different m_F states, which results into a blurring of the summed up interference fringes. Therefore, great care has to be taken to optimize the rf ramp down duration and the rf phase at switch-off [Langen 13a].

Please also note that the recorded interference contrast strongly depends on the detuning of the imaging beam, which can even lead to an enhancement of contrast [Gring 12a].

5.2.4. Why does the splitting create a non-equilibrium situation?

As there have been debates and discussions why this is a non-equilibrium system, a collection of arguments and point of views are presented here.

The Luttinger Liquid picture: symmetric and anti-symmetric modes

As discussed in sec. 2.2.1, before splitting, the initial equilibrium quasi-condensate has a longitudinally fluctuating phase caused by the population of longitudinal excited states in the gas. These excitations are thermally populated with an exponentially decaying correlation function (eq. 2.42) and a thermal phase correlation length given by eq. 2.43. By phase-coherently splitting the quasi-condensate, almost perfect correlation between the relative longitudinal phase profiles of the two halves of the split system is created. As we have seen in sec. 2.5, the excitations of the split system can be described by anti-symmetric (relative) and symmetric (common) degrees of freedom (DOF). The anti-symmetric DOF are defined by the difference in phase and density between the two well, whereas the symmetric DOF are determined by the respective sums. Let's focus on the phase dynamics. After splitting, the phase profiles of the two halves are almost identical and hence the anti-symmetric degree shows almost perfect correlations as illustrated in Fig. 5.4. This means that, nearly all the excitations of the phase are initially stored in the symmetric mode, which is essentially thermally populated. The anti-symmetric mode is initially only populated by the quantum noise of the splitting process, which according to eq. 2.66 and eq. 2.67, results mainly in density fluctuations. Actually, this quantum shot noise populates the initial relative density fluctuations.

In conclusion, this initial state is very much unlike the thermal equilibrium state of two independently created quasi-condensates, where the symmetric and anti-symmetric modes both share the same thermal population.

The energy picture

The splitting prepares a superposition for each atom being in the left or right well. In thermal equilibrium for two independent condensates the atoms would be localized in one of the wells. Due to this splitting Poissonian quantum noise is induced which scales as \sqrt{N} . This results in the imprint of local, relative density fluctuations along the condensate, which would be suppressed for a thermal quasi-condensate as derived in section 2.3. In the realm of the relative DOF, the Hamiltonian given by eq. 2.65 applies. In conclusion, the initial state after splitting is highly out of equilibrium as the energy is mainly stored in the density fluctuations.

The dephasing process [Bistritzer 07] leads to an equipartition of this energy between the two quadratic DOF of the Hamiltonian of eq. 2.65. In this sense the dephasing can be understood as the thermalization process of the relative degrees, leading to a thermal equilibrium state of the relative modes. This quantum thermal equilibrium state is meant in the sense of [Cazalilla 11], meaning that the ergodic hypothesis (phase space and time averages are the same) holds at almost all times. As the TLL theory describes an integrable and further harmonic system, the dephased modes will be able to rephase at some later time, breaking the equilibrium for some short time intervals.

In conclusion, the dephasing describes the thermal equilibration in the relative DOF, which is the prethermalized state of the complete system of common and relative DOF. Yet true thermal equilibrium between common and relative DOF is not achieved. Only

5. Prethermalization

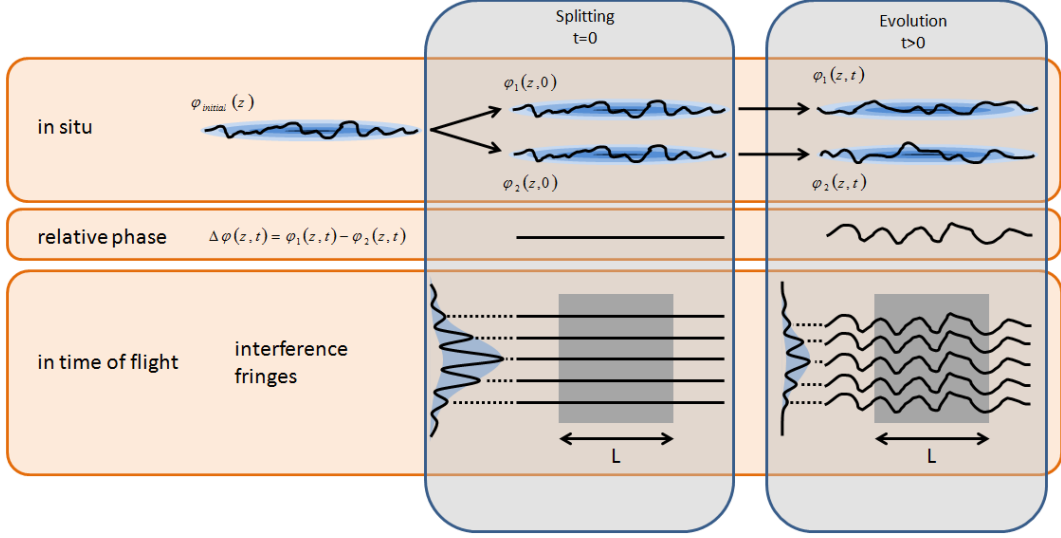


Figure 5.4.: Schematic drawing of the splitting process and subsequent evolution. At $t_e = 0$, the gas is phase-coherently split into two atom clouds, creating a constant relative phase profile $\Delta\varphi(z,0) \approx 0$. This means that the population of the phase fluctuations in the anti-symmetric degrees of freedom (DOF) are practically zero and that nearly all of the thermally populated phase fluctuations before splitting are now stored in the symmetric DOF. Therefore, symmetric and anti-symmetric DOF are strongly out of equilibrium.

In the experiment, the relative phase profile along the clouds can be measured via matterwave-interference fringes in time of flight, which according to the above statements show straight interference fringes at $t_e = 0$. Integrating the fringe patterns over specific integration lengths L then leads to a high fringe visibilities. In the course of the evolution ($t_e > 0$), the amount of relative phase fluctuations increases and the observable fringe visibilities decrease. Therefore, the dynamics of the non-equilibrium system can be experimentally studied via interference measurements.

5. Prethermalization

higher-order processes, which are not captured by Luttinger-Liquid theory may lead to a mixing of the symmetric and anti-symmetric modes connecting the two states.

Parameters before and after the quench

	transverse trap frequency ω_{tr} [kHz]	longitudinal trap frequency ω_{long} [Hz]	typical peak density n_{1d} [μm^{-1}]	Luttinger Parameter K	total longitudinal length [μm]
Unsplit Trap	$2\pi \times (2.1 \pm 0.1)$	$2\pi \times (11 \pm 1)$	89.6	34.2	106
Split Trap	$2\pi \times (1.4 \pm 0.1)$	$2\pi \times (7 \pm 1)$	43.5	29.2	107

Table 5.1.: Typical trap parameters before and after splitting. Measured values for trap frequencies. A total atom number of 6000 atoms, which is typical for many measurements, was used as the reference to calculate the density n_{1d} and total longitudinal length following [Gerbier 04] and estimate the Luttinger parameter K . Unless otherwise noted this trap configuration has been used.

Before the splitting, there are N atoms in the condensate. After splitting, the atom number in each well is $\sim N/2$. This reduces the density and thus changes the Luttinger Liquid parameter K given by eq. 2.59. Table 5.1 gives relevant system parameters before and after the splitting.

5.3. Properties of the Prethermalized State

The following sections will present experimental data that led to the achievement of the first direct experimental observation of prethermalization in the evolution of a many-body quantum system, well isolated from the environment.

In order to facilitate the discussions and spare unnecessary repetitions the main properties of the prethermalized state, in the context of matter-wave interferometry, are summarized below [Bistritzer 07, Kitagawa 10, Kitagawa 11, Gring 12b, Gring 12a].

As discussed in sec. 2.5.2, the fast, phase-coherent splitting creates an initial state, with small relative phase correlations, but strong density fluctuations. As the density term in the Hamiltonian 2.65 is independent on the wavenumber k , all k modes receive the same amount of energy E_{split} , as determined by the quantum shot noise of the splitting process. As discussed in 5.2.4, energy is transferred into the phase DOF over time and phase fluctuations grow with evolution time t_e . Finally, in the prethermalized state, the energy is equipartitioned [Huang 87] between the phase and density DOF. This leads to

5. Prethermalization

the scaling of population of each k-mode as

$$n_k = \frac{E_{split}}{E_K} = \frac{E_{split}}{\hbar c_s} \frac{1}{k}. \quad (5.1)$$

For a system in thermal equilibrium, the mode population is given by the Bose-Einstein distribution which can be approximated for low momentum modes as

$$n_k = \frac{1}{\exp(\hbar c_s k / k_B T) - 1} \approx \frac{k_B T}{\hbar c_s} \frac{1}{k}. \quad (5.2)$$

Therefore, the fast splitting process populates the modes with a $1/k$ scaling, with an effective temperature of the prethermalized state T_{pre} , with $E_{split} = k_B T_{pre}$. In summary, in the prethermalized state, the effective temperature of relative DOF is given by T_{pre} , whereas the thermally populated common modes inherit the initial temperature of the unsplit gas T_{in} , with $T_{in} \neq T_{pre}$. This dynamical evolution is summarized in table 5.2. The dynamics leading to full thermal equilibrium meaning the temperature of common mode equals the temperature in the relative modes is beyond the TLL framework. In the integrable TLL description, the prethermalized state is the final state of the system, assuming a perfectly symmetric splitting process. Observing a further evolution in the experiment due to a slight breaking of integrability will be the topic of chapter 6.

	common		relative	
	E_ϕ	E_n	E_ϕ	E_n
initial	$\frac{k_B T_{in}}{2}$	$\frac{k_B T_{in}}{2}$	~ 0	$\sim k_B T_{pre}$
prethermal	$\frac{k_B T_{in}}{2}$	$\frac{k_B T_{in}}{2}$	$\frac{k_B T_{pre}}{2}$	$\frac{k_B T_{pre}}{2}$
thermal	$\frac{k_B T_f}{2}$	$\frac{k_B T_f}{2}$	$\frac{k_B T_f}{2}$	$\frac{k_B T_f}{2}$

Table 5.2.: Energy distribution between common and relative modes, where E_n denotes the energy in the density fluctuations and E_ϕ the energy in the phase fluctuations. The final, thermal equilibrium temperature T_f is assumed to be given by the sum of initial T_{in} and prethermalized T_{pre} temperature as $T_f = (T_{in} + T_{pre})/2$.

According to [Kitagawa 11] the prethermalized temperature T_{pre} can be calculated as,

$$k_B T_{pre} = E_{split} = \frac{m c_s^2}{2} = \frac{g n}{2} = \hbar \rho a_S \omega_R. \quad (5.3)$$

As the prethermalized temperature originates from the quantum shot noise of the splitting process, the prethermalized temperature scales proportional to the chemical potential $\mu = g n$.

In conclusion, the prethermalized state shows thermal like mode population scaling and thermal-like correlation functions in the relative DOF, with an assigned effective temperature T_{pre} . This temperature is completely independent on the initial temperature

of the unsplit system.

5.4. The Contrast as an observable

5.4.1. Information encoded in the Contrast: What do we learn?

What can we learn by measuring the contrast of a matter-wave interference pattern? What physics affect the value of the contrast on specific length scales and how can this be related to the Luttinger Liquid picture?

As we have seen in section 2.5, the split 1d Bose gas can be described by a Tomonaga-Luttinger Liquid (TLL) approach, which consists of collective modes with linear dispersion relation. In Fourier space, these collective excitations can be described by a set of uncoupled harmonic oscillators, i.e. phonons of momentum $k = 2\pi/\lambda$, corresponding to sound-waves modulating the relative density $\hat{n}_r(z)$ and phase fields $\hat{\phi}_r(z)$ of the TLL Hamiltonian given by eq. 2.56. The amplitude of these excitations is given by the population of the k -mode.

In this context, the experimentally measured interference patterns are used to probe the local relative phase $\hat{\phi}_r(r) = \hat{\phi}_1(z) - \hat{\phi}_2(z)$ between the two coherently-split gases. The strength of these phase fluctuations directly affect the contrast of the integrated line profile. The choice of a variable integration length L acts as a filter for the effects of the different excitations in the system. For a given integration length L , sound-waves with wavelengths $\lambda < L$ produce strong fluctuations of the relative phase $\hat{\phi}_r(z)$ within L while modes with wavelengths $\lambda > L$ have approximatively no effect on $\hat{\phi}_r(z)$, apart from a global phase shift of the mean $\langle \hat{\phi}_r(z) \rangle$. The contrast $C(L)$ of the integrated interference pattern is therefore mainly influenced by the sound-waves with wavelength shorter than L . Thus, measuring the contrast $C(L)$ for different length scales L along the cloud, allows one to directly probe population of excitations on different energy scales. Furthermore, measuring the contrast for different evolution times $C(L, t_e)$ then probes the dynamics of the phase fluctuations as well.

Fig. 5.5 shows two exemplary fringe patterns at different evolution times t_e . At short evolution times, just after the splitting, there are almost no phase fluctuations present and the fringes form almost straight lines along the longitudinal z -direction, leading to high contrasts $C(L)$ on all length scales L . For longer evolution times, the phase fluctuations are increased, resulting in a “wiggly” shape of the fringe pattern. The integrated contrasts $C(L)$ becomes highly dependant on the length scale L . At short integration lengths, high contrasts can be found, while for longer integration lengths, approaching the system size, the observed contrasts are highly diminished, which is a direct consequence of increased relative phase fluctuations. This means that long length scales start to loose the memory of the initial state and the long-range phase correlations start to decay.

5.4.2. Extracting the Contrast

The following procedure is used to measure the contrast of an interference picture.

5. Prethermalization

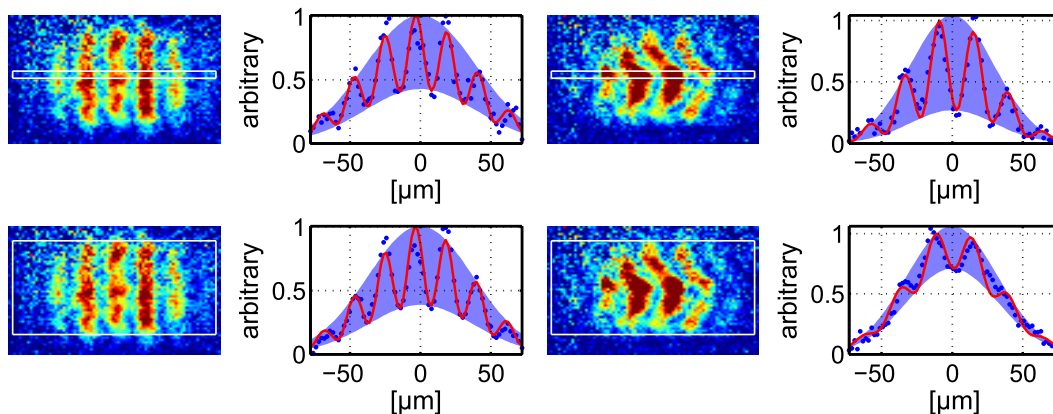


Figure 5.5.: Probing the Contrast along the longitudinal direction. Measuring the contrast on different length scales provides information about the correlations still present in the system. Out of many of these pictures, the squared contrast distributions (squared FDFs) can be built, see for example Fig. 5.13. The correlation properties are accessible by studying the shape of the squared contrast distribution functions $P(C(L)^2)$ (see section 5.7) or by looking at the $C^2(L)$ decay (see section 5.9). This figure provides a phenomenological insight into the physics.

- (a) At short evolution times, just after the splitting, there are almost no phase fluctuations present and the fringes form almost straight lines along the longitudinal z -direction. When integrating along the z -direction, the resulting line profiles show high fringe visibilities on all length scales and the contrast is almost not length dependent.
- (b) For moderate evolution times in the prethermalized state, the phase fluctuations are increased resulting in a “wiggly” shape of the fringe pattern. The integrated contrast becomes highly dependant on the length scale.

By integrating longitudinally over a length L , a line profile (Fig. 5.5) can be extracted from the matter-wave interference pattern, from which a contrast $C(L)$ can be obtained by fitting a sine function and a Gaussian profile. The contrast is the height of the interference fringes relative to the height of the Gaussian background and is extracted, following eq. 4.26 to 4.28, using the fit function

$$f_L(x) = A \cdot \exp\left(-\frac{(x-x_0)^2}{2\sigma^2}\right) \cdot \left(1 + C(L) \cos\left(\frac{2\pi(x-x_0)}{\lambda} + \phi(L)\right)\right), \quad (5.4)$$

where σ is the rms radius of the Gaussian profile, λ is the fringe spacing and $\phi(L)$ is the phase of the interference fringes relative to the peak at x_0 of the Gaussian profile.

5.4.3. Measuring the Contrast during the Splitting Ramp

When measuring the contrast at different fringe spacings during the end of the splitting ramp, the influence of the finite imaging resolution has to be accounted for.

5. Prethermalization

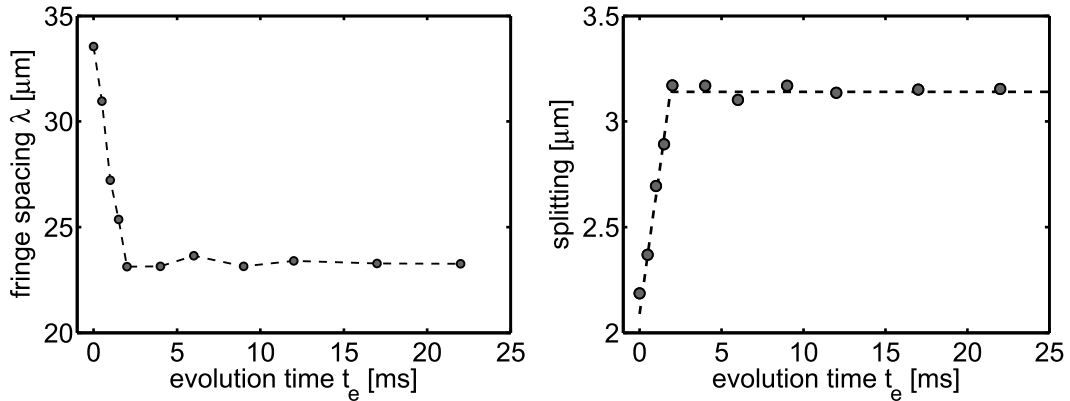


Figure 5.6.: Fringe spacing and splitting distance in the final part of the splitting ramp. (a) Measured fringe spacing λ versus evolution time t_e . The dashed line is a guide to the eye. (b) Calculated splitting distance d versus evolution time t_e , using $\lambda = \frac{ht_e}{md}$. Tunnel coupling between the two Bose gases becomes negligible at $t_e = 0$ ms as shown in [Langen 13a]. The tunnel coupling, given by the overlap of the wave functions between the two wells is very sensitive to the chemical potential and thus on small atom number variations and further to the barrier height of the double well potential. The 2 ms further increase in splitting distance ensures a reproducible zero tunnel coupling and thus zero phase-locking for different initial conditions of the experiment, like atom number and temperature. The dashed lines are linear fits.

As explained in sec. 5.2.2, the condensate is phase coherently split within 17 ms. In order to reproducibly create the same non-equilibrium state of two completely decoupled condensates, we split significantly further than just to the decoupling point in time at 15 ± 0.5 ms. This means that the interesting relaxation dynamics already start 2 ± 0.5 ms before the end of the splitting ramp.

In this final part of the splitting ramp the splitting distance d_{split} between the two clouds increases linearly with ramp time as illustrated in Fig. 5.6. The resulting fringe spacing λ of the interference pattern in 16 ms time-of-flight t_{TOF} decreases as $\lambda_{fringe} = h \cdot t_{TOF} / md_{split}$ [Andrews 97b, Pethick 01]. When measuring the contrast during the splitting ramp at different fringe spacings, the maximal measurable contrast scales with the fringe spacing, according to the finite resolution of the vertical imaging system. Thus, to be able to compare the measured contrasts at different fringe spacings, a rescaling factor has to be applied. This rescaling takes mainly the point spread function (PSF) of the imaging system into account. To include the effects of other noise sources, a detailed simulation of the vertical imaging was performed, including the measured PSF, the finite cloud size in time of flight and imaging shot noise. Furthermore, as the imaging beam is reflected on the atom chip, stray light generated by the chip structures was also taken into account. The simulated absorption pictures were analysed using our standard fringe fitting code applying the fit function of eq. 5.4. The results are shown in Fig. 5.7

5. Prethermalization

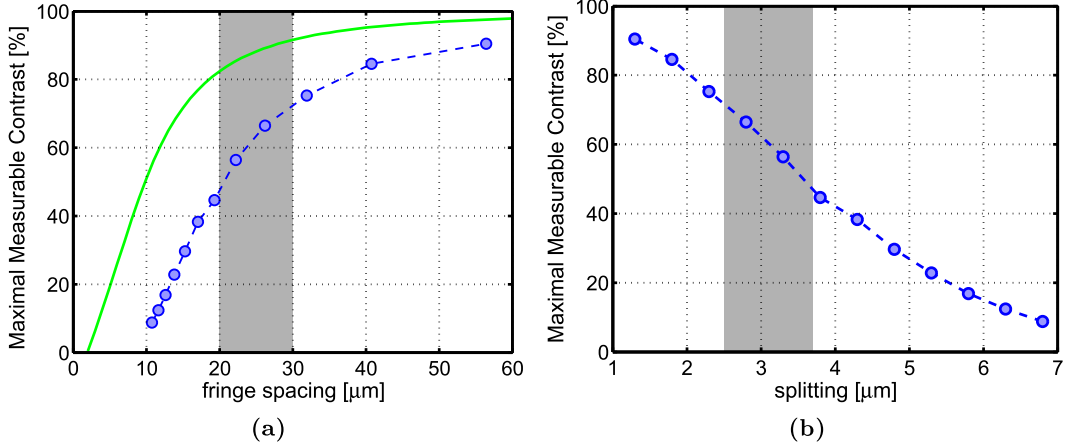


Figure 5.7.: Scaling of Contrast with respect to fringe spacing and splitting distance. (a) Maximal measurable contrast versus fringe spacing. (green, solid) modulation transfer function, (blue, circles) detailed simulation of the absorption imaging, including the point spread function of $3.8 \mu\text{m}$ Gaussian rms width, shot noise, finite cloud size in time of flight and stray light generated by chip structures. The result of the simulations are used to rescale the measured contrast in case of varying fringe spacings. (b) Maximal measurable contrast versus splitting distance. The grey shaded areas denote typical fringe spacings and splitting distances, respectively.

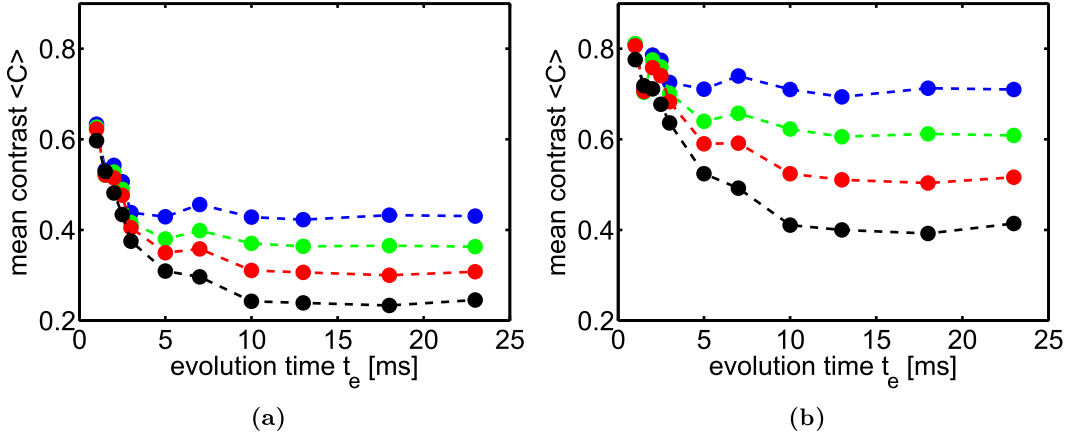


Figure 5.8.: Time evolution of the mean contrast for the integration lengths from top to bottom $L = 18 \mu\text{m}$ (blue), $40 \mu\text{m}$ (green), $60 \mu\text{m}$ (red) and $110 \mu\text{m}$ (black). The splitting ramp ends at $t_e = 2 \text{ ms}$ as shown in Fig. 5.6. Tunnel coupling between the two Bose gases becomes negligible at $t_e = 0 \text{ ms}$. (a) without PSF correction. (b) including PSF correction.

and qualitatively agree with the simple MTF prediction. This rescaling procedure is used to study the time evolution of the mean contrast.

5.4.4. Time Evolution of the Mean Contrast

Fig. 5.8a shows the time evolution of the mean contrast for various integration lengths L without taking the imaging effects into account. Fig. 5.8b shows the rescaled mean contrast. By comparing the two, it becomes obvious that the fast initial decrease in contrast on all length scales stems from the decrease in fringe spacing λ and is mainly governed by the finite resolution of the imaging system. The really interesting physics, namely the contrast decay due to the evolution of the non-equilibrium state, becomes apparent when correcting for the imaging resolution.

Still we do not measure 100 % contrast at zero evolution time, which may result from several reasons. The finite splitting time used in the experiment results in an uncertainty on the point in time where the two quasi-condensates decouple. This uncertainty is approximately ± 0.5 ms large. During this time the fast dephasing of high energy excitations contributes to a reduction of contrast. Moreover, technical imperfections reduce the contrast, mainly the residual projection of atoms to other Zeeman states during the switch off of the trapping potential as well as slight misalignments of the imaging optics. On all length scales, the maximum contrast that we detect is approximately 85 ± 3 %. This leads to a necessary rescaling factor of the theory.

The rescaling of the contrast is actually only important when looking at the mean values. When measuring full distribution functions of contrast or squared contrast, the distributions are normalized to the mean contrast and are thus not affected by finite imaging resolution and other noise sourced. Also the $C(L)$ plots presented in section 5.9 are renormalized to the smallest measurable length scale.

Fig. 5.9 compares the evolution of the measured mean contrast $\langle C(L) \rangle$ on different length scales (data points) with the predictions from the TLL theory (solid lines). To account for the non-perfect splitting, the theory is rescaled by a single common factor $r = 0.85$, common for all times and all integration lengths, in line with the maximum contrast that we detect of approximately 85 ± 3 %. The high agreement between data and theory is very convincing. Fig. 5.9 shows that the observed time scales for relaxation are different for different length scales. For short integration lengths the decay of the mean contrast settles at much earlier evolution times t_e than for long length scales. This is a direct evidence of the multimode nature of the dynamics, leading to a length scale dependant relaxation time scale, which according to the TLL theory scales as $t_{relax} \approx L/4c$ [Kitagawa 11], with the sound velocity c of the homogeneous theory. In this context t_{relax} is defined as three times the e^{-1} decay time scale. Furthermore, after this first, very rapid decay within less than 10 ms, the dynamical evolution of the non-equilibrium system seems to come to an end. The natural question coming up, is this already the thermal equilibrium state of the system? If this would be true, how does this fit to the harmonic TLL theory only predicting the dephasing of k-modes and unable to couple between relative and common degrees of freedom?

To answer the last question a large number of measurements at different initial

5. Prethermalization

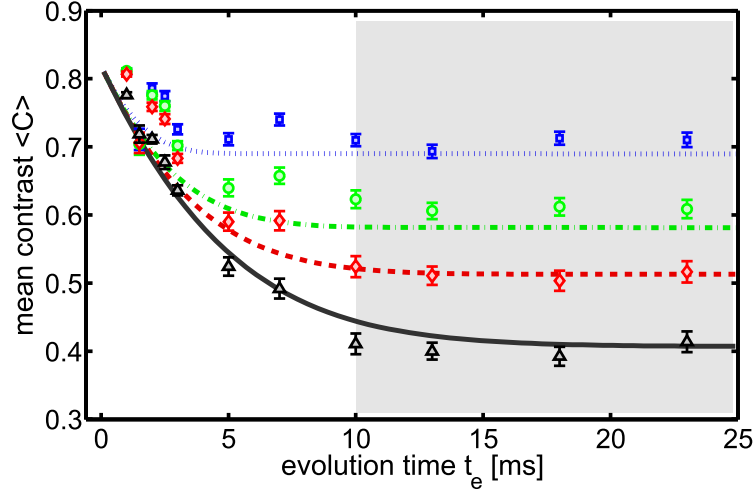


Figure 5.9.: Time evolution of the mean contrast compared to TLL theory for the same data as in Fig. 5.8b. To account for the non-perfect splitting, the theory is rescaled by a common factor of 0.82. The grey shaded area denotes the steady-state after the fast evolution.

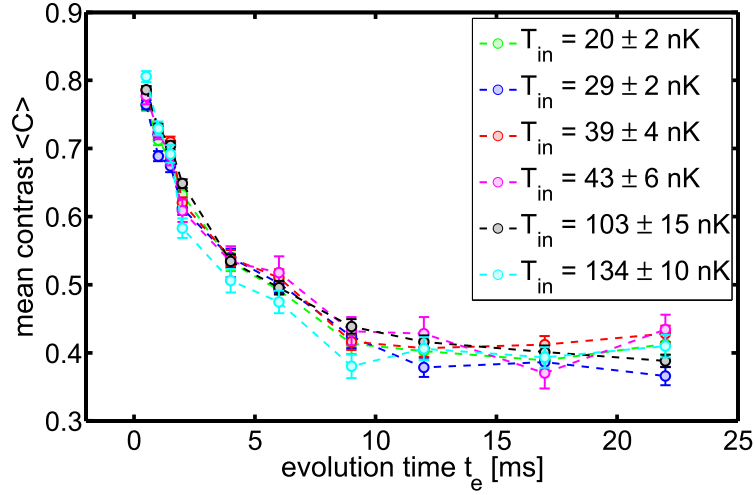


Figure 5.10.: Mean Contrast Decay of $L = 110 \mu\text{m}$ at different initial temperatures T_{in} . Within the errorbars the decay is independent on the initial temperature in agreement with the TLL prediction and in contrast to typical thermalization theories [Mazets 08, Mazets 10, Stimming 11, Burkov 07]. Dashed lines are guides to the eye.

temperatures have been performed. Henceforth, initial temperature T_{in} refers to the temperature of the unsplit gas, as measured before applying the splitting. If this fast relaxation process indeed leads to full thermal equilibrium, one would typically expect to find a high temperature dependence, which is true for most of thermalization theories

5. Prethermalization

for 1d quasi-condensates [Mazets 08, Mazets 10, Stimming 11, Burkov 07]. A detailed discussion is postponed to chapter 6. Fig. 5.10 shows the time evolution of the mean contrast for data sets in the temperature range of 20 to 130 nK, for $L = 110 \mu\text{m}$, which are identical within the errorbars. This observation strongly supports the TLL picture.

As we have seen, there is a lot of information contained in the mean contrast. But it remains unclear if this steady state is to be identified as the thermal equilibrium state of the system or if a further subsequent evolution on a probably much larger time scale is to be expected. To be able to address this topic, the contrast and phase statistics shall be measured and used to determine the nature of the observed steady state as well as the multimode physics behind the relaxation dynamics. To this end, the measured contrast distributions will be compared to the calculated thermal equilibrium distributions of sec. 4.4, first of all, to see if they are thermal and, second, to check that they show the correct temperatures. This will be the topic of the following sections.

5.5. Measuring joint FDFs

The joint Full probability Distribution Functions (joint FDFs) are a handy, phenomenological tool to illustrate the dynamics of contrast and phase simultaneously on a circular statistics representation. Basically, they show the joint probability distributions of the phase distributions and contrast distributions, which can be calculated numerically using the TLL description [Kitagawa 11] and are easily compared to the experimentally measured distributions. Fig. 5.11 illustrates how the joint FDFs are being obtained from the measured data. Each integrated line profile gives a contrast and phase pair $\{C(L), \phi(L)\}$, which is plotted on a polar plot, where the contrast is represented in the radial direction and the phase in the azimuthal direction, respectively. The resulting contrast and phase pairs of many repeated realisations are collected in a scatter plot as depicted in Fig. 5.11e. Finally, to give a measure of the probability of finding a certain contrast and phase pair, the scatter plot is converted to a polar density plot.

Measuring these joint FDFs puts high constraints on the experiment. The experiment needs to run very stable and very reproducible to generate a sufficient amount of repeated realisations at the same parameters. Here the most obvious main parameter is density of the degenerate Bose gas, which needs to be kept constant, at least, during the data acquisition time. Other important parameters are the mean and spread of the number balance between the two wells, as well as preparation of the non-equilibrium state (see section 5.2) and the stability of the switch-off process of the dressed-state trap.

5.5.1. Effects of Number Imbalance

Let's now focus on the effects of number imbalance between the two double-wells. A number imbalance leads to a global phase shift of the interference pattern that scales linearly with time. Due to technical noise sources we find an additional statistical broadening of the imbalance distribution beyond the Poissonian quantum splitting noise as defined by \sqrt{N} . This results in a broadening of the phase distribution, which needs to

5. Prethermalization

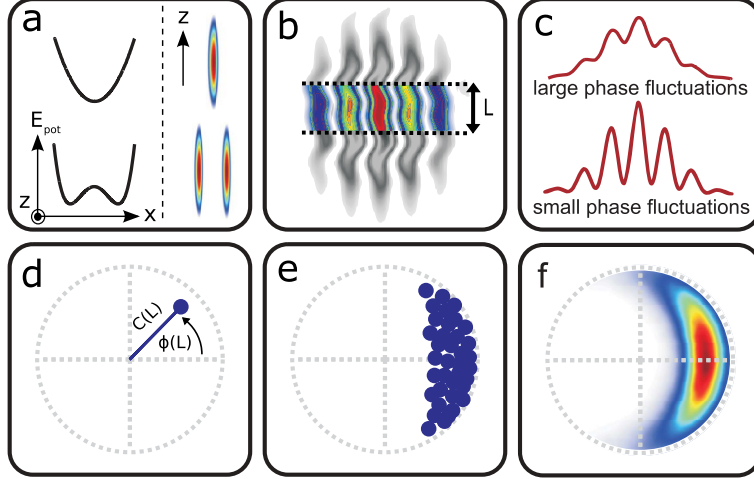


Figure 5.11.: Measuring joint FDFs. (a) Schematic plot of single and symmetric-double-well potential. (b) After switching off the trap, the two matter-waves expand and overlap. The resulting fringe pattern is probed via the vertical absorption imaging system, giving access to the relative phase fluctuations in the longitudinal direction. The contrast, being measured on different integration length scales L , is directly affected by the strength of the local phase fluctuations (c). Short integration lengths are affected by the population of high k -mode, whereas long integration length are affected by the population of all k -modes. (d) For a specific evolution time t_e , the phase $\phi(L)$ and contrast $C(L)$ are extracted from the fit function 5.4 and plot on a polar plot. Repeating the experiment many times results in the scatter plot (e), which is finally converted to a polar density plot, with red denoting high probability of finding a specific contrast, phase pair. Figure from [Kuhnert 13], copyright APS.

be included when comparing the measured and calculated joint FDFs from theory and experiment.

The global phase shift $\Delta\Phi(t_e)$ due to number imbalance can be calculated using the following considerations. The net number difference $\Delta N = N_1 - N_2$ in each shot leads to a difference in chemical potential $\Delta\mu$ between the two wells. This chemical potential difference

$$\Delta\mu = \mu_1 - \mu_2 = \hbar\omega_{tr} \left(\sqrt{1 + 4a_s n_1} - \sqrt{1 + 4a_s n_2} \right) \quad (5.5)$$

leads to a time dependant global phase shift of [Lewenstein 96, Javanainen 99, Schumm 05a]

$$\Delta\Phi(t_e) = \frac{t_e}{\hbar} \Delta\mu \approx 2t_e\omega_{tr} (n_1 - n_2) \quad (5.6)$$

The nett mean imbalance between left and right well results in a global phase rotation of the distribution by $\Delta\Phi(t_e)$. To compare measured and calculated joint FDFs the experimental global phase drift is rotated back so that the phase distributions are always centered at zero degrees.

5. Prethermalization

In conclusion, additional technical noise broadening the imbalance distribution leads to a broadening of the phase distribution, heavily affecting properties like the coherence factor $\Psi = \text{Re}\left[\frac{1}{L} \int_L dz \exp(-i\phi_r - \Delta\Phi)\right]$.

5.5.2. Measuring Number Imbalance

The number imbalance is determined independently for each scan, by using the longitudinal imaging system. As the resolution of the imaging is inadequate to resolve the double-well splitting distance ($2.8 - 3.8 \mu\text{m}$), the number imbalance needs to be measured in expansion. Thus, the dressed-state trap is switched off slightly earlier than the static trap, such that the two clouds receive a small nett velocity kick towards each other. The static trap is switched off before the two clouds collide. After release from the trap, the clouds expand and do not interact anymore with each other, due to low density. After some time of flight (12-16 ms) the absorption image is taken and shows two distinct clouds. To determine the atom number between left and right well, the position of each cloud is obtained via a Gaussian fit and the region of interest positioned likewise. The crucial part is to get the timing of the rf currents ramp down correct. Standard rf ramp down procedure lasts for about 5 cycles (section 5.2.3). For the number balance measurement, the number of ramp down cycles is increased to 20 or 25 cycles, which corresponds to 53-67 μs for an rf frequency of $\nu_{rf} = 375 \text{ kHz}$. Typically, a mean number imbalance of $\frac{|\langle N_1 \rangle - \langle N_2 \rangle|}{\langle N_1 + N_2 \rangle} \leq 1\%$ is obtained in the experiment, with rms standard deviations in the range of 4% to 6%. A more detailed discussion will be presented in [Langen 13a].

5.5.3. Fit Uncertainty

Another effect, broadening the distributions of contrast and phase, is the uncertainty of the fit parameters of eq. 5.4 itself. This effect needs to be taken into account by convolving the calculated distributions with the normally distributed fitting uncertainties of phase ϕ and contrast C . Typical rms fit errors for the contrasts are $\pm 6\%$ for $L = 6 \mu\text{m}$ to $\pm 3\%$ for $L = 110 \mu\text{m}$ and respectively for the phase $\pm 13^\circ$ for $L = 6 \mu\text{m}$ decreasing to $\pm 7^\circ$ for $L = 110 \mu\text{m}$.

5.6. Joint FDF Results

Fig. 5.12 shows the measured FDFs of 140 repeats at increasing evolution times t_e and at different integration length scales L . Furthermore the FDFs are compared to the result of the harmonic TLL model discussed in section 2.5. The initial temperature before splitting T_{in} of this data set was measured, using the density ripples method discussed in sec. 4.3, to be $T_{in} = 20 \pm 2 \text{ nK}$. A measured number balance rms width of 5% was included in the theory distributions as discussed in the previous section.

The three main observations of Fig. 5.12 are the following. First, for the shortest evolution time (1.5 ms) the high contrasts and small phase spreads demonstrate the coherence of the splitting process for all lengths L . Second, as time evolves, two distinct

5. Prethermalization

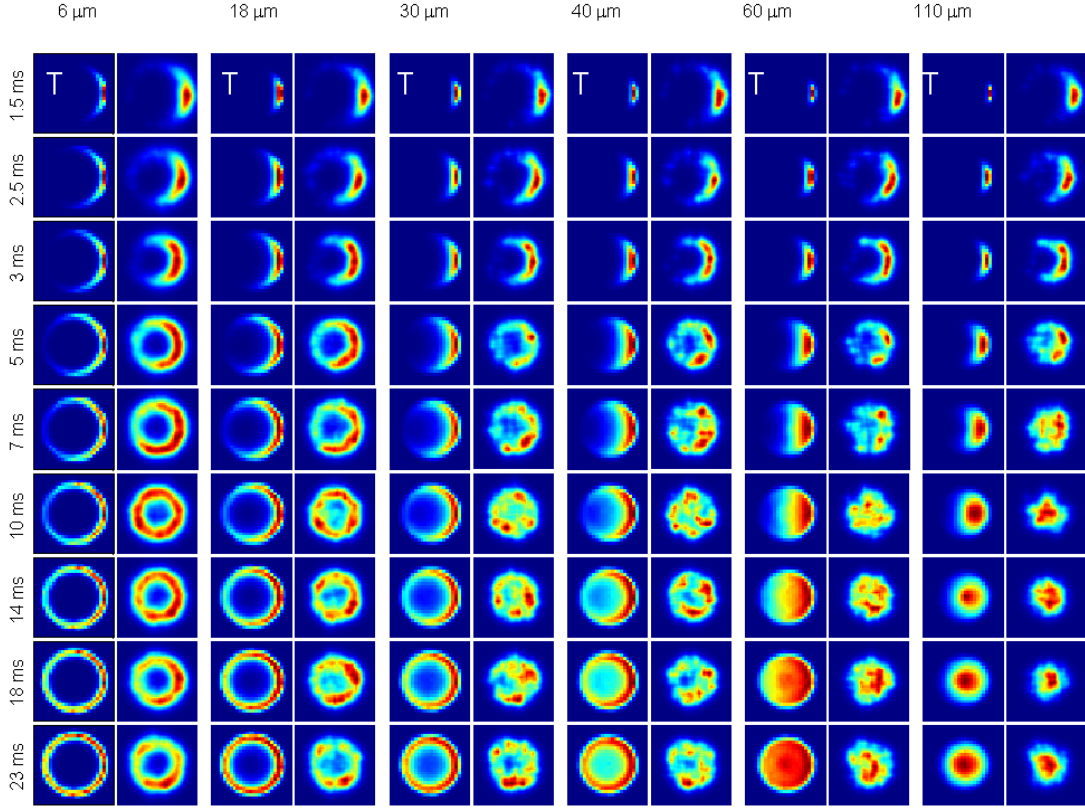


Figure 5.12.: Joint FDFs of phase and contrast for the following parameters: $T = 20 \pm 2$ nK, $n = 42 \pm 5 \mu\text{m}^{-1}$, $K = 28.6 \pm 1.8$, 144 repeats. The calculated theory FDFs are marked in the top row with a T. A detailed discussion is given in the main text.

regimes emerge, which are a direct consequence of the multimode nature of 1d Bose gases. For long integration length L , the phase randomizes and contrast strongly decays, resulting in a disk-like structure in the FDF plots. For short integration lengths a different behaviour is observed: the phase randomizes, but the contrast almost does not decay (compare Fig. 5.9), forming a ring shape in the FDF. Third, the dynamics show a two-step process. The system evolves quickly for the first 10 ms and then seems to settle into an apparent steady state.

Let's first discuss the dynamical evolution of the system into this prethermalized stationary state in the LL picture. During the dynamics, the energy of each harmonic oscillator mode k oscillates between the fluctuations in density and fluctuations in phase, driven by (s-wave scattering) interactions between the atoms. This results in a harmonic time dependence of the fluctuation strength with a period of $\pi/c_s|k|$, where c_s is the speed of sound. For short evolution times, all phase fluctuation amplitudes grow in magnitude, which leads to a scrambling of the relative phase $\hat{\phi}_s(z)$ along the longitudinal direction.

5. Prethermalization

This results in an initial rapid decrease of the interference contrast C . For longer times, the oscillations in different k modes dephase and the system reaches a quasi-steady state as seen in Fig. 5.12 and also in the mean contrast evolution in Fig. 5.9.

Moreover, these dynamics lead to two distinct length-scale-dependent regimes of relaxation, separated by a smooth crossover.

For *short* integration lengths L , the contrast $C(L)$ is influenced only by very few, sparsely populated modes with high momenta. Modes with wavelength $\lambda = 2\pi/k \gg L$ only lead to an overall phase evolution, but not to contrast reduction. The FDF evolves to a ring shape. This is the *phase diffusion regime*.

For *long* integration lengths L there are many significantly populated modes satisfying $\lambda = 2\pi/k < L$ and their dynamics leads to a randomization of the phase within the integration length, the integrated contrast decays and FDF evolves to a shrinking disk-like structure. This is the *contrast decay regime*.

The crossover length scale separating the two regimes can be calculated analytically in the framework of the TTL theory as

$$l_0 = \frac{4K_{Lutt}\xi\hbar}{\pi^2} = \frac{2\hbar^2}{mg} = \frac{\hbar}{ma_s\omega_{tr}}, \quad (5.7)$$

which gives for the data set of Fig. 5.12 at $\omega_{tr} = 2\pi \times 1400 \pm 80$ Hz a value of $l_0 = 15.8 \pm 0.9 \mu\text{m}$. Interestingly, l_0 is independent on the density of the system and scales only with the 1d interaction strength g^{-1} .

Section 5.9 will show how to independently measure the effective correlation length, separating the two regimes. In the next section the squared contrast distributions will be studied in detail and sec. 5.8 will discuss the distributions of the relative phase.

5.7. Contrast squared FDF Results

The good agreement between experiment and theory in the joint distributions can mainly be used to get a phenomenological insight into the non-equilibrium dynamics. To take a more quantitative approach, the distributions of the squared contrast are studied in this section. These squared contrast probability distributions or full distribution functions (FDFs) give the probability $P(C^2) dC^2$ of finding a value of C^2 in the interval between C^2 to $C^2 + dC^2$. Actually, these squared contrast FDFs provide information about all even, higher-order correlations in the system, through the moments $\langle C^{2m} \rangle = \int C^{2m} P(C^2) dC^2$ and thereby measure the non-equilibrium state of the system in great detail [Gring 12a].

Using $P(C^2)$ instead of $P(C)$

As discussed in [Gring 12a], the contrast distribution $P(C)$ stays always peaked, even in the uncorrelated case, whereas the shape of the squared contrast distribution $P(C^2)$ changes drastically from peaked, in the highly correlated case, to exponentially decaying, in the uncorrelated case. This is due to the fact that $P(C) \propto C \exp(-C^2)$ and therefore always stays of Gaussian shape with $P(C=0) = 0$. A constrained that can be neatly

5. Prethermalization

circumvented by plotting $P(C^2) \propto \exp(-C^2)$, which fulfils $P(C^2 = 0) \neq 0$. In this context uncorrelated refers to a correlation length λ being much smaller than integration length L . Therefore it is preferably to study the $P(C^2)$ distributions in the following.

Using the normalized squared contrast $C^2/\langle C^2 \rangle$?

The absolute value of the contrast is affected by various systematic effects. Experimental imperfections in the splitting (see sec. 5.2.2) as well as in the release process (see sec. 5.2.3) strongly affect the maximally measurable contrast. Furthermore, the finite optical resolution in combination with slight optical misalignments reduce the observable contrast. In order to discard these systematic effects, it makes sense to renormalise the squared contrast distributions by their mean $\langle C^2 \rangle$ value and then properly compare the resulting distributions to the relevant theory.

Results

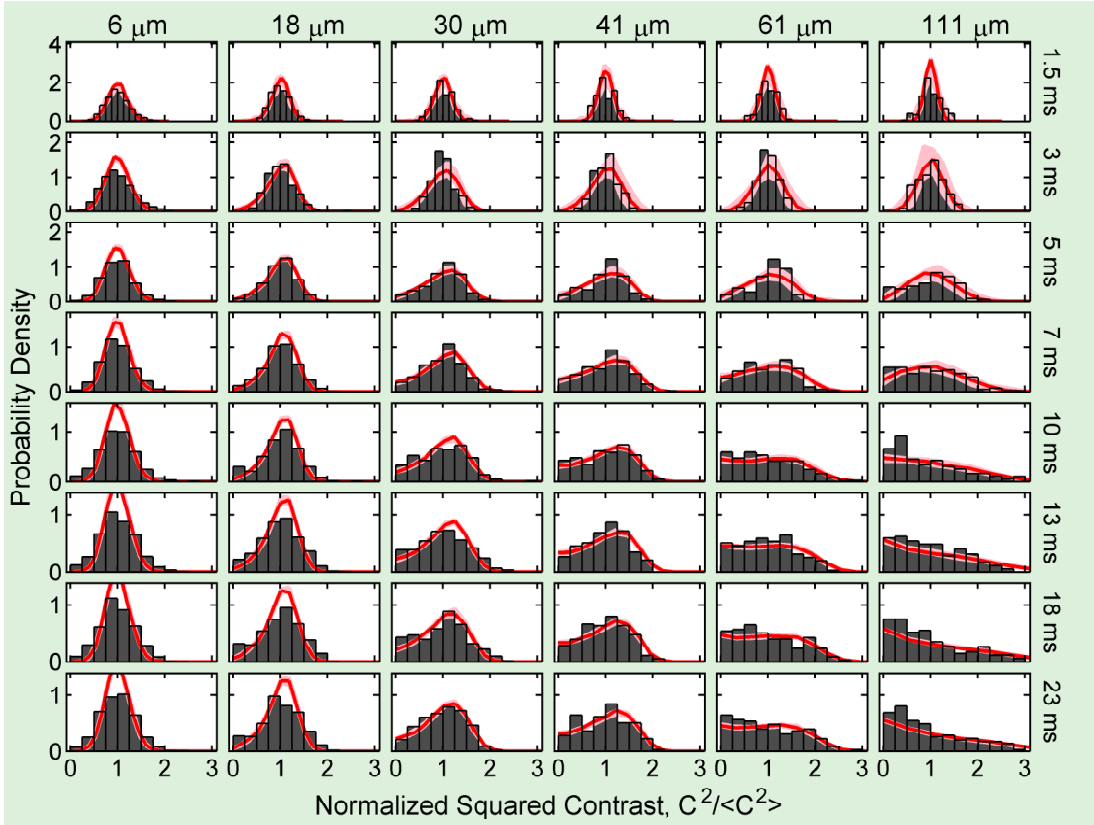


Figure 5.13.: Squared Contrast FDFs for the same data set as in Fig. 5.12, with the following parameters: $T = 20 \pm 2$ nK, $n = 42 \pm 5 \mu\text{m}^{-1}$, $K = 28.6 \pm 1.8$, 144 repeats. Experimental distributions (histograms) are compared to TLL theory (solid red lines). A detailed discussion is given in the main text.

5. Prethermalization

Fig. 5.13 compares the measured distributions with the TLL theory. The solid red line depicts the TLL prediction without any fit parameters for the independently measured input parameters mean peak density $n = 42 \pm 5 \mu\text{m}^{-1}$ and transverse trap frequency $\omega_{tr} = 2\pi \times (1400 \pm 100)$ Hz determining the coupling strength $g = 2\hbar\omega_{tr}a_s$ (secondary parameters are the initial temperature $T_{in} = 20 \pm 2$ nK and number imbalance $N_{imbal} = 1 \pm 5\%$). The red shaded area denotes the rms error bounds with respect to the uncertainties of the input parameters. The black histogram bars show the distribution of the experimental data. To achieve satisfactory statistics, 144 repeats have been accumulated at each evolution time t_e .

At early times, the probability distributions are peaked on all length scales, which verifies that a highly correlated, phase-coherent non-equilibrium state has been created by the fast splitting process.

Similar to the observations made for the joint FDFs and for the decay of the mean contrast, we find that the dynamical evolution strongly depends on the probed length-scale. During the course of the evolution the shape of the FDFs changes most strongly on long length scales from peaked, Gumbel-like to an exponential decay, which is related to the loss of phase-correlations on long length scales. Exponentially decaying FDFs is exactly what one expects if the phase correlation length is much smaller than the integration length and thus the binning over L samples over a large number of random phase domains, in essence similar to a random walk.

For short integration lengths, the contrast FDFs stay peaked at all times. Once more, a crossover can be observed at intermediate length scales.

Once again, the rapid, initial evolution is visible, which leads to the quasi-steady, prethermalized state for evolution times $t_e > 10$ ms.

The agreement between theory and experiment has improved in comparison to the results published in [Gring 12b] by taking the maximal measurable contrast of $85 \pm 3\%$ into account and by further convolving the calculated distributions with the uncertainty of the fitting (one standard deviation of fit uncertainty corresponds typically to $\pm 6\%$ at $6 \mu\text{m}$, $\pm 3\%$ at $110 \mu\text{m}$). This effectively smears out the sharp decay towards 100% contrast at early evolution times.

The remaining small discrepancy of the distributions between theory and experiment for early times is likely to be the result of an inaccurate description of the system for high-energy excitations. The Tomonaga-Luttinger theory used to obtain the distributions is valid only at low energies and for evolution times $t_e \gg \hbar/\mu \approx 1$ ms, and thus the theory is unable to capture the dynamics at short times which is dominated by high-energy excitations. In addition, the theory assumes a fast splitting process which results in large particle number fluctuations in the initial state. The experiment splits the system in a finite time and thus the initial state may differ slightly from the assumptions of the theory.

Overall, the TLL predictions fit remarkably well to the data. This leads to the conclusion that the TLL description captures the physics of the initial evolution very well and the dynamics are driven by the dephasing of harmonic k-modes.

In the TLL framework, the initial fast evolution and the prethermalized state should both be independent on the initial temperature, which is exactly what one finds when

5. Prethermalization

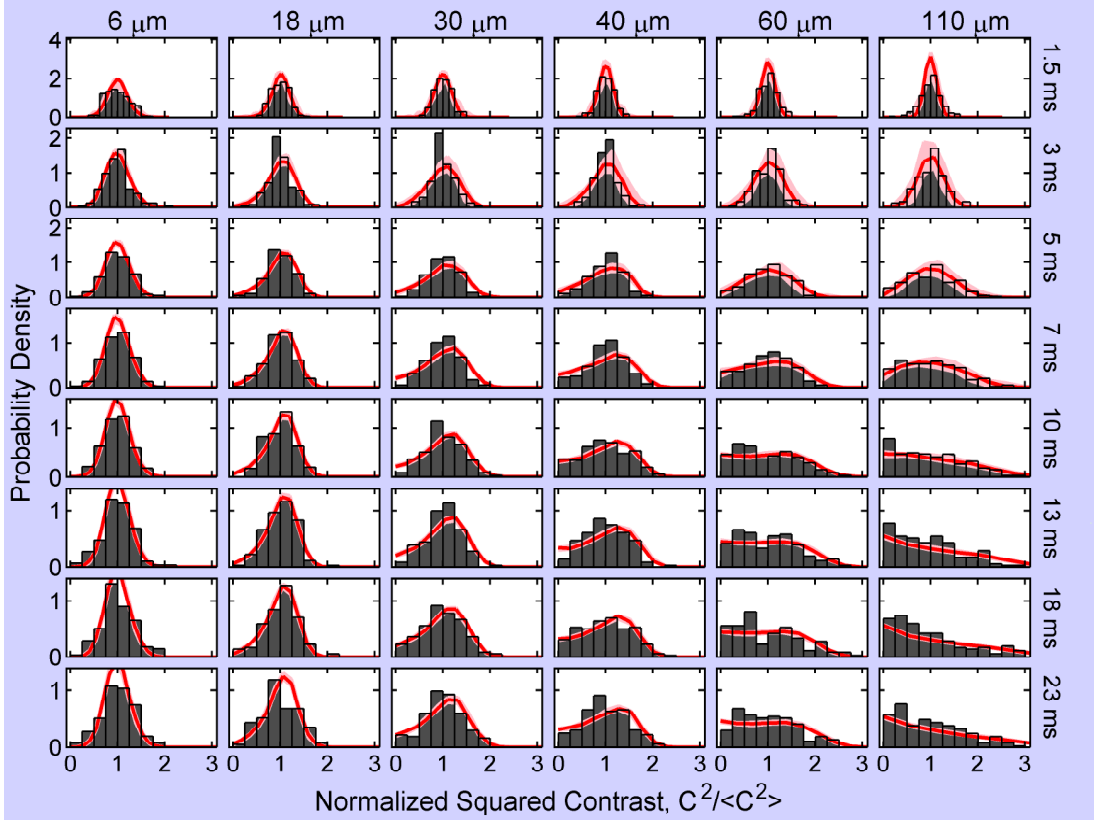


Figure 5.14.: Squared contrast FDFs for a data set at higher initial temperature, with the following parameters: $T = 103 \pm 15$ nK, $n = 45 \pm 5 \mu\text{m}^{-1}$, $K = 29.6 \pm 1.7$, 300 repeats. Experimental distributions (histograms) are compared to TLL theory (solid red lines).

comparing Fig. 5.13 taken at $T = 20 \pm 2$ nK and Fig. 5.14 for a data set of $T = 103 \pm 15$ nK. The prethermalized state is only defined by the quantum shot noise introduced by the splitting process.

After dephasing, the system is in the prethermalized state, which is a quasi-stationary state in the course of thermalization. Whether true thermal equilibrium is going to be reached at some later stage remains unclear. Fig. 5.15, shows the contrast squared FDFs for $t_e = 23$ ms to $t_e = 183$ ms, i.e. the subsequent evolution following Fig. 5.14. The TLL theory (solid red line) predicts no further time evolution, whereas the experimental data shows a further decay of correlation, or in other words a further loss of information, which is clearly an effect beyond the TLL description. This means that either higher-order anharmonic terms, omitted by the TLL Hamiltonian of eq. 2.56, become relevant that may lead to a coupling between relative and common degrees of freedom on the long time evolution, or that the “near” integrability of the experimental system is broken far enough such that 3d thermalization processes might come into effect. Both processes would lead

5. Prethermalization

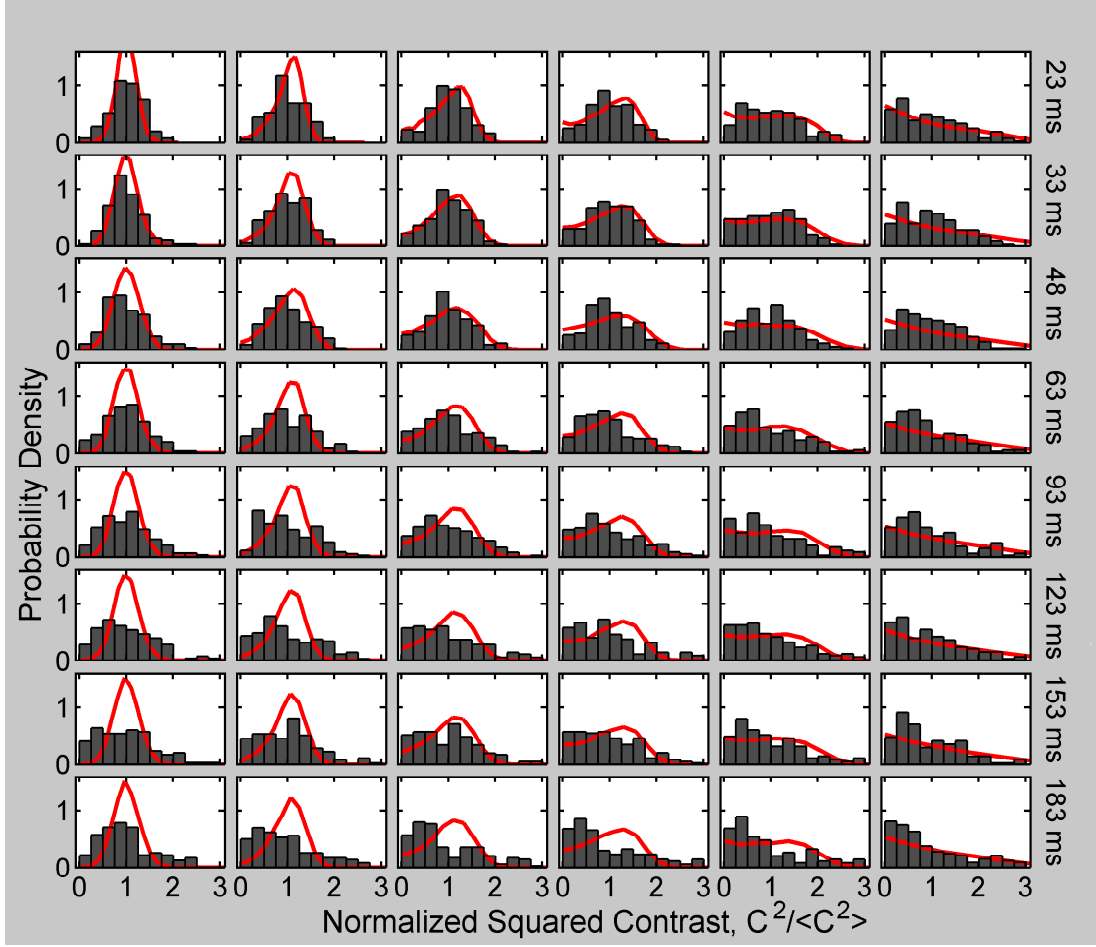


Figure 5.15.: Squared Contrast FDFs for the same data set as in Fig. 5.14, with the following parameters: $T = 103 \pm 15$ nK, $n = 45 \pm 5 \mu\text{m}^{-1}$, $K = 29.6 \pm 1.7$, 300 repeats. Experimental distributions (histograms) are compared to TLL theory (solid red lines). A detailed discussion is given in the main text.

to a second much longer time scale for the relaxation towards thermal equilibrium. This topic will be treated in chapter 6.

The issue of observing possible revivals of the phase coherence in the experiment is an ongoing topic will be treated elsewhere [Langen 13a].

In conclusion, the TLL theory is able to explain the early evolution up to $t_e \sim 30$ ms, which consists of an initial rapid dephasing process that leads to the emergence of a prethermalized, temperature-independent state. For higher evolution times, the experimental data shows a further loss of correlations on a much longer time scale, which is not covered by the TLL theory.

5.7.1. Measuring the Temperature of the Relative Degrees of Freedom

As we have seen in sec. 5.3, the prethermalized state is expected have thermal-like correlation functions. Therefore, in the spirit of sec. 4.4.5, equilibrium $P(C^2)$ can be fitted to the experimentally measured squared contrast FDFs, to probe the emergence of thermal like distributions and obtain the effective temperature T_{pre} of the prethermalized state. Finally, the predicted scaling of T_{pre} (eq. 5.3) is to be verified.

The effective temperature at each evolution time t_e is determined by fitting the calculated equilibrium distributions to the experimental distributions with the temperature being the only free fit parameter. As a figure of merit, the χ^2 value is used [Huang 87, Hughes 10]

$$\chi^2 = \sum_i \frac{(O_i - E_i)^2}{E_i}, \quad (5.8)$$

where O_i are the observed counts and E_i are the expected counts of the $P(C^2)$ distribution.

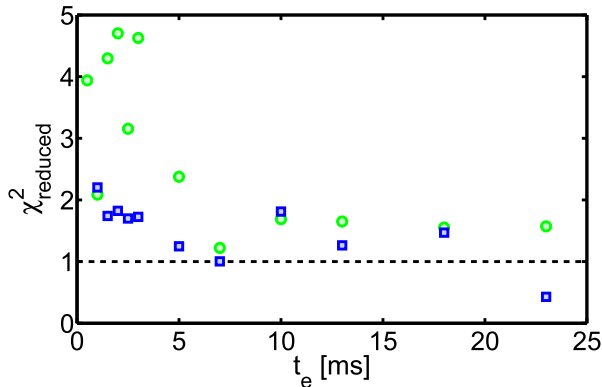


Figure 5.16.: Reduced- χ^2 comparison between non-equilibrium TLL theory (blue squares) and thermal equilibrium OU theory (green circles) to the measured data of Fig. 5.13. For early evolution times, the equilibrium theory shows worse agreement than the TLL distributions.

Fig. 5.16, compares the results of the reduced χ^2 test for the non-equilibrium TLL theory (blue squares) and equilibrium OU theory (green circles) with respect to the experimentally obtained distributions of Fig. 5.13. The reduced χ_r^2 is given by $\chi_r^2 = \chi^2/n$, with n being the number of degrees of freedom, defined by the number of observations N and the number of fit parameters as $n = N - N_{fit} - 1$. A reduced χ_r^2 value close to one means that the null hypothesis cannot be rejected [Hughes 10]. For $\chi_r^2 \gg 1$ the observed agreement between experiment and theory is not statistically relevant. For early evolution times $t_e < 10$ ms, we find that the observed distributions are non-thermal and the TLL predictions explain the data much better. In the prethermalized state, for $t_e > 10$ ms both non-equilibrium and equilibrium theory show similar χ_r^2 values close

5. Prethermalization

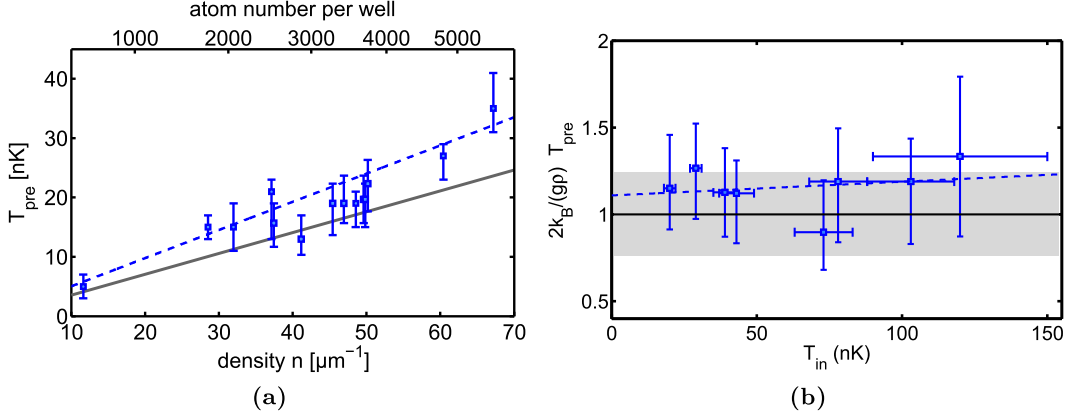


Figure 5.17.: Scaling of the prethermalized Temperature T_{pre} versus peak density n (a) and initial temperature T_{in} (b). The black solid lines correspond to the TLL predictions, which are in good agreement with the obtained data (blue squares) over a wide parameter range, despite a small offset (see text) from the linear fit (dashed blue line).

to one, demonstrating that the prethermalized state has indeed thermal-like properties and that it makes sense to assign an effective temperature T_{pre} to the relative degrees of freedom.

5.7.2. Results

Additional data sets at varying peak densities in the range of $n = 10 - 70 \mu\text{m}^{-1}$ have been acquired, to probe the linear scaling of T_{pre} with density n as given by eq. 5.3. Fig. 5.17a shows a collection of these measurements, which are in good agreement with theory.

Furthermore, in order to verify that T_{pre} is indeed independent on the initial temperature T_{in} , many data sets have been acquired, spanning a wide range of temperatures in the thermal quasi-condensate regime $T_{in} = 20 - 120$ nK. The results, shown in Fig. 5.17b, confirm that T_{pre} is indeed constant. To correct for small variations in peak densities n from scan to scan, the measured T_{pre} is renormalized by the prefactor $\frac{2k_B}{ng}$.

In both graphs, the $\sim 20\%$ offset to higher temperatures is probably due to the effects of the finite splitting time. The theoretic description presented in [Kitagawa 11] assumes an infinitely fast splitting process, so that the coupling vanishes simultaneously for all k modes, independent on their energy. Due to the quantum noise of the splitting process, each k -mode receives the same amount of energy given by $E_{split} = \frac{\hbar c \pi \rho}{4K}$, independent of k and the population of modes scales as $1/k^2$. If the splitting is not fast enough, the initial mode population will deviate from $1/k^2$, which, eventually, will produce a squeezed initial state resulting in the observed offset of T_{pre} .

In conclusion, the contrast distributions are a neat tool to analyze the non-equilibrium dynamics.

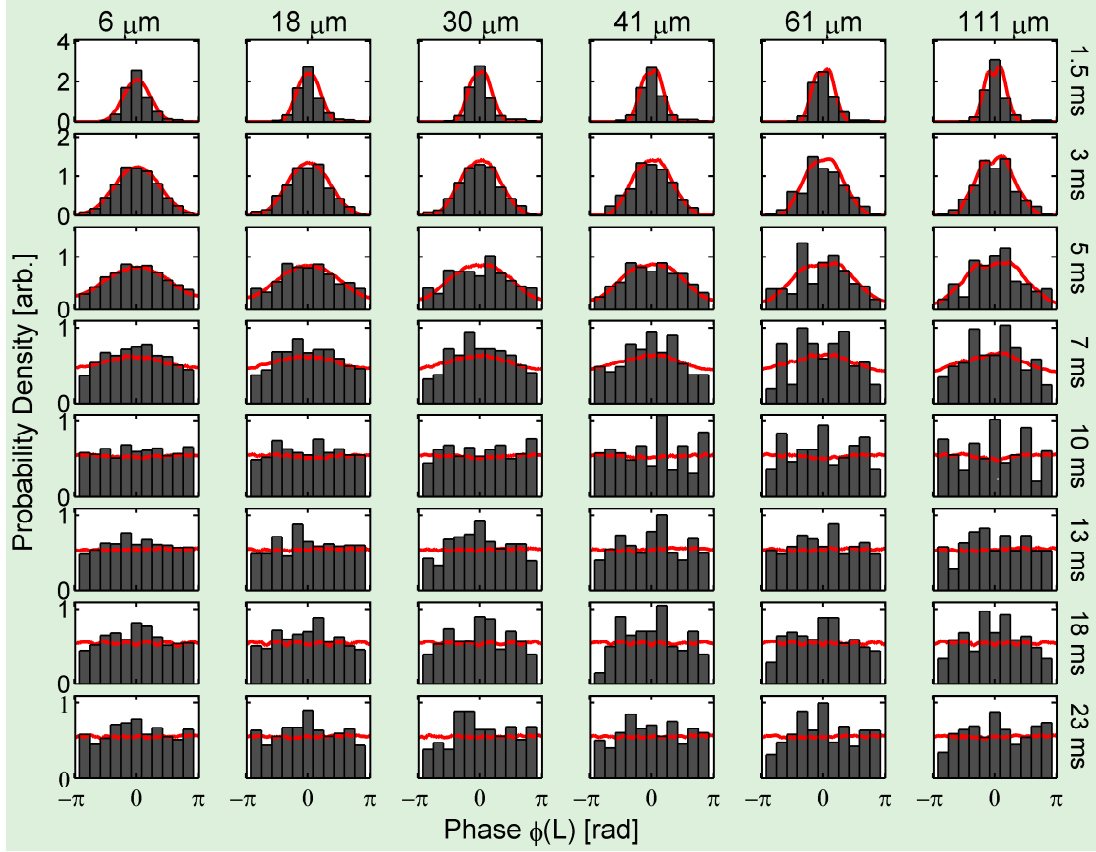


Figure 5.18.: Phase FDFs for the same data set as in Fig. 5.13 and Fig. 5.12. Experimental distributions (histograms) are compared to TLL theory (solid red lines). The initial distributions are peaked on all length scales as expected for a phase-coherent splitting process with an initial width defined by the quantum shot noise. Once the prethermalized state is reached at $t_e \geq 10$ ms the phase is uniformly distributed.

5.8. Relative Phase FDF Results

Fig. 5.18, shows the probability distributions of the relative phase $\phi(L)$ for the same data set as Fig. 5.13 and Fig. 5.12. For short evolution times the distributions are peaked on all length scales, which verifies that the splitting process is indeed phase-coherent. The initial width is given by the quantum shot noise of the splitting process and as it turns out, mainly by technical noise sources. The shot noise generates a Poissonian number balance distribution between the wells which needs to be convolved with the additional normally-distributed imbalance due to technical fluctuations from shot to shot. The initial number balance distributions are measured following the procedure explained in sec. 5.2.3. The further evolution of the phase distributions is governed by the TLL physics, where due to the effects of the initial imbalance noise, the width of the phase distribution increases almost independently from the probed length scale, diametrically

5. Prethermalization

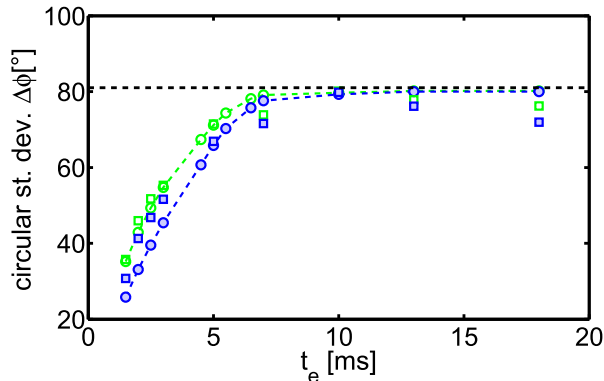


Figure 5.19.: Phase spread versus time for $L = 6 \mu\text{m}$ (green, open squares) and $L = 110 \mu\text{m}$ (blue, filled squares) the data of Fig. 5.13. The respective circles connected via the dashed line correspond to the TLL calculation. The black dashed line corresponds to the limit of a random phase distribution. shot noise generates a Poissonian number balance distribution between the wells which needs to be convolved with the additional normally-distributed imbalance due to technical fluctuations from shot to shot. The initial distribution of number balance is measured, following the procedure explained at the beginning of this section, to be $\Delta N/N = 1 \pm 5\%$. The further evolution of the phase distributions is governed by the TLL physics.

opposite to the evolution of the squared contrast FDFs of Fig. 5.13. Therefore, the two regimes of relaxation are not observable with the information of the phase FDFs alone. The relative phases are randomly distributed, once the prethermalized state is reached ($t_e \approx 10$ ms).

Fig. 5.19, compares the measured phase spread at $6 \mu\text{m}$ (green, filled squares) and at $L = 110 \mu\text{m}$ (blue, filled squares) with the TLL results (respective circles) at increasing evolution times. The phase spread is calculated as one circular standard deviation, which is defined in [Fisher 95] as

$$\Delta\phi = \sqrt{2(1 - R)}, \quad (5.9)$$

where R is the length of the mean vector of a set of N phases φ_j and thus given by $R = \frac{1}{N} \sum_{j=1}^N e^{i(\varphi_j - \bar{\varphi})}$, with $\bar{\varphi} = \arg\left(\sum_{j=1}^N e^{i\varphi_j}\right)$. The circular standard deviation lies between $[0, \sqrt{2}]$ rad = $[0, 81.03]^\circ$. Once again, convincing agreement is found when including the measured number balance of $\Delta N/N = 1 \pm 5\%$. Both plotted length scales show very similar behaviour and become close to a uniform distribution, at times earlier than $t_e = 10$ ms.

In conclusion, the phase is not a good observable to study the multimode nature of the system. This is mainly due to the effects of technical noise in the splitting process, that eventually lead to a significant broadening of the phase distributions that scramble the multimode physics. On the other hand, the contrast is a much more robust observable

than the phase, as it is not affected by the technical imbalance noise of the splitting process.

5.9. Contrast Decay versus Integration Length

So far, we have probed the system via the measurement of contrast and phase statistics and compared the results to the TLL theory. In this way, we basically probed the correlation properties of the dynamics or in other words the loss of memory of the initial state. One drawback of the TLL calculations is their intrinsic dependence on many parameters, especially on the density of the system. To get an independent measurement on the resulting prethermalized state compared to the TLL results it would be advantageous to probe the crossover length scale l_0 , which is a characteristic property of the prethermalized state, that does not depend on density as seen in eq. 5.7. As we have seen in sec. 4.4.4 and eq. 4.35, the thermal phase correlation length becomes experimentally measurable by studying the contrast decay $\langle C^2(L) \rangle$ versus the integration length L . According to the properties of the prethermalized state, this $\langle C^2(L) \rangle$ decay should be independent on the initial temperature T_{init} and be thermal-like in form with an effective correlation length λ_{eff} being equal to the crossover length l_0 .

The equivalence of the crossover length-scale l_0 and the effective thermal correlation length λ_{eff} of the relative phase field in the prethermalized state can be understood in the following way. In the case of two uncoupled quasi-condensates at thermal equilibrium (temperature T), the thermal phase correlation length λ_ϕ is given by eq. 4.21. Because of the rapid splitting process, the energy initially stored in the system is equally distributed between the different modes [Kitagawa 11]. This equipartition of energy results in thermal-like correlations of the prethermalized state, characterized by the effective temperature $k_B T_{eff} = \langle \hat{H}|_{t=0} \rangle = \rho g/2$. with the 1d coupling constant g (eq. 2.17). The effective thermal correlation length can thus be identified with $\lambda_{eff} = \hbar^2 \rho / m k_B T_{eff} = 2\hbar^2 / mg$, and is equivalent to the crossover length scale l_0 .

In conclusion, by measuring $\langle C^2(L) \rangle$, an independent estimation of the prethermal correlation length l_0 is obtained, without the need of using any input parameters like the density n or the coupling strength g . Thereby the $\langle C^2(L) \rangle$ decay is a completely independent measurement, which can be used to verify the non-equilibrium nature of the prethermalized state.

5.9.1. Taking Finite Imaging Resolution into Account

As discussed in sec. 5.3, the prethermalized state has thermal like properties and correlations. In particular, the relative phase correlation function $PCF(z, z') \equiv \langle \exp(i\hat{\phi}(z_1) - i\hat{\phi}(z_2)) \rangle$ as defined in eq. 2.35 is given by a thermal-like exponentially decaying form $PCF(\bar{z}) \propto \exp(-\bar{z}/l_0)$, similar to eq. 4.20, with the characteristic length scale being equal to the crossover length scale l_0 , as shown in [Kitagawa 11]. In this context l_0 separates the phase diffusion and contrast decay regime and thereby governs the dynamical evolution to and the properties of the prethermalized state.

5. Prethermalization

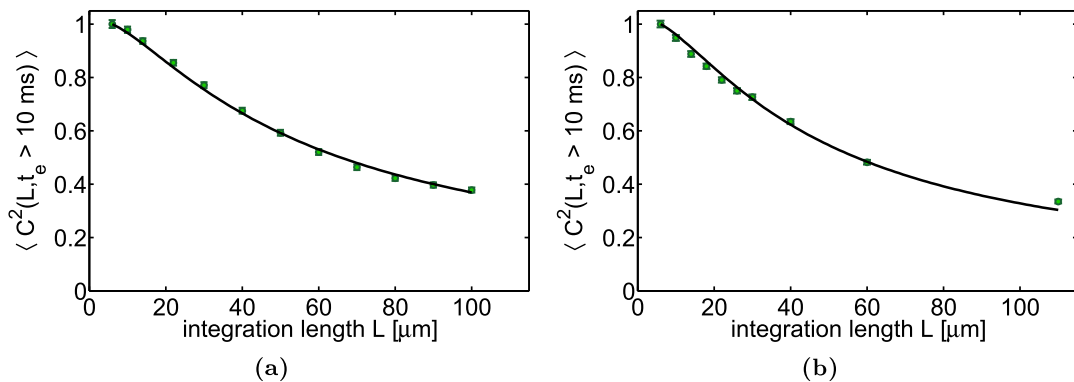


Figure 5.20.: $C(L)$ decay versus integration length scale in the prethermalized state ($t_e > 10$ ms). Green circles correspond to the measured data, whereas the solid black line is a fit using eq. 5.12. The measured data has been normalized to the value at $C^2(L = 6 \mu\text{m})$. (a) The resulting fitted correlation lengths are $\lambda_{eff}^{fit} = 15.7 \pm 0.9 \mu\text{m}$ at an initial temperature of $T_{init} = 20 \pm 2$ nK (a) and $\lambda_{eff}^{fit} = 15.4 \pm 0.8 \mu\text{m}$ at initial temperature of $T_{init} = 103 \pm 15$ nK (b). This is in stark contrast to the expected phase correlation length for the thermal equilibrium case. In thermal equilibrium, phase correlation lengths of $\approx 11 \mu\text{m}$ (a) and $\approx 2 \mu\text{m}$ (b) would be instead expected.

Similar to eq. 4.35, we find for the mean integrated squared contrast

$$\langle C^2(L) \rangle \equiv \frac{1}{L^2} \int_L \int_L dz dz' PCF(z, z') = 2R \left[\frac{l_0}{L} - \left(\frac{l_0}{L} \right)^2 \left(1 - \exp\left(-\frac{L}{l_0}\right) \right) \right] \quad (5.10)$$

where $R = e^{-k_c/4\pi\rho}$ is a reduction of the interference contrast due to the contributions of high energy excitations (of wavelength smaller than the healing length $\xi = 2\pi/k_c$ [Kitagawa 11]). For typical experimental parameters one finds $R = e^{-1/4K} \approx 1$. Thus the effective phase correlation length λ_ϕ , given by eq. 4.21, is equal to the crossover length scale l_0 and we simplify to $l_0 = \lambda_\phi = \lambda$. However, eq. 5.10 does not include the finite resolution of the imaging system and, therefore, does not represent the measured data.

To include the finite imaging resolution, the PCF has to be convolved with the correlation function of the imaging PSF, which results in

$$\widetilde{PCF}(z) = \frac{1}{2\sqrt{2\pi}} e^{\frac{\sigma^2}{\lambda^2} - \frac{z}{\lambda}} \left(\text{erf}\left(\frac{z}{2\sigma} - \frac{\sigma}{\lambda}\right) + e^{\frac{2z}{\lambda}} \text{erfc}\left(\frac{z}{2\sigma} + \frac{\sigma}{\lambda}\right) + 1 \right), \quad (5.11)$$

where erf and erfc denote the error function and the complementary error function, respectively and σ is the rms width of the PSF. Finally, the length-scale dependence of the measured integrated squared contrast $C^2(L)$ evaluates to

5. Prethermalization

$$C^2(L) = \frac{\lambda^2}{\sqrt{8\pi}L^2} e^{\frac{\sigma^2}{\lambda^2}} \left[4 \operatorname{erf}\left(\frac{\sigma}{\lambda}\right) + 2e^{-\frac{L}{\lambda}} \left(\operatorname{erf}\left(\frac{L}{2\sigma} - \frac{\sigma}{\lambda}\right) + 1 \right) - 2e^{\frac{L}{\lambda}} \left(\operatorname{erf}\left(\frac{\sigma}{\lambda} + \frac{L}{2\sigma}\right) - 1 \right) + \frac{4L}{\lambda} e^{-\frac{\sigma^2}{\lambda^2}} \operatorname{erf}\left(\frac{L}{2\sigma}\right) + \frac{8\sigma}{\lambda\sqrt{\pi}} e^{-\frac{\sigma^2}{\lambda^2}} \left(e^{-\frac{L^2}{4\sigma^2}} - 1 \right) - 4 \right]. \quad (5.12)$$

Given the object space pixel size of the vertical imaging system ($2\ \mu\text{m}$) and the rms PSF width of $3.8\ \mu\text{m}$, the minimum integration length which can be probed via the vertical imaging system (see sec. 3.1.5) is conservatively estimated as $L = 6\ \mu\text{m}$. To account for the contrast reduction resulting from the contributions of the excitations within this integration length, the experimental data as well as the theory are normalized by the value of $C^2(L = 6\ \mu\text{m})$. Finally, the correlation length is obtained by fitting the experimental data to eq. 5.12 with λ being the single free parameter. Fig. 5.20a shows a fit to the data set at $T = 20 \pm 2\ \text{nK}$, resulting in an effective correlation length of $l_0 = \lambda_{eff} = 15.7 \pm 0.9\ \mu\text{m}$ and Fig. 5.20b shows a fit to the data set at $T = 103 \pm 15\ \text{nK}$ yielding $l_0 = \lambda_{eff} = 15.4 \pm 0.8\ \mu\text{m}$. Both fit results are in good agreement with the calculated value of $l_0 = 15.8 \pm 0.9\ \mu\text{m}$, which is temperature independent.

5.9.2. Comparison of Thermal and Prethermal Correlation Lengths

Fig. 5.21 shows a comparison of prethermal $\lambda_{pre} = 2\hbar^2/mg$ and thermal phase correlation lengths $\lambda_\phi = \hbar^2 n/mk_B T$. As we have seen in section 5.6, while the prethermalized system reveals thermal-like correlations, its correlation length depends only on the 1d coupling constant g . This is in stark contrast to a system of two quasi-condensates at thermal equilibrium, where λ_ϕ is a function of density and temperature as given by eq. 4.21. To reveal this difference experimentally, the initial temperature T_{init} of the quasi-condensate before splitting is varied and the resulting correlation length is measured by fitting eq. 5.12. The temperature before splitting, T_{init} , is obtained through density ripples measurements. The results (blue squares) confirm the independence of the prethermalized state on the initial temperature T_{init} , having a constant effective correlation length λ_{eff} , which is equal to the crossover length scale l_0 , as observed in sec. 5.6. The equilibrium data (green circles and cyan triangles) shows the expected temperature scaling of λ_ϕ as given by eq. 4.21, where the mean density $\bar{n} = \langle n_{scans} \rangle$ of all data sets was used. To account for slight variations of the density, the equilibrium data points have been rescaled to this mean density \bar{n} . The green data was obtained similar to the prethermalized data, by fitting eq. 5.12. The cyan data was extracted from density ripples measurements of the prethermalized state, which measure the temperature of both the relative and common degrees of freedom simultaneously. The resulting temperature should be given by $T = (T_{rel} + T_{com})/2$. The correlation length is then derived from the measured temperature and density. Accessing solely the common degrees of freedom is not possible in the current experimental setup as one would need to measure the second order correlation function g_2 of each gas independently. The density ripples data scales

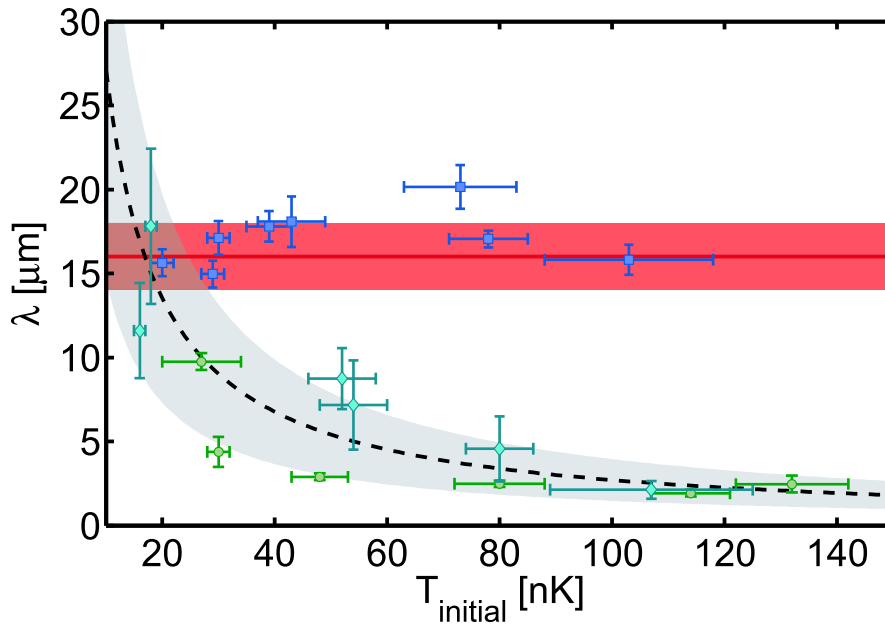


Figure 5.21.: Comparison of prethermal and thermal phase correlation lengths. The blue squares (prethermalized state) and green circles (thermal equilibrium state) have been obtained using the fit function given in eq. 5.12. The cyan diamonds have been derived from temperature measurements (via the density ripples method) of additional non-equilibrium data sets, where the corresponding fringe patterns were not recorded. Both cyan and green data are in agreement with the thermal phase correlation length $\lambda_\phi \propto 1/T$ of eq. 4.21 (black dashed line). In contrast, the prethermalized data shows no temperature dependence within the errorbars and is in good agreement with the calculated crossover length scale $l_0 = 15.8 \pm 0.9 \mu\text{m}$ (red solid line). The shaded areas depict two standard deviations of the calculated values. Errorbars denote one standard deviation.

according to λ_ϕ , with the tendency of slightly higher correlation lengths than expected, which fits to the described intuitive picture above. These results support the view that while the relative degrees of freedom are merely populated by the quantum shot noise of the splitting process, the common degrees of freedom store the thermal energy given by T_{init} . To reach full thermal equilibrium, a coupling between common and relative DOF is needed that leads to a transfers of thermal energy into the relative modes. This will be the topic of the next chapter.

5.10. Summary

In conclusion, this chapter presented a detailed survey of the non-equilibrium dynamics that follow a rapid quantum quench of a nearly integrable, 1d system of weakly inter-

5. Prethermalization

acting Bosons. The resulting dynamics were probed through the quantum probability distributions (full distribution functions) of the relative phase and contrast of matter-wave interference patterns. The distributions of the relative phase turn out to be governed by technical noise in the splitting process, that eventually leads to a significant broadening of the phase distributions. Therefore they are not ideally suited to study the multimode nature of the system. On the other hand, the contrast is a much more robust observable than the phase, as it is much less affected by the technical imbalance noise of the splitting process. The distributions of the squared contrast were used to probe the resulting dynamics and further to determine the nature of the emerging quasi-steady state.

The observations fiercely support the theoretical description via a Luttinger Liquid formalism and the interpretation that the rapid initial loss of coherence does not lead to a thermal equilibrium state, as was initially believed in [Hofferberth 07], but that the system instead dephases to a prethermalized state, determined by the splitting process and not by the initial temperature T_{in} .

The properties of this prethermalized state were studied in great detail. Being defined by the quantum noise of the fast splitting process, the prethermalized state shows thermal like mode population scaling and thermal-like correlation functions in the relative degrees of freedom, which makes it possible to assign an effective temperature T_{pre} . This temperature is completely independent on the initial temperature of the unsplit system. T_{pre} is rather defined by the energy introduced by the fast splitting process as $k_B T_{pre} = E_{split} = \frac{mc_s^2}{2} = \frac{gn}{2}$. Therefore the memory of the initial non-equilibrium state remains partially conserved, characterized by still observing two unequal temperatures in the relative and common degrees of freedom $T_{rel} \neq T_{com}$. The equilibration of these two degrees of freedom on a second, much longer time scale will be the topic of chapter 6.

Moreover, the multimode-nature of the observed dynamics leads to two distinct, length-scale-dependent regimes of relaxation, which are separated by a smooth crossover. The *phase diffusion regime* and the *contrast decay regime*. The critical length scale l_0 separating these two regimes has been identified as the prethermal correlation length $\lambda_{pre} = l_o = \frac{2\hbar^2}{mg}$, which actually determines the early time dynamics and only depends on the 1d coupling strength g of the Lieb-Liniger Hamiltonian.

Finally, an independent estimation of the prethermal correlation length l_0 was obtained, by measuring the $\langle C^2(L) \rangle$ decay, thereby verifying the non-equilibrium nature of the prethermalized state in contrast to measurements performed at thermal equilibrium conditions, without applying the quantum quench.

6

Chapter 6.

Going beyond Prethermalization: Is there Thermalization in the long time evolution?

With the first link, the chain is forged. The first speech censored, the first thought forbidden, the first freedom denied, chains us all irrevocably.

- Judge Aaron Satie

Abstract

The chapter starts with an in depth study of the heating and atom loss rate in the experimental setup, confirming that external heating mechanisms can practically be neglected on the experimentally probed time scales, thus allowing to study the long-time evolution of the non-equilibrium system. This long-time evolution shows signs of a further second relaxation process, happening after the establishment of the prethermalized state. This further loss of correlations happens on a second much slower time scale than the dephasing to the prethermalized state and might be attributed to relaxation towards the true thermal equilibrium state, characterized by a complete loss of information of the initial conditions. Once more, the contrast squared FDFs are used to determine the effective temperature of the relative degrees of freedom. The corresponding time evolution of the effective temperature is compared to a thermalization model based on two-body scattering involving transversally excited states. The model shows qualitative agreement, but slightly underestimates the observed relaxation rates.

6. Going beyond Prethermalization: Is there Thermalization in the long time evolution?

6.1. Heating and Loss Processes

Ultracold gases trapped in optical or magnetic traps have shown a remarkable good isolation from the environment [Kinoshita 06, Gring 12b, Smith 12]. These ultracold experiments allow the study of essentially closed quantum systems, where almost no information is leaking into the external world. In this context, environment is a very broad concept, essentially referring to the whole universe with the ultracold sample being the only exception. Transfer of information of a quantum state to the environment may lead to the collapse to an eigenstate [Bohr 28, Faye 08, Zurek 09].

In the long time evolution, when extending the evolution times beyond several tens of milliseconds, coupling to the environment may become relevant. Coupling to the noisy environment may induce unwanted heating [Kinoshita 06] and decoherence of the ultracold sample. Technical noise and inherent physical processes result in atom loss. Eventually, heating and atom loss limit the experimentally accessible time scales. In the following, we want to study the processes that lead to heating and atom loss in atom chip traps and find out which are the most dominant ones.

6.1.1. Heating

At first, let's look at possible sources of heating an ultracold sample trapped in a magnetic potential. A small coupling to the environment (which is usually at room temperature) may lead to energy transfer to the ultracold sample.

A simple model

In a simple 1d-harmonic oscillator model, this energy transfer leads to transitions between ground and excited vibrational states. These excitations are a result of fluctuations of the trap minimum or of the trap frequency. Changes in the position Δx of the trap minimum lead to a force $F = m\omega^2\Delta x$, exciting the first excited state at a transition rate $\Gamma_{0\rightarrow 1} \propto \omega^3 S_x(\omega)$ [Gehm 98], where $S_x(\omega) = 2 \int_{-\infty}^{\infty} d\tau \exp(i\omega\tau) \langle x(t+\tau)x(t) \rangle$ is the fluctuation spectrum of the trap minimum and ω is the trap frequency. Fluctuations in the trap frequency $\Delta\omega$ exert a force $F = m\omega\Delta\omega x^2$ and lead to excitations of the second excited state at a transition rate $\Gamma_{0\rightarrow 2} \propto \omega^2 S_\omega(2\omega)$ [Gehm 98] proportional to the frequency noise spectrum $S_\omega(2\omega)$, where parametric heating is strongest at the second harmonic component of the noise spectrum [Pain 78]. These stochastic fluctuations are mainly caused by either technical noise or thermally induced noise, which are discussed in the following.

Noise sources inducing heating

Technical noise is generated by uncorrelated fluctuations in the currents of the trapping wires, the bias and compensation coils. This noise randomly shifts the position of the trap minimum and alters the trap frequency, thereby heating the ultracold sample [Manz 11]. The effects of technical noise can be reduced by correlating the current fluctuations in the

6. Going beyond Prethermalization: Is there Thermalization in the long time evolution?

different devices [Folman 02] and by decreasing the noise amplitudes (usage of low-noise power-supplies, current feedback loops, etc.).

Thermally induced Johnson current noise cannot be simply decreased by cooling the conducting metal as discussed in sec. 3.1.2. It has rather to be regarded as a material property, which can be improved by a proper selection of the current carrying metals or alloys [Dikovskiy 05], or by applying superconducting currents for example.

Other noise sources include current shot noise [Schottky 18, Blanter 00] and light induced heating [Folman 02]. For light induced heating, the probability of momentum transfer Δk is given by the Debye-Waller factor $P_{0 \rightarrow 0} \propto \exp(-\Delta k^2 a_0^2) \approx \exp(-\eta^2)$, with the Lamb-Dicke parameter $\eta = \frac{2\pi}{\lambda} a_0$ being the ratio of the ground-state size a_0 of the trap and the photon wavelength λ , assuming $\Delta k \approx k$. To reduce light induced heating, the vacuum chamber needs to be properly protected from stray light sources by using blackout materials and mechanical optical shutters.

Last but not least, all above near field effects from current carrying wires have been shown to be orders of magnitudes larger compared to magnetic black-body radiation [Henkel 99].

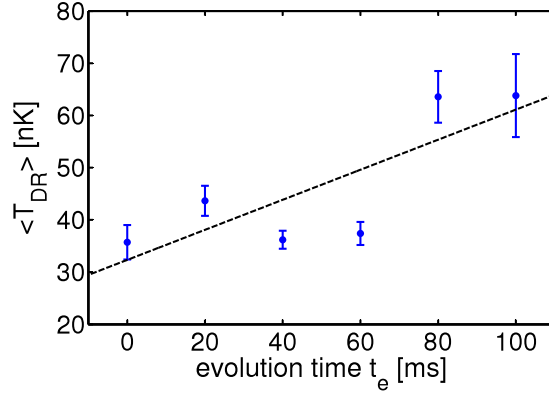


Figure 6.1.: Estimating heating rates in undressed traps. Density Ripples temperature versus evolution time t_e . A linear fit gives a heating rate of ~ 300 nK/s in the undressed trap.

Measured Heating Rates

To decrease the technical noise level the chip current drivers are connected to free floating batteries, which help to drastically decrease 50 Hz contributions. Other groups use commercially available low-noise current supplies¹ and report satisfactory results [Hessmo 13]. Fortunately, applying rf-dressing to the trap acts as a stabilising mechanism to the Ioffe field, which is then defined by the Rabi coupling Ω of the dressed potential $V = m_F g_F \mu_B \sqrt{\Delta^2 + \Omega^2}$ at positions of zero detuning Δ . Therefore, when measuring the

¹Keithley Programmable DC Power Supply 2200-32-3

6. Going beyond Prethermalization: Is there Thermalization in the long time evolution?

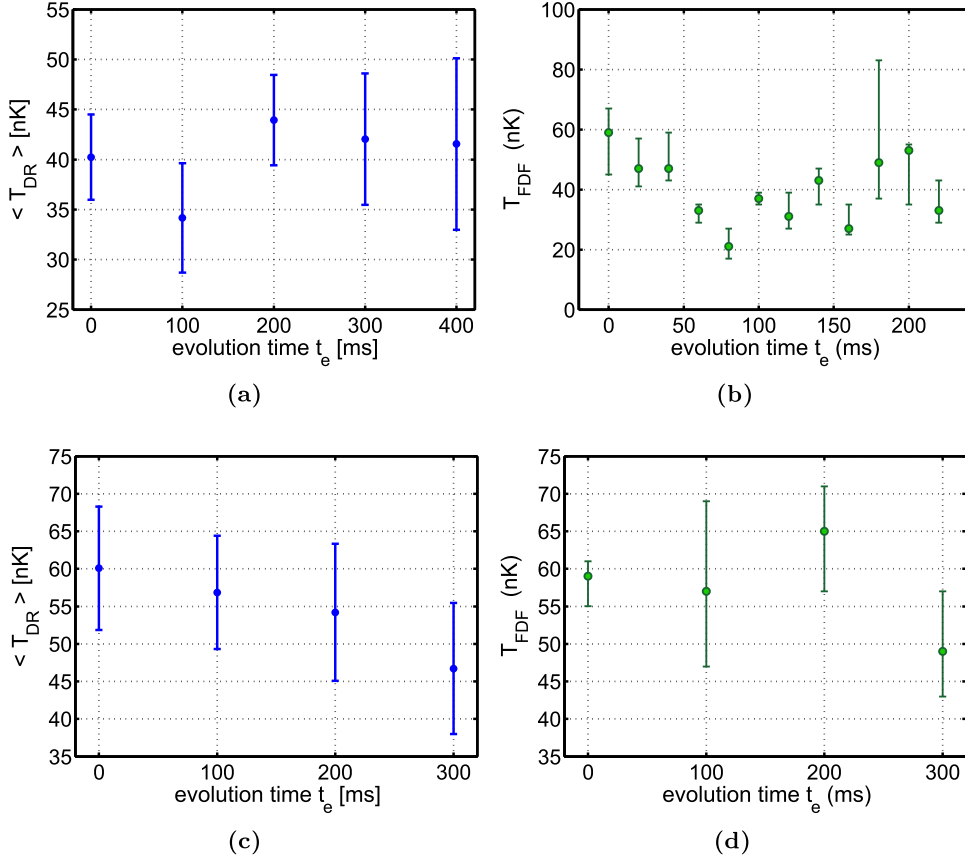


Figure 6.2.: Estimating heating rates in equilibrium system in the dressed trap.

- (a) Temperature measured via density ripples method starting at $T_{DR, initial} = 40 \pm 4$ nK and $N_{initial} \approx 6000$ atoms. Within the errorbars there is no heating observable.
- (b) Temperature inferred from Contrast squared FDFs for another data set with the initial parameters $T_{DR, initial} = 27 \pm 7$ nK and $N_{initial} \approx 4200$ atoms. Again, within the errorbars there is no heating observable.
- (c) Temperature measured via density ripples method for another data set with the initial parameters $T_{DR, initial} = 60 \pm 8$ nK and $N_{initial} \approx 5300$ atoms.
- (d) Temperature inferred from Contrast squared FDFs of same data set as in (c). Within the errorbars both methods give comparable temperatures.

temperature in the equilibrium trap, no heating could be observed over several hundreds of ms, whereas density ripple measurements in the pure (undressed) magnetic trap (Fig. 6.1) show a heating rate on the order of ~ 300 nK/s².

Fig. 6.2 shows measurements of the equilibrium double-well system versus time, trying to measure possible heating rates, introduced by technical noise or by atom loss. The

²as measured by 20120810

6. Going beyond Prethermalization: Is there Thermalization in the long time evolution?

equilibrium system is prepared by first splitting a thermal atom cloud. In a second step the two thermal clouds are cooled further into the quasi-condensate regime. After finishing the cooling procedure, the completely independent and uncoupled quasi-condensates are kept trapped for various hold times, before taking interference pictures in time-of-flight and building the contrast squared FDFs. The shape of the FDFs are then again used to extract the temperature of the gas. As can be seen, several data sets do not find any signs of heating over several hundreds of milliseconds, neither by using the FDFs, nor by probing the density ripples in time-of-flight.

Conclusion

Concerning the non-equilibrium quasi-condensate, heating may result in collective and quasiparticle excitations, leading to a break down of the low-energy, purely phononic Luttinger Liquid description. As we were reproducibly unable to find any heating in the dressed equilibrium system with all measurement methods at hand³, a long-time study of the non-equilibrium temperature evolution becomes possible and we can experimentally address the topic of full thermalization in the nearly-integrable non-equilibrium system.

6.1.2. Atom Loss

General Considerations

One main problem when looking at the long-time evolution of the non-equilibrium system is the inherent atom loss out of the magnetic trap.

A decreasing atom number obviously changes the 1d density n_z and thereby affects important parameters like the thermal correlation length λ_T , the sound velocity c_s and last but not least the collision and thermalization rates. The main problem of atom loss is the reduced signal to noise ratio in the absorption images, which eventually limits experimentally accessible time scales.

The effective Temperature T_{eff} of the prethermalized state is not affected by atom loss as it is defined by the quantum shot noise of the splitting process (see section 5.3). Therefore, it is set by the current atom number at the moment of splitting and remains well-defined throughout time evolution. Being independent on atom loss as well as being independent on thermal fluctuations of the initial state is actually a very unique feature of the prethermalization phenomenon, relying totally on quantum noise.

Furthermore, atom loss might affect the population of the longitudinal modes. We have to make the important assumption that atoms are lost independently on their energy i.e. longitudinal mode they occupy such that the distribution of mode population is effectively kept unchanged. If, for example predominantly high energy modes would be depleted by atom loss, the system would be effectively cooled similar as in evaporative cooling. In a sense this would be a thermal quantum quench, with unknown affects to the time evolution of the contrast squared FDFs (section 5.6). The long time dynamics would be changed drastically. However, there are no signs of energy-dependant atom loss

³density-ripples temperature and relative temperature measured via FDFs

6. Going beyond Prethermalization: Is there Thermalization in the long time evolution?

in the density ripple temperature evolution, nor in the FDF evolutions of the equilibrium system (compare Fig. 6.2). Therefore, the atom loss probably only leads to uniform changes of the longitudinal mode population and does not affect the FDF shapes.

Let's now focus on the reasons for atom loss. Atoms continuously leave the trap due to several processes. These processes can be classified by the number of participating trapped atoms into 1-, 2- and 3-body processes. One-body processes include collisions with the hot (300 K) background gas, which easily eject the atoms from the magnetic trap (trap depths \leq mK), Majorana spin flips and spin flips due to ambient rf noise fields as well as through energy transfer from ambient resonant stray light. For the applied Ioffe-Pritchard like traps, with a Ioffe field on the order of $B_I \sim 0.57$ G (400 kHz), the rate of Majorana spin flips (sec. 3.2.5) can be neglected. Technical noise, generating AC fluctuations in the magnetic fields, may also induce spin flips into untrapped states [Folman 02]. The 1-body loss rate is mainly set by the pressure and technical noise sources generating a broad noise spectrum in the rf domain. 2-body spin-exchange collisions are not allowed for rubidium in the fully stretched state $|F = 2, m_F = 2\rangle$ as total F and m_F need to be conserved. Dipolar relaxation, coming from interactions between nuclear and electric dipole moments of the colliding atoms, is usually neglectable [Folman 02]. Three-body collisions lead to the formation of untrapped diatomic molecules, where the third atom receives a fraction of the binding energy. This energy is typically much larger than the trap depths confining the atoms, thus all three participating atoms leave the trap. The 2- and 3-body inelastic collision rates play an important role in the condensation process, where, for example, the unexpectedly high 2-body dipolar relaxation rate prevented the first attempts of condensation of caesium atoms in the late 90s (three orders larger than expected [Söding 98], due to a second-order spin enhancement [Tiesinga 92]).

Atom Loss Model

In the following, we want to find out which processes are predominantly responsible for the observed atom loss in our setup and if there is still room for future improvements. Fig. 6.3 shows the measured scaling of density loss rate versus initial density $n_{3d}(t = 0)$. Here, the density loss rate was determined for evolution times $t_e > 60$ ms, by a linear fit to the density evolution⁴ in the non-equilibrium split system. The rates in the equilibrium system are comparable. The results are plotted in Fig. 6.3 together with a fit function $f(n) = an + bn^3$, assuming only 1- and 3-body processes. The coefficients a and b give estimates of the 1- and 3- body loss coefficients γ_b and L_3 .

Now, let's have a closer look by writing down the rate equation. In the absence of two-body losses the atom loss rate $\frac{dN}{dt}$ can be written as [Burt 97]

$$\frac{dN}{dt} = -\gamma_b N - L_3 \int [n_{3d}(r, t)]^3 d^3r, \quad (6.1)$$

with the background collision rate γ_b and the 3-body recombination rate coefficient L_3 . The $1/e$ lifetime τ due to background collisions is then given by the inverse of γ_b . Using the definition $\langle n_{3d}^2(r, t) \rangle = \frac{1}{N(t)} \int n_{3d}^3(r, t) d^3r$ [Burt 97] eq. 6.1 can be rewritten as

⁴The linear fit is in good agreement with the data at long times ($t_e > 60$ ms)

6. Going beyond Prethermalization: Is there Thermalization in the long time evolution?

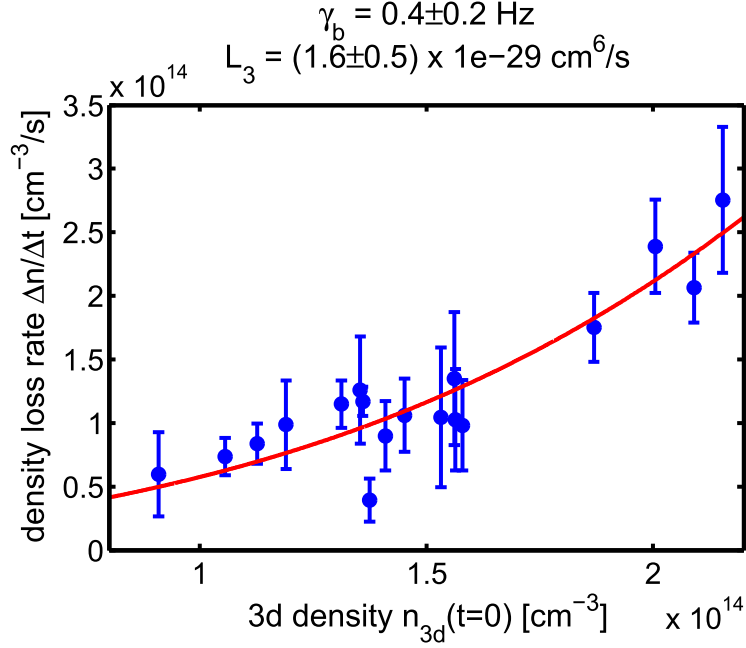


Figure 6.3.: Density loss versus initial density. The solid red line is a fit of the function $f(n) = an + bn^3$ and leads to the following estimates: $L_3 = (1.6 \pm 0.5) \times 10^{-29} \text{ cm}^6 \text{ s}^{-1}$ and $\gamma_b = 0.4 \pm 0.2 \text{ Hz}$. Errorbars are one standard deviation of fit uncertainty.

$$\frac{1}{N} \frac{dN}{dt} = -\gamma_b - L_3 \langle n_{3d}^2(r, t) \rangle. \quad (6.2)$$

The spatial integral of eq. 6.2 can be easily calculated for a 3d BEC. For all three-dimensions the atoms are in the ground-state, which, for non-interacting bosons in a harmonic potential, results in a Gaussian density distribution of the form $n_{3d}(x, y, z; t) = n_{3d,0}(t) \cdot \exp\left(\sum_{i=x,y,z} \left(\frac{-i^2}{2\sigma_i^2}\right)\right)$ [Schumm 05a, Arnold 99]. Under this assumption one finds

$$\langle n_{3d}^2(r, t) \rangle = \frac{\int n_{3d}^3(r, t) d^3r}{\int n_{3d}(r, t) d^3r} = \frac{n_{3d,0}^2(t)}{\sqrt{3^3}}. \quad (6.3)$$

In case of a quasi-condensate, we have to assume, according to section 2.2.1, that the ground-state is only occupied in the two transverse directions and to evaluate the density profile along the longitudinal direction eq.2.20 needs to be applied. The density profile is then given by $n_{3d}(x, y, z; t) = n_{x,0}n_{y,0} \cdot \exp\left(\sum_{i=x,y} \left(\frac{-i^2}{2\sigma_i^2}\right)\right) \cdot n_z(z; t)$. In the range of our typical trap frequency the longitudinal averaged density $\langle n^2(z, t) \rangle$ scales as $\langle n^2(z, t) \rangle = 1.8394 \cdot n_{z,0}^2 \approx \frac{11}{6} n_{z,0}^2$. Here and in the following, we assume that the 1d linear peak density $n_{z,0} = \max(n(z))$ of the quasi-condensate (see section 2.2.1) and the 3d peak density $n_{3d,0} = \max(n_{3d}(x, y, z))$ can be related via the ground state oscillator

6. Going beyond Prethermalization: Is there Thermalization in the long time evolution?

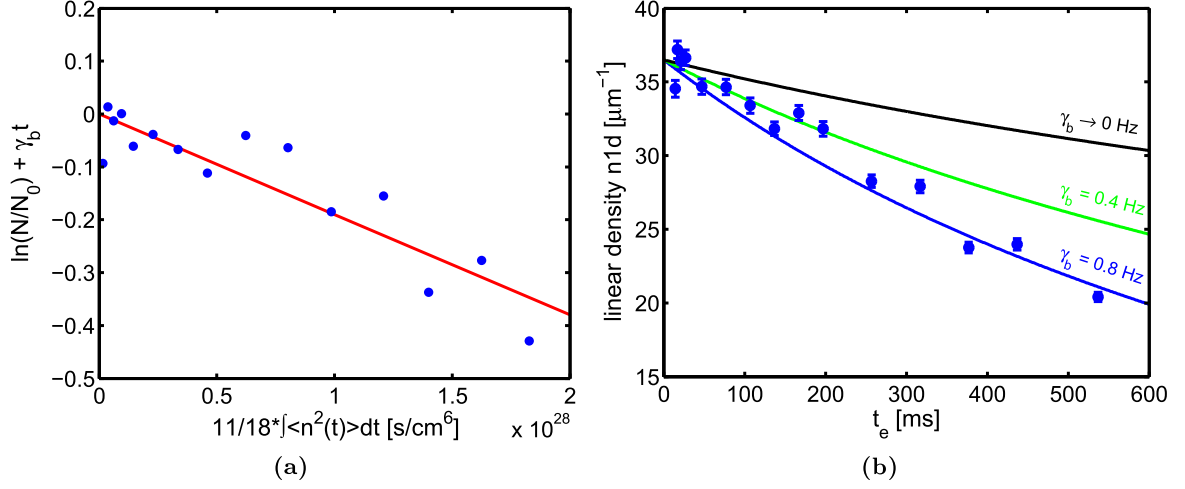


Figure 6.4.: Estimating 1- and 3-body loss rate in dressed trap. (a) Following eq.6.5, the slope of the linear fit is equal to the negative 3-body loss rate L_3 . For the presented data, a value of $L_3 = (1.9 \pm 0.4) \times 10^{-29} \text{ cm}^6 \text{ s}^{-1}$ is found for $^{87}\text{Rb}(F = 2, m_F = 2)$. (b) Estimating the background collision rate γ_b by comparing the time evolution of the measured 1d peak density $n_{z,0}(t)$ to the result of eq.6.7 for three different values of $\gamma_b = 0, 0.4, 0.8$ Hz (from top to bottom) using $L_3 = (1.9 \pm 0.4) \times 10^{-29} \text{ cm}^6 \text{ s}^{-1}$. Best agreement is found for $\gamma_b = 0.8$ Hz. Errorbars are one standard deviation of the mean.

width $a_{tr} = \sqrt{\frac{\hbar}{m\omega_{tr}}}$ through the simple expression $n_{z,0} = \pi a_{tr}^2 \cdot n_{3d,0}$ [Tolra 04]. This leads to the following expression for a quasi-condensate

$$\langle n_{3d}^2(r, t) \rangle = \frac{\int n_{3d}^3(r, t) d^3r}{\int n_{3d}(r, t) d^3r} \approx \frac{n_{x,0}^2 n_{y,0}^2}{\sqrt{3}^2} \cdot \frac{11}{6} n_{z,0}^2(t) = \frac{11}{18} \frac{n_{z,0}^2}{\pi^2 a_{tr}^4}. \quad (6.4)$$

Now, eq.6.2 can be written in integral form as

$$\ln \frac{N}{N_0} = -\gamma_b t - \frac{11}{18} L_3 \int n_{3d,0}^2 dt. \quad (6.5)$$

Plotting $\ln \frac{N}{N_0} + \gamma_b t$ against $\frac{11}{18} \int n_{3d,0}^2 dt$ should give a straight line, whose slope is the negative of the three body coefficient L_3 . Fig. 6.4a shows such a plot for the atom loss in the double-well, which gives $L_3^{condensed} = (1.9 \pm 0.4) \times 10^{-29} \text{ cm}^6 \text{ s}^{-1}$ based on the estimated value $\gamma_b = 0.8$ Hz for the one-body loss (see below). The error on L_3 is given by one standard deviation of the fit uncertainty and does not include any statistics nor systematics. The result for L_3 is in good agreement with experimentally $L_3^{condensed} = (2.23 \pm 0.11) \times 10^{-29} \text{ cm}^6 \text{ s}^{-1}$ [Söding 99] and theoretically $L_3^{condensed} = 1.9 \times 10^{-29} \text{ cm}^6 \text{ s}^{-1}$ [Esry 99] obtained values for $^{87}\text{Rb}(F = 2, m_F = 2)$. The value of L_3 is not supposed to be significantly reduced by the 1d confinement as the Lieb-Liniger interaction parameter $\gamma = 0.003$ is fairly small [Tolra 04]. Why it is difficult to measure γ_b in an atom chip

6. Going beyond Prethermalization: Is there Thermalization in the long time evolution?

setup and how the estimated value of $\gamma_b = 0.8\text{Hz}$ is obtained will be discussed in the next paragraph. On first sight $\gamma_b = 0.8\text{Hz}$ appears to be fairly large, and gives a respective lifetime of only $\tau = 1.25\text{s}$ for the quasi-condensate in the dressed trap. However, condensate lifetimes on the order of $\tau = 500\text{ms}$ have been reported for similar atom chip setups in undressed traps [Wildermuth 05a]. Still there might be room for improvement.

To determine the number loss due to background collisions one usually plots the long-time evolution of the natural log of the atom number. At long-times (tens of seconds) the slope of the expected linear scaling gives the background loss rate. Deviations from the linear scaling at small times are then due to the three-body loss. In an atom chip setup, the limitations on extending the trapping time are quite stringent due to the ohmic heating of the atom chip wires as already discussed in section 3.1.2. In the current setup, the chip trap time after condensation cannot be increased above one second. At these short times available, the 3-body loss rate is not distinguishable from 1-body loss rate. Thus one has to find an alternative.

One alternative is to look directly at the 1d density evolution with time. For the transverse directions we use again the rather unsophisticated model of non-interacting bosons occupying the ground state. The 3d density can then be written as $n_{3d}(x, y, z, t) = n_x n_y n_z(t) = n_x^2 n_z(t)$. Then, the rate equation 6.1 can be approximately written as

$$\frac{dn_z}{dt} = -\gamma_b n_z - \frac{L_3}{\pi^2 a_{tr}^4} n_z^3 \quad (6.6)$$

and can be solved analytically, which gives

$$n_z(t) = \left[\frac{\gamma_b}{-\frac{L_3}{\pi^2 a_{tr}^4} + e^{2\gamma_b t} \cdot \left(\frac{L_3}{\pi^2 a_{tr}^4} + \frac{\gamma_b}{n_{t=0}^2} \right)} \right]^{\frac{1}{2}}. \quad (6.7)$$

Fig. 6.4b shows the time evolution of the linear density for three different values of $\gamma_b = 0, 0.4, 0.8$ for fixed L_3 in comparison to experimentally obtained data. Clearly, the three-body rate alone is insufficient to account for the observed density loss, which suggests a background rate on the order of $\gamma_b \approx 0.8\text{Hz}$. Starting from the values found by Fig. 6.3, the correct combination of L_3 and γ_b can be found iteratively using Fig. 6.4a to get L_3 , which is less sensitive on changes in γ_b and Fig. 6.4b to finally get γ_b .

It is interesting to note that already this simplistic model delivers competitive results for the 3-body loss rate L_3 . More elaborate models make use of Thomas-Fermi profiles in the transversal directions to properly include the effects of interactions, which is out of the scope of this work. The main objective of this discussion was to get a good estimate of the background collision rate γ_b .

The expected collision rate γ_{bg} between atoms and background gas is approximately given by

$$\gamma_{bg} = n_{bg} \bar{v}_{bg} \sigma, \quad (6.8)$$

6. Going beyond Prethermalization: Is there Thermalization in the long time evolution?

where the mean relative velocity \bar{v}_{bg} for a thermal gas at temperature T is given by $\bar{v}_{bg} = \sqrt{\frac{8k_B T}{\pi m}}$, under the assumption that the relative velocity is given by the hot ($T = 300$ K) background particle and $v_{Rb} \ll \bar{v}_{bg}$.

Assuming the background gas consists mainly of hydrogen molecules this can be approximated by [Folman 02]

$$\gamma_{bg} = 4.8 \times 10^{-3} \frac{p}{10^{-10} \text{ mbar}} \frac{\sigma}{1 \text{ nm}^2}, \quad (6.9)$$

At a background pressure⁵ of $p = 10^{-10}$ mbar and at typical collision cross sections of $\sigma_{Rb-H_2} = 3 \text{ nm}^2$ [Bali 99] for rubidium-hydrogen collisions, one calculates $\gamma_{bg}^{(Rb-H_2)} = 1.4 \times 10^{-2}$ Hz, which is two orders of magnitude less than what we observe. Collisions between rubidium and helium have similar cross sections of $\sigma_{Rb-He} = 2 \text{ nm}^2$ [Bali 99] and give even smaller rates of $\gamma_{bg}^{(Rb-H_2)} = 6.8 \times 10^{-3}$ Hz. Collisions with hot rubidium atoms have one order of magnitude higher cross sections of $\sigma_{Rb-Rb} = 25 \text{ nm}^2$ [Bali 99] and give rates of $\gamma_{bg}^{(Rb-Rb)} = 8.4 \times 10^{-2}$ Hz, which are still by one order less than what we have found above. Therefore, the background pressure does not seem to be the only limiting factor for the lifetime of the ultracold sample.

Conclusion

The current value for the one-body loss rate in the experimental setup is given by $\gamma_b = 0.8$ Hz. This is a rather high value compared to magnetic traps without atom chips [Burt 97, Tolra 04, Wang 11] and leads to comparatively small lifetimes of $\tau = 1.25$ s. However, atom chip trap experiments have reported similar values [Wildermuth 05a] in undressed magnetic traps, the reasons being elusive so far. Comparisons of loss rates between currently active experimental setups are to be brought under way. In the current setup, the calculated rates of background gas collisions suggest that there is still much room for improvement. In principle, an increase in the lifetime τ on the order of one magnitude seems easily possible. This might be achieved by further reduction of technical noise sources or using a different Ioffe field. Lifetime improvement will be the topic of future efforts.

⁵as measured by an Bayard-Alpert-type ion gauge in the pumping chamber

6.2. Long Time Evolution

Now, that we have understood the early time multimode dynamics, leading to a prethermalized state, we want to address the long time evolution. As we have already seen in Fig. 5.15, for substantial longer evolution times t_e on the order of several hundred milliseconds a distinct deviation from the prethermalized squared contrast FDFs becomes visible. So far, it remains unclear if this additional evolution on a second much longer time scale has intrinsic (thermalization) or extrinsic (coupling to the environment) reasons. This will be discussed in the following.

6.2.1. Long time Evolution of the Mean Contrast

Let's again start with the most simple observable, the mean contrast $\langle C(t_e) \rangle$. Similar to Fig 5.9, Fig. 6.5 depicts the long time evolution of the $T = 20 \pm 2$ nK data set (blue squares) for the longest integration length $L = 110 \mu\text{m}$. The rapid initial decay up to $t_e \sim 10$ ms has been attributed to the dephasing process (time domain I), which establishes the prethermalized quasi-steady state (time domain II), characterized by almost constant mean contrast up to $t_e \sim 40$ ms. Compared to the initial dynamics the prethermalized state is quiet long lived. Ultimately, the contrast starts to decrease slowly with evolution time (time domain III), where a linear fit (dashed blue) gives a slope of approximately $-8\%/100$ ms, clearly distinct from the practically constant TLL prediction (dashed black). This second, slow evolution could be attributed to thermalization processes that are not covered by the harmonic TLL theory or by a coupling to the noisy environment (see sec. 6.1) generating an increasing thermal background for instance.

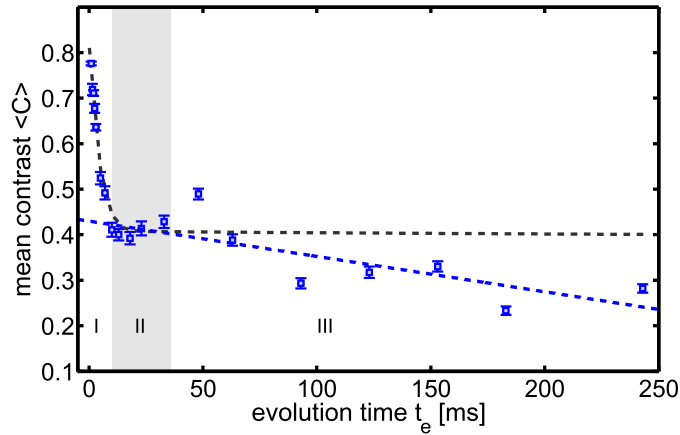


Figure 6.5.: Mean contrast evolution for long times for the longest integration length $L = 110 \mu\text{m}$. After the rapid initial decay, the mean contrast (blue squares) shows a further decrease on a second much longer time scale, which is not predicted by the TLL model (black dashed). The dashed blue line is a linear fit to slow decrease of the mean contrast in time domains II and III.

6. Going beyond Prethermalization: Is there Thermalization in the long time evolution?

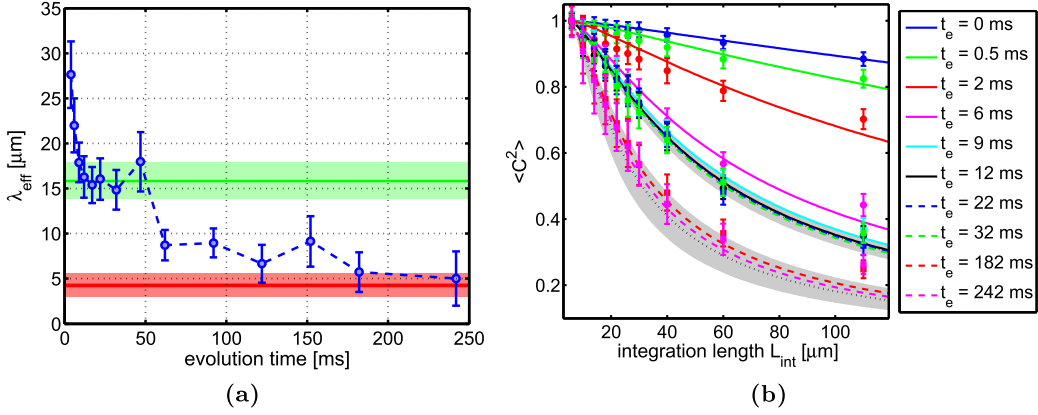


Figure 6.6.: Measuring the correlation loss on long time scales via fitting to the $C(L)$ decay for the same data set as in Fig. 5.14 with the following parameters: $T_{\text{in}} = 103 \pm 15$ nK, $n = 45 \pm 5$ μm^{-1} , $K = 29.6 \pm 1.7$, 300 repeats.

(a) Evolution of the fitted correlation length λ_{fit} (blue circles), compared to the crossover length l_0 (green line) and the calculated thermal correlation length $\lambda_\phi(T_f)$ (red line), assuming equipartition between all degrees of freedom leading to a final temperature of $T_f = (T_{\text{in}} + T_{\text{pre}})/2$, with $T_{\text{pre}} \approx 15.8$ nK. Dashed blue line is a guide to the eye.

(b) Measured (data points) and fitted $C(L)$ decays (solid lines) for increasing evolution times t_e . The upper dotted black line and grey shaded area corresponds to the calculated prethermalized correlation length l_0 . The lower dotted black line and dashed area corresponds to the estimated equilibrium correlation length $\lambda_\phi(T_f)$.

(a+b) Error bars denote one standard deviation. Shaded areas denote two standard deviations.

To get more insight, we want to study if this contrast decrease coincides with an intrinsic loss of correlations. An increasing thermal background would just add an overall offset of the $C(L)$ dependence and thereby merely affect the correlations, but decreasing the absolute value of the contrast. Therefore, the time evolution of the effective correlation length λ is studied in the following, where λ is determined via the fitting function of eq. 5.12.

6.2.2. Long Time Evolution of the Effective Correlation Length

Fig. 6.6 studies the correlation loss on long time scales for the same data set as in Fig. 5.14, applying the $C(L)$ fit function of eq. 5.12. In the dephasing time domain $t_e < 10$ ms, the fit formula should actually be not applicable, as the system has not yet reached the thermal-like prethermalized state. To demonstrate the high amount of initial correlations after the splitting and their obvious decay towards the prethermalized correlation length $l_0 = \lambda_\phi(T_{\text{pre}}) = \lambda_{\text{fit}}$, the early times $C(L)$ data are plotted additionally in Fig. 6.6b,

6. Going beyond Prethermalization: Is there Thermalization in the long time evolution?

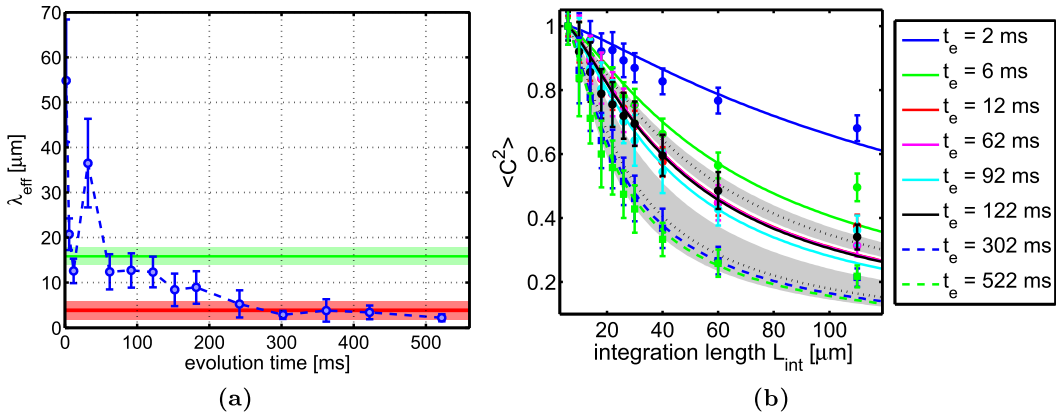


Figure 6.7.: Similar to Fig. 6.6, the correlation loss on long time scales is measured for a data set with extended evolution times, with the following parameters: $T_{in} = 69 \pm 11$ nK, $n = 27 \pm 7 \mu\text{m}^{-1}$, $K = 23 \pm 3$, 150 repeats. After $t_e \approx 300$ ms, thermal equilibrium correlations seem to be reached, without any further evolution within the error bounds. (a+b) Strictly speaking the fit function of eq. 5.12 is only valid for thermal-like correlations, so for $t_e \gtrsim 10$ ms. Error bars denote one standard deviation. Shaded areas denote two standard deviations.

keeping in mind that the resulting fit values $\lambda_{fit}(t_e < 10 \text{ ms})$ in Fig. 6.6a are not to be regarded as an effective thermal correlation length. Once the prethermalized state has been reached, the FDFs are of thermal-like form (Fig. 5.16) and λ_{fit} becomes a proper measure of the correlation length of the system. After the initial rapid loss of correlations, the prethermalized state shows an almost constant correlation length equal to the calculated value of $l_0 = 15.8 \pm 0.9 \mu\text{m}$ (eq. 5.7). The prethermalized correlations last for approximately 40 ms, leading to a bunching of $C(L)$ curves in Fig. 6.6b. For times $t_e \gtrsim 50$ ms, the correlation length starts an abrupt decrease towards the estimated thermal equilibrium value given by the equipartition of thermal energy between all four degrees of freedom (see tab. 5.2), equilibrating the temperature of the relative modes T_{rel} with the temperature of the common modes T_{com} . As we do not observe any cooling induced by the splitting process ($T(t_e < 0) = T(t_e = 0)$), the final equilibrium temperature can be estimated as [Stimming 11]

$$T_f = \frac{T_{rel} + T_{com}}{2} = \frac{T_{pre} + T_{in}}{2}, \quad (6.10)$$

which is used to calculate the correlation length $\lambda_\phi(T_f) = \frac{\hbar^2 n}{mk_B T_f}$ of the thermal equilibrium state in Fig. 6.6. Both figures support the interpretation that the second loss of correlations might be attributed to an intrinsic, slow relaxation towards thermal equilibrium conditions. Increasing the thermal fraction by external, technical noise sources, for instance, should not affect the $C(L)$ shapes. Therefore, studying the $C(L)$ decay is better than just looking at the time evolution of the mean contrast, as in Fig. 6.5.

6. Going beyond Prethermalization: Is there Thermalization in the long time evolution?

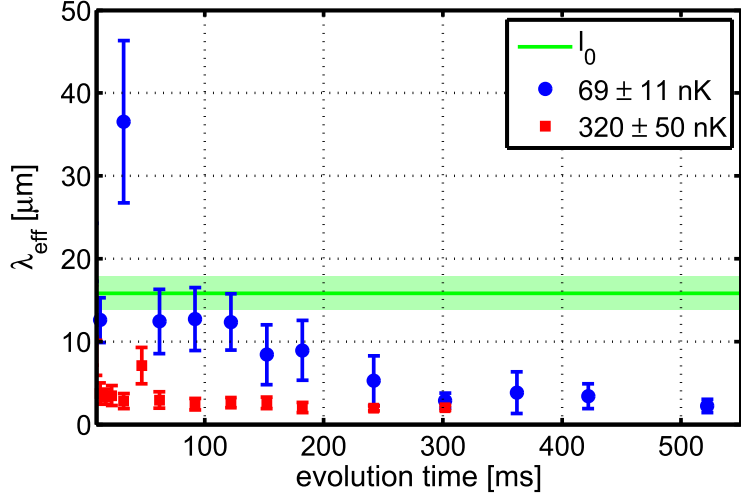


Figure 6.8.: Comparison of loss of correlations for a hot (red squares) and cold data (blue circles) with respect to the calculated value of l_0 (green horizontal line and shaded area). Error bars correspond to one standard deviation. The prethermalized plateau is only visible for the cold data set. The hot data set rapidly decays towards thermal equilibrium.

To make the case stronger, Fig. 6.7 examines a data set extended up to $t_e = 520$ ms. Fig. 6.7b suggests, that once the thermal state has been reached (at $t_e \approx 300$ ms), the $C(L)$ evolution settles⁶. The slightly slower relaxation to equilibrium values in comparison to Fig. 6.6, can be attributed by the colder initial temperature of this data set (see figure captions). The reason for the outlier at $t_e \approx 50$ ms is unclear, but could be a sign of a revival of correlations. An in depth analysis of phase revivals will be covered in [Langen 13a].

Fig. 6.8 compares the evolution of the correlation length for an extremely hot ($k_B T_{in} \approx 4.5 \times \hbar \omega_{tr}$) and a cold ($k_B T_{in} \lesssim \hbar \omega_{tr}$) data set. Whereas the cold data set shows clear features of prethermalized intermediate state, the hot data set rapidly decays towards thermal equilibrium. This conceptually different behaviour shall be rigorously studied in the following section.

In conclusion, the long time evolution of the measured correlation lengths shows signs of thermalization, motivating a further study. To this end, probing thermalization in an effectively 1d system turns out to be hard due to the extensively long equilibration times needed. To accelerate the thermalization rates and thereby be able to probe their scaling, we will go to the 1d/3d crossover regime in the following.

⁶However, this settling can also be understood in terms of finite imaging resolution, which results in a lower bound for measurable correlation lengths of $\sim 2 \mu\text{m}$.

6.3. Probing Thermalization in the 1d/3d Crossover

Here and throughout this thesis, a system being in the true thermal equilibrium means that, apart from conserved quantities like the initial energy, a complete loss of memory of the initial state has happened and that the relaxation is irreversible in character.

Quantum thermalization and the emergence of ergodicity in a closed, interacting quantum system is generally far less understood than thermalization in classical statistical mechanics [Polkovnikov 11]. Furthermore, following the KAM theorem [Arnol'd 63], thermalization is not to be expected in truly integrable systems where the final state has to be described via a generalized Gibbs ensemble (GGE), as defined by the many constants of motion [Polkovnikov 11, Rigol 08]. On the other hand, small perturbations from integrability may lead to the establishment of true thermalization. In a purely 1d system, these perturbations may arise from higher-order (>2) scattering processes [Mazets 10]. Interestingly, classical [Bonini 99] and quantum [Gasenzer 05] statistical calculations of isolated systems predict that the resulting pathways towards true thermal equilibrium, are indirect and complex. Roughly speaking, these pathways can be differentiated into two time scales, originating from different underlying processes. The first process being in general associated with dephasing, the second process being associated with particle scattering.

For much longer evolution times, the experimental data shows a deviation from the harmonic TLL theory (Fig. 5.15 and Fig. 6.5) combined with a loss of correlations (sec. 6.2.2). However if and how true thermal equilibrium is reached remains elusive.

Thermalization of highly non-equilibrium quantum systems near an integrable point is experimentally an unresolved question [Kinoshita 06, Rigol 07]. Theoretically, the equilibration of a non-integrable system close to an integrable point has been studied extensively in [Kollar 11], which predicts the duration of the system, staying trapped in this fixed point of its evolution, [Berges 08, Nowak 13] to increase when getting closer to integrable conditions and to finally extend to infinity in the pure integrable case, thus being unable to reach thermal equilibrium. In this context, we want to lift the integrability on purpose by going into the 1d/3d crossover regime, study how this affects the prethermalized state and see if the quantum system shows signs of true thermalization.

6.3.1. Processes leading to Thermalization

In elongated 3d systems, thermalization mainly depends on the two-body elastic collision rate. The probability of exciting higher transverse states drops exponentially, by a factor $\exp\left(-\frac{2\hbar\omega_{tr}}{k_B T_{in}}\right)$ [Mazets 08], the colder and the more 1d the system gets. However, higher excited states are necessary for thermalization to occur (Fig. 6.9). Let's consider a homogeneous 1d system in the longitudinal direction with frozen out transverse degrees of freedom of an harmonic oscillator (ω_{tr}). If two atoms, of longitudinal momenta p_1 and p_2 and mass m , collide, they can merely exchange their momenta, but a transfer of arbitrary momenta is impossible. Thus, the momentum distribution remains unchanged. This can be seen by the following considerations.

Case 1: $E_1 + E_2 \ll \hbar\omega_{tr}$: Say the momentum of atom 1 changes by $\epsilon > 0$, such that

6. Going beyond Prethermalization: Is there Thermalization in the long time evolution?

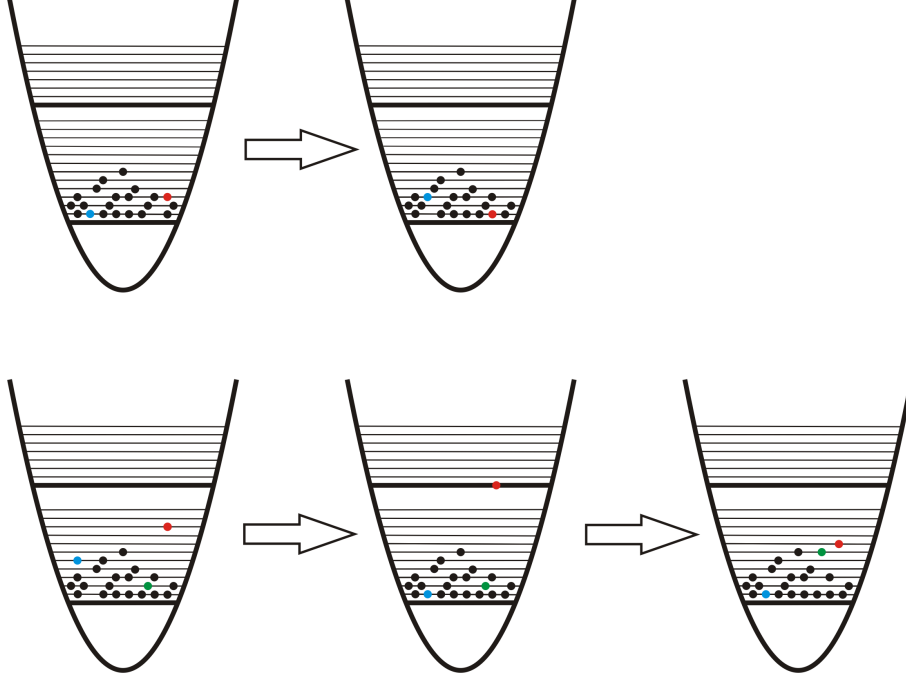


Figure 6.9.: Schematic plot of transverse energy levels $\hbar\omega_{tr}$ (thick horizontal lines) with longitudinal energy levels $\hbar\omega_{long}$ (thin horizontal lines) depicted on top for simplicity (not to scale). The colored atoms take part in the collision. For $E_1 + E_2 \ll \hbar\omega_{tr}$ (top), the two atoms may only exchange their longitudinal momenta, rendering thermalization impossible. For $E_1 + E_2 \gtrsim \hbar\omega_{tr}$ (bottom), one of the colliding atoms can be excited into the transverse 1st excited state, which, by undergoing a second collision with a different atom, leads to a redistribution of longitudinal momenta and thereby acts as a thermalization process in the longitudinal degrees of freedom.

$p_1 \rightarrow p_1 + \epsilon$. According to momentum conservation $p_1 + p_2 = p'_1 + p'_2$, the momentum of atom 2 is changed by $p_2 \rightarrow p_2 - \epsilon$. Inserting this into energy conservation leads to

$$p_1^2 + p_2^2 = p_1'^2 + \epsilon^2 + p_2'^2 + \epsilon^2, \quad (6.11)$$

which shows that $\epsilon \equiv 0$ and thus no change of values of p_1, p_2 is possible in the purely 1d case ($k_B T \ll \hbar\omega_{tr}$).

Case 2: $E_1 + E_2 \gtrsim \hbar\omega_{tr}$: On the other hand, when two colliding atoms have enough kinetic energy, such that one of them (let's assume atom #2) is excited into a higher transverse state, the picture changes dramatically.

$$E_1 + E_2 = \frac{p_1^2}{2m} + \frac{p_2^2}{2m} = \frac{p_1'^2}{2m} + \left(\frac{p_2'^2}{2m} + \hbar\omega_{tr} \right) = E_1' + E_2' \quad (6.12)$$

$$p_1 + p_2 = p_1' + p_2' + \hbar k,$$

6. Going beyond Prethermalization: Is there Thermalization in the long time evolution?

The values of momenta are now subject to change with $p'_1 \neq p_1$ and/or $p'_2 \neq p_2$. Furthermore, considering that the excited atom undergoes a second collision with a 3rd atom leads to

$$E'_2 + E_3 = \left(\frac{p_2'^2}{2m} + \hbar\omega_{tr} \right) + \frac{p_3^2}{2m} = \frac{p_2''^2}{2m} + \frac{p_3^2}{2m} = E''_2 + E'_3 \quad (6.13)$$

$$p'_2 + p_3 + \hbar k = p''_2 + p'_3, \quad (6.14)$$

de-exciting atom #2 and redistributing the transverse energy $\hbar\omega_{tr}$ into the longitudinal energy states of atoms 2 and 3. This process, enables a redistribution of momenta in the 1d direction, such that an initially non-equilibrium momentum distribution may relax into a thermal one.

In summary, thermalizing two-body collisions are strongly suppressed the more one-dimensional (in energy-scales) a system is [Mazets 10], resulting in thermalization time scales that are inaccessible by current experiments. In this context, we want to study thermalization in the 1d/3d crossover by on purpose breaking the 1d criteria and thus allowing two-body collisions, populating transverse excited states, to slowly lift the integrability of the system. Possible relevant thermalization mechanisms, populating transverse excited states really or virtually, are reviewed in the following.

Two-Body Thermalization Rate

Following [Mazets 10] the two-body thermalization rate can be written as

$$\Gamma^{(2)} \approx 0.93 n a_s^2 \sqrt{\frac{m\omega_{tr}^3}{\hbar}} \exp\left(-\frac{2\hbar\omega_{tr}}{k_B T_{in}}\right) \quad (6.15)$$

with the 1d density in each well n and the initial Temperature T_{in} . The prefactor of 0.93 has been determined numerically for a trapped system [Mazets 10]. The $1/e$ thermalization time τ is then given by the inverse of the thermalization rate $\tau = 1/\Gamma^{(2)}$. This formula is valid for a non-degenerate gas and neglects any suppression of thermalization imposed by correlations (more relevant in the strongly interacting case $\gamma > 1$) or enhancements due to bosonic amplification [Miesner 98] of scattering into thermally-populated, transverse-excited states. Furthermore, the non-degenerate Bogoliubov excitation spectrum is neglected, which is likewise expected to lead to further acceleration of thermalization [Mazets 10, Miesner 98].

Virtual Three-Body Thermalization Rate

For $k_B T < 2\hbar\omega_{tr}$ the two-body thermalization rate is exponentially “frozen” out as the energy of two colliding atoms is insufficient to excite transverse excited state. In this regime, only three-body collisions may lead to transverse excitations that are needed to effectively break the integrability of the Lieb-Liniger Hamiltonian (eq. 2.2) and thereby support thermalization [Mazets 10], with a temperature independent rate of

6. Going beyond Prethermalization: Is there Thermalization in the long time evolution?

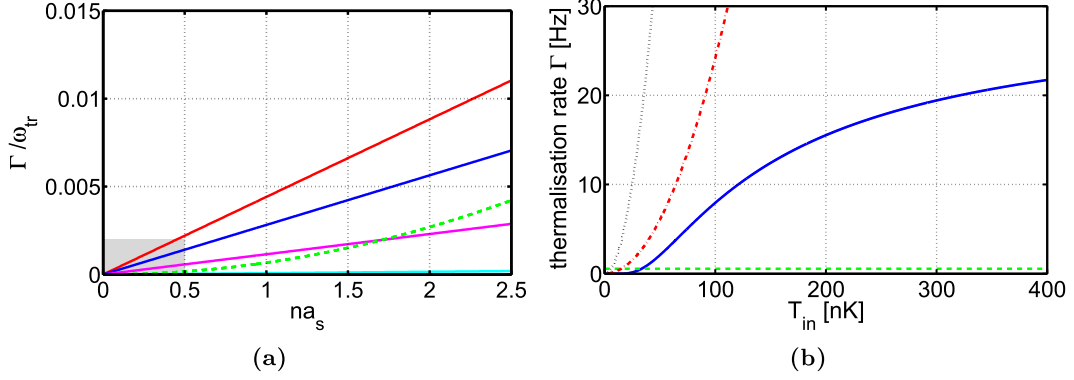


Figure 6.10.: (a) Calculated two- (solid lines) and three-body (green dashed line) thermalization rates for various temperatures, according to eq. 6.15 and 6.16. From top to bottom: $T = 100, 75, 50, 25$ nK. The grey shaded area depicts the typical experimental parameter range. (b) Calculated two- (blue solid line), three-body (green dashed line) and thermalization rates for typical experimental parameters ($n = 40 \mu\text{m}^{-1}$). The three body rate ($\Gamma^{(3)} \approx 0.5$ Hz) starts to exceed the two-body rate below ~ 30 nK. The purely 1d models of [Burkov 07] (black dotted) and [Stimming 11] (red dotted-dashed) are plotted for comparison and predict much higher thermalization rates.

$$\Gamma^{(3)} = 2.04 \frac{ma_s^4}{\hbar} n^2 \omega_{tr}^2. \quad (6.16)$$

Similar to the two-body, rate this formula applies to a non-degenerate gas. As indicated in Fig. 6.10b, the 3-body rate is in the typical experimental parameter range practically negligible in comparison to the two-body rate.

Damping and mixing of phononic modes in 1d

Even in a truly 1d case equilibration and thermalization mechanisms have been suggested and shall be briefly mentioned for completeness. As discussed in sec. 2.5, a number imbalance between left and right gas leads to a coupling of common and relative modes, resulting in an energy transfer. Here and throughout this work, this effect is minimized by an almost perfect symmetric splitting with typical experimental number imbalances of less than 1%. Other sources resulting in a coupling of relative and common DOF are higher order contributions which are neglected by the approximations used to derive the Luttinger Hamiltonian (see sec. 2.4). These higher order contributions are studied in detail in [Burkov 07]. Stimming et al predict that the results of [Burkov 07] contain an over-damping of phononic modes [Stimming 11] and derive slightly smaller thermalization rates.

6. Going beyond Prethermalization: Is there Thermalization in the long time evolution?

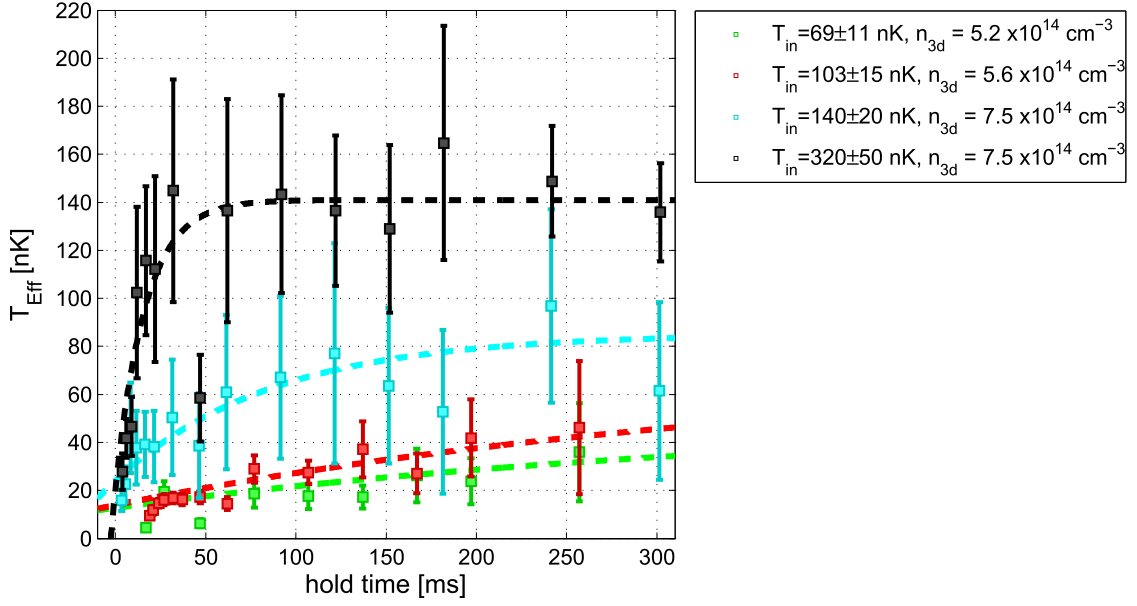


Figure 6.11.: Breaking integrability on purpose by increasing the initial temperature T_{in} far above $1 \times \hbar\omega_{tr} \triangleq 70$ nK. Errorbars correspond to one standard deviation. Dashed lines are exponential saturation fits following eq. 6.17. On long time scales, the resulting time evolution of the effective relative temperature T_{Eff} strongly depends on the initial temperature T_{in} .

6.3.2. Breaking Integrability

Integrability is lifted by raising the initial temperature T_{in} , such that the 1d criteria $k_B T_{in} < \hbar\omega_{tr}$ is not fulfilled anymore and the two-body collision rate is significantly enhanced. This is experimentally much easier (applying small changes to the rf evaporation ramp) than increasing the density n such that the second criteria $\mu \ll \hbar\omega_{tr}$ is sufficiently broken. In this context, the initial temperature T_{in} is used to tune the dimensionality of the system and T_{in} is raised so far that even transverse excited states become significantly populated. The data of Fig. 6.11 has been taken in the temperature range of 70 to 320 nK ($1 - 4.5 \hbar\omega_{tr}$). Similar to sec. 4.4.4, the squared contrast decay versus integration lengths are used to determine the relative phase correlation length, which is then used to calculate the temperature of the relative modes T_{rel} following eq. 4.21. The temperature of the common mode is assumed to be equal to the initial temperature before splitting $T_{in} = T_{com}$. Clearly, the more the system gets towards 3d, the faster the increase in relative temperature after the quantum quench at $t = 0$ ms, in accordance with Fig. 6.8. The dashed lines are exponential fits according to the model described below. As can be seen, the lifetime of the prethermalized state decreases drastically to practically zero at large temperatures.

6. *Going beyond Prethermalization: Is there Thermalization in the long time evolution?*

Time Evolution Model for $T(t_e)$

The time evolution of the FDF temperature is modelled via exponential saturation to the final temperature T_f . To describe the thermalization process the following fit function is used.

$$T(t_e) = (T_f - T_{pre}) \left(1 - e^{-\Gamma t_e}\right) + T_{pre}, \quad (6.17)$$

with an unknown thermalization rate Γ and the final temperature again defined as $T_f = (T_{in} + T_{pre}) / 2$.

Determining the Initial Temperature

The initial temperature T_{in} of the single gas is measured via density-density correlations in time-of-flight, as described in sec. 4.3, which works reliably up to $T_{in} \approx 200$ nK. For larger temperatures, fits to the thermal wings are used (see sec. 4.2).

6.3.3. Results: Squared Contrast FDFs in the 1d/3d Crossover

Similar to the correlation length results the FDFs show a further evolution at longer time scales, which is highly dependent on the initial temperature T_{in} . The following figures show the drastic difference in the time evolution and relaxation dynamics of the squared contrast FDFs for two different initial temperatures T_{in} in the effectively 1d regime and in the 1d/3d crossover regime. The initial temperature is used to tune the dimensionality of the system.

On the border of the effectively 1d regime, the long-time evolution consists of three, clearly distinct dynamical states, as visible in Fig. 6.12. The three states are the initial highly coherent state, the intermediate prethermalized state and a further thermal-like state of even less coherence. For $t_e = 0$ ms the initial state shows high coherence throughout all integration lengths leading to the peaked distributions, which are actually non-thermal (χ^2 test with equilibrium distributions fails, see sec. 5.7.1). The intermediate prethermalized state has already lost some amount of coherence. A subsequent further loss of coherence results in an unknown thermal-like state at an arbitrary evolution time of $t_e = 120$ ms, which probably lies on the pathway to full thermal equilibrium of the system.

A data set at much higher temperature, deep in the 1d/3d crossover regime, shows a much faster evolution of the FDF shapes, as illustrated in Fig. 6.13. The initial state is very similar to the one above, however, the prethermalized state is practically not-at-all visible anymore.

Summarizing these observations, in the effectively 1d, nearly-integrable regime, the pathway towards thermal equilibrium suggests to be a two-step process with an intermediate, long-lived prethermalized state. Integrability seems to be slightly broken in the experimental realisation, leading to a second decay of correlations on a much longer time-scale that might end up in the thermal equilibrium state characterized by having equal temperature in common and relative modes ($T_{rel} = T_{com}$). On the other hand,

6. Going beyond Prethermalization: Is there Thermalization in the long time evolution?

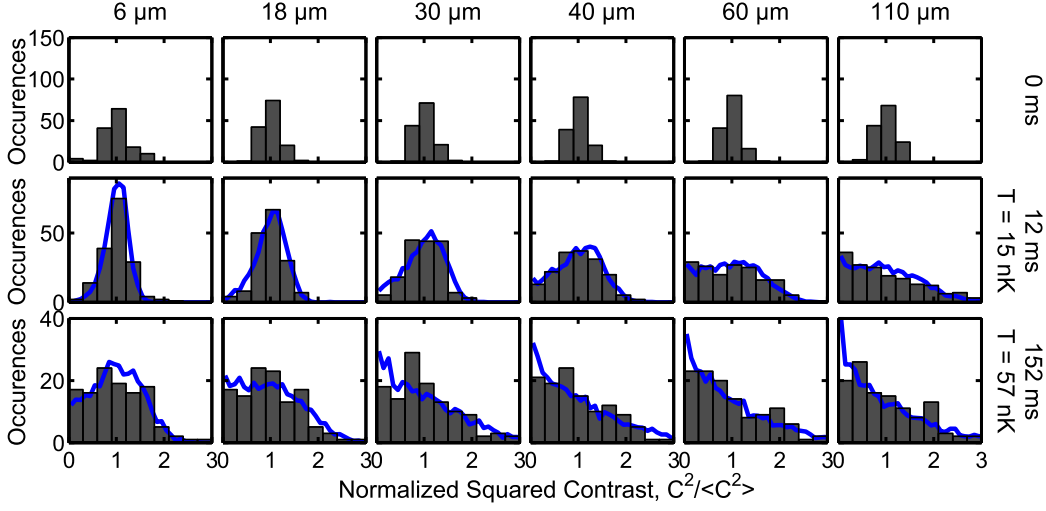


Figure 6.12.: Squared contrast FDFs for a cold temperature set with the following parameters: $T_{in} = 73 \pm 10$ nK ($\sim 1 \times \hbar\omega_{tr}$), $n_{3d} = 4.3 \times 10^{14}$ cm $^{-3}$. At 12 ms, the FDF data agrees with the prethermalized state. At much longer times (152 ms), we find a further increase of the relative temperature, which might be attributed to equilibration or even thermalization.

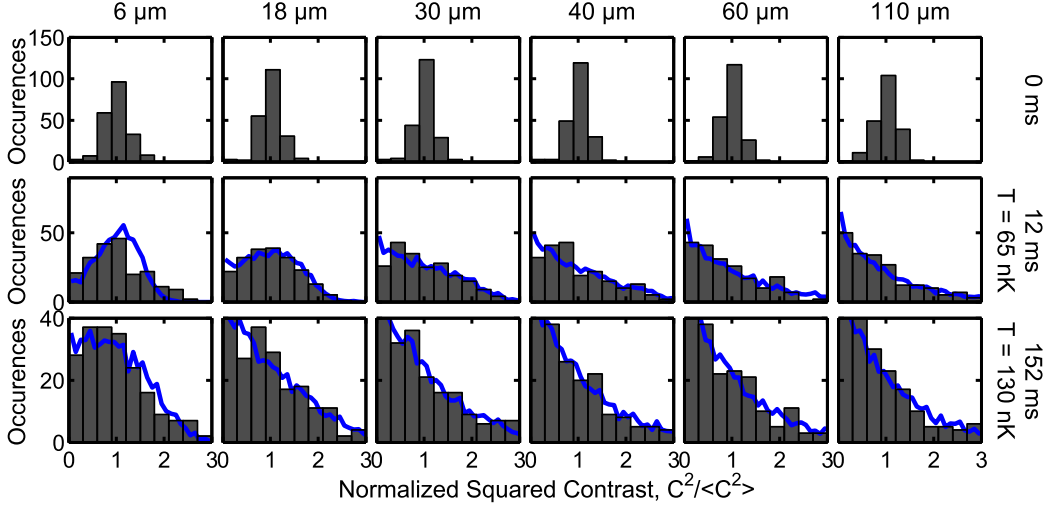


Figure 6.13.: Squared contrast FDFs for a hot data set with the following parameters: $T_{in} = 320 \pm 50$ nK ($\sim 4.5 \times \hbar\omega_{tr}$), $n_{3d} = 6.2 \times 10^{14}$ cm $^{-3}$. This hot data set starts with the same initial state (peaked FDFs) as Fig. 6.12, but shows a much faster dynamics. It does not establish the prethermalized temperature at 12 ms, but a much higher temperature of $T = 60$ nK and continues to heat up for much longer times.

6. Going beyond Prethermalization: Is there Thermalization in the long time evolution?

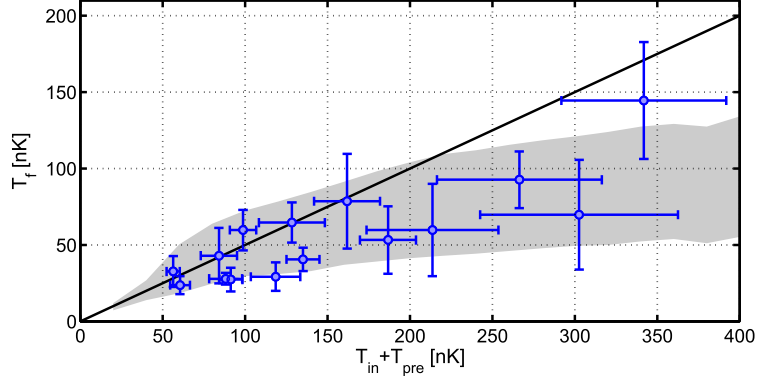


Figure 6.14.: Final temperature $T_f = \langle T_{fit}(t_e > 150 \text{ ms}) \rangle$ (blue circles) versus the sum of measured initial T_{in} and calculated prethermalized T_{pre} temperatures. The black solid line has a slope of $\frac{1}{2}$ according to the equipartition of energy between common and relative modes $T_f = (T_{in} + T_{pre}) / 2$. The shaded area depicts the expected scaling according to the finite imaging resolution in the experiment, which is the result of a numerical simulation based phase profiles created by the Ornstein-Uhlenbeck as discussed in sec. 4.3. The data shows good agreement to simulation results. The point at highest temperature is off due to its much higher density in respect to the other data points.

breaking integrability on purpose by a high enough initial temperature changes the picture dramatically, such that only one time scale of relaxations is visible. In the following, we want to compare the acquired data to existing thermalization theories, to verify the above statements. To do so, the correlation length is determined using the fit formula of eq. 5.12. The relative temperature is then calculated using eq. 4.21. Fitting the contrast decay rather than the FDFs is slightly more robust (less statistical samples are needed as mean values are fitted rather than distribution functions) and computationally much faster than fitting the FDF data to obtain the relative temperatures.

6.3.4. Results: Temperature Evolution of the Relative Degrees of Freedom

First of let us verify the assumption that the final equilibrium temperature is given by $T_f = (T_{in} + T_{pre}) / 2$. For the data in Fig. 6.14, T_f (blue circles) is estimated by taking the average of the fitted temperatures for $t_e > 150 \text{ ms}$ and plotted versus the sum of the measured initial temperature T_{in} (before splitting) and calculated prethermalized temperature $T_{pre} = T_{pre}(n(t=0 \text{ ms})) = ng/2$. The data shows good agreement to simulation results (grey shaded area), which takes the finite imaging resolution into account and starts to deviate at $\approx 100 \text{ nK}$ from the $\frac{1}{2}$ slope.

6.3.5. Results: Evolution of Density Ripples Temperature

To examine the thermal energy in the system after splitting, the density ripples are used to determine the temperature just after the splitting process for evolution times t_e smaller

6. Going beyond Prethermalization: Is there Thermalization in the long time evolution?

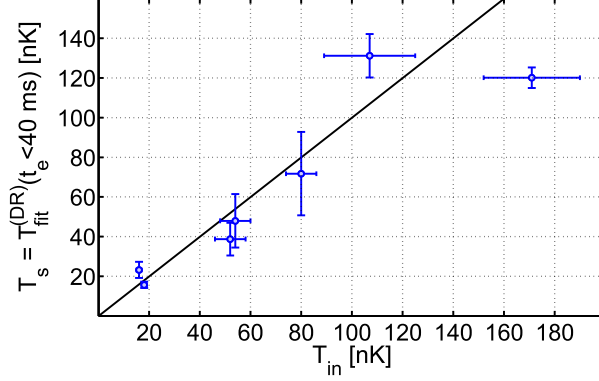


Figure 6.15.: Measured density ripples temperature after splitting $T_s = \langle T_{fit}^{(DR)}(t_e \in [0, 40] \text{ ms}) \rangle$ (blue circles) versus the initial temperature T_{in} before splitting. Within experimental accuracy T_s is equal to T_{in} .

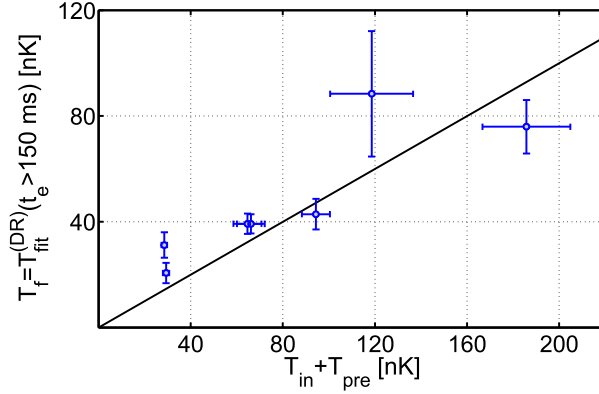


Figure 6.16.: Final density ripples temperature $T_f = \langle T_{fit}^{(DR)}(t_e > 150 \text{ ms}) \rangle$ (blue circles) versus the sum of measured initial T_{in} and calculated prethermalized T_{pre} temperature. The data shows good agreement to the equipartition of energy between common and relative modes according to $T_f = (T_{in} + T_{pre})/2$ (black solid line).

than 40 ms. The measured g_2 functions are compared to the calculated incoherent-sum of the simulated thermal phase fluctuations in the two gases⁷. In the prethermalized state, the measured g_2 are dominated by the temperature in the common mode, as $T_{pre} \leq T_{com}$ in the observed data range. The results are plotted in Fig. 6.15. As can be seen, the temperature after splitting $T_s = \langle T_{fit}^{(DR)}(t_e \in [0, 40] \text{ ms}) \rangle$ is basically equivalent to the measured initial temperature $T_{in} = T_{in}^{(DR)}$ before splitting. This suggests that the common mode is likewise out of equilibrium after splitting. Furthermore, Fig. 6.15 shows the strong temperature dependence of the common modes, which is in stark contrast to the temperature independent scaling of the relative modes (Fig. 5.17b). Once more, this

⁷Correlations only show minor affects to the shape of the g_2 functions.

6. Going beyond Prethermalization: Is there Thermalization in the long time evolution?

confirms that, by splitting, the common modes receive the thermal energy of the initial gas, in contrast to the relative modes, which are merely populated by the quantum noise of the splitting process.

Fig. 6.16 shows the measured final temperature $T_f = \langle T_{fit}^{(DR)}(t_e > 180 \text{ ms}) \rangle$ in comparison to the sum of calculated prethermalized temperature T_{pre} and measured initial temperature T_{in} . It demonstrates that the common mode cools down for large evolution times, such that the scaling of eq. 6.10 is established.

6.3.6. Results: Time Evolution of the Relative Temperature

Fig. 6.17 compares the time evolution of many different data sets at different initial temperatures and densities with an exponential temperature increase following the model of eq. 6.17, where the two-body thermalization rate of eq. 6.15 is used. No free fit parameter is used. The relative temperature $T_{rel}(t_e)$ increases faster when the system goes more and more away from the 1D regime, and settles at long times to T_f . The exponential dependence of the two-body rate $\Gamma^{(2)}$ is well captured, and fair agreement between theory and experiment is found.

Fig. 6.18 shows the temperature scaling of the fitted thermalization rates using the model of eq. 6.17 in comparison to several suggested thermalization models that were discussed in sec. 6.3.1. The data shows best qualitative agreement to the two-body rate (solid blue line). Let me note that virtual three-body rates $\Gamma^{(3)}$ are practically negligible in the presented parameter range ($\Gamma^{(3)} \approx 0.50 \text{ Hz}$). In the 1d regime ($T_{in} < 70 \text{ nK}$), the data clearly does not support the quantum decoherence model by [Burkov 07], which predicts a much faster increase of the thermalization rates. In this regime, the data is in qualitative agreement with the two-body scattering model of eq. 6.15 [Mazets 10]. In the 1d/3d crossover regime, the data follows the trend of the two-body model.

In Fig. 6.19, the thermalization rates are plotted versus the initial correlation lengths $\lambda(T_{in})$. Once again, the data points show fair agreement to the 1d model of [Stimming 11] (red dashed line) as well as to the two-body model. The absolute values are in favour for the two-body rate (blue solid line). Once again, the model by [Burkov 07] (green dotted-dashed line) can be ruled out.

Finally, Fig. 6.20 studies the density scaling of the fitted thermalization rates for two different temperature ranges, now only comparing to the two-body model ($\Gamma^{(2)} \propto n_{1d}$) and to the model of Stimming et al. ($\Gamma \propto n_{1d}^{-2}$). The n_{1d}^{-2} scaling of the 1d model of [Stimming 11] is not reproduced. The data is in qualitative agreement with the linear density scaling of the two-body theory. This suggests that for temperatures above 1d ($T_{in} > 70 \text{ nK}$) the two-body model is an appropriate description.

6.3.7. Conclusions

In the long time evolution of this nearly-integrable system, further dynamics set in after the prethermalized state has been established. The common mode temperature decreases, while the relative mode temperature increases. Both temperatures equilibrate to a final

6. Going beyond Prethermalization: Is there Thermalization in the long time evolution?

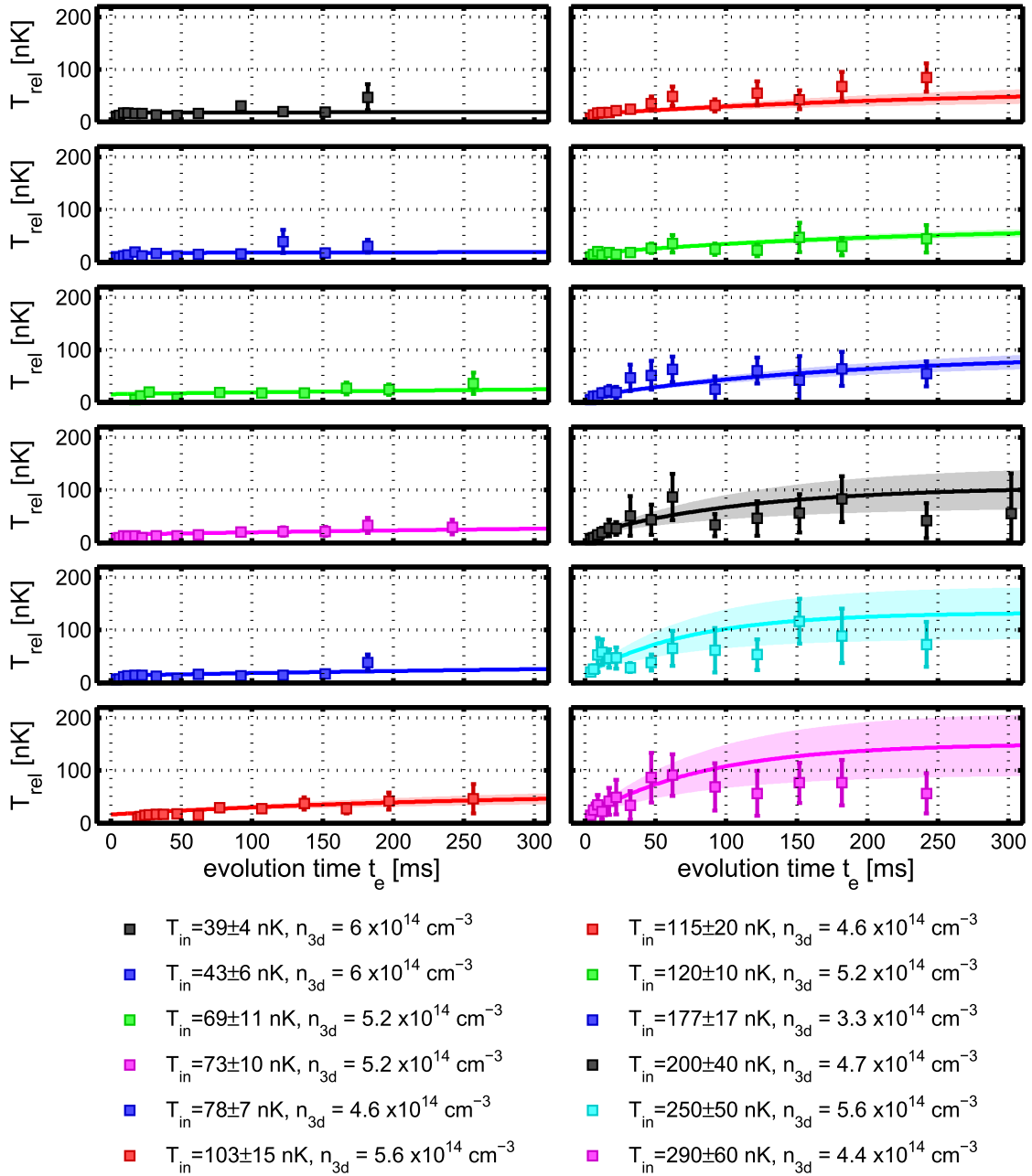


Figure 6.17.: Comparing the time evolution of the relative temperature (data points) to the calculated two-body thermalization rate $\Gamma^{(2)}$ (solid line) for a variety of initial parameters. The dashed vertical lines correspond to $\tau = 1/\Gamma^{(2)}$. Over a wide parameter range, the two-body rate shows good agreement with the data. Exponential fits following eq. 6.17 are used to derive the data for Fig. 6.18.

6. Going beyond Prethermalization: Is there Thermalization in the long time evolution?

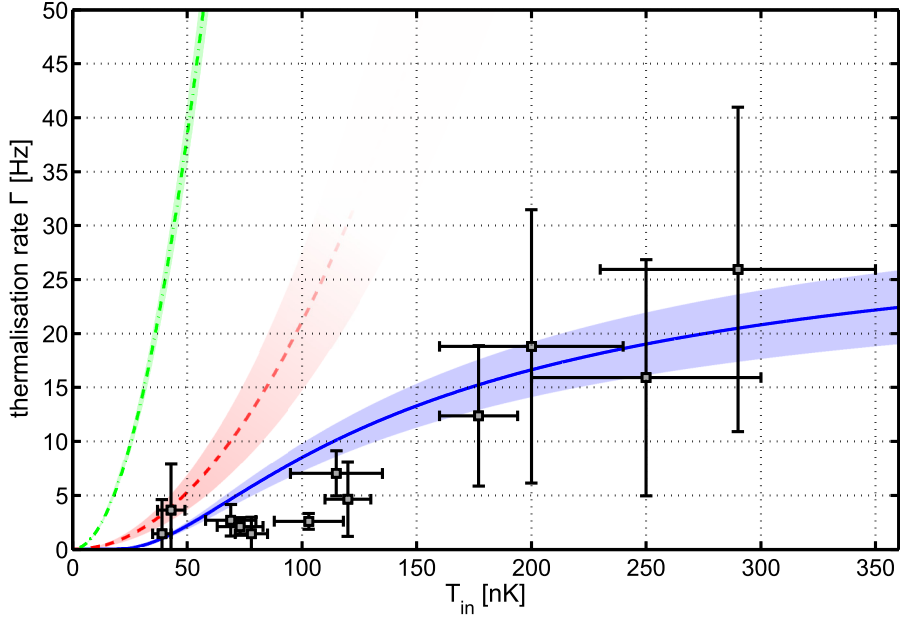


Figure 6.18.: Temperature scaling of the measured thermalization rates (filled squares) in comparison to three theory models: damping of phonons due to two body collisions (solid blue), damping due to non-linearities in 1D [Stimming 11] (dashed red) and the quantum decoherence model of [Burkov 07] (dotted green). The latter two models are valid for 1D systems only. In the 1d regime ($T_{in} < 70$ nK), the strong increase in thermalization rate suggested by the quantum decoherence model is not supported by the data. The data is in qualitative agreement with the two-body model. In the 1d/3d crossover regime ($T_{in} \geq 70$ nK), transverse excitations are becoming more relevant and the Stimming theory should not be applicable anymore. The observed thermalization rates are slightly higher than the calculated two-body rates, which has to be expected as the two-body theory is for a non-degenerate Bose gas. Thus the observed increased thermalisation rates might be attributed to Bosonic amplification [Mazets 10]. The shaded areas depict the rms deviation according to the density spread of the different data sets.

temperature, which is defined by the sum of initial and prethermalized temperatures, divided by two.

The observed dynamics of the relative degrees of freedom are in fair agreement to a two-body collisional model, populating higher excited transverse states and thereby lifting integrability. The collisions lead to a damping and mixing of phononic modes which is necessary for the system to be able to relax towards thermal equilibrium. In this context, further theoretical and experimental efforts are ongoing and may, in future, lead to a full understanding of the relaxation dynamics of a split quasi-condensate in the 1d/3d crossover regime as well as in the purely 1d regime.

In conclusion, the presented results strongly encourage the viewpoint that we are ob-

6. Going beyond Prethermalization: Is there Thermalization in the long time evolution?

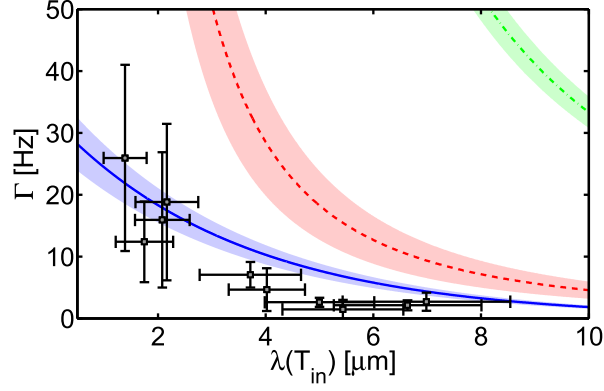


Figure 6.19.: Measured thermalization rates versus initial phase correlation length $\lambda(T_{in})$. The shaded areas depict the rms deviation according to the density spread of the different data sets.

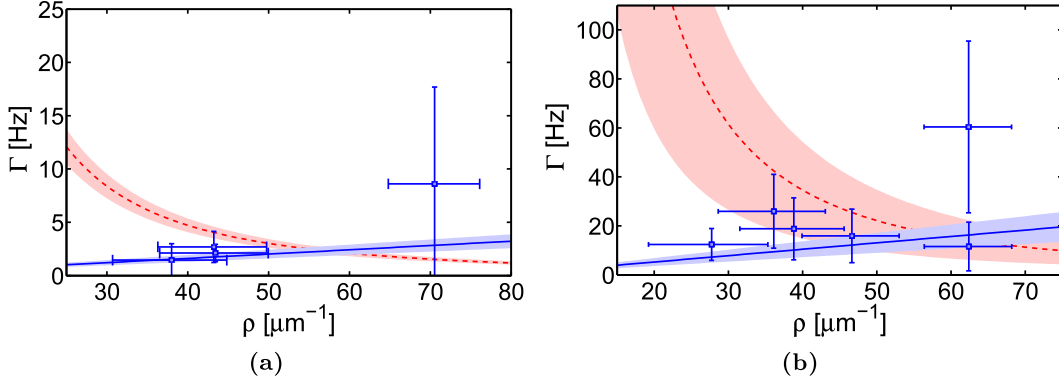


Figure 6.20.

The two figures show the scaling of the thermalization rate with density in the temperature range of $\langle T \rangle \approx 70 - 80$ nK (a) and $\langle T \rangle \approx 140 - 320$ nK (b). For both plots the trend follows the linear density scaling of the two-body model (solid blue) rather than the n_{1d}^{-2} scaling of the 1d model of [Stimming 11] (red dashed). The shaded areas depict the uncertainties due to the temperature spread.

serving thermalization of an isolated, many-body quantum system in the 1d/3d crossover regime. The intermediate prethermalization phenomenon becomes more pronounced, the more 1d and integrable the system gets. On the other hand, the observed thermalization rates increase the more 3d the system gets, eventually blurring the prethermalized state.

Apparently, thermalization of this isolated quantum system can be understood in terms of two processes as illustrated in Fig. 6.21. First, dephasing of excitations and second, damping of these excitations due to an effective phonon-phonon scattering. In the 1d regime, the dephasing process establishes the observed prethermalized state

6. Going beyond Prethermalization: Is there Thermalization in the long time evolution?

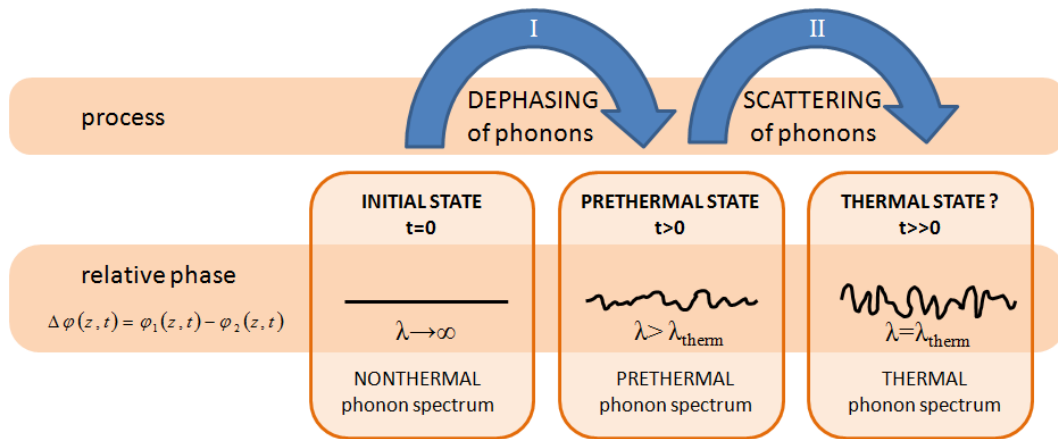


Figure 6.21.: The matter-wave interference experiment measures the correlations in the relative phase field (relative DOF), which is described by phononic modes. The loss of correlations over time can be attributed to two processes. First, the dephasing of phononic modes rapidly establishes a prethermalized state, where the mode populations are conserved. Second, damping and mixing of phononic modes alters the mode populations such that a thermal equilibrium state can be achieved.

typically on much shorter time scales than two-body scattering processes need to establish thermal equilibrium. Together, these two processes seem to form the general path to thermalization in a nearly integrable system, and the specific system under investigation provides an example where the damping and mixing of phononic modes is mediated via two-body collisions.

7

Chapter 7.

Conclusion and Outlook

Begriffe, welche sich bei der Ordnung der Dinge als nützlich erwiesen haben, erlangen über uns leicht eine solche Autorität, dass wir ihres irdischen Ursprungs vergessen und sie als unabänderliche Gegebenheiten hinnehmen.

Sie werden dann zu “Denkgewohnheiten”, “Gegeben a priori” usw. gestempelt. Der Weg des wissenschaftlichen Fortschritts wird durch solche Irrtümer oft für längere Zeit ungangbar gemacht. Es ist deshalb durchaus keine müßige Spielerei, wenn wir darin geübt werden, die längst geläufigen Begriffe zu analysieren und zu zeigen, von welchen Umständen ihre Berechtigung und Brauchbarkeit abhängt, wie sie im einzelnen aus den Gegebenheiten der Erfahrung herausgewachsen sind. Dadurch wird ihre allzugroße Autorität gebrochen.

- A. Einstein, Nachruf auf Ernst Mach, *Physikalische Zeitschrift* 17 (1916)

7.1. Conclusion

How classical statistical mechanics and the concept of thermalization can be extended into quantum mechanics is an ongoing issue, as it is unclear how unitary time evolutions may transform an initially pure quantum state into a mixed state in thermal equilibrium [Linden 09, Polkovnikov 11, Ikeda 13]. This problem lead to the formulation of the quantum ergodic theorem [Neumann 10, Goldstein 10], the (ETH) [Deutsch 91, Srednicki 94, Rigol 08, Polkovnikov 11] and quantum Darwinism [Zurek 09]. The ETH has been verified numerically for many different quantum systems far from integrable points [Rigol 08, Rigol 09a, Rigol 09b, Santos 10]. On the other hand, the ETH is not supposed to work in integrable and nearly integrable systems [Rigol 09a, Cassidy 11, Rigol 12]. In this context, the emergence of the second law of thermodynamics in an

7. Conclusion and Outlook

isolated quantum system has been studied in [Ikeda 13]. In this context, this thesis studies the time evolution of a well isolated, non-equilibrium, quantum many-body system in the 1d and the 1d/3d crossover regimes. How this system of weakly-interacting Bosons inherently loses information about the highly-correlated initial state is examined and the resulting relaxation dynamics are studied in detail. In contrast to the simple classical view of one relaxation time scale establishing the thermal equilibrium state, the non-equilibrium dynamics reveal the existence of an intermediate, steady-state in the course of the evolution. This state, preserving a high amount of correlations and thereby the memory of the initial state, has been identified as a prethermalized state, which is essentially a thermal-fixed point of the relaxation process [Bonini 99, Aarts 00, Berges 08, Schmidt 12, Nowak 13]. A fixed-point in the evolution means that for a wide range of different initial parameters, the system always relaxes to the same state, characterized by the same amount of correlation. As it was shown in this work, these prethermal correlations are indeed independent over wide parameter ranges of the initial temperatures or densities of the system. Furthermore, the source of this prethermalized state is found to be of intrinsic quantum nature. The mechanism behind the first part of the evolution is identified as the dephasing of a multimode system in good agreement with calculations based on a Tomonaga Luttinger Liquid description.

In the final part of this work, the question how quantum and initial thermal energy can eventually equilibrate is analysed. To be able to address this topic on experimentally accessible time scales, the integrability of the system is lifted on purpose. A second relaxation time scale, much longer than the time scale needed for dephasing, is observed. This second loss of correlations is interpreted as the final part of the thermalization process, which is mediated through two-body scattering processes. These scattering processes are populating transverse excited states, thereby breaking the integrability of the initial 1d system. In the 1d/3d crossover regime, the observed relaxation is in qualitative agreement with calculated two-body rates [Mazets 08, Mazets 10].

In conclusion, the thermalization of an almost integrable system happens on two different time scales. The first time scale given by multimode dephasing establishing a prethermalized state with thermal-like correlations, which is yet much more correlated than the thermal equilibrium state. The second time scale depends on the rate of integrability breaking mechanisms, which are, on experimentally realizable time scales, given by the rate of two-body collision of high enough energy, such that higher transverse modes are populated.

The results of this work are highly relevant for many areas of physics, from the dynamics of the early universe [Berges 04], condensed matter physics [Moeckel 08, Eckstein 09b, Mitra 13] to classical [Bonini 99] and quantum statistical mechanics [Gasenzer 05] and quantum chaos [Gutzwiller 91] and will be of high importance through stimulating ongoing efforts on developing a universal non-equilibrium theory framework [Karl 13].

7. Conclusion and Outlook

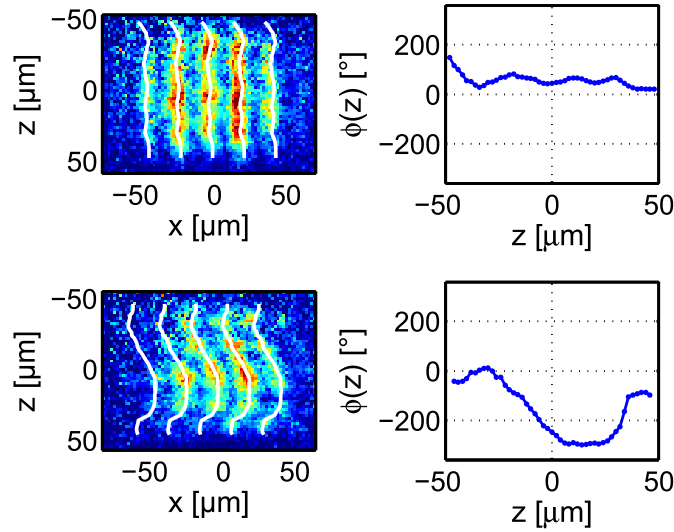


Figure 7.1.: Measuring the local relative phase profiles $\phi(z)$ just after splitting (top) and in the prethermalized state (bottom). Instead of measuring the contrast at different integration lengths L , the first order (PCF) $PCF(z, z') = \langle \exp(i\phi(z) - i\phi(z')) \rangle$ can be used to locally measure the correlation properties and thereby study how the loss of information spreads in the system.

7.2. Outlook

As it happens so frequently in science and research, successfully answering some initial questions, imperatively raises many more, previously unanticipated, resulting questions. The experimental observation of prethermalization in the course of the non-equilibrium evolution of a nearly-integrable, many-body system opens up many new research paths. Just a view shall be highlighted in the following.

One unresolved question is how the non-equilibrium system locally establishes the prethermalized state. This is currently under investigation by measuring the phase correlation function (PCF) of the interference patterns. Fig. 7.1, shows phase profiles obtained just after splitting (top row) and in the prethermalized state (bottom row). The PCF can be calculated by taking the average $\langle \exp(i\phi(z) - i\phi(z')) \rangle$ of many pictures, probing the local correlations at distance $|z - z'|$. Just after splitting the relative phase $\phi(z)$ is almost constant resulting in a flat PCF shape, whereas the PCF of the prethermalized state should show a thermal like PCF and thus be exponentially decaying. How the initially flat PCF evolves into the prethermal PCF is studied in detail in [Langen 13a]. The perspectives of this new observable are of wide range. As the PCF probes the local correlation properties, it will be a very good measure of the sound velocity, of possible revivals of correlations and, furthermore, opens up a new, sensitive observable for studying the loss of correlations in the long-time evolution leading to full thermalization.

It has been argued that the prethermalized state can be described as a generalized Gibbs

7. Conclusion and Outlook

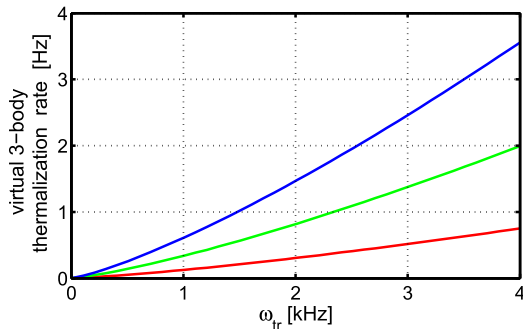


Figure 7.2.: Virtual three-body thermalization rate according to [Mazets 08], for three different atom numbers (from top to bottom: 12000, 9000, 6000).

ensemble, but an unambiguous experimental identification is still missing. The reason is quite simple. The prethermalized state created so far, has thermal-like properties as the fast splitting process populates the modes with a $1/k$ scaling. It would be very interesting to create a prethermalized state with unique non-thermal properties in the relative degrees of freedom. If this non-thermal state would be indeed long-lived, this would verify the generalized Gibbs ensemble picture. However, to be able to experimentally create such a non-thermal fixed state, further theoretical understanding of the splitting process is needed. To that end, a calculation, reliably modelling the splitting process, is a necessary precondition.

Other perspectives, following recent publications [Karpiuk 12], are studying the emergence of thermal solitons in the non-equilibrium system in comparison to the number of solitons in the equilibrium system. These dark and sometimes shallow solitons can be probed via the phase profiles, where they lead to phase kinks. However, a satisfying differentiation of solitons to simple phase slips, resulting from density ripples, is not yet available.

Establishing a quasi-steady prethermalized state in the evolution of a non-equilibrium system, raises the question under which conditions the system shows a further relaxation towards thermal equilibrium i.e. fills the complete phase space on the respective energy shell. We have been able to address this question in the 1d/3d crossover regime, where the two-body excitation rate is sufficiently fast enough to lead to thermalization on experimental time scales (< 500 ms). For truly 1d and integrable system parameters, further studies are needed to probe other possible thermalization mechanisms, three-body virtual excitations for instance. Currently, the expected three-body time scales are on the order of several seconds, which is beyond reach of the experiment. As shown in Fig. 7.2, by increasing the transverse trapping frequency by a factor of two as well as the atom number by a factor of three, the calculated three-body rates become > 3 Hz (< 333 ms) and should thereby be observable by the experiment. Such an increase in trap frequency is in principle feasible in the current setup, by making use of the second, much smaller ($20 \mu\text{m}$ wide) trapping wire (sec. 3.1.2) and will certainly be the topic of future efforts.

Other possibilities of studying thermalization processes and heat exchange mechanisms

7. Conclusion and Outlook

include the addition of a second species acting as a heat bath for the non-equilibrium system. In this context, the current setup has already the advantage of built-in potassium dispensers and a set up laser system for fermionic ^{40}K . Due to the different Rabi couplings species selective trap geometries are possible [Göbel 08]. To this end the ^{40}K can act as a heat bath for the ^{87}Rb , being split into a double-well potential, or vice versa.

Furthermore, ^{40}K attractively interacts with ^{87}Rb . This attractive interaction makes it possible to control the resulting double well-potential of the ^{87}Rb species with the number of fermions and create a very precisely controllable small tunnel coupling between the two wells. Additionally, the temperature would be well defined by the prethermalized temperature T_{pre} , which is determined by the number of ^{87}Rb atoms. As, the coupled system is a realisation of the Sine-Gordon Hamiltonian, this opens up many new fascinating perspectives, like studying Sine-Gordon dynamics in a very well-controlled two-species system, where both temperatures and couplings are defined by atom numbers.

Certainly, the addition of ^{40}K will lead to a huge manifold of upcoming research proposals, like the formation of bright solitons [Karpiuk 04] and studying charge density separation [Recati 03, Kollath 06], just to name a few.

A

Appendix A.

Relevant Nature Constants

	Symbol	Value	Unit	
Speed of light in vacuum	c	299 792 458 [Mohr 08]	m s^{-1}	
Planck constant	h	$6.62606896(33) \times 10^{-34}$ [Mohr 08]	J s	
reduced Planck constant	$\hbar = \frac{h}{2\pi}$	$1.054571628(53) \times 10^{-34}$ [Mohr 08]	J s	
Boltzmann constant	k_B	$1.3806504(24) \times 10^{-23}$ [Mohr 08]	J K^{-1}	
Earth Standard Gravity	g	9.80665 [Taylor 08]	m s^{-2}	
Bohr magneton	μ_B	$927.400968(20) \times 10^{-26}$ [Mohr 08]	J T^{-1}	
Bohr radius	a_0	$5.2917720859(36) \times 10^{-11}$ [Mohr 08]	m	
^{87}Rb triplet s-wave scattering length	$a_s = a_{ 2,2\rangle}$	$98.99(2) \times a_0$ [van Kempen 02]	m	
atomic mass unit	amu	$1.660538921(73) \times 10^{-27}$ [Mohr 08]	kg	
^{87}Rb Atomic Mass	m	86.909180520(20) [Steck 01]	amu	
^{87}Rb D ₂ -line	Wavelength (Vacuum)	λ_{Rb}	780.241209686(13) [Steck 01]	nm
	Frequency	ω_0	$2\pi \cdot 384.2304844685(62)$ [Steck 01]	THz
	Transition Energy	$\hbar\omega_0$	1.589049439(58) [Steck 01]	eV

Table A.1.: Nature Constants

B Appendix B.

Useful Conversions

From		To				
		kHz	eV	aJ	nK	
1 kHz		1	4.136×10^{-12}	6.626×10^{-13}	4.799×10^1	
1 eV		2.418×10^{11}	1	1.602×10^{-1}	1.160×10^{13}	
1 aJ		1.509×10^{12}	6.242×10^0	1	7.241×10^{-13}	
1 nK		2.084×10^{-2}	8.621×10^{-14}	1.381×10^{-14}	1	
$^{87}\text{Rb } m_F = 2, F = 2\rangle$		1 G	1400	5.790×10^{-9}	8.764×10^{-10}	6.719×10^4
		1 m/s	4.150×10^{-31}	4.509×10^{-7}	7.223×10^{-8}	1.992×10^{-29}
		ω_{tr}	$2\pi \times 1400$	5.790×10^{-12}	9.276×10^{-13}	6.719×10^1
		ω_{long}	$2\pi \times 7$	2.895×10^{-14}	4.638×10^{-15}	3.359×10^{-1}

Table B.1.: Useful Conversions. Based on: $E = h\nu = k_B T = \frac{1}{2}mv^2$, $e = 1.602 \times 10^{-19}$ J. Additionally the respective values of typical trap frequencies ω_{tr} , ω_{long} of the double well trap are given.

C

Appendix C.

Bose-Einstein functions $g_n(x)$

C.1. Enhanced Computation of the Polylogarithmic / Bose-Einstein Function

The polylogarithmic function $g_n(z)$ also known in Literature as the de Jonquière's function or Bose Einstein function is of high relevance in the context of degenerate Bose or Fermi gases. Integrals of the form $\int_0^\infty dx \frac{x^{n-1}}{z^{-1}e^x - 1} = \Gamma(n) g_n(z)$ appear quiet often as for example for an ideal 3d Bose gas the Bose Einstein phase transition occurs when the phase-space density is given by $PSD = n\lambda_{dB}^3 = g_{3/2}(1) \approx 2.612$, with the thermal de Broglie wavelength $\lambda_{dB} = (2\pi\hbar^2/mk_B T)^{1/2}$. Other prominent examples are the occupation of the excited states. For a trapped Fermi gas, the Fermi Temperature T_F and the fugacity ξ relate via $g_3(\xi) = -\frac{1}{6}(T_F/T)^3$, with the temperature T .

The polylogarithmic or Bose-Einstein function is defined for a complex number $|z| < 1$, $n \in \mathbb{R}$ [SyLOW 81, Huang 87]

$$g_n(z) = \sum_{k=1}^{\infty} \frac{z^k}{k^n} = z + \frac{z^2}{2^n} + \frac{z^3}{3^n} + \dots \quad (\text{C.1})$$

However easy this function can be implemented in a numerical code, it is demanding long computation times. Approximations enabling numerically efficient computations have been reported for $g_{3/2}$ and $g_{5/2}$ in [MacLeod 97], with an accuracy up to 16 digits.

A full closed form approximation, with variable base n , is given by [Bhagat 03]. This approximation still computes reasonably fast and is easy to implement in e.g. MATLAB environments. As this is very useful and appears to be pretty unknown in the ultracold atoms community, it shall be briefly presented in the following.

C.2. How to calculate $g_n(z)$ reasonably fast

For $|z| > 0.55$ (correct up to 4 digits) [Bhagat 03]:

$$g_n(z) = \frac{\Gamma(1-n)}{\alpha^{1-n}} + \frac{b_0 - \alpha \left(b_1 - \frac{4b_0b_4}{7b_3} \right) + \alpha^2 \left(\frac{b_2}{2} + \frac{b_0b_4}{7b_2} - \frac{4b_1b_4}{7b_3} \right) - \alpha^3 \left(\frac{b_3}{6} - \frac{2b_0b_4}{105b_1} + \frac{b_1b_4}{7b_2} - \frac{2b_2b_4}{7b_3} \right)}{1 + \alpha \frac{4b_4}{7b_3} + \alpha^2 \frac{b_4}{7b_2} + \alpha^3 \frac{2b_4}{105b_1} + \alpha^4 \frac{b_4}{840b_0}} \quad (\text{C.2})$$

with $b_i = \zeta(n-i)$ and

$$\zeta(n) = \frac{2^{n-1}}{2^{n-1}-1} \times \dots$$

$$\dots \times \frac{\left(1 + 36 \cdot 2^n S_2^{(n)} + 315 \cdot 3^n S_3^{(n)} + 1120 \cdot 4^n S_4^{(n)} + 1890 \cdot 5^n S_5^{(n)} + 1512 \cdot 6^n S_6^{(n)} + 462 \cdot 7^n S_7^{(n)} \right)}{(1 + 36 \cdot 2^n + 315 \cdot 3^n + 1120 \cdot 4^n + 1890 \cdot 5^n + 1512 \cdot 6^n + 462 \cdot 7^n)} \quad (\text{C.3})$$

with $S_l^{(n)} = \sum_{k=1}^l \frac{z^k}{k^n}$ being defined as the partial sums of eq. C.1.

For large negative n eq. C.3 does not give correct results but can be used in conjunction with the following expression

$$\zeta(1-n) = \pi^n 2^{1-n} \Gamma(n) \cos\left(\frac{n\pi}{2}\right) \zeta(n). \quad (\text{C.4})$$

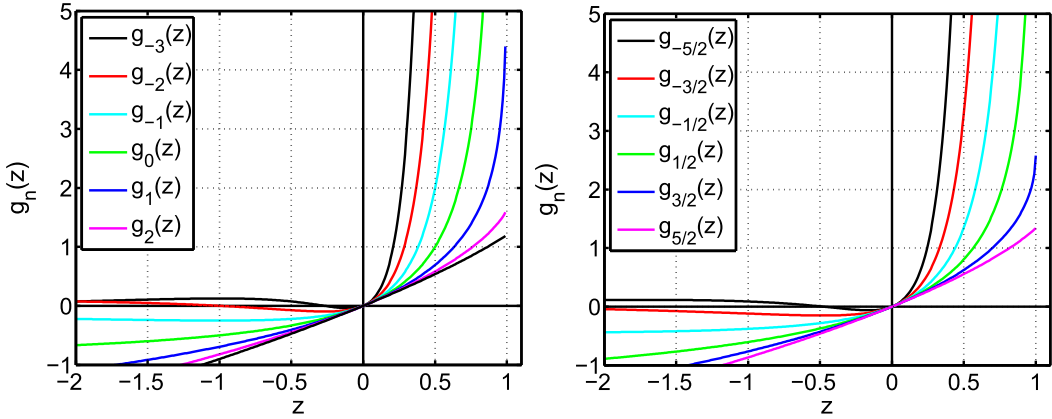


Figure C.1.: Bose-Einstein functions $g_n(z)$ for integer bases $n = -3, -2, \dots, +2$ (left) and non-integer bases $n = -5/2, -3/2, \dots, +3/2$ (right) calculated using the closed form approximations. Whereas $g_{3/2}(1) = 2.612$, $g_{1/2}(z)$ diverges for $z \rightarrow 1$.

For $|z| < 0.55$ (correct up to 10 digits) [Bhagat 03]:

C. Bose-Einstein functions $g_n(x)$

$$g_n(z) = \frac{nom}{denom} \quad (C.5)$$

$$\begin{aligned} nom &= 6435 9^n S_8^{(n)} - 27456 8^n S_7^{(n)} z + 48048 7^n S_6^{(n)} z^2 - 44352 6^n S_5^{(n)} z^3 + \dots \\ &\dots + 23100 5^n S_4^{(n)} z^4 - 6720 4^n S_3^{(n)} z^5 + 1008 3^n S_2^{(n)} z^6 - 64 2^n S_1^{(n)} z^7 \end{aligned} \quad (C.6)$$

$$\begin{aligned} denom &= 6435 9^n - 27456 8^n z + 48048 7^n z^2 - 44352 6^n z^3 + \dots \\ &\dots + 23100 5^n z^4 - 6720 4^n z^5 + 1008 3^n z^6 - 64 2^n z^7 + z^8 \end{aligned} \quad (C.7)$$

A MATLAB implementation can be provided upon request¹.

¹kuhnert@ati.ac.at

D Appendix D.

Error Estimation via Bootstrapping

The error of the density ripples as well as of the $C(L)$ measurement is estimated by a bootstrapping method [Hughes 10]. For simplicity only the latter case shall be discussed in the following.

Bootstrapping means that the acquired data, in our case the $C_i(L)$ data of N absorption pictures, for $i = 1 \dots N$, is randomly sampled with replacement. Each bootstrapped sample $\langle C(L) \rangle_n$ consists of N randomly selected pictures. The mean of these N random samples gives the bootstrapped data $\langle C(L) \rangle_n$ to be fitted by eq. 5.12, where $\langle C(L) \rangle_n = \langle C_{randi([1, N], N)}(L) \rangle$ and $randi([1, N], N)$ generates N random integers in the interval $[1, N]$. Fig. D.1a and Fig. D.1b show the distribution of 1000 bootstrapped samples (blue bars) for the two different data sets of Fig. 5.20, which are indeed normally distributed as tested by fitting a Gaussian distribution (solid red line). This fact ensures that the bootstrapping works and sufficient bootstrapping samples have been generated. The rms fit errors are typically much smaller than the obtained uncertainties of the bootstrapping method and are therefore neglected.

In summary, the bootstrapping helps to properly include the statistical shot to shot fluctuations of the experiment in the error estimate, which are not part of the rms fit errors.

D. Error Estimation via Bootstrapping

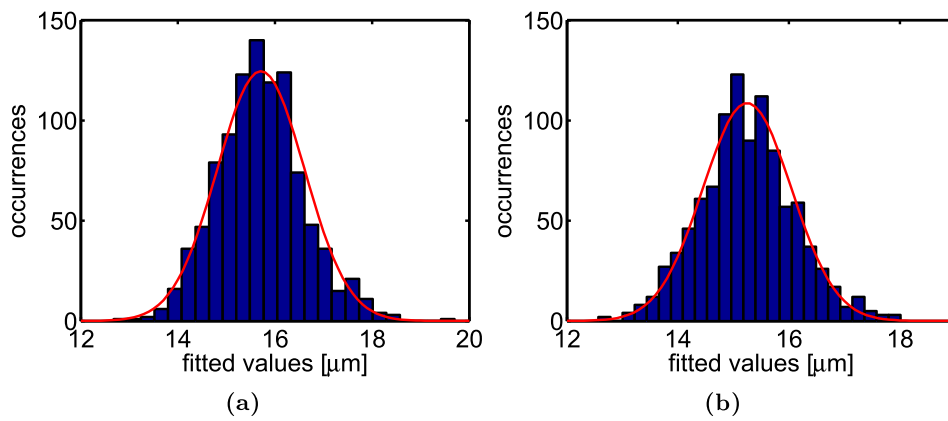


Figure D.1.: Bootstrapped distributions of Fig. 5.20 (a) and (b) respectively. To determine the statistical uncertainty of the fit, the distribution of 1000 bootstrapped samples (blue bars) is used, which is shown to be normally distributed (red solid line).

E Appendix E.

List of Publications

The following publications are related to the work presented in this thesis:

- *Relaxation and Prethermalization in an Isolated Quantum System*
M. Gring, M. Kuhnert, T. Langen, T. Kitagawa, B. Rauer, M. Schreitl, I. E. Mazets, D. Adu Smith, E. Demler and J. Schmiedmayer
Science, 337, 1318-1322 (2012)
- *Multimode dynamics and emergence of a characteristic length-scale in a one-dimensional quantum system*
M. Kuhnert, R. Geiger, T. Langen, M. Gring, B. Rauer, T. Kitagawa, E. Demler, D. Adu Smith and J. Schmiedmayer
Phys. Rev. Lett., 110, 090405 (2013)
- *Prethermalization Revealed by the Relaxation Dynamics of Full Distribution Functions*
D. Adu Smith, M. Gring, T. Langen, M. Kuhnert, B. Rauer, R. Geiger, T. Kitagawa, I. E. Mazets, E. Demler and J. Schmiedmayer
New J. Phys. 15 075011 (2013)
- *Prethermalization in one-dimensional Bose gases: description by a stochastic Ornstein-Uhlenbeck process*
T. Langen, M. Gring, M. Kuhnert, B. Rauer, R. Geiger, D. Adu Smith, I. E. Mazets and J. Schmiedmayer
The European Physical Journal Special Topics, 217, 43-53, (2013)
- *Local emergence of thermal correlations in an isolated quantum many-body system*
T. Langen, R. Geiger, M. Kuhnert, B. Rauer and J. Schmiedmayer
Nat. Phys. 9, 640–643 (2013)

E. List of Publications

- *Thermalization and Prethermalization in the 1D/3D Crossover*
M. Kuhnert, T. Langen, R. Geiger, B. Rauer, T. Schweigler, I. Mazets and J. Schmiedmayer
in preparation

Bibliography

- [Aarts 00] G. Aarts, G. F. Bonini & C. Wetterich. *Exact and truncated dynamics in nonequilibrium field theory*. Phys. Rev. D, vol. 63, page 025012, Dec 2000.
- [Aigner 08] S. Aigner, L. Della Pietra, Y. Japha, O. Entin-Wohlman, T. David, R. Salem, R. Folman & J. Schmiedmayer. *Long-Range Order in Electronic Transport Through Disordered Metal Films*. Science, vol. 319, no. 5867, pages 1226–1229, 2008.
- [Ananikian 06] D. Ananikian & T. Bergeman. *Gross-Pitaevskii equation for Bose particles in a double-well potential: Two-mode models and beyond*. Phys. Rev. A, vol. 73, no. 1, page 013604, Jan 2006.
- [Anderson 95] M. H. Anderson, J. R. Ensher, M. R. Matthews, C. E. Wieman & E. A. Cornell. *Observation of Bose-Einstein Condensation in a Dilute Atomic Vapor*. Science, vol. 269, no. 5221, pages 198–201, 1995.
- [Andrews 97a] M. R. Andrews, D. M. Kurn, H.-J. Miesner, D. S. Durfee, C. G. Townsend, S. Inouye & W. Ketterle. *Propagation of Sound in a Bose-Einstein Condensate*. Phys. Rev. Lett., vol. 79, pages 553–556, Jul 1997.
- [Andrews 97b] M. R. Andrews, C. G. Townsend, H.-J. Miesner, D. S. Durfee, D. M. Kurn & W. Ketterle. *Observation of Interference Between Two Bose Condensates*. Science (New York, N.Y.), vol. 275, no. 5300, pages 637–641, January 1997.
- [Armijo 11a] J. Armijo. *Fluctuations de densité dans des gaz de bosons ultrafroids quasi-unidimensionnels*. PhD thesis, Laboratoire Charles Fabry de l'Institut d'Optique Ecole doctorale de Physique de la région parisienne, 2011.
- [Armijo 11b] J. Armijo, T. Jacqmin, K. Kheruntsyan & I. Bouchoule. *Mapping out the quasicondensate transition through the dimensional crossover from one to three dimensions*. Phys. Rev. A, vol. 83, no. 2, page 021605, Feb 2011.
- [Arnol'd 63] V I Arnol'd. *Proof of a theorem of A.Â N.Â Kolmogorov on the invariance of quasi-periodic motions under small perturbations of the*

Bibliography

- hamiltonian*. Russian Mathematical Surveys, vol. 18, no. 5, page 9, 1963.
- [Arnold 99] A. Arnold. *Preparation and Manipulation of an ^{87}Rb Bose-Einstein Condensate*. PhD thesis, University of Sussex, 1999.
- [Bañuls 11] M. C. Bañuls, J. I. Cirac & M. B. Hastings. *Strong and Weak Thermalization of Infinite Nonintegrable Quantum Systems*. Phys. Rev. Lett., vol. 106, no. 5, page 050405, Feb 2011.
- [Bagnato 91] M. . Bagnato VandAndrews. *Bose-Einstein condensation in low-dimensional traps*. Phys. Rev. A, vol. 44, pages 7439–7441, Dec 1991.
- [Bali 99] S. Bali, K. M. O’Hara, M. E. Gehm, S. R. Granade & J. E. Thomas. *Quantum-diffractive background gas collisions in atom-trap heating and loss*. Phys. Rev. A, vol. 60, pages R29–R32, Jul 1999.
- [Barnett 11] R. Barnett, A. Polkovnikov & M. Vengalattore. *Prethermalization in quenched spinor condensates*. Phys. Rev. A, vol. 84, no. 2, page 023606, Aug 2011.
- [Berges 04] J. Berges, Sz. Borsányi & C. Wetterich. *Prethermalization*. Phys. Rev. Lett., vol. 93, page 142002, 2004.
- [Berges 08] J. Berges, A. Rothkopf & J. Schmidt. *Nonthermal Fixed Points: Effective Weak Coupling for Strongly Correlated Systems Far from Equilibrium*. Phys. Rev. Lett., vol. 101, page 041603, Jul 2008.
- [Bethe 31] H. Bethe. *Zur Theorie der Metalle*. Zeitschrift für Physik, vol. 71, pages 205–226, 1931.
- [Betz 11] T. Betz, S. Manz, R. Bücken, T. Berrada, Ch. Koller, G. Kazakov, I. E. Mazets, H.-P. Stimming, A. Perrin, T. Schumm & J. Schmiedmayer. *Two-Point Phase Correlations of a One-Dimensional Bosonic Josephson Junction*. Phys. Rev. Lett., vol. 106, no. 2, page 020407, Jan 2011.
- [Bhagat 03] V. Bhagat, R. Bhattacharya & D. Roy. *On the evaluation of generalized Bose-Einstein and Fermi-Dirac integrals*. Computer Physics Communications, vol. 155, no. 1, pages 7 – 20, 2003.
- [Biroli 10] G. Biroli, C. Kollath & A. M. Läuchli. *Effect of Rare Fluctuations on the Thermalization of Isolated Quantum Systems*. Phys. Rev. Lett., vol. 105, page 250401, Dec 2010.
- [Bistritzer 07] R. Bistritzer & E. Altman. *Intrinsic dephasing in one-dimensional ultracold atom interferometers*. PNAS, vol. 104, no. 24, pages 9955–9, June 2007.

Bibliography

- [Blanter 00] Ya. M. Blanter & M. Büttiker. *Shot noise in mesoscopic conductors*. Physics Reports, vol. 336, pages 1–166, 2000.
- [Bogoliubov 47] N. N. Bogoliubov. *On the Theory of Superfluidity*. Journal of Physics, vol. 11, page 23, 1947.
- [Bohr 28] N. Bohr. *The Quantum Postulate and the Recent Development of Atomic Theory*. Nature, vol. 121, pages 580–590, 1928.
- [Bonini 99] G. Franco Bonini & C. Wetterich. *Time evolution of correlation functions and thermalization*. Phys. Rev. D, vol. 60, page 105026, Oct 1999.
- [Bouchoule 07] I. Bouchoule, K. V. Kheruntsyan & G. V. Shlyapnikov. *Interaction-induced crossover versus finite-size condensation in a weakly interacting trapped one-dimensional Bose gas*. Phys. Rev. A, vol. 75, page 031606, Mar 2007.
- [Bouchoule 11] I. Bouchoule, N. J. van Druten & C. I. Westbrook. *Atom chips and one-dimensional bose gases*, pages 331–363. Wiley-VCH Verlag GmbH & Co. KGaA, 2011.
- [Bradley 95] C. C. Bradley, C. A. Sackett, J. J. Tollett & R. G. Hulet. *Evidence of Bose-Einstein Condensation in an Atomic Gas with Attractive Interactions*. Phys. Rev. Lett., vol. 75, pages 1687–1690, Aug 1995.
- [Brajdic 02] M. Brajdic. *Entwicklung einer computersteuerung und ihre anwendung in einem experiment zur vereinfachten bose-einstein kondensation in einer oberflächenfalle*. Master’s thesis, Universität Heidelberg, 2002.
- [Brink 06] D. M. Brink & C. V. Sukumar. *Majorana spin-flip transitions in a magnetic trap*. Phys. Rev. A, vol. 74, page 035401, Sep 2006.
- [Brunello 00] A. Brunello, F. Dalfovo, L. Pitaevskii & S. Stringari. *How to Measure the Bogoliubov Quasiparticle Amplitudes in a Trapped Condensate*. Phys. Rev. Lett., vol. 85, pages 4422–4425, Nov 2000.
- [Burkov 07] A. A. Burkov, M. D. Lukin & E. Demler. *Decoherence Dynamics in Low-Dimensional Cold Atom Interferometers*. Phys. Rev. Lett., vol. 98, no. 20, page 200404, May 2007.
- [Burt 97] E. A. Burt, R. W. Ghrist, C. J. Myatt, M. J. Holland, E. A. Cornell & C. E. Wieman. *Coherence, Correlations, and Collisions: What One Learns about Bose-Einstein Condensates from Their Decay*. Phys. Rev. Lett., vol. 79, pages 337–340, Jul 1997.

Bibliography

- [Calogero 69] F. Calogero. *Solution of a Three-Body Problem in One Dimension*. Journal of Mathematical Physics, vol. 10, no. 12, pages 2191–2196, 1969.
- [Cassidy 11] A. C. Cassidy, C. W. Clark & M. Rigol. *Generalized Thermalization in an Integrable Lattice System*. Phys. Rev. Lett., vol. 106, page 140405, Apr 2011.
- [Castin 97] Y. Castin & J. Dalibard. *Relative phase of two Bose-Einstein condensates*. Phys. Rev. A, vol. 55, pages 4330–4337, Jun 1997.
- [Castin 04] Y. Castin. *Simple theoretical tools for low dimension Bose gases*. J. Phys. IV, vol. 116, page 89, 2004.
- [Cazalilla 04] M. A. Cazalilla. *Bosonizing one-dimensional cold atomic gases*. Journal of Physics B: Atomic, Molecular and Optical Physics, vol. 37, no. 7, page S1, 2004.
- [Cazalilla 11] M. A. Cazalilla, R. Citro, T. Giamarchi, E. Orignac & M. Rigol. *One dimensional bosons: From condensed matter systems to ultracold gases*. Rev. Mod. Phys., vol. 83, pages 1405–1466, Dec 2011.
- [Cirac 12] J. Ignacio Cirac & Peter Zoller. *Goals and opportunities in quantum simulation*. Nat Phys, vol. 8, no. 4, pages 264–266, April 2012.
- [Das 03] K. K. Das. *Bose-Fermi Mixtures in One Dimension*. Phys. Rev. Lett., vol. 90, page 170403, May 2003.
- [David 08] T. David, Y. Japha, V. Dikovsky, R. Salem, C. Henkel & R. Folman. *Magnetic interactions of cold atoms with anisotropic conductors*. The European Physical Journal D, vol. 48, pages 321–332, 2008.
- [Davis 95] K. B. Davis, M. O. Mewes, M. R. Andrews, N. J. van Druten, D. S. Durfee, D. M. Kurn & W. Ketterle. *Bose-Einstein Condensation in a Gas of Sodium Atoms*. Phys. Rev. Lett., vol. 75, pages 3969–3973, Nov 1995.
- [Dettmer 01] S. Dettmer, D. Hellweg, P. Ryytty, J. J. Arlt, W. Ertmer, K. Sengstock, D. S. Petrov, G. V. Shlyapnikov, H. Kreutzmann, L. Santos & M. Lewenstein. *Observation of Phase Fluctuations in Elongated Bose-Einstein Condensates*. Phys. Rev. Lett., vol. 87, page 160406, Oct 2001.
- [Deuar 09] P. Deuar, A. G. Sykes, D. M. Gangardt, M. J. Davis, P. D. Drummond & K. V. Kheruntsyan. *Nonlocal pair correlations in the one-dimensional Bose gas at finite temperature*. Phys. Rev. A, vol. 79, page 043619, Apr 2009.

Bibliography

- [Deutsch 91] J. M. Deutsch. *Quantum statistical mechanics in a closed system*. Phys. Rev. A, vol. 43, pages 2046–2049, Feb 1991.
- [Dikovskiy 05] V. Dikovskiy, Y. Japha, C. Henkel & R. Folman. *Reduction of magnetic noise in atom chips by material optimization*. The European Physical Journal D - Atomic, Molecular, Optical and Plasma Physics, vol. 35, pages 87–95, 2005.
- [Donner 07] T. Donner, S. Ritter, T. Bourdel, A. Öttl, M. Köhl & T. Esslinger. *Critical Behavior of a Trapped Interacting Bose Gas*. Science, vol. 315, no. 5818, pages 1556–1558, 2007.
- [D.S. Petrov 04] D.S. Petrov, D.M. Gangardt & G.V. Shlyapnikov. *Low-dimensional trapped gases*. J. Phys. IV France, vol. 116, pages 5–44, 2004.
- [Earnshaw 33] S. Earnshaw. *On the nature of the molecular forces which regulate the constitution of the luminiferous ether*. Transactions of the Cambridge Philosophical Society., vol. 7, 1833.
- [Eckstein 09a] M. Eckstein, A. Hackl, S. Kehrein, M. Kollar, M. Moeckel, P. Werner & F.A. Wolf. *New theoretical approaches for correlated systems in nonequilibrium*. The European Physical Journal - Special Topics, vol. 180, pages 217–235, 2009. 10.1140/epjst/e2010-01219-x.
- [Eckstein 09b] M. Eckstein, M. Kollar & P. Werner. *Thermalization after an Interaction Quench in the Hubbard Model*. Phys. Rev. Lett., vol. 103, page 056403, 2009.
- [Efron 79] B. Efron. *Bootstrap Methods: Another Look at the Jackknife*. Ann. Statist., vol. 7, pages 1–26, 1979.
- [Erhard 04] M. Erhard. *Experimente mit mehrkomponentigen Bose-Einstein-Kondensaten*. PhD thesis, Universität Hamburg, 2004.
- [Esry 99] B. D. Esry, Chris H. Greene & James P. Burke. *Recombination of Three Atoms in the Ultracold Limit*. Phys. Rev. Lett., vol. 83, pages 1751–1754, Aug 1999.
- [Esteve 06] J. Esteve, J.-B. Trebbia, T. Schumm, A. Aspect, C. I. Westbrook & I. Bouchoule. *Observations of Density Fluctuations in an Elongated Bose Gas: Ideal Gas and Quasicondensate Regimes*. Phys. Rev. Lett., vol. 96, page 130403, Apr 2006.
- [Faye 08] J. Faye. *Copenhagen Interpretation of Quantum Mechanics*. In Edward N. Zalta, editeur, The Stanford Encyclopedia of Philosophy. Fall 2008 edition, 2008.

Bibliography

- [Feynman 82] R. P. Feynman. *Simulating physics with computers*. International Journal of Theoretical Physics, vol. 21, no. 6-7, pages 467–488, 1982.
- [Fisher 95] N. I. Fisher. Statistical analysis of circular data. Cambridge University Press, 1995.
- [Folman 00] R. Folman, P. Krüger, D. Cassettari, B. Hessmo, T. Maier & J. Schmiedmayer. *Controlling Cold Atoms using Nanofabricated Surfaces: Atom Chips*. Phys. Rev. Lett., vol. 84, page 4749, 2000.
- [Folman 02] R. Folman, P. Kruger, J. Schmiedmayer, J. Denschlag & C. Henkel. *Microscopic atom optics: from wires to an atom chip*. Adv. At. Mol. Opt. Phys., vol. 48, pages 263–356, 2002.
- [Fortágh 02] J. Fortágh, H. Ott, S. Kraft, A. Günther & C. Zimmermann. *Surface effects in magnetic microtraps*. Phys. Rev. A, vol. 66, page 041604, Oct 2002.
- [Fortágh 07] J. Fortágh & C. Zimmermann. *Magnetic microtraps for ultracold atoms*. Rev. Mod. Phys., vol. 79, pages 235–289, Feb 2007.
- [Fuchs 03] J. N. Fuchs, X. Leyronas & R. Combescot. *Hydrodynamic modes of a one-dimensional trapped Bose gas*. Phys. Rev. A, vol. 68, page 043610, Oct 2003.
- [Gardiner 85] C. Gardiner. Handbook of stochastic methods: for physics, chemistry and the natural sciences. Springer, 1985.
- [Gasenzer 05] T. Gasenzer, J. Berges, M. G. Schmidt & M. Seco. *Nonperturbative dynamical many-body theory of a Bose-Einstein condensate*. Phys. Rev. A, vol. 72, page 063604, Dec 2005.
- [Gasenzer 09] T. Gasenzer. *Ultracold gases far from equilibrium*. The European Physical Journal Special Topics, vol. 168, no. 1, pages 89–148, 2009.
- [Göbel 08] M. Göbel. *Low-Dimensional Traps for Bose-Fermi Mixtures*. PhD thesis, Universität Heidelberg, 2008.
- [Gehm 98] M. E. Gehm, K. M. O’Hara, T. A. Savard & J. E. Thomas. *Dynamics of noise-induced heating in atom traps*. Phys. Rev. A, vol. 58, pages 3914–3921, Nov 1998.
- [Gerbier 04] F. Gerbier. *Quasi-1D Bose-Einstein condensates in the dimensional crossover regime*. Europhysics Letters, vol. 66, pages 771–777, 2004.
- [Gerlach 22] W. Gerlach & O. Stern. *Der experimentelle Nachweis der Richtungsquantelung im Magnetfeld*. Zeitschrift für Physik, vol. 9, no. 1, pages 349–352, 1922.

Bibliography

- [Giamarchi 04] T. Giamarchi. Quantum physics in one dimension. Internat. Ser. Mono. Phys. Clarendon Press, Oxford, 2004.
- [Gillespie 96] D. T. Gillespie. *Exact numerical simulation of the Ornstein-Uhlenbeck process and its integral*. Phys. Rev. E, vol. 54, pages 2084–2091, Aug 1996.
- [Girardeau 60] M. Girardeau. *Relationship between Systems of Impenetrable Bosons and Fermions in One Dimension*. Journal of Mathematical Physics, vol. 1, no. 6, pages 516–523, 1960.
- [Glauber 63] R. J. Glauber. *The Quantum Theory of Optical Coherence*. Phys. Rev., vol. 130, pages 2529–2539, Jun 1963.
- [Goldstein 10] S. Goldstein, J. L. Lebowitz, C. Mastrodonato, R. Tumulka & N. Zanghi. *Normal typicality and von Neumann’s quantum ergodic theorem*. Proceedings of the Royal Society A: Mathematical, Physical and Engineering Sciences, vol. 466, no. 2123, pages 3203–3224, May 2010.
- [Görlitz 01] A. Görlitz, J. M. Vogels, A. E. Leanhardt, C. Raman, T. L. Gustavson, J. R. Abo-Shaer, A. P. Chikkatur, S. Gupta, S. Inouye, T. Rosenband & W. Ketterle. *Realization of Bose-Einstein Condensates in Lower Dimensions*. Phys. Rev. Lett., vol. 87, page 130402, Sep 2001.
- [Gov 00] S. Gov, S. Shtrikman & H. Thomas. *Magnetic trapping of neutral particles: Classical and quantum-mechanical study of a Ioffe-Pritchard type trap*. Journal of Applied Physics, vol. 87, no. 8, pages 3989–3998, 2000.
- [Greiner 01] M. Greiner, I. Bloch, O. Mandel, T. W. Hänsch & T. Esslinger. *Exploring Phase Coherence in a 2D Lattice of Bose-Einstein Condensates*. Phys. Rev. Lett., vol. 87, page 160405, Oct 2001.
- [Greiner 02] M. Greiner, T. W. Mandel O.and Hansch & I. Bloch. *Collapse and revival of the matter wave field of a Bose-Einstein condensate*. Nature, vol. 419, no. 6902, pages 51–54, September 2002.
- [Gring 12a] M. Gring. *Prethermalization in an Isolated Many Body System*. PhD thesis, Technische Universität Wien, 2012.
- [Gring 12b] M. Gring, M. Kuhnert, T. Langen, T. Kitagawa, B. Rauer, M. Schreitl, I. Mazets, D. Adu Smith, E. Demler & J. Schmiedmayer. *Relaxation and Prethermalization in an Isolated Quantum System*. Science, vol. 337, no. 6100, pages 1318–1322, 2012.

Bibliography

- [Grisins 11] P. Grisins & I. E. Mazets. *Thermalization in a one-dimensional integrable system*. Phys. Rev. A, vol. 84, page 053635, Nov 2011.
- [Grisins 14] P. Grisins, B. Rauer, R. Geiger, T. Langen, M. Kuhnert, T. Schweigler, I. Mazets & J. Schmiedmayer. *Evaporative Cooling of one-dimensional Bose gases*. in preparation, 2014.
- [Gross 61] E.P. Gross. *Structure of a quantized vortex in boson systems*. II Nuovo Cimento Series 10, vol. 20, no. 3, pages 454–477, 1961.
- [Gutzwiller 91] M. C. Gutzwiller. *Chaos in classical and quantum mechanics*. Springer, 1991.
- [Haldane 81a] F. D. M. Haldane. *Effective Harmonic-Fluid Approach to Low-Energy Properties of One-Dimensional Quantum Fluids*. Phys. Rev. Lett., vol. 47, pages 1840–1843, Dec 1981.
- [Haldane 81b] F. D. M. Haldane. *'Luttinger liquid theory' of one-dimensional quantum fluids. I. Properties of the Luttinger model and their extension to the general 1D interacting spinless Fermi gas*. Journal of Physics C: Solid State Physics, vol. 14, no. 19, page 2585, 1981.
- [Hall 98] D. S. Hall, M. R. Matthews, C. E. Wieman & E. A. Cornell. *Measurements of Relative Phase in Two-Component Bose-Einstein Condensates*. Phys. Rev. Lett., vol. 81, pages 1543–1546, Aug 1998.
- [Haller 09] E. Haller, M. Gustavsson, M.J. Mark, J. G. Danzl & G. and Nägerl H.-C. Hart R.and Pupillo. *Realization of an Excited, Strongly Correlated Quantum Gas Phase*. Science, vol. 325, no. 5945, pages 1224–1227, 2009.
- [Haller 10] Elmar Haller, Manfred J. Mark, Russell Hart, Johann G. Danzl, Lukas Reichsöllner, Vladimir Melezhik, Peter Schmelcher & Hanns-Christoph Nägerl. *Confinement-Induced Resonances in Low-Dimensional Quantum Systems*. Phys. Rev. Lett., vol. 104, page 153203, Apr 2010.
- [Hanbury Brown 56] R. Hanbury Brown & R. Q. Twiss. *Correlation between photons in two coherent beams of light*. Nature, vol. 177, pages 27–29, 1956.
- [Hellweg 01] D. Hellweg, S. Dettmer, P. Ryytty, J.J. Arlt, W. Ertmer, K. Sengstock, D.S. Petrov, G.V. Shlyapnikov, H. Kreutzmann, L. Santos & M. Lewenstein. *Phase fluctuations in Bose-Einstein condensates*. Applied Physics B, vol. 73, no. 8, pages 781–789, 2001.
- [Henkel 99] C. Henkel, S. Pötting & M. Wilkens. *Loss and heating of particles in small and noisy traps*. Applied Physics B, vol. 69, pages 379–387, 1999.

Bibliography

- [Henkel 03] C. Henkel, P. Krüger, R. Folman & J. Schmiedmayer. *Fundamental limits for coherent manipulation on atom chips*. Applied Physics B, vol. 76, pages 173–182, 2003.
- [Hessmo 13] B. Hessmo, private communications, 02. 2013.
- [Hofferberth 07] S. Hofferberth, I. Lesanovsky, B. Fischer, T. Schumm & J. Schmiedmayer. *Non-equilibrium coherence dynamics in one-dimensional Bose gases*. Nature, vol. 449, pages 324–327, September 2007.
- [Hofferberth 08] S. Hofferberth, I. Lesanovsky, T. Schumm, A. Imambekov, V. Gritsev, E. Demler & J. Schmiedmayer. *Probing quantum and thermal noise in an interacting many-body system*. Nature Physics, vol. 4, pages 489–495, 2008.
- [Hohenberg 67] P. C. Hohenberg. *Existence of Long-Range Order in One and Two Dimensions*. Phys. Rev., vol. 158, pages 383–386, Jun 1967.
- [Huang 87] K. Huang. Statistical mechanics. J. Wiley, 1987.
- [Hugbart 05] M. Hugbart, J. A. Retter, F. Gerbier, A. F. Varon, S. Richard, J. H. Thywissen, D. Clement, P. Bouyer & A. Aspect. *Coherence length of an elongated condensate*. The European Physical Journal D - Atomic, Molecular, Optical and Plasma Physics, vol. 35, pages 155–163, 2005.
- [Hughes 10] I. Hughes & T. Hase. Measurements and their uncertainties: A practical guide to modern error analysis. Oxford University Press, 2010.
- [Ikeda 13] T. N. Ikeda, N. Sakumichi, A. Polkovnikov & M. Ueda. *Emergent Second Law in Pure Quantum States*. arXiv:1303.5471, 2013.
- [Imambekov 09] A. Imambekov, I. E. Mazets, D. S. Petrov, V. Gritsev, S. Manz, S. Hofferberth, T. Schumm, E. Demler & J. Schmiedmayer. *Density ripples in expanding low-dimensional gases as a probe of correlations*. Phys. Rev. A, vol. 80, no. 3, page 033604, Sep 2009.
- [Jacqmin 11] T. Jacqmin, J. Armijo, T. Berrada, K. V. Kheruntsyan & Isabelle B. *Sub-Poissonian Fluctuations in a 1D Bose Gas: From the Quantum Quasicondensate to the Strongly Interacting Regime*. Phys. Rev. Lett., vol. 106, page 230405, Jun 2011.
- [Javanainen 99] J. Javanainen & M. Y. Ivanov. *Splitting a trap containing a Bose-Einstein condensate: Atom number fluctuations*. Phys. Rev. A, vol. 60, pages 2351–2359, Sep 1999.

Bibliography

- [Jeltes 07] T. Jeltes, J. M. McNamara, W. Hogervorst, W. Vassen, V. Krachmalnicoff, M. Schellekens, A. Perrin, H. Chang, D. Boiron, A. Aspect & C. I. Westbrook. *Comparison of the Hanbury Brown-Twiss effect for bosons and fermions*. Nature, vol. 445, pages 402–405, 2007.
- [Jompol 09] Y. Jompol, C. J. B. Ford, J. P. Griffiths, I. Farrer, G. A. C. Jones, D. Anderson, D. A. Ritchie, T. W. Silk & A. J. Schofield. *Probing Spin-Charge Separation in a Tomonaga-Luttinger Liquid*. Science, vol. 325, no. 5940, pages 597–601, 2009.
- [Karl 13] M. Karl, B. Nowak & T. Gasenzer. *Tuning universality far from equilibrium*. Sci. Rep., vol. 3, pages –, August 2013.
- [Karpiuk 04] T. Karpiuk, M. Brewczyk, S. Ospelkaus-Schwarzer, K. Bongs, M. Gajda & K. Rzażewski. *Soliton Trains in Bose-Fermi Mixtures*. Phys. Rev. Lett., vol. 93, page 100401, Sep 2004.
- [Karpiuk 12] T. Karpiuk, P. Deuar, P. Bienias, E. Witkowska, K. Pawłowski, M. Gajda, K. Rzażewski & M. Brewczyk. *Spontaneous Solitons in the Thermal Equilibrium of a Quasi-1D Bose Gas*. Phys. Rev. Lett., vol. 109, page 205302, Nov 2012.
- [Kasper 03] A. Kasper. *Bose-Einstein condensation in a robust microtrap - the combination of wire traps and atom chips*. PhD thesis, Universität Heidelberg, 2003.
- [Ketterle 96a] W. Ketterle & N. J. van Druten. *Bose-Einstein condensation of a finite number of particles trapped in one or three dimensions*. Phys. Rev. A, vol. 54, pages 656–660, Jul 1996.
- [Ketterle 96b] W. Ketterle & N.J van Druten. *Evaporative cooling of trapped atoms*. Adv. At. Mol. Opt. Phys., vol. 37, page 181, 1996.
- [Ketterle 99] W. Ketterle, D. S. Durfree & D. M. Stamper-Kurn. *Making, probing and understanding bose-einstein condensates*. Proceedings of the 1998 Enrico Fermi school on Bose-Einstein condensation in Varenna, Italy, page 67, 1999.
- [Kheruntsyan 03] K. Kheruntsyan, D. Gangardt, P. Drummond & G. Shlyapnikov. *Pair Correlations in a Finite-Temperature 1D Bose Gas*. Physical Review Letters, vol. 91, no. 4, pages 1–4, July 2003.
- [Kheruntsyan 05] K. Kheruntsyan, D. Gangardt, P. Drummond & G. Shlyapnikov. *Finite-temperature correlations and density profiles of an inhomogeneous interacting one-dimensional Bose gas*. Physical Review A, vol. 71, no. 5, page 053615, May 2005.

Bibliography

- [Kinoshita 04] T. Kinoshita, T. Wenger & D. S. Weiss. *Observation of a One-Dimensional Tonks-Girardeau Gas*. Science, vol. 305, pages 1125–1128, 2004.
- [Kinoshita 06] T. Kinoshita, T. Wenger & D. S. Weiss. *A quantum Newton’s cradle*. Nature, vol. 440, no. 7086, pages 900–903, 04 2006.
- [Kitagawa 10] T. Kitagawa, S. Pielawa, J. Imambekov A.and Schmiedmayer, V. Gritsev & E. Demler. *Ramsey Interference in One-Dimensional Systems: The Full Distribution Function of Fringe Contrast as a Probe of Many-Body Dynamics*. Phys. Rev. Lett., vol. 104, no. 25, page 255302, Jun 2010.
- [Kitagawa 11] T. Kitagawa, A. Imambekov, J. Schmiedmayer & E. Demler. *The dynamics and prethermalization of one dimensional quantum systems probed through the full distributions of quantum noise*. New J. Phys., vol. 13, page 073018, 2011.
- [Kollar 11] M. Kollar, F. A. Wolf & M. Eckstein. *Generalized Gibbs ensemble prediction of prethermalization plateaus and their relation to non-thermal steady states in integrable systems*. Phys. Rev. B, vol. 84, page 054304, Aug 2011.
- [Kollath 06] C. Kollath & U. Schollwöck. *Cold Fermi gases: a new perspective on spin-charge separation*. New Journal of Physics, vol. 8, no. 10, page 220, 2006.
- [Kollath 07] C. Kollath, A. M. Läuchli & E. Altman. *Quench Dynamics and Nonequilibrium Phase Diagram of the Bose-Hubbard Model*. Phys. Rev. Lett., vol. 98, page 180601, Apr 2007.
- [Koller 12] C. Koller, private communications, 10 2012.
- [Kreutzmann 03] H. Kreutzmann, A. Sanpera, L. Santos, M. Lewenstein, D. Hellweg, L. Cacciapuoti, M. Kottke, T. Schulte, K. Sengstock, J.J. Arlt & W. Ertmer. *Characterization and control of phase fluctuations in elongated Bose-Einstein condensates*. Applied Physics B, vol. 76, no. 2, pages 165–172, 2003.
- [Kuhnert 08] M. Kuhnert. *A Dual-Species Two-MOT Setup for Preparing a Bose-Fermi Mixture on an Atom Chip*. PhD thesis, Vienna University of Technology, 2008.
- [Kuhnert 13] M. Kuhnert, R. Geiger, T. Langen, M. Gring, B. Rauer, T. Kitagawa, E. Demler, D. Adu Smith & J. Schmiedmayer. *Multimode Dynamics and Emergence of a Characteristic Length Scale in a One-Dimensional Quantum System*. Phys. Rev. Lett., vol. 110, page 090405, Feb 2013.

Bibliography

- [Landau 96] L. D. Landau & E. M. Lifshitz. *Statistical physics*. Butterworth Heinemann, 1996.
- [Langen 13a] T. Langen. *tba.* PhD thesis, University of Technology, 2013.
- [Langen 13b] T. Langen, M. Gring, M. Kuhnert, B. Rauer, R. Geiger, D. Adu Smith, I. E. Mazets & J. Schmiedmayer. *Prethermalization in one-dimensional Bose gases: description by a stochastic Ornstein-Uhlenbeck process*. *The European Physical Journal Special Topics*, vol. 217, page 43, 2013.
- [Leggett 01] A. J. Leggett. *Bose-Einstein condensation in the alkali gases: Some fundamental concepts*. *Rev. Mod. Phys.*, vol. 73, pages 307–356, Apr 2001.
- [Lesanovsky 06] I. Lesanovsky, T. Schumm, S. Hofferberth, L. M. Andersson, P. Krüger & J. Schmiedmayer. *Adiabatic radio frequency potentials for the coherent manipulation of matter waves*. *Phys. Rev. A*, vol. 73, page 033619, 2006.
- [Lewenstein 96] M. Lewenstein & L. You. *Quantum Phase Diffusion of a Bose-Einstein Condensate*. *Phys. Rev. Lett.*, vol. 77, pages 3489–3493, Oct 1996.
- [Lieb 63a] E. H. Lieb. *Exact Analysis of an Interacting Bose Gas. II. The Excitation Spectrum*. *Phys. Rev.*, vol. 130, pages 1616–1624, May 1963.
- [Lieb 63b] E. H. Lieb & W. Liniger. *Exact Analysis of an Interacting Bose Gas. I. The General Solution and the Ground State*. *Physical Review*, vol. 130, no. 4, pages 1605–1616, May 1963.
- [Linden 09] N. Linden, S. Popescu, A. J. Short & A. Winter. *Quantum mechanical evolution towards thermal equilibrium*. *Phys. Rev. E*, vol. 79, page 061103, Jun 2009.
- [MacLeod 97] A. J. MacLeod. *Accurate and efficient evaluation of the Bose-Einstein functions $g_{3/2}$ and $g_{5/2}$* . *Computers in Physics*, vol. 11, pages 385–387, July 1997.
- [Manmana 07] S. R. Manmana, S. Wessel, R. M. Noack & A. Muramatsu. *Strongly Correlated Fermions after a Quantum Quench*. *Phys. Rev. Lett.*, vol. 98, page 210405, May 2007.
- [Manz 10] S. Manz, R. Buecker, T. Betz, Ch. Koller, S. Hofferberth, I. E. Mazets, A. Imambekov, E. Demler, A. Perrin, J. Schmiedmayer & T. Schumm. *Two-point density correlations of quasicondensates in free expansion*. *Phys. Rev. A*, vol. 81, no. 3, MAR 2010.

Bibliography

- [Manz 11] S. Manz. *Density correlations of expanding one-dimensional Bose gases*. PhD thesis, Technische Universität Wien, 2011.
- [Marte 03] A. Marte. *Feshbach-Resonanzen bei Stößen ultrakalter Rubidiumatome*. PhD thesis, Technische Universität München, 2003.
- [Mateo 08] A. Muñoz Mateo & V. Delgado. *Effective mean-field equations for cigar-shaped and disk-shaped Bose-Einstein condensates*. Phys. Rev. A, vol. 77, page 013617, Jan 2008.
- [Mathey 10] L. Mathey & A. Polkovnikov. *Light cone dynamics and reverse Kibble-Zurek mechanism in two-dimensional superfluids following a quantum quench*. Phys. Rev. A, vol. 81, page 033605, 2010.
- [Mazets 08] I. E. Mazets, T. Schumm & J. Schmiedmayer. *Breakdown of Integrability in a Quasi-1D Ultracold Bosonic Gas*. Phys. Rev. Lett., vol. 100, no. 21, page 210403, May 2008.
- [Mazets 10] I. E. Mazets & J. Schmiedmayer. *Thermalization in a quasi-one-dimensional ultracold bosonic gas*. New J. Phys., vol. 12, no. 5, page 055023, 2010.
- [Mermin 66] N. D. Mermin & H. Wagner. *Absence of Ferromagnetism or Antiferromagnetism in One- or Two-Dimensional Isotropic Heisenberg Models*. Phys. Rev. Lett., vol. 17, pages 1133–1136, Nov 1966.
- [Mewes 96] M.-O. Mewes, M. R. Andrews, N. J. van Druten, D. M. Kurn, D. S. Durfee & W. Ketterle. *Bose-Einstein Condensation in a Tightly Confining dc Magnetic Trap*. Phys. Rev. Lett., vol. 77, pages 416–419, Jul 1996.
- [Miesner 98] H.-J. Miesner, D. M. Stamper-Kurn, M. R. Andrews, D. S. Durfee, S. Inouye & W. Ketterle. *Bosonic Stimulation in the Formation of a Bose-Einstein Condensate*. Science, vol. 279, no. 5353, pages 1005–1007, 1998.
- [Mitra 13] A. Mitra. *Correlation functions in the prethermalized regime after a quantum quench of a spin chain*. Phys. Rev. B, vol. 87, page 205109, May 2013.
- [Moeckel 08] Michael Moeckel & Stefan Kehrein. *Interaction Quench in the Hubbard Model*. Phys. Rev. Lett., vol. 100, page 175702, May 2008.
- [Moeckel 10] M. Moeckel & S. Kehrein. *Crossover from adiabatic to sudden interaction quenches in the Hubbard model: prethermalization and non-equilibrium dynamics*. New J. Phys., vol. 12, no. 5, page 055016, 2010.

Bibliography

- [Mohr 08] P. J. Mohr, B. N. Taylor & D. B. Newell. *CODATA recommended values of the fundamental physical constants: 2006*. Rev. Mod. Phys., vol. 80, pages 633–730, Jun 2008.
- [Moore 09] J. H. Moore. *Building scientific apparatus*. Cambridge University Press, 2009.
- [Mora 03] C. Mora & Y. Castin. *Extension of Bogoliubov theory to quasicondensates*. Phys. Rev. A, vol. 67, no. 5, page 053615, May 2003.
- [Moritz 03] T. Moritz, H. Stöferle, M. Köhl & T. Esslinger. *Exciting Collective Oscillations in a Trapped 1D Gas*. Phys. Rev. Lett., vol. 91, no. 25, page 250402, Dec 2003.
- [Moritz 05] H. Moritz, T. Stöferle, Kenneth G. & T. Köhl M. and Esslinger. *Confinement Induced Molecules in a 1D Fermi Gas*. Phys. Rev. Lett., vol. 94, page 210401, Jun 2005.
- [Morrison 98] R. Morrison. *Grounding and shielding techniques*. Wiley-Interscience, 1998.
- [Naraschewski 98] M. Naraschewski & D. M. Stamper-Kurn. *Analytical description of a trapped semi-ideal Bose gas at finite temperature*. Phys. Rev. A, vol. 58, pages 2423–2426, Sep 1998.
- [Neumann 29] J.v. Neumann. *Beweis des Ergodensatzes und des H-Theorems in der neuen Mechanik*. Zeitschrift für Physik, vol. 57, no. 1-2, pages 30–70, 1929.
- [Neumann 10] J. Neumann. *Proof of the ergodic theorem and the H-theorem in quantum mechanics*. The European Physical Journal H, vol. 35, no. 2, pages 201–237, September 2010.
- [Nowak 13] B. Nowak, S. Erne, M. Karl, J. Schole, D. Sexty & T. Gasenzer. *Non-thermal fixed points: universality, topology & turbulence in Bose gases*. arXiv:1302.1448, 2013.
- [Ockeloen 10] C. F. Ockeloen, A. F. Tauschinsky, R. J. C. Spreeuw & S. Whitlock. *Detection of small atom numbers through image processing*. Phys. Rev. A, vol. 82, page 061606, Dec 2010.
- [Olshanii 98] M. Olshanii. *Atomic Scattering in the Presence of an External Confinement and a Gas of Impenetrable Bosons*. Phys. Rev. Lett., vol. 81, no. 5, pages 938–941, Aug 1998.
- [Orzel 01] C. Orzel, A. K. Tuchman, M. L. Fenselau, M. Yasuda & M. A. Kasevich. *Squeezed States in a Bose-Einstein Condensate*. Science, vol. 291, no. 5512, pages 2386–2389, 2001.

Bibliography

- [Pain 78] H. J. Pain. The physics of vibration. Cambridge University Press, 1978.
- [Paredes 04] B. Paredes, A. Widera, V. Murg, O. Mandel, S. Fölling, I. Cirac, G. V. Shlyapnikov, T. W. Hänsch & I. Bloch. *Tonks-Girardeau gas of ultracold atoms in an optical lattice*. Nature, vol. 429, pages 277–281, 2004.
- [Perrin 12] A. Perrin, R. Bucker, S. Manz, T. Betz, C. Koller, T. Plisson, T. Schumm & J. Schmiedmayer. *Hanbury Brown and Twiss correlations across the Bose-Einstein condensation threshold*. Nat Phys, vol. 8, no. 3, pages 195–198, March 2012.
- [Pethick 01] C. J. Pethick & H. Smith. Bose-einstein condensation in dilute gases. Cambridge University Press, 2001.
- [Petrov 00] D. S. Petrov, G. V. Shlyapnikov & J. T. M. Walraven. *Regimes of Quantum Degeneracy in Trapped 1D Gases*. Phys. Rev. Lett., vol. 85, no. 18, pages 3745–3749, Oct 2000.
- [Petrov 01] D. S. Petrov, G. V. Shlyapnikov & J. T. M. Walraven. *Phase-Fluctuating 3D Bose-Einstein Condensates in Elongated Traps*. Phys. Rev. Lett., vol. 87, page 050404, Jul 2001.
- [Pitaevskii 03] Lev. P. Pitaevskii & Sandro Stringari. Bose-einstein condensation. Oxford University Press, 2003.
- [Podolsky 06] D. Podolsky, G. N. Felder & M. Kofman L.and Peloso. *Equation of state and beginning of thermalization after preheating*. Phys. Rev. D, vol. 73, page 023501, Jan 2006.
- [Polkovnikov 11] K.and Silva A. Polkovnikov A.and Sengupta & M. Vengalattore. *Colloquium : Nonequilibrium dynamics of closed interacting quantum systems*. Rev. Mod. Phys., vol. 83, pages 863–883, 2011.
- [Popov 72] V. N. Popov. *On the theory of the superfluidity of two- and one-dimensional bose systems*. Theoretical and Mathematical Physics, vol. 11, pages 565–573, 1972.
- [Popov 83] V. N. Popov. Functional integrals in quantum field theory and statistical physics. Springer, 1983.
- [PrPopov 83] V. . E. PrPopov. *Cooling Neutral Atoms in a Magnetic Trap for Precision Spectroscopy*. Phys. Rev. Lett., vol. 51, pages 1336–1339, Oct 1983.
- [Rapp 04] R. Rapp. *Theory highlights of Quark Matter 2004me*. Journal of Physics G: Nuclear and Particle Physics, vol. 30, no. 8, page S951, 2004.

Bibliography

- [Rauer 12] B. Rauer. Evaporative cooling of one-dimensional bose gases. Master's thesis, Technische Universität Wien, 2012.
- [Recati 03] A. Recati, P. O. Fedichev, W. Zwerger & P. Zoller. *Spin-Charge Separation in Ultracold Quantum Gases*. Phys. Rev. Lett., vol. 90, page 020401, Jan 2003.
- [Reichel 99] J. Reichel, W. Hänsel & T. W. Hänsch. *Atomic Micromanipulation with Magnetic Surface Traps*. Phys. Rev. Lett., vol. 83, pages 3398–3401, Oct 1999.
- [Reichel 11] J. Reichel & V. Vuletic. Atom chips. Wiley VCH, 2011.
- [Reinaudi 07] G. Reinaudi, T. Lahaye, Z. Wang & D. Guéry-Odelin. *Strong saturation absorption imaging of dense clouds of ultracold atoms*. Opt. Lett., vol. 32, no. 21, pages 3143–3145, Nov 2007.
- [Rigol 07] M. Rigol, V. Dunjko, V. Yurovsky & M. Olshanii. *Relaxation in a Completely Integrable Many-Body Quantum System: An Ab Initio Study of the Dynamics of the Highly Excited States of 1D Lattice Hard-Core Bosons*. Physical Review Letters, vol. 98, page 050405, February 2007.
- [Rigol 08] M. Rigol, V. Dunjko & M. Olshanii. *Thermalization and its mechanism for generic isolated quantum systems*. Nature, vol. 452, no. 7189, pages 854–858, April 2008.
- [Rigol 09a] M. Rigol. *Breakdown of Thermalization in Finite One-Dimensional Systems*. Phys. Rev. Lett., vol. 103, page 100403, Sep 2009.
- [Rigol 09b] M. Rigol. *Quantum quenches and thermalization in one-dimensional fermionic systems*. Phys. Rev. A, vol. 80, page 053607, Nov 2009.
- [Rigol 12] M. Rigol & M. Srednicki. *Alternatives to Eigenstate Thermalization*. Phys. Rev. Lett., vol. 108, page 110601, Mar 2012.
- [Roux 09] G. Roux. *Quenches in quantum many-body systems: One-dimensional Bose-Hubbard model reexamined*. Phys. Rev. A, vol. 79, page 021608, Feb 2009.
- [Sadler 06] L. E. Sadler, J. M. Higbie, S. R. Leslie, M. Vengalattore & D. M. Stamper-Kurn. *Spontaneous symmetry breaking in a quenched ferromagnetic spinor Bose-Einstein condensate*. Nature, vol. 443, no. 7109, pages 312–315, September 2006.
- [Santos 10] L. F. Santos & M. Rigol. *Localization and the effects of symmetries in the thermalization properties of one-dimensional quantum systems*. Phys. Rev. E, vol. 82, page 031130, Sep 2010.

Bibliography

- [Schellekens 05] M. Schellekens, R. Hoppeler, A. Perrin, J. Viana Gomes, D. Boiron, A. Aspect & C. I. Westbrook. *Hanbury Brown Twiss Effect for Ultracold Quantum Gases*. Science, vol. 310, no. 5748, pages 648–651, 2005.
- [Schmidt 12] M. Schmidt, S. Erne, B. Nowak, D. Sexty & T. Gasenzer. *Non-thermal fixed points and solitons in a one-dimensional Bose gas*. New Journal of Physics, vol. 14, no. 7, page 075005, 2012.
- [Schollwöck 05] U. Schollwöck. *The density-matrix renormalization group*. Rev. Mod. Phys., vol. 77, pages 259–315, Apr 2005.
- [Schottky 18] W. Schottky. *Über spontane Stromschwankungen in verschiedenen Elektrizitätsleitern*. Annalen der Physik, vol. 362, no. 23, pages 541–567, 1918.
- [Schreck 01] F. Schreck, L. Khaykovich, K. L. Corwin, G. Ferrari, T. Bourdel, J. Cubizolles & C. Salomon. *Quasipure Bose-Einstein Condensate Immersed in a Fermi Sea*. Phys. Rev. Lett., vol. 87, page 080403, Aug 2001.
- [Schreitl 10] M. Schreitl. Creating and purifying ultracold degenerate gases using hyperfine transitions. Master's thesis, Technische Universität Wien, 2010.
- [Schumm 05a] T. Schumm. *Bose-Einstein condensates in magnetic double well potentials*. PhD thesis, UNIVERSITE PARIS, 2005.
- [Schumm 05b] T. Schumm, S. Hofferberth, L. M. Andersson, S. Wildermuth, S. Groth, I. Bar-Joseph, J. Schmiedmayer & P. Krüger. *Matter-wave interferometry in a double well on an atom chip*. Nature Physics, vol. 1, no. 1, pages 57–62, 2005.
- [Söding 99] J. Söding, D. Guéry-Odelin, P. Desbiolles, F. Chevy, H. Inamori & J. Dalibard. *Three-body decay of a rubidium Bose-Einstein condensate*. Applied Physics B, vol. 69, pages 257–261, 1999.
- [Sinatra 98] A. Sinatra & Y. Castin. *Phase dynamics of Bose-Einstein condensates: Losses versus revivals*. The European Physical Journal D - Atomic, Molecular, Optical and Plasma Physics, vol. 4, no. 3, pages 247–260, 1998.
- [Sinatra 08] A. Sinatra & Y. Castin. *Genuine phase diffusion of a Bose-Einstein condensate in the microcanonical ensemble: A classical field study*. Phys. Rev. A, vol. 78, page 053615, Nov 2008.
- [Smith 12] R. P. Smith, S. Beattie S. and Moulder, R. L. D. Campbell & Z. Hadzibabic. *Condensation Dynamics in a Quantum-Quenched Bose Gas*. Phys. Rev. Lett., vol. 109, page 105301, Sep 2012.

Bibliography

- [Smith 13] D. Adu Smith, M. Gring, T. Langen, M. Kuhnert, B. Rauer, R. Geiger, T. Kitagawa, I. Mazets, E. Demler & J. Schmiedmayer. *Prethermalization Revealed by the Relaxation Dynamics of Full Distribution Functions*. New J. Phys. Special Issue, vol. 15, page 075011, 2013.
- [Söding 98] J. Söding, D. Guéry-Odelin, P. Desbiolles, G. Ferrari & J. Dalibard. *Giant Spin Relaxation of an Ultracold Cesium Gas*. Phys. Rev. Lett., vol. 80, pages 1869–1872, Mar 1998.
- [Srednicki 94] M. Srednicki. *Chaos and quantum thermalization*. Phys. Rev. E, vol. 50, pages 888–901, 1994.
- [Steck 01] D. A. Steck. *Rubidium 87 D Line Data*. 2001.
- [Steinhauer 02] J. Steinhauer, R. Ozeri, N. Katz & N. Davidson. *Excitation Spectrum of a Bose-Einstein Condensate*. Phys. Rev. Lett., vol. 88, page 120407, Mar 2002.
- [Stimming 10] H.-P. Stimming, N. J. Mauser, J. Schmiedmayer & I. E. Mazets. *Fluctuations and Stochastic Processes in One-Dimensional Many-Body Quantum Systems*. Phys. Rev. Lett., vol. 105, no. 1, page 015301, Jul 2010.
- [Stimming 11] H.-P. Stimming, N. J. Mauser, J. Schmiedmayer & I. E. Mazets. *Dephasing in coherently split quasicondensates*. Phys. Rev. A, vol. 83, no. 2, page 023618, Feb 2011.
- [Stix 08] B. Stix. A new imaging system for dual-species atomchip experiments. Master’s thesis, Technische Universität Wien, 2008.
- [Strohmaier 10] N. Strohmaier, D. Greif, R. Jördens, L. Tarruell, H. Moritz, T. Esslinger, R. Sensarma, D. Pekker, E. Altman & E. Demler. *Observation of Elastic Doublon Decay in the Fermi-Hubbard Model*. Phys. Rev. Lett., vol. 104, no. 8, page 080401, Feb 2010.
- [Sylow 81] L. Sylow & S. Lie. Oeuvres complètes de niels henrik abel, nouvelle édition, tome ii. Christiania, 1881.
- [Taglieber 08] M. Taglieber. *Quantum Degeneracy in an Atomic Fermi-Fermi-Bose Mixture*. PhD thesis, LMU München, 2008.
- [Taylor 08] B. N. Taylor & A. Thompson. *The International System of Units (SI)*. NIST Special Publication, vol. 330, pages 1–97, 2008.
- [Tiesinga 92] E. Tiesinga, A. J. Moerdijk, B. J. Verhaar & H. T. C. Stoof. *Conditions for Bose-Einstein condensation in magnetically trapped atomic cesium*. Phys. Rev. A, vol. 46, pages R1167–R1170, Aug 1992.

Bibliography

- [Tolra 04] B. L. Tolra, K. M. O'Hara, J. H. Huckans, W. D. Phillips, S. L. Rolston & J. V. Porto. *Observation of Reduced Three-Body Recombination in a Correlated 1D Degenerate Bose Gas*. Phys. Rev. Lett., vol. 92, page 190401, May 2004.
- [Tonks 36] L. Tonks. *The Complete Equation of State of One, Two and Three-Dimensional Gases of Hard Elastic Spheres*. Phys. Rev., vol. 50, pages 955–963, Nov 1936.
- [Trotzky 12] S. Trotzky, Y.-a. Chen, A. Flesch, I. P. McCulloch, U. Schollwöck, J. Eisert & I. Bloch. *Probing the relaxation towards equilibrium in an isolated strongly correlated one-dimensional Bose gas*. Nature Phys., vol. 8, no. 3, pages 1–6, February 2012.
- [van Amerongen 08] A. H. van Amerongen, J. J. P. van Es, P. Wicke, K. V. Kheruntsyan & N. J. van Druten. *Yang-Yang Thermodynamics on an Atom Chip*. Phys. Rev. Lett., vol. 100, no. 9, page 090402, Mar 2008.
- [van Kempen 02] E. G. M. van Kempen, S. J. J. M. F. Kokkelmans, D. J. Heinzen & B. J. Verhaar. *Interisotope Determination of Ultracold Rubidium Interactions from Three High-Precision Experiments*. Phys. Rev. Lett., vol. 88, page 093201, Feb 2002.
- [Vogels 02] J. M. Vogels, K. Xu, C. Raman, J. R. Abo-Shaeer & W. Ketterle. *Experimental Observation of the Bogoliubov Transformation for a Bose-Einstein Condensed Gas*. Phys. Rev. Lett., vol. 88, page 060402, Jan 2002.
- [vom Hagen 08] C. Graf vom Hagen. *Towards a low-dimensional degenerate Fermi-Fermi-Bose mixture*. PhD thesis, Ruperto-Carola University of Heidelberg, Germany, 2008.
- [Wang 11] J. Wang, Y. Wang, Y. Wang, G. Fang & S. Liu. *Measurements of total absolute collision cross section of ultracold Rb atom using magneto-optic and pure magnetic traps*. Chin. Opt. Lett., vol. 09, page 060201, 2011.
- [Weidemüller 03] M. Weidemüller & C. Zimmermann. *Interactions in ultracold gases*. Wiley-VCH Verlag, 2003.
- [Wetterich 12] C. Wetterich. *Prethermalization*. http://www.thphys.uni-heidelberg.de/%7Ewetteric/Talks/NonequilibriumQFT/Prethermalization_Heidelberg_0612.pdf, accessed 05.09.2012.
- [Whitlock 03] Nicholas K. Whitlock & Isabelle Bouchoule. *Relative phase fluctuations of two coupled one-dimensional condensates*. Phys. Rev. A, vol. 68, page 053609, Nov 2003.

Bibliography

- [Wick 50] G. C. Wick. *The Evaluation of the Collision Matrix*. Phys. Rev., vol. 80, pages 268–272, Oct 1950.
- [Widera 08] S. Widera A.and Trotzky, P. Cheinet, S. Fölling, F. Gerbier, I. Bloch, V. Gritsev & E. Lukin M.and Demler. *Quantum Spin Dynamics of Mode-Squeezed Luttinger Liquids in Two-Component Atomic Gases*. Phys. Rev. Lett., vol. 100, no. 14, page 140401, 2008.
- [Wildermuth 05a] S. Wildermuth. *One-dimensional Bose-Einstein condensates in micro-traps*. PhD thesis, Ruperto-Carola University of Heidelberg, 2005.
- [Wildermuth 05b] S. Wildermuth, S. Hofferberth, E. Lesanovsky I.and Haller, L. M. Andersson, S. Groth, P. Bar-Joseph I.and Kruger & J. Schmiedmayer. *Bose-Einstein condensates Microscopic magnetic-field imaging*. Nature, vol. 435, no. 7041, pages 440–440, May 2005.
- [Wildermuth 06] S. Wildermuth, S. Hofferberth, I. Lesanovsky, S. Groth, P. Kruger, J. Schmiedmayer & I. Bar-Joseph. *Sensing electric and magnetic fields with Bose-Einstein condensates*. Applied Physics Letters, vol. 88, no. 26, page 264103, 2006.
- [Wing 84] W. H. Wing. *On neutral particle trapping in quasistatic electromagnetic fields*. Progress in Quantum Electronics, vol. 8, pages 181–199, 1984.
- [Yasuda 96] M. Yasuda & F. Shimizu. *Observation of Two-Atom Correlation of an Ultracold Neon Atomic Beam*. Phys. Rev. Lett., vol. 77, pages 3090–3093, Oct 1996.
- [Zhang 01] Y.-B. Zhang & H.J.W. Müller-Kirsten. *Instanton approach to Josephson tunneling between trapped condensates*. The European Physical Journal D - Atomic, Molecular, Optical and Plasma Physics, vol. 17, pages 351–363, 2001. 10.1007/s100530170010.
- [Zurek 09] W. H. Zurek. *Quantum Darwinism*. Nature Physics, vol. 5, pages 181–188, 2009.

F Appendix F.

Curriculum Vitae

Personal Data

Name: Maximilian Kuhnert
Date of Birth: Vienna, February 13, 1982
Nationality: Austria
Email: kuhnert@ati.ac.at
Languages: German (mother tongue), English (fluent), French (basic), Spanish (basic)

Education

Since 2008 PhD student in the group of Jörg Schmiedmayer at the Vienna University of Technology
2001-2008 Master of Technical Physics, Vienna University of Technology, Vienna, Austria
thesis topic: *A Dual-Species Two-MOT Setup for Preparing a Bose-Fermi Mixture on an Atom Chip*, (with distinction), Advisors: Dr. David Adu Smith, Prof. Jörg Schmiedmayer
2000 BRG Haizingergasse 18, 1180 Vienna

F. Curriculum Vitae

Research Interests

Non-Equilibrium Dynamics, Thermalization in Many-Body Quantum Systems, Ultracold Bose-Fermi-Mixtures, Cold and Ultracold Molecules, Molecular Spectroscopy

Research Visits

- 2013 Prof. Jun Ye, JILA, University of Colorado, June - August, Boulder, USA
2011 Prof. Tilman Esslinger, ETH Zürich, Laser Frequency Stabilization using a frequency comb as reference, February - April, Zürich, Switzerland

Engagement in Public Outreach Activities

- Lab and reactor tours for the general public and visiting school classes, 2010-2013
- Long Night of Research in Vienna, 2012
- Summer University for school children, 2011
- Liquid Nitrogen hands on experience, 2010-2013

Publications

Relaxation and Prethermalization in an Isolated Quantum System

M. Gring, M. Kuhnert, T. Langen, T. Kitagawa, B. Rauer, M. Schreitl, I. E. Mazets, D. Adu Smith, E. Demler and J. Schmiedmayer
Science, 337, 1318-1322 (2012)

Multimode dynamics and emergence of a characteristic length-scale in a one-dimensional quantum system

M. Kuhnert, R. Geiger, T. Langen, M. Gring, B. Rauer, T. Kitagawa, E. Demler, D. Adu Smith and J. Schmiedmayer
Phys. Rev. Lett., 110, 090405 (2013)

Prethermalization Revealed by the Relaxation Dynamics of Full Distribution Functions

D. Adu Smith, M. Gring, T. Langen, M. Kuhnert, B. Rauer, R. Geiger, T. Kitagawa, I. E. Mazets, E. Demler and J. Schmiedmayer
New J. Phys. 15 075011 (2013)

Prethermalization in one-dimensional Bose gases: description by a stochastic Ornstein-Uhlenbeck process

F. Curriculum Vitae

T. Langen, M. Gring, M. Kuhnert, B. Rauer, R. Geiger, D. Adu Smith, I. E. Mazets and J. Schmiedmayer

The European Physical Journal Special Topics, 217, 43-53, (2013)

Local emergence of thermal correlations in an isolated quantum many-body system

T. Langen, R. Geiger, M. Kuhnert, B. Rauer and J. Schmiedmayer

Nat. Phys. 9, 640-643, 2013

Thermalization and Prethermalization in the 1D/3D Crossover

M. Kuhnert, T. Langen, R. Geiger, B. Rauer, T. Schweigler, I. Mazets and J. Schmiedmayer

in preparation